Author:
Jenkins, Josh J

Title:
An Alternative Approach to Combat Antimicrobial Resistant Infections of Medical Implants and Devices

An Alternative Approach to Combat Antimicrobial Resistant Infections of Medical Implants and Devices

Joshua Jack Jenkins

A dissertation submitted to the University of Bristol in accordance with the requirements for award of the degree of

Doctor of Philosophy in the Faculty of Health Sciences

Bristol Dental School

September 2019

Word count: 59,105

ABSTRACT

Dragonfly wings have evolved surface nanoprotrusions that are reported to induce mechanical rupture and lysis of bacteria and fungi upon contact. This unique antimicrobial mechanism has drawn significant research interest, as the physical nature of killing could provide an effective strategy to prevent infections of medical implants and devices, whilst negating the current need to use materials impregnated with antibiotics. To date, no consensus has been reached on the precise mechanism that leads to microbial cell death on nanotextured materials, addressing this fundamental knowledge gap is crucial to facilitate the translation of this technology into clinical applications. In this study, dragonfly mimetic nanotopographies were generated on grade 5 titanium alloy (Ti-6Al-4V) using a simple, low-cost and scalable thermal oxidation technique. Multiple experimental approaches were employed to robustly assess bacterial physiology on dragonfly mimetic nanotopographies, including culture based and microscopic investigations (CFU analysis and LIVE/DEAD staining), biochemical methods (BacTiter-Glo and RealTime-Glo) and quantitative proteomic analysis. Dragonfly mimetic nanotopographies mediated time-dependent antibacterial effects toward Gram-positive (*Staphylococcus aureus* and *Staphylococcus epidermidis*) and Gram-negative (*Escherichia coli* and *Klebsiella pneumoniae*) bacteria, with enhanced activity against Gram-negative cell types. To obtain a more complete and accurate understanding of the antibacterial mechanism, advanced imaging techniques including SEM, TEM tomography and focused ion beam milling, were used to determine the effect of dragonfly mimetic nanotopographies on Gram-positive and Gram-negative envelope morphology and ultrastructure. Here we show four possible mechanisms via which dragonfly mimetic nanotopographies mediate antibacterial effects: 1) nanowire-induced envelope deformation, 2) nanowire-induced envelope penetration, 3) nanowire-induced cell impedance and 4) nanowire-induced oxidative stress. Of note, nanowire-induced envelope deformation and penetration was most prominent in Gram-negative bacteria, yet this did not result in mechanical rupture and lysis of the cell.

ACKNOWLEDGEMENTS

I would like to express my gratitude to my supervisors, Prof. Bo Su, Dr. Angela Nobbs and Prof Paul Verkade for their guidance, intellect and encouragement throughout my PhD. I would also like to extend my appreciation to the research technicians who provided training and technical support. To Dr. Terje Sjöström for training me in thermal oxidation. To Dr. Lindsay Dutton and Dr. Jane Brittan for training me in microbiological techniques. I would also like to thank the Wolfson Bioimaging Facility, which has provided continued support throughout this project: To Judith Mantell for training and guidance using the SEM and TEM and for helping to explain and analyse complex tomography data. To Dr. Chris Neal, for his willingness to cut "just one more" TEM section. I would also like to acknowledge Dr. Ali Gholinia for his help in FIB-SEM analysis and to the members of DESY NanoLab for access to their FIB-SEM and XPS equipment. A special thanks to Marcus Eales and Irill Ishak for all their help in experimental work and advice.

Finally, I would like to thank my entire family for their continued support and encouragement during my PhD and most of all, I am forever grateful to Jess, for keeping me focused and driven to realise my goals.

AUTHOUR`S DECLARATION

I declare that the work in this dissertation was carried out in accordance with the requirements of the University's Regulations and Code of Practice for Research Degree Programmes and that it has not been submitted for any other academic award. Except where indicated by specific reference in the text, the work is the candidate's own work. Work done in collaboration with, or with the assistance of, others, is indicated as such. Any views expressed in the dissertation are those of the author.

SIGNED:…….. DATE:…….

TABLE OF CONTENTS

LIST OF EQUATIONS, FIGURES AND TABLES

CHAPTER 1

Introduction

1.1 Prosthetic joint replacement

In the last century, significant progress has been made in developing new and more effective treatments for human diseases. As a result of medical advancement, adults in developing countries are living longer (Gautreau et al., 2016), with the global average life expectancy approaching 70 years; a two-fold increase since 1900 (Roser, 2019). As such, a significant proportion of the world's population are currently over 65 years, specifically, 15% of the population in the United States (US), 16% in Canada, 18% in the United Kingdom (UK), 20% in Sweden and 26% in Japan (Gautreau et al., 2016; Storey, 2018). Alongside the global rise in life expectancy, an increasing number of the patients are developing chronic conditions, such as arthritis and musculoskeletal disorders. Conditions such as these are accelerated by the aging process and are further exacerbated by obesity, which increases the risk of joint injury or damage (Briggs, 2011). Recent estimates from the World Health Organisation (WHO) indicate that global obesity has nearly tripled since 1975, with approximately 1.9 billion adults being overweight or obese (World Health Organization, 2018). Consequently, an increasing number of patients are being referred to orthopaedic care each year, to undergo prosthetic joint replacement (PJR). The fundamental aim of PJR is to replace a damaged or diseased joint such that the original joint function is restored. PJR are currently performed on millions of patients each year globally, and this is expected to rise substantially over the next decade, driven by population ageing and rising levels of obesity (Briggs, 2011; Tande and Patel, 2014).

The NHS allocates 10 billion GBP a year for the treatment of musculoskeletal disorders, which comprise over 25% of all surgical interventions performed annually (Briggs, 2011). Orthopaedic specialties, including hip and knee replacements constitute a significant proportion of these operations. In 2003/04 the National Joint Registry (NJR) recorded a total of 62,191 hip and knee replacement procedures; nearly a decade later in 2012/2013, a total of 192,332 were recorded, representing just under a fourfold increase (Figure 1.1) (Drury et al., 2007; Porter et al., 2013). Analysis performed by the Swedish Hip Arthroplasty Registry, forecast that by 2030, a total of 83,600 total hip replacements will be performed, in comparison to the 16,021 performed in 2013 (Arciola et al., 2015). Another example of the expansion of orthopaedic procedures can be seen in the US. Recent projections have estimated that by 2030

the number of primary hip and knee arthroplasties will reach 572,000 and 3.48 million respectively, which equates to a percentage increase of 174% and 673% from 2005 (Kurtz, 2007).

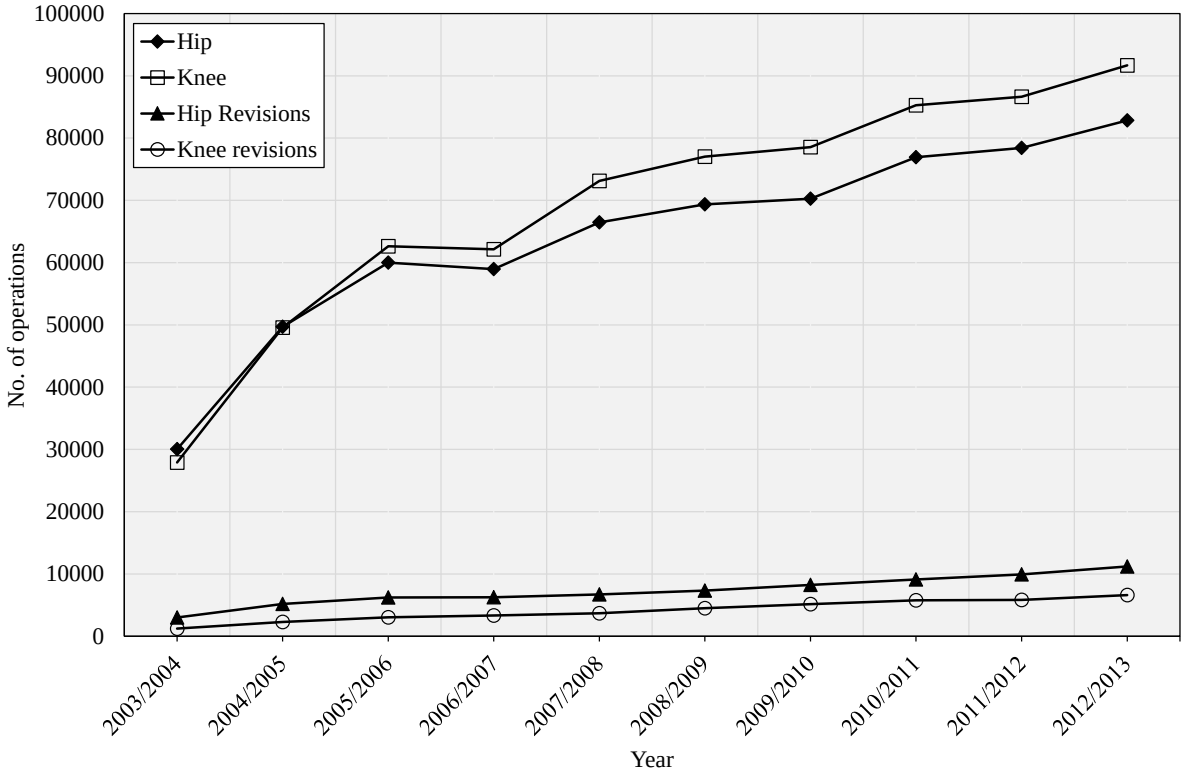

Figure 1.1 | Trends in hip and knee replacements and revision procedures, within NHS and independent hospitals between 2003-2013. (Drury et al., 2007; Porter et al., 2013).

1.2 Titanium and titanium alloys as medical implants

The increasing demand for joint replacement has driven the search for materials that can suitably mimic the biomechanical properties of bone. To date, titanium and its alloys have proved good matches for hard tissue replacements, finding applications in prosthetic joints, dental implants, surgical splints, stents and screws (Figure 1.2) (Viteri and Fuentes, 2013). Commercially pure titanium (cp Ti, grade 2) and Ti-6Al-4V (grade 5) alloy are among the most frequently used, with dental implants often consisting of cp titanium while Ti-6Al-4V is favoured for hip and knee implants, owing to its higher tensile and yield strength (Shah et al., 2016). Allotropism is another notable characteristic of titanium and its alloys. This denotes the ability of titanium atoms to switch between crystal structures (unit cell arrangements) in a temperature dependent manner. For cp titanium, allotropic transformation occurs at 883°C, whereby titanium atoms rearrange from a hexagonal close-packed (HCP) unit cell structure, also known as the alpha(α)-phase, to a body centred cubic (BCC) unit cell structure, also known as the beta(β)-phase. For Ti-6Al-4V, the presence of alloying elements increases the allotropic transformation temperature (980°C) (Dinan, 2012). This has important implications for the growth of nanowire arrays on titanium, that are discussed at the end of this chapter.

The extensive use of titanium and its alloys relates to their desirable chemical and mechanical properties. Firstly, titanium has a low density and high strength to weight ratio compared to other common metals (i.e. steel), making it suitable as a light weight, load bearing replacement for joints and teeth. However, the most notable property of titanium relates to its biocompatibility, reducing the chance of adverse tissue reactions. The biocompatibility of titanium stems from its ability to form a stable oxide layer in ambient air, resulting in a chemically passive and corrosion resistant barrier. Furthermore, the titanium oxide layer promotes implant osseointegration, the process by which new bone formation helps to fix the implant within the surrounding hard tissues (ADA council, 2003; Viteri and Fuentes, 2013).

a

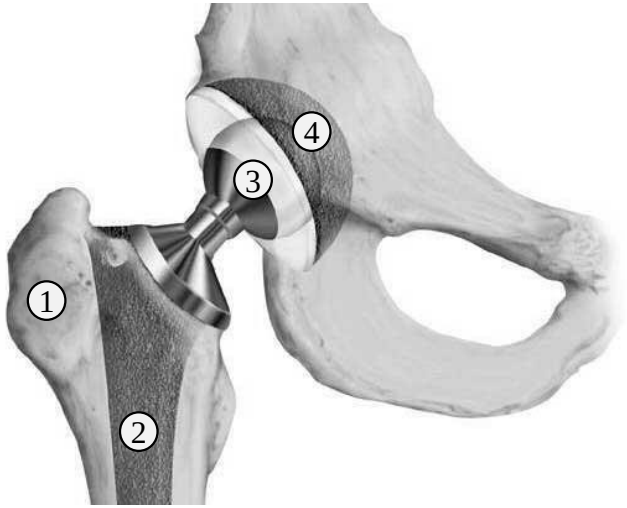

① Femur
② Femoral stem
③ Femoral head
④ Acetabular component

b

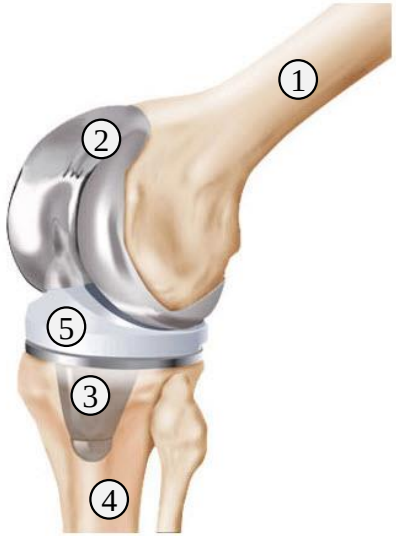

① Femur
② Femoral component
③ Tibial component
④ Tibia
⑤ Spacer

c

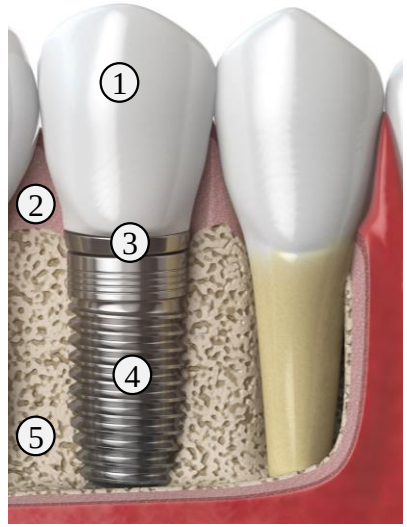

① Artificial tooth crown
② Gum tissue
③ Implant abutment
④ Ti screw
⑤ Bone

Figure 1.2 | Titanium implants. Total hip replacement (a), total knee replacement (b) and dental implant (c). (www.healthpages.org, titanium hip implant), (www.cobourgosic.com, titanium knee implant), (www.elitesmilessc.com, titanium dental implant).

1.3 Titanium implant failures

Millions of patients undergo PJR each year, and for the vast majority, these occur successfully, resulting in the restoration of joint function, mobility and alleviation of pain (Tande and Patel, 2014). Nonetheless, there are a number of complications which can arise post-surgery, which increase the probability of device failure and necessitate revision surgery. In the UK, the leading cause for prosthetic joint failure is aseptic loosening, accounting for 44.5% of hip revisions and 32.7% of knee revision (Porter et al., 2018). This is where the connection between bone and the implant fails, resulting in loosening. Other complications include pain, lysis, implant wear and dislocation (Table 1.1). Many of the above complications will develop over time (i.e. implant wear), however, in the first year following PJR, infection is the leading cause for revision surgery and represents one of the most serious, life-threatening and expensive complications that can develop (Porter et al., 2018; Tande and Patel, 2014).

Table 1.1 | Reasons for hip and knee revision operations within NHS and independent hospitals between 2002-2017 (Porter et al., 2018).

Reason for revision	Hip revisions	Knee revisions	Total revisions
Aseptic loosening	47,267	22,250	69,517
Adverse reaction to particulate debris	8,583	-	8,583
Dislocation	14,887	2,428	2,428
Head-socket size mismatch	723	-	723
Infection	13,885	15,311	29,196
Implant wear	13,536	8,061	21,597
Instability	-	9,961	9,961
Implant fracture	3,498	722	4,220
Lysis	15,019	6,315	21,334
Malalignment	5,307	4,417	9,724
Other indication	7,661	11,937	19,598
Pain	19,098	9,650	28,748
Periprosthetic fracture	10,293	2,341	12,634
Stiffness	-	3,384	3,384

1.4 Prosthetic joint infections

Infections that develop following PJR, referred to as prosthetic joint infections (PJI), are predominantly caused by bacteria (Cataldo et al., 2010), and to a lesser extent, fungi (Cobo et al., 2017). This process only requires a few microorganisms to colonise the surgical site or prosthesis (Von Eiff et al., 2005). The exact route via which bacteria contaminate the implant, and the stage at which patients develop symptoms of infection may vary. As such, PJIs can be broadly classified into three stages depending on the point at which infections develop (Arciola et al., 2015; Honkanen et al., 2019; Moran et al., 2010):

1) Early stage or acute post-operative infections generally occur within the first three months post-surgery. These infections are usually the result of bacterial contamination during implantation and are most likely to originate from the patient's commensal microbiota. However, it is also possible to contract infections from surgical staff or the surrounding environment during hospitalisation.
2) Delayed post-operative infections are observed between 3-24 months after surgery. The route of infection in this case is often the same as above; however, the bacterium causing infection may be less virulent, explaining the delayed onset.
3) Late post-operative infections generally arise between 12-24 months post-surgery, and in most cases are the result of haematogenous spreading of bacteria. In this case, PJI can occur due to colonisation of the sterile prosthesis during bacteraemia.

The majority of PJI are caused by staphylococci, which are isolated in over 50% of cases (Arciola et al., 2015; Cataldo et al., 2010; Stefánsdóttir et al., 2009). The high prevalence of staphylococci relates to their status as skin microflora, which increases the probability of entering the surgical site. The most common staphylococci found include methicillin-sensitive *S. aureus* (MSSA), methicillin-resistant *S. aureus* (MRSA) and coagulase-negative staphylococci (CoNS) such as *Staphylococcus epidermidis* (Arciola et al., 2018). PJI that are mediated by staphylococci can be especially difficult to treat, owing to high levels of antibiotic resistance, immune evasion and most importantly, biofilm tolerance, a topic discussed in the following section (Valour et al., 2013; Yang et al., 2018). Streptococci generally account for < 10% of PJI, most of these have acute onset with patients presenting with fever and systemic symptoms (Tande and Patel, 2014).

The next most common infecting microorganisms are enterococci, which account for <15% of PJI, and aerobic Gram-negative bacilli (*Escherichia coli*, *Klebsiella pneumoniae* and *Pseudomonas aeruginosa*), which generally constitute a similar proportion (Stefánsdóttir et al., 2009; Tande and Patel, 2014). These bacteria are frequently isolated from acute polymicrobial infections and are likely to originate from the gastrointestinal tract. In contrast, patients with monomicrobial enterococcal infections generally show delayed onset of symptoms, owing to the reduced virulence of enterococci (Tande and Patel, 2014). Fungi are responsible for < 1% of PJI, with the majority of these caused by *C. albicans*. Of note, most fungal infections occur after revision surgery, not the primary replacement. This is suspected to be caused by antibiotic use, which clears the site for fungal colonisation (Tande and Patel, 2014).

Patients suspected of having a PJI often require increased wound drainage and will present with pain and impaired wound healing around the surgical site (Osmon et al., 2013). In the case of haematogenous spread, systemic infection may occur. The exact incidence of PJIs varies between different countries and hospital centres. In the UK, the national infection rate following PJR is between 1-5% and this reduces significantly in specialist orthopaedic hospitals (0.2%). A significant financial burden is placed on the NHS due to PJI; a single infection from a total hip or knee replacement can accumulate costs of £75,000-100,000 per patient, which is significantly higher than successful procedures (£5,000-10,000). If the incidence of PJI could be reduced to its lowest national rate, the NHS would stand to make annual savings of £200 - 300 million, which would cover the cost of an additional 60,000 joint replacements each year (Briggs, 2016, 2011). The incidence of PJI following hip and knee replacement is similar in the US (2-2.4%) and is also associated with a significant cost. Between 2001 and 2009, the annual cost of treating PJI increased from $320 million to $566 million, and this is expected to reach $1.62 billion by 2020 (Kurtz et al., 2012). Although the incidence of PJI remains low after primary hip and knee replacement (< 5%), the total number of infections are projected to increase significantly in the coming decade, in line with the rising demands for PJR surgery. Furthermore, while the incidence of PJI is low following primary PJR, the risk of infection increases substantially following revision surgery, with an incidence of 20% (Cataldo et al., 2010).

Conventionally, PJI are treated using a combination of antibiotic therapy and revision surgery. Although antibiotics are frequently used, there are significant variations in practice with respect to the type of antibiotic(s), the route of drug administration and the duration of therapy (Table 1.2). This will also be influenced by patient comorbidities and the type of surgical intervention that is performed, if any (Moran et al., 2010). In general, the choice of antibiotic is informed by the infecting microorganism(s) and the antibiotic resistance profile (Von Eiff et al., 2005).

In most cases, surgical intervention is required to treat and resolve a PJI. As for antibiotic treatment, there is significant variation with respect to the type of surgical procedure that is performed, again, this will depend on the type of infection and patient history. In patients with multiple-comorbidities (i.e. fragile, diabetes, cancer), it is common for no surgical intervention to be performed, instead long-term antibiotics may be used to supress the infection. For patients that can undergo surgery, there are four possible approaches: 1) Debridement, antibiotics and implant retention (DAIR), 2) one-stage revision, 3) two-stage revision and 4) full amputation. The DAIR approach is most commonly used for patients which have well-fixed, functional implants and where the causative microorganism has been identified as showing antibiotic susceptibility. In this approach, the prosthesis is retained while the surrounding infected tissue is removed (debridement) and the appropriate antibiotic is administered. In situations where the infected prosthesis must be removed (i.e. pain or implant loosening), this can be achieved by a one or two-stage revision. For one-stage revisions, the entire infected prosthesis is removed, and the infected area is debrided before the insertion of a new prosthesis with antibiotic loaded bone cement. In contrast, for two-stage revision surgery the new prosthesis is implanted several weeks after the infected implant is removed and debrided. Finally, in extreme cases, amputation may be required to resolve the infection (Moran et al., 2010). Because of the complex surgical procedures that are required, and prolonged use of antimicrobials, the financial costs of revision are far greater than the initial operation. For instance, the cost of one-stage and two-stage revisions are 3 and 6 times greater than the initial implantation surgery (Tande and Patel, 2014).

Despite significant improvements in surgical revision, they are not a cure. The success rate of DAIR varies from 31-82%, while one and two-stage revisions are generally more effective (>70%) (Tande and Patel, 2014). The difficultly in treating PJI is in part, attributed to the ability of bacteria to form biofilms, which display high levels of antibiotic resistance and tolerance. These are discussed in the following sections.

Table 1.2 | Intravenous antimicrobial treatments for bacteria commonly isolated from PJR. Antimicrobial selection is based on *in vitro* susceptibility testing and patient allergies or intolerances (Osmon et al., 2013).

Microorganism	Preferred treatment	Alternative treatment	Duration
Staphylococci, oxacillin-susceptible	Nafcillin, Cefazolin or Ceftriaxone	Vancomycin, Daptomycin or Linezolid	4-6 weeks
Staphylococci, oxacillin-resistant	Vancomycin	Daptomycin or Linezolid	4-6 weeks
Enterococcus spp, penicillin-susceptible	Penicillin G or Ampicillin	Vancomycin, Daptomycin or Linezolid	4-6 weeks
Enterococcus spp, penicillin-resistant	Vancomycin	Daptomycin or Linezolid	4-6 weeks
P. aeruginosa	Cefepime or Meropenem	Ciprofloxacin or Ceftazidime	4-6 weeks
Enterobacter spp	Cefepime or Ertapenem	Ciprofloxacin	4-6 weeks
Enterobacteriaceae	Beta-lactam or ciprofloxacin	-	4-6 weeks
β-haemolytic streptococci	Penicillin G or Ceftriaxone	Vancomycin	4-6 weeks

1.5 Antibiotic resistance: a historical perspective and the current state of play

At the start of the 20th century, infectious diseases contributed significantly to worldwide morbidity and mortality. Between 1900 and 1910, infections such as tuberculosis, pneumonia and cholera were among the top 5 causes of death in the US, while mortality attributed to cancer was lower than causes of accidental death (Centers for Disease Control and Prevention, 1998). The discovery of penicillin in 1928 by Alexander Fleming marked the turning point in the fight against bacterial infections and led to a golden era of antibiotic discovery in which many new antibiotic classes were identified (Adedeji, 2016). Antibiotics have since become an integral part of modern medicine, underpinning the success of many clinical areas, including cancer therapy, surgery and intensive care (Blair et al., 2014). However, bacterial resistance to antibiotics has rapidly emerged in recent times and is now widely recognised as a serious threat to global health. The clinical outcome for patients infected with multidrug resistant (MDR) strains of bacteria is typically far worse than for patients infected by susceptible strains of the same bacterium. As a direct consequence, these infections lead to increased patient mortality and higher healthcare costs. Each year, MDR bacterial infections are accountable for approximately 25,000 patient deaths in EU countries; the associated cost of dealing with this problem is estimated to be €1.5 billion. A similar scenario is unfolding in the US, where 23,000 patient deaths are linked to MDR bacterial infections each year (Blair et al., 2014). If action is not taken to combat antimicrobial resistance (AMR), the future socioeconomic costs will be immense, with drug resistant infections estimated to claim 10 million lives each year by 2050 (Figure 1.3), resulting in costs extending to 100 trillion USD (O'Neill, 2014).

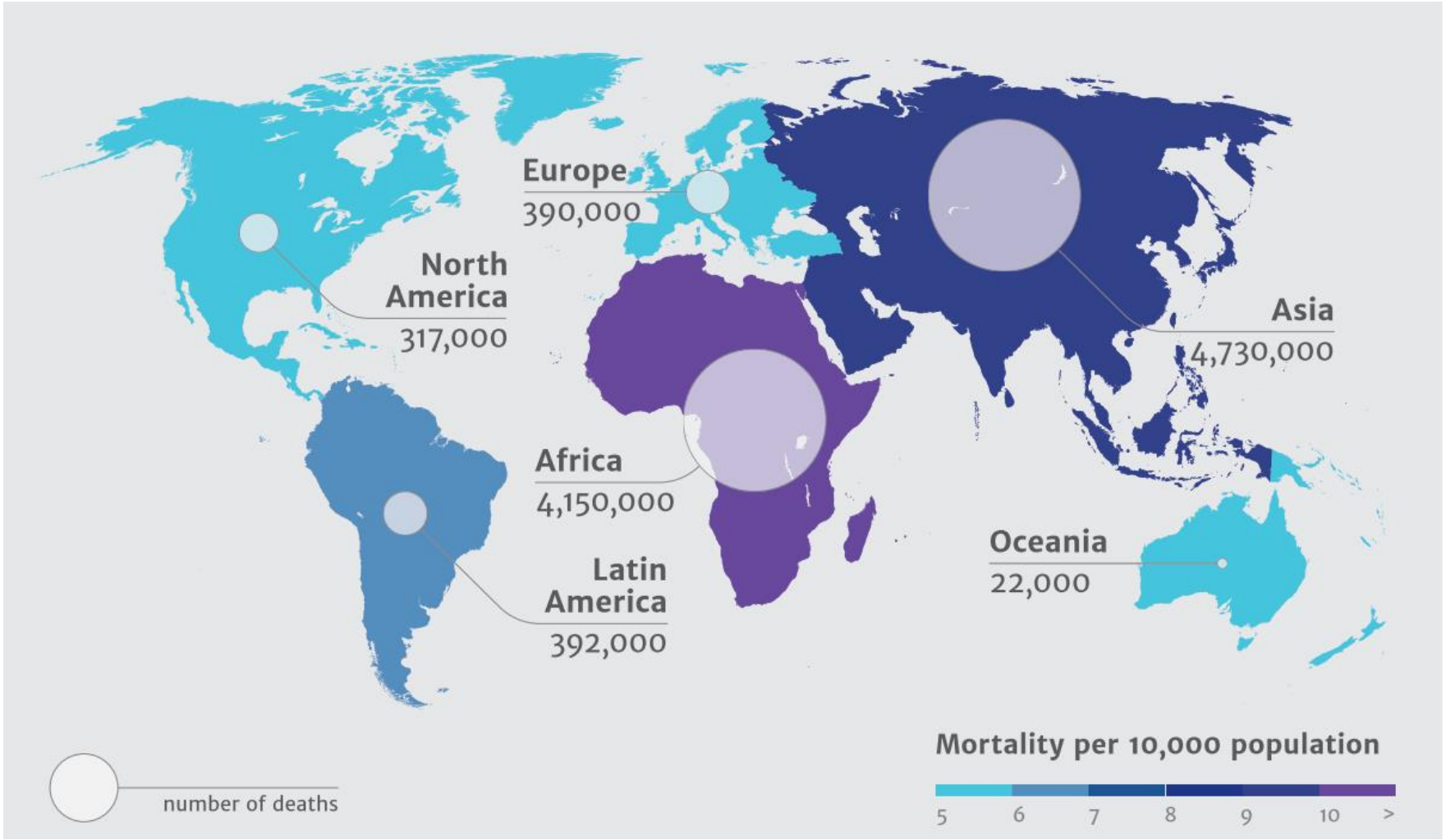

Figure 1.3 | Map of the world showing the projected deaths attributed to AMR by 2050 (O`Neil et al., 2014).

There are numerous mechanisms by which bacteria have developed resistance to antibiotics. These include i) enzymatic inactivation, such as β-lactamases that hydrolyse β-lactam antibiotics; ii) target site modifications, whereby mutations lead to structural changes in antibiotic targets; iii) replacement of the antibiotic targets, such that current antibiotics are no longer effective; or iv) changes in permeability and drug efflux, which exclude antibiotics from the bacterial cell or increase their removal (Blair et al., 2014).

Normally, individual mechanisms confer resistance to specific antibiotics, which enables bacteria to survive higher antibiotic concentrations, regardless of the dose duration. However, bacteria can also develop tolerant or persistent phenotypes, which can render many antibiotics ineffective. Tolerance describes a phenomenon whereby bacteria can survive temporary exposure to a high concentration of antibiotic, without changing the minimum inhibitory concentration (MIC) of that antibiotic; this phenotype is often caused by reduced metabolism in response to limiting environmental conditions. In contrast, persistence relates to the ability of a sub-population of bacteria to outlive the rest of a population when exposed to an antibiotic, despite the population being clonal (Brauner et al., 2016). The differences between resistance, tolerance and persistence are shown in Figure 1.4. Both tolerance and persistence are often observed in biofilms, which contribute significantly to human infections, including those relating to titanium prostheses.

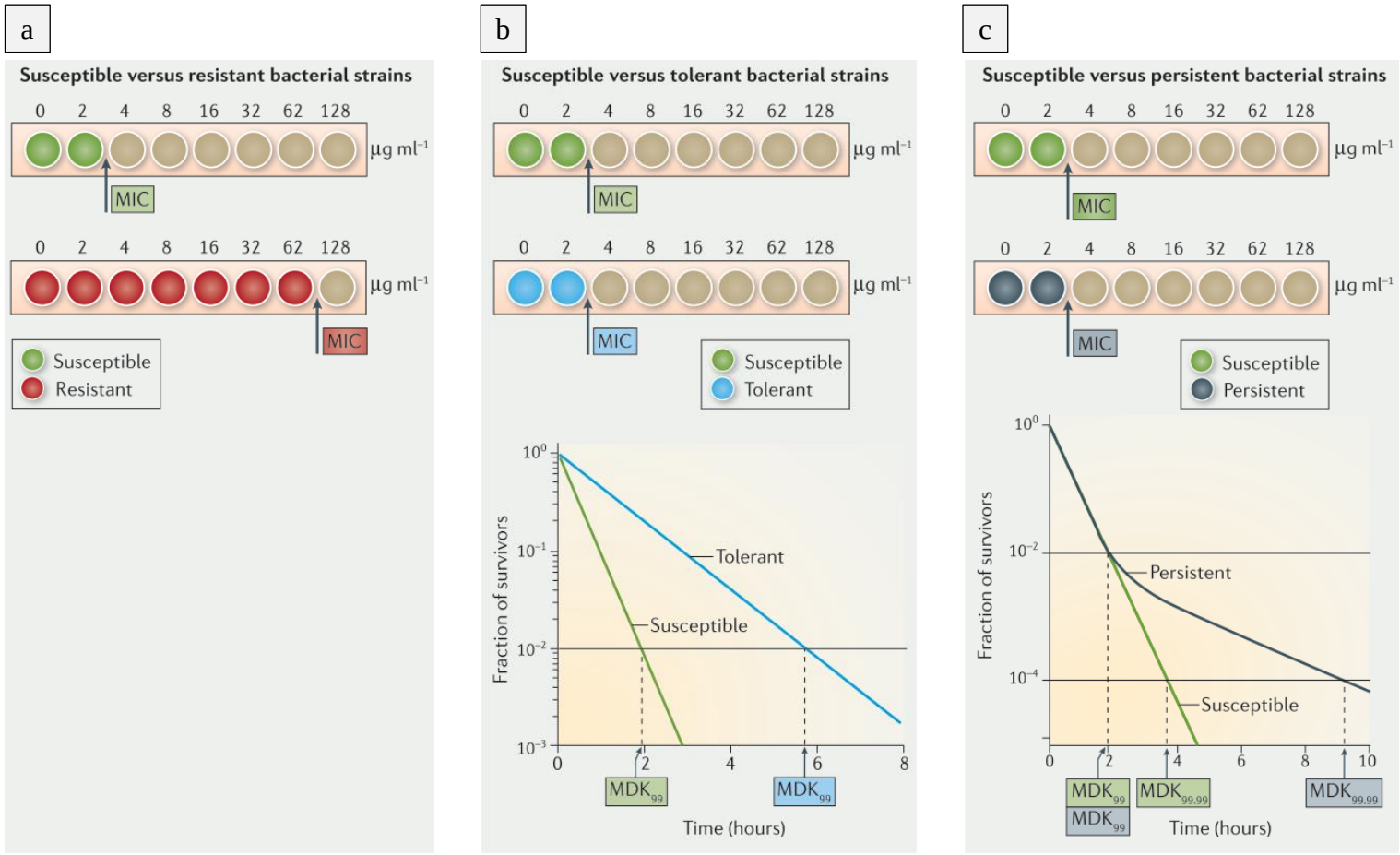

Figure 1.4 | Characteristic drug responses of resistant, tolerant or persistent bacterial populations. Resistance phenotypes display MIC values that are significantly higher than susceptible strains (a). Tolerant strains of bacteria display similar MIC values to susceptible strains, however, the minimum duration of killing for 99% of the bacterial population (MDK_{99}) is significantly higher than a susceptible strain (b). Biofilm phases frequently exhibit tolerance to antibiotic therapies, owing to reduced metabolic activity. A persistent phenotype will often display similar MIC and MDK_{99} values to susceptible strains, however, the MDK for 99.99% ($MDK_{99.99}$) of bacterial cells is significantly greater than the $MDK_{99.99}$ for a susceptible strain (Brauner et al., 2016).

1.6 Biofilms

Bacteria have evolved the ability to survive and proliferate in two forms, the first of which is described as a planktonic state. This is characterised primarily as single-cells, suspended in liquid culture medium (Hall-Stoodley et al., 2004). Over the past century, pure broth cultures have been the predominant method used to cultivate bacteria for microbiological analysis (Bjarnsholt et al., 2013; Flemming and Wingender, 2010). However, outside of these laboratory conditions, bacteria often exist as part of complex ecological communities known as biofilms. The broad definition of a biofilm is a multicellular aggregation of bacteria, attached to a surface, that is embedded within a self-produced matrix comprised of extracellular polymeric substance (EPS) (Davey and O'Toole, 2000; Flemming et al., 2016). The ability to form biofilms is considered a hallmark of prokaryotes, and this is supported by early fossil records (3.2 - 3.4 billion years ago), which have revealed spherical and rod-shapes assembled into biofilm-like structures (Hall-Stoodley et al., 2004; Westall et al., 2001). Today, biofilms are ubiquitous, having been identified in a diverse range of environments, spanning from deep-sea hydrothermal vents (Anantharaman et al., 2016) to plant roots (Davey and O'Toole, 2000) to the microbiota of multicellular organisms (Gilbert et al., 2018).

As members of the resident microbiota, bacteria can perform essential functions within the human digestive system or oral cavity, and can contribute to the skin serving as a barrier (Gilbert et al., 2018). However, the symbiotic relationships between humans and bacteria are not always mutualistic; several infections are associated with the uncontrolled growth of biofilms, including cystic fibrosis, periodontitis, chronic wounds and orthopaedic implant infections (Bjarnsholt et al., 2013). Indeed, the role of biofilms in infections is widely acknowledged today, with the Centre for Disease Control and Prevention (CDC) and National Institute for Health (NIH) indicating that biofilms are involved in the majority of infections (65% and 80% respectively) (Joo and Otto, 2012). Understanding how biofilms are formed and their characteristics is key to the development of novel anti-biofilm strategies.

1.7 The life cycle of a biofilm

The transition from a planktonic to a surface-attached lifestyle is a complex and multifactorial process in bacteria, governed by the expression of a biofilm phenotype and a number of physical and chemical forces (Davey and O'Toole, 2000; Sauer, 2003).

1.7.1 Surface discovery

Bacteria can reach the surface via two approaches: active or passive movement (Berne et al., 2018). The former requires the expression of specialised flagella proteins that propel the bacteria through a liquid medium in response to chemoreceptor activation. Many bacteria have evolved mechanisms to follow chemical and physical gradients. One such example is the switch complex found in *E. coli*. In this system, transmembrane chemoreceptors are activated by environmental stimuli (nutrients, oxygen, temperature), resulting in the phosphorylation of chemotaxis protein CheY, which in turn binds to the flagella protein FliM within the switch complex, initiating clockwise flagella rotations (Paul et al., 2011). Alternatively, nonmotile bacteria reach the surface by passive movement, which is partly influenced by Brownian motion and gravitational forces. Another critical factor that determines the efficiency of attachment are the hydrodynamic forces exerted on bacteria. To reach the surface, bacteria must transition from the bulk liquid and surpass the hydrodynamic boundary layer (liquid-surface interface), where flow dynamics generated by the surface can lead to strong shear forces that hinder attachment (Berne et al., 2018).

1.7.2 Attachment

Upon reaching close proximity to the surface, the fate of bacterial adhesion is then influenced by a number of attractive and repulsive forces, which originate from the bacterial cell, the surface interface and the microenvironment. Ultimately, it is the sum of these interactions that dictates whether or not a bacterium colonises a surface (Garrett et al., 2008). According to the extended DVLO theory (Derjagiun, Verwey, Landau and Overbeek), bacteria experience a combination of forces when in close proximity to a surface; these include Lifshitz-van der Waals interactions (generally attractive), electrostatic interactions (influenced by osmolarity and pH), acid-base hydrophobic interactions (influenced by local environment) and steric forces (Chen and Strevett, 2003; Hermansson, 1999). The micro- and nano- topography of surfaces is another important determinant of bacterial attachment. Micropatterning of stainless steel has been shown to increase the retention of *P. aeruginosa* and streptococci; of note, retention was greatest on surfaces with roughness values close to the size of the bacteria (Flint et al., 2000; Medilanski et al., 2002). In contrast, literature regarding the impact of nanopatterning on bacterial adhesion is generally conflicting, with evidence that nanoscale features can both promote and reduce bacterial adhesion, depending on the precise feature size and shape (Berne et al., 2018).

The charge and topography of surfaces can be masked by the absorption of macromolecules (proteins, lipids, carbohydrates), forming what is commonly known as a conditioning layer. Conditioning layers are generated immediately when solid surfaces are placed into aqueous environments, and therefore, the composition will vary depending upon the type of medium and bacteria present. Consequently, the physicochemical properties of a surface can change significantly, which in turn will influence bacterial attachment. Conditioning films have been reported to have both inhibitory and promoting effects on bacterial adhesion and biofilm formation (Berne et al., 2018; Cheng et al., 2019; Dunne, 2002).

The interactions described by the extended DVLO theory are relatively weak, meaning that bacterial attachment is reversible following initial adsorption. To overcome this, bacteria have evolved many extracellular appendages that can mediate firm adhesion, such as curli, pili, fimbriae and non-fimbriae adhesins (Figure 1.5). For example, in *E. coli,* initial attachment is mediated by type-1 fimbriae and, upon sensing the surface, FimH adhesin undergoes conformational changes to mediate irreversible attachment. Biofilm formation is significantly hindered in *E. coli* strains deficient in this appendage (Berne et al., 2018; Pratt and Kolter, 1998). Fimbriae are also important for colonisation in other Gram-negative pathogens such as *K. pneumoniae* (type-1 and -3 fimbriae) (Martino et al., 2003; Murphy et al., 2013) and *P. aeruginosa* (type-4 fimbriae) (Berne et al., 2015). In Gram-positive bacterium *Staphylococcus aureus*, Bap adhesin and teichoic acids facilitate the colonisation of abiotic surfaces (Lejeune, 2003). Bacteria may utilise different adhesins to mediate attachment to different substrata; for example, to colonise the intestinal epithelium, *Vibrio cholerae* El Tor uses a toxin-coregulated pilus for attachment, while in aquatic environments, mannose-sensitive hemagglutinin is used to adhere to abiotic surfaces (Dunne, 2002). In addition to adhesins, the position of bacteria with respect to the surface is important for permanent attachment; for example, in *E. coli* and *P. aeruginosa*, the cell transitions from a polar to a longitudinal orientation to maximise the effective contact area with the surface (Berne et al., 2018).

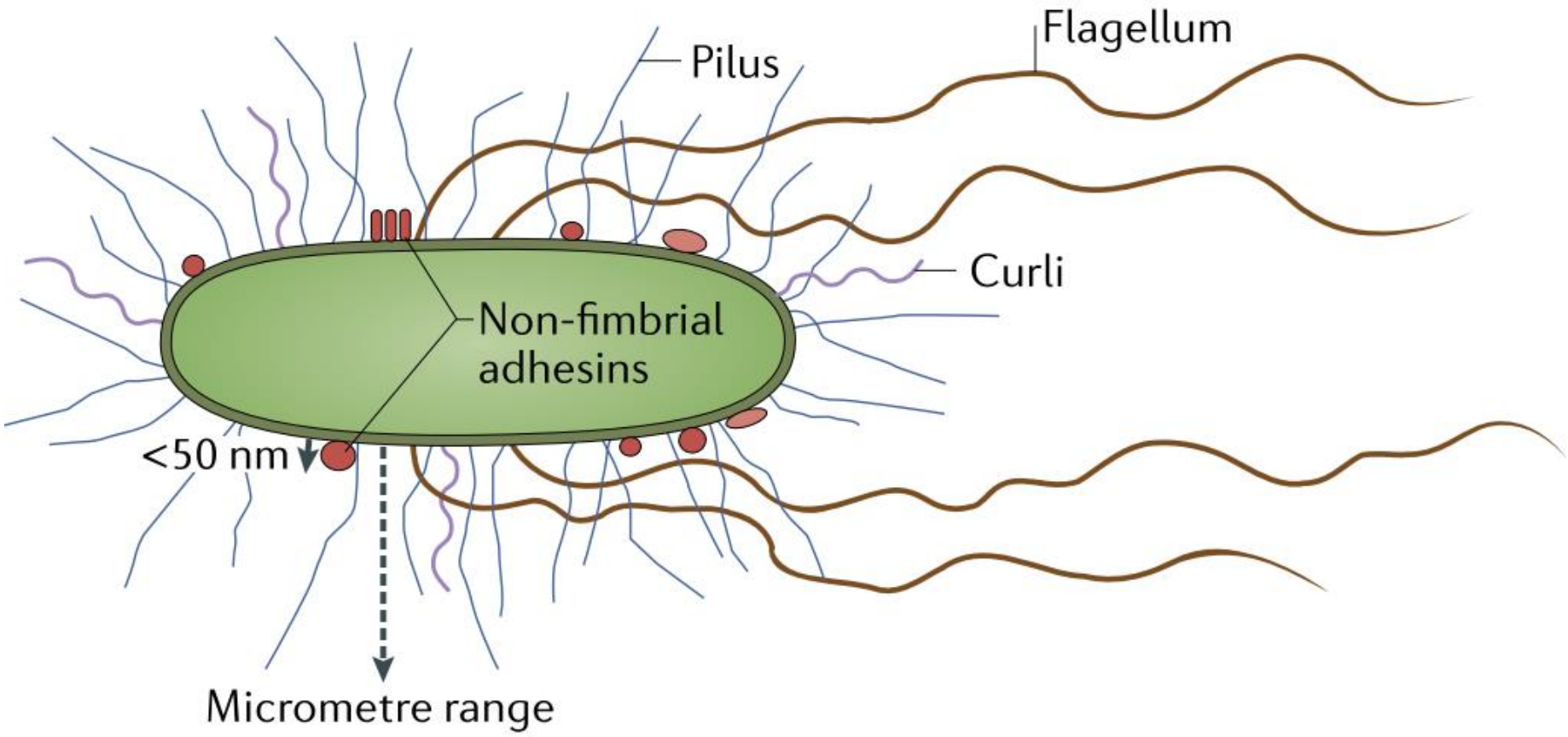

Figure 1.5 | Bacterial extracellular appendages involved in surface adhesion. A number of surface expressed proteins are important for bacterial adhesion to a solid surface, including flagella (brown), long fimbriae adhesins such as pili (blue) and curli (purple) that can extend several micrometres from the surface and non-fimbriae adhesins (red) that normally protrude <50 nm from the cell envelope (Berne et al., 2018).

1.7.3 Population growth and maturation

Once bacteria have established firm interactions with the surface or conditioning layer, individual cells begin to proliferate via binary fission in both vertical and horizontal planes, leading to multicellular clusters known as microcolonies. At first, this process will occur slowly (lag phase), as bacteria adapt to the environment by modulating their gene expression in a stage-specific manner (Dunne, 2002; Mcdougald et al., 2011). Following the initial lag phase, bacteria will enter exponential phase growth, characterised by rapidly dividing cells. It is important to note that the rate of exponential growth (and thus biofilm growth) is directly related to the environmental conditions (e.g. nutrient availability, oxygen concentration, pH, temperature, shear flow) and hence the size of biofilms will vary. Biofilms isolated from patients with chronic infections have been shown to vary significantly from 10s to 1000s of microns in length, as determined by SEM analysis (Bjarnsholt et al., 2013; Garrett et al., 2008).

It is during exponential phase growth when bacteria within the developing biofilm will initiate the expression of genes that leads to the production of EPS, a complex network of macromolecules including polysaccharides, proteins, lipids and nucleic acids. This network forms a hydrated, three-dimensional matrix around the microbial aggregate, and can constitute up to 97% of the total biomass (Flemming and Wingender, 2010). Mature biofilms often exhibit mushroom-like or tower-like morphologies (Figure 1.6), which consist of water channels through which nutrients can be transported. The exact composition of EPS is dependent on the microorganisms that comprise the biofilm, and the environmental conditions under which the biofilm exists. In general, however, proteins and polysaccharides are the predominant macromolecules, while lipids and nucleic acids are found in lower abundance (Flemming and Wingender, 2010; Garrett et al., 2008; Jefferson, 2004; Stewart, 2002). Mature biofilms may be comprised of single bacterial species, therefore being monospecies; these are frequently observed in PJIs (Arciola et al., 2018). Alternatively, multiple species may form a polymicrobial biofilm, such as dental plaque (Nobbs and Jenkinson, 2015).

1.7.3 Dispersal

The 3D-structure of biofilms naturally leads to heterogeneous subpopulations of bacteria, located at different regions within the biofilm. Ultimately, a time will come when the surrounding microenvironment is not able to sustain survival, which can result in bacterial cell death. For many bacteria, biofilms will disperse following the death of sub-populations at their centre, which may be driven by a number of environmental factors, such as changes in nutrient and ion availability, oxygen concentration or temperature (Mcdougald et al., 2011). To promote biofilm dispersion, bacteria may also release EPS-degrading enzymes; one example is alginate lyase production by *P. aeruginosa*, which promotes the release of surface-bound bacteria. Quorum sensing molecules such as acyl-homoserine lactones, cell-cell autoinducing peptides and diffusible fatty acids are also factors that can promote biofilm dispersal. Bacteria that are dispersed from the biofilm upregulate the expression of genes that promote a planktonic lifestyle e.g. flagella, while genes involved in the biofilm phenotype are downregulated e.g. exopolysaccharides. From an evolutionary perspective, biofilm dispersion is an effective mechanism to promote bacterial survival, as planktonic cells and microcolonies can locate to new environments to begin a new biofilm lifecycle (Dunne, 2002; Garrett et al., 2008; Mcdougald et al., 2011).

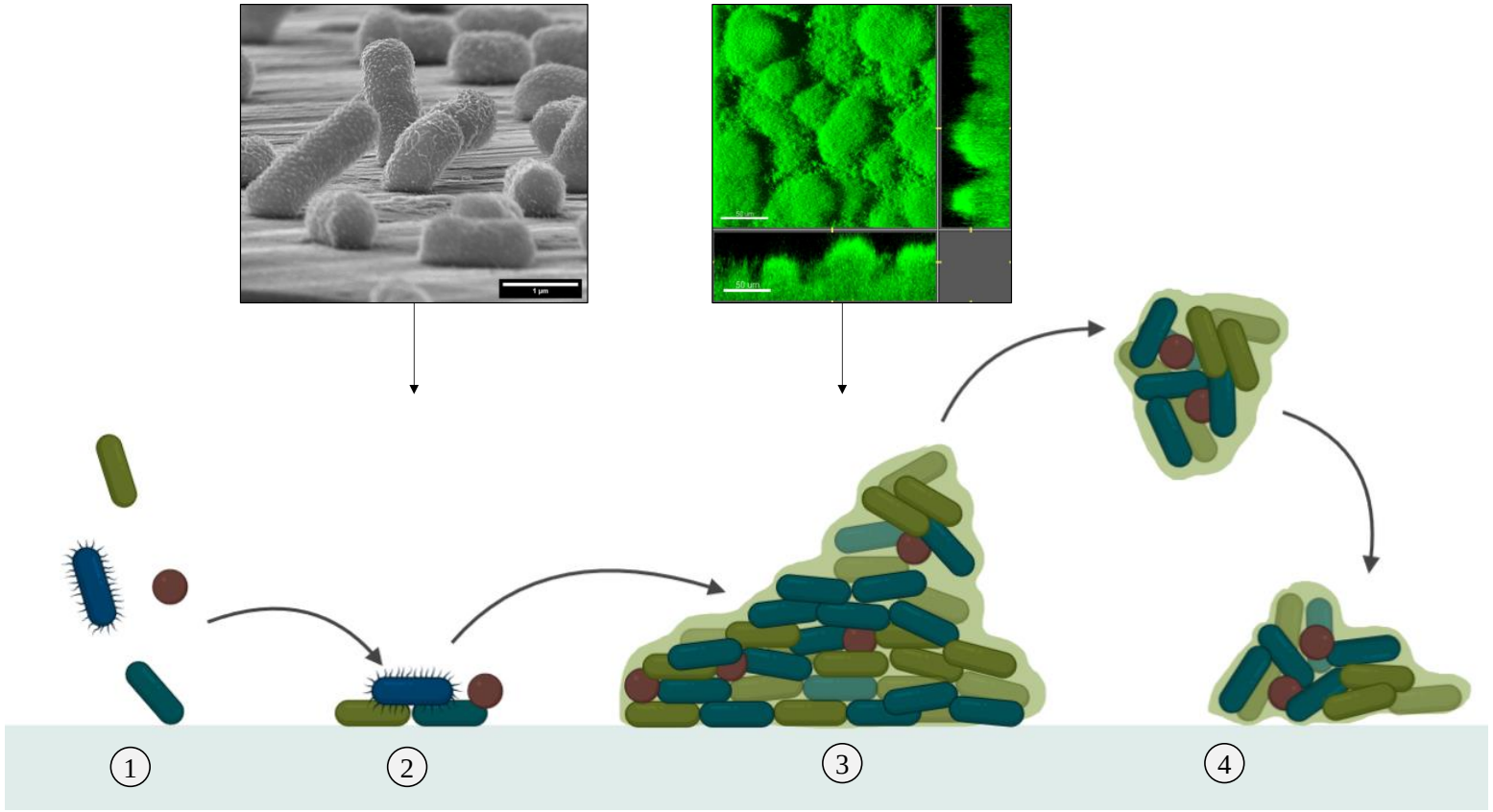

Figure 1.6 | Stages of biofilm formation. Bacteria must first come into contact with the surface (1). This initial step can be achieved via passive or active (flagella) movement and is influenced by a number of factors, including hydrodynamic forces, XDLVO forces and extracellular appendages. At first, the interactions between bacteria and a surface are weak and reversible, mediated by forces such as van der Waals. However, over time the interaction may become more permanent, facilitated by extracellular appendages on bacteria (e.g. type-1 fimbriae) (2). *K. pneumoniae* cells in different stages of attachment are shown above stage 2. Once bacteria have attached to a surface, they may undergo population growth and maturation (3), which can result in the formation of mushroom or tower like formations, as shown above stage 3. Biofilm dispersal occurs when the environmental conditions are no longer able to sustain the population (4). (Stages of biofilm formation were generated using BioRender software) (McDougald et al., 2011; Haagensen et al., 2015; Berne et al., 2018).

1.8 The biofilm advantage

The discovery of biofilms in fossil records from billions of years ago (Westall et al., 2001) strongly indicates that a fitness advantage is afforded to bacteria when growing as part of a community. Indeed, many benefits can be conferred upon bacteria growing in a biofilm state, such as colonisation of favourable environments, protection from stress, enhanced communication and information exchange, to name but a few (Flemming and Wingender, 2010; Jefferson, 2004).

As mentioned, the EPS matrix is a major component of the microbial biofilm (Lin et al., 2014), and can promote adhesion to abiotic and biotic surfaces. This is an effective strategy to ensure the persistence of bacteria within a favourable environmental niche (Jefferson, 2004). Another critical function of the EPS matrix is that it forms a protective barrier around the bacteria, meaning that biofilms are incredibly tolerant to physical stresses, including desiccation, osmolarity changes, phagocytosis, shifts in pH, shear stress and UV radiation (Figure 1.7) (Davey and O'Toole, 2000; Flemming et al., 2016; Jefferson, 2004). Biofilms also afford protection against chemical stresses such as antibiotics. Underpinning mechanisms that have been proposed for this include impaired antibiotic penetration due to the physical structure of the biofilms, and the physiological status (e.g. reduced metabolic activity) of the bacteria within (Stewart, 2015). Penetration times of different antimicrobial agents into biofilms are known to vary over orders of magnitude, which may reduce the efficacy of some antibiotics depending upon the biofilm size, composition and the dose duration (Bridier et al., 2011; Corbin et al., 2011; Joo and Otto, 2012; Stewart, 2002). Furthermore, antibiotics may be enzymatically inactivated during diffusion, or sequestered through binding EPS moieties, both of which could lead to reduced antimicrobial efficacy (Stewart, 2015).The mode of action of several antibiotic classes involves targeting proliferating and metabolically active bacteria; for example, β-lactams target peptidoglycan synthesis (Kong et al., 2010). However, biofilm states exhibit a profound tolerance to many antibiotics, whereby the concentration required to kill bacteria can increase by 10 – 1000-fold relative to under planktonic conditions (Mah and Toole, 2001). This trait stems from the 3D structure of biofilms. As bacteria proliferate in a growing biofilm, the concentration of nutrients and oxygen will deplete at variable rates. This forces bacteria to adapt, which frequently means that bacteria growing at the centre of a biofilm will enter a dormant phase or adopt slower grow rates, which enhance antibiotic tolerance. This process is often referred to as adaptive resistance, because the tolerant phenotype can be reversed upon biofilm dispersal (Stewart, 2015).

The structural organisation of biofilms enables bacteria to communicate via chemical signalling molecules known as autoinducers. This type of cell-cell signalling is known as quorum sensing. The advantage of such a process is that gene expression can be regulated at a population level, meaning that coordinated behaviours can be performed to the benefit of the biofilm, including virulence mechanisms and symbiotic processes (Miller and Bassler, 2001). In addition to the adaptive resistance (e.g. tolerance) displayed by biofilms, resistance can also be acquired from the exchange of genetic material by horizontal gene transfer. The frequency of horizontal gene transfer has been shown to be higher in biofilms than in planktonic culture. One possible explanation for this is the close proximity of bacteria within biofilms, which promotes the efficacy of genetic exchange mechanisms (Flemming and Wingender, 2010; Madsen et al., 2012).

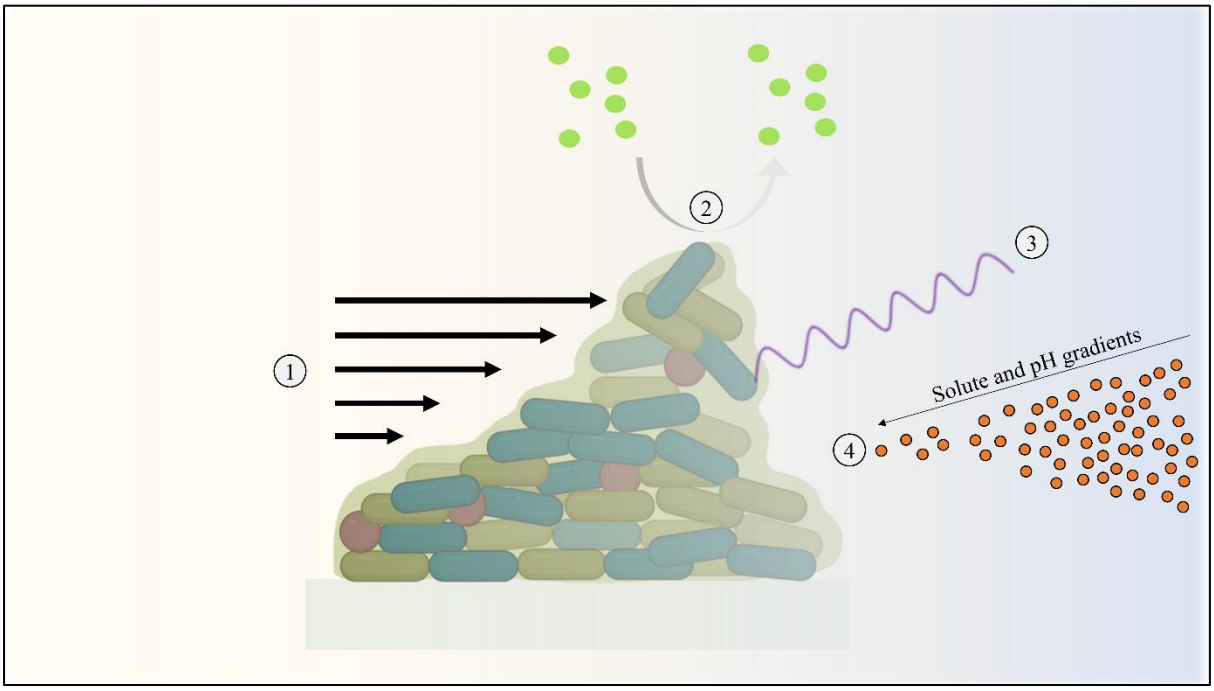

Figure 1.7 | Biofilm tolerance mechanisms. The presence of EPS within biofilms helps to protect bacteria from shear stress/hydrodynamic forces (depicted by black arrows) (1). Bacteria at the centre of biofilms experience nutrient and oxygen deprivation, which results in lower metabolic activity. This can reduce the efficacy of antibiotics that target metabolic processes (e.g. β-lactams target cell wall synthesis). Furthermore, antibiotics may not be able to penetrate the biofilm or can be inactivated during movement through the biofilm (2). Biofilms also display tolerance to UV radiation (3) and resilience to changes in osmolarity or pH (4). (Davey et al., 2000; Jefferson et al., 2004; Stewart, 2015; Flemming et al., 2016).

1.9 Implant design strategies for biofilm prevention

1.9.1 Antibiofouling

As discussed, a key event in the formation of biofilms is the initial attachment of bacteria, which is ultimately governed by the net contribution of attractive and repulsive forces. Therefore, one approach to prevent bacterial colonisation of implanted and indwelling medical devices has been to modify the surfaces, such that the initial attachment of bacteria is impaired; these types of surfaces are categorised as antibiofouling (Mikulskis et al., 2018). A number of techniques have been developed to confer antibiofouling properties, such as hydrophilic polymeric brush coatings, ion functionalisation and nano and micro-patterned surfaces (M. Chen et al., 2013; Higaki et al., 2016; Romanò et al., 2015). These can be broadly divided into chemical and physical surface modifications.

1.9.1.1 Chemical surface modifications

A widely adopted method to prevent bacterial adhesion onto surfaces is to modify the interface with a hydrophilic polymer, such as poly(ethylene glycol) (PEG) and high-molecular weight PEG, also known as poly(ethylene oxide) (PEO) (Cheng et al., 2007). In aqueous environments, polymeric chains behave as highly mobile brushes, effectively repelling incoming bacteria by forming an exclusion volume close to the surface (Roosjen et al., 2004). The short and long-term antibiofouling efficacy of polymer coated surfaces has been reported in multiple studies. PEO coated surfaces were shown to reduce the adhesion of bacteria (*S. epidermidis, P. aeruginosa*) and fungi (*C. albicans, Candida tropicalis*) over 4 hours compared to glass-only controls. Of note, the reductions in fungal adhesion were less pronounced than those of bacteria, indicating that cell size had influenced attachment. Furthermore, hydrophobic cells (*P. aeruginosa, C. tropicalis*) were reported to adhere in larger numbers than their hydrophilic counterparts (*S. epidermidis, C. albicans*) (Roosjen et al., 2004). Another study investigated the *in vivo* and *in vitro* kinetics of staphylococcal biofilm formation on a commercially produced PEG polymer coating (OptiChem®). Using a flow chamber, *S. epidermidis* biofilm growth was significantly delayed on OptiChem® coated glass compared to control. This was proposed to have been caused by the increased detachment rate. After a 5 day murine implant model, *S. aureus* attachment was not detected on any OptiChem® coated discs (0/6) compared to silicon rubber, which showed high levels of attachment (5/6) (Fernández et al., 2010).

1.9.1.2 Physical surface modifications

An alternative way to confer antifouling properties onto materials has been to modify the micro and nano-textures of surfaces. Inspiration for this approach has stemmed from nature, where the physical structure of many surfaces has been shown to impart highly efficient antifouling characteristics; such examples include lotus leaves, rose petals and shark skin (Bhushan, 2012). The self-cleaning properties of these natural surfaces have been generated on synthetic materials. Photolithography was utilised to generate superhydrophobic silicon surfaces mimicking the effects of lotus leaves (Bhushan et al., 2009). Shark skin mimetic surfaces (Sharklet AF™) were created on poly(dimethyl siloxane) elastomer (PDMSe) by replication of silicon wafer molds. Sharklet micro-patterns have consistently been reported to reduce microbial attachment, transfer between surfaces and viability. In one study, Sharklet MP was shown to reduce MRSA attachment by 94% after 90 minutes (Mann et al., 2014). Likewise, a different study found that Sharklet MP disrupted *S. aureus* biofilm formation compared to smooth PDMSe, reporting 35% and 77% biofilm coverage respectively after 21 days (Figure 1.8) (Chung et al., 2007).

Despite the reported efficacy of many antifouling materials, there are potential drawbacks that may arise from the use of such coatings on implant surfaces. Firstly, while it may be beneficial to prevent bacterial attachment, this could be expected to inhibit the attachment (Kim et al., 2015) and migration of mammalian cells (Magin et al., 2015), which could impair the fixation of implanted devices. Furthermore, even if bacterial adhesion is prevented on the implant itself, this does not protect the surrounding tissues from bacterial colonisation. To the contrary, antifouling surfaces may actually enhance the spread of bacteria and infection. Indeed, in the previous example with OptiChem®, while *S. aureus* adhesion was not observed on the polymer coated surfaces after 5 days, the surrounding tissues were shown to be culture positive in all but one case (Fernández et al., 2010). A final drawback relates to bacterial physiology. Although it is widely accepted that bacteria possess an overall negative charge, the envelope of bacteria is highly heterogeneous, meaning that the charge and physicochemical properties of the surface expressed appendages varies (Berne et al., 2018). A foreseeable consequence of this is that antibiofouling coatings may not work for all pathogens commonly isolated from implant infections (Mikulskis et al., 2018).

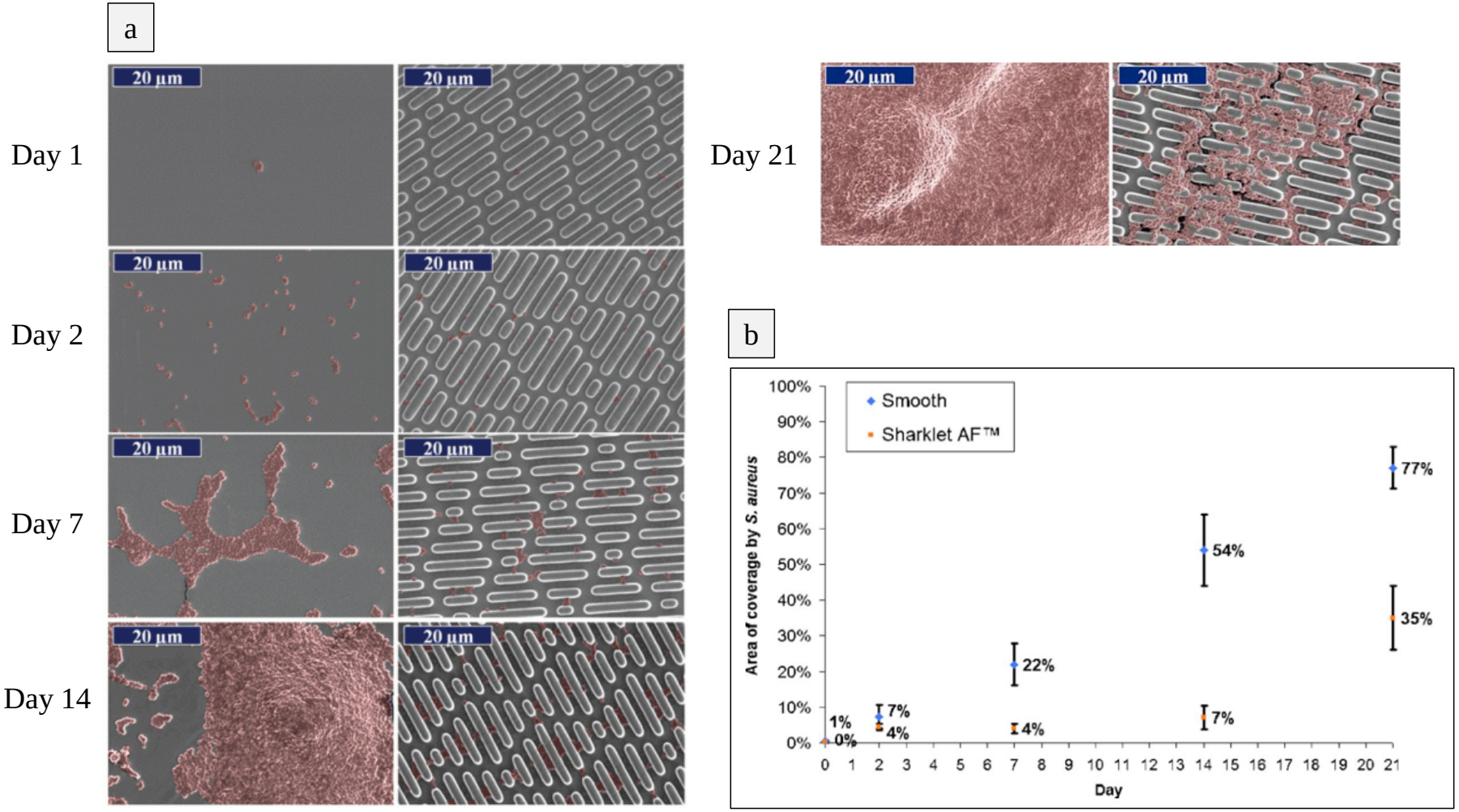

Figure 1.8 | Antibiofouling strategy for biofilm prevention. Sharklet AF™ is a microtopography based on the skin of sharks. Chung and colleagues reported significant reductions in *S. aureus* biofilm formation over 21 days on Sharklet AF™ patterned PDMSe compared to control PDMSe (a). Reductions in *S. aureus* biofilm formation were quantified from SEM analysis using Fiji software (b) (Chung et al., 2007).

1.9.2 Antimicrobial release

The most common approach taken in preventing infections of titanium implants has been to modify the surface with an antimicrobial agent. A wide variety of coatings have been studied in relation to their antibiofilm properties, such as antibiotics, antimicrobial peptides, enzymes, metals and metal ions (Damiati et al., 2018; Romanò et al., 2015). Furthermore, the methods used to incorporate these agents onto the implant vary; some utilise covalent attachment, while others have adopted physical deposition methods. A number of systems developed for clinical use have incorporated the antimicrobial agent into a matrix, promoting controlled release over time; some examples include hydroxyapatite, hydrogels, biodegradable polymers and non-biodegradable polymers. The antibiofilm efficacy of such coatings is ultimately dependent on the physical and chemical properties of the matrix, which determine the antimicrobial release profile (Hetrick and Schoenfisch, 2006).

1.9.2.1 Antibiotic releasing non-biodegradable polymers

Several coatings have been developed from non-biodegradable polymers to control the release of antibiotics, such as polyurethane, silicone rubber and polymethylmethacrylate (PMMA) (Francolini et al., 2017). Gentamicin releasing PMMA has been widely used since 1970, prepared by mixing liquid (monomer) and powder (polymer) forms of MMA to generate a viscous paste that solidifies into a bone cement around the titanium implant (Bistolfi et al., 2011; Hendriks et al., 2004). While this system is straightforward to apply, the porous structure of polymerised MMA results in variable antibiotic delivery; in some cases, less than 10% of the total load is released even several years after implantation (Price et al., 1996). Of course, the presence of antimicrobials at low (below MIC) concentrations raises concerns over the potential for driving bacterial resistance (Hendriks et al., 2004). Additionally, the solidification of PMMA cement is exothermic, therefore, the antibiotic used must be thermostable between 60°C – 80°C, placing restrictions on the types that can be used (Bistolfi et al., 2011). Furthermore, the addition of high doses of gentamicin to PMMA can significantly reduce the compressive strength of the resulting bone cement, leading to a higher chance of implant failure (Arora et al., 2013). The antibiofilm efficacy of gentamicin loaded PMMA remains a topic of debate, with some studies reporting clinically significant reductions in biofilm formation (Arora et al., 2013; Van De Belt et al., 2001), while others have shown no tangible benefits (Bistolfi et al., 2011; Francolini et al., 2017).

1.9.2.2 Antibiotic releasing biodegradable polymers

Considering the limitations associated with PMMA bone cements, drug delivery systems that utilise biodegradable polymers have been developed to control antibiotic release, including collagen and polylactide-co-glycolide (PLGA). Biodegradable coatings offer many advantages, including reduced cytotoxicity and increased control over antibiotic release (Price et al., 1996). PLGA is one of the most common synthetic polymers used in tissue engineering. In particular, it has attracted considerable interest as a coating for titanium implants, owing to its modifiable biodegradation rate (Gentile et al., 2014). Neut and colleagues developed a PLGA system loaded with gentamicin for hydroxyapatite coated hip prosthesis. This system demonstrated a burst release profile, with 95% of the gentamicin being released within the first 2 hours, the remaining 5% released up to 168 hours, and complete degradation observed after 336 hours. The PLGA coating was reported to exhibit antibacterial effects against *S. epidermidis in vivo,* providing infection prophylaxis for 7 days in a rabbit model (Neut et al., 2015).

1.9.2.3 Antibiotic loaded hydrogels

More recently, orthopaedics has seen the use of fast-resorbable hydrogels as effective antibiotic delivery systems. As the major constituent of hydrogels is water (70% - 99%) and in many cases, hyaluronic acid, they provide biocompatible and biodegradable layers that share many physical characteristics with tissue. Furthermore, the aqueous environment afforded by hydrogels has been shown to reduce the risk of antibiotic denaturation (Pitarresi et al., 2013). The safe and efficacious use of antibiotic loaded hydrogels has recently been shown for joint arthroplasty, in the first randomised clinical trial. In this study, ten-fold reductions in the occurrence of surgical site infections (SSI) were observed in patients that had been treated with a novel hydrogel coating (DAC®). Furthermore, no local or systemic side effects were observed (Romanò et al., 2016).

1.9.3 Contact killing

1.9.3.1 Chemical contact killing

Another approach to prevent biofilm formation on medical implants is to coat the surface with a chemical that kills bacteria upon contact, without releasing the antimicrobial agent. This has been achieved with antibiotics, antimicrobial peptides, quaternary ammonium compounds and metal nanoparticles (Mas-Moruno et al., 2019). The broad-spectrum antibacterial properties of silver coatings are widely reported (Asharani et al., 2009) with bactericidal effects observed against many bacteria isolated from titanium implant infections, such as *S. aureus, S. epidermidis, E. coli* and *P. aeruginosa* (Hetrick and Schoenfisch, 2006). A number of studies have used silver coatings to generate contact killing surfaces for dental and orthopaedic implants.

In one study liquid injection atomic layer deposition was used to coat titanium implant scaffolds with silver nanolayers. In brief, a silver source was vaporised at 130°C and introduced into the reaction chamber by Ar carrier gas, this process was performed in 4 second pulses. Following 8 seconds, a coreactor, Propan-1-ol, was introduced into the reaction chamber for the same duration as the silver source. This cycle was repeated 500 times at temperatures of 125°C, resulting in a silver film 13 nm thick. The titanium scaffold coated with silver was reported to mediate 2-log reductions in *S. epidermidis* growth over 96 hours, compared to titanium only scaffolds (Devlin-Mullin et al., 2017). Physical vapour deposition (PVD) techniques have been used to deposit silver nanoparticle layers onto titanium screws and discs. By changing the duration of the deposition process, silver nanoparticle layers of different thicknesses were generated, starting at 50 nm and extending to 2 µm. The resulting surfaces were reported to inhibit *E. coli* growth, whilst supporting the adhesion of osteoblasts and fibroblasts (Vogel et al., 2014). Similarly, another study used PVD to generate silver coatings of approximately 2 µm thickness on titanium. In brief, the titanium samples to be coated were placed in an argon (Ar) atmosphere at 7.5 x 10^{-3} mbar. Vaporisation of titanium and silver targets was achieved by cathodic arc sputtering (80A) and magnetron sputtering (112-900W) respectively. The substrate was held at a potential of -300V for a duration of 30 minutes to complete the coating. Silver coated titanium surfaces were reported to have significant reductions in *S. epidermis* and *K. pneumoniae* adhesion following 24 hour incubations, compared to titanium only surfaces (Ewald et al., 2006).

Despite widespread acceptance that silver possesses antibacterial activity, the non-specific mode of action (e.g. membrane disruption) has prompted concerns over the development of antimicrobial resistance. Indeed, repeated exposure to silver nanoparticles was recently shown to mediate resistance in *E. coli* and *P. aeruginosa* (Panáček et al., 2018). Furthermore, silver nanoparticles have been shown to mediate cytotoxic and genotoxic effects on human cells (Asharani et al., 2009), bringing into question the suitability of silver coatings for clinical use.

1.9.3.2 Physical contact killing

With growing concerns over antimicrobial resistance and, specifically, bacterial resistance to antibiotics, a strong emphasis has been placed on preventative approaches that work via physical rather than chemical modes of action. As previously stated, an area of growing interest is the field of biomimetics, where inspiration from nature is applied to the design and fabrication of surfaces with antibacterial or antibiofouling properties.

It is now well-established that insect wings, including the cicada and dragonfly, possess antimicrobial activity towards many bacterial and fungal species. Studies to date indicate that this process is mediated by the physical nanoprotrusions found on the wing surface, which ultimately stretch and damage the microbial cell upon contact, leading to lysis and death (Bandara et al., 2017; Hasan et al., 2013; Ivanova et al., 2013, 2012; Kelleher et al., 2016; Nowlin et al., 2014). This effect was first observed for *P. aeruginosa*, where individual bacterial cells were shown to sink and spread between the nanoprotrusions found on *Psaltoda claripennis* (cicada) wings. *P. claripennis* wings were found to consist of nanopillars, each measuring 200 nm in height, with a reducing diameter from the base to the tip (100 nm to 60 nm) and a constant spacing of 170 nm. These structures were organised into periodic hexagonal arrays. It was only through serendipity that this discovery was made, as the research had originally intended to investigate the antibiofouling abilities of *P. claripennis* wings, which are known to possess superhydrophobic water contact angles (WCA) (>150°) and self-cleaning properties. However, inspection of *P. claripennis* wings by confocal laser scanning microscopy (CLSM) revealed that most *P. aeruginosa* cells had been killed within 5 minutes of attachment, as determined by LIVE/DEAD viability stains. Further still, the same bactericidal activity was noted after coating the wing with a layer of gold, thereby ruling out the possibility of chemically mediated contact killing. These observations led to the proposal that *P. aeruginosa* killing was mediated by mechanical, physical rupture of the cell (Ivanova et al., 2012). In agreement with these findings, *P. claripennis* wings were later shown to exhibit bactericidal activity towards other Gram-negative bacteria, including *Branhamella catarrhalis, E. coli* and *Pseudomonas*

fluorescens (Figure 1.9) (Hasan et al., 2013). Other studies have investigated the bactericidal and fungicidal properties of cicada wings with distinct periodical designs, reporting that feature size and spacing are important determinants of bactericidal efficiency (Kelleher et al., 2016; Nowlin et al., 2014).

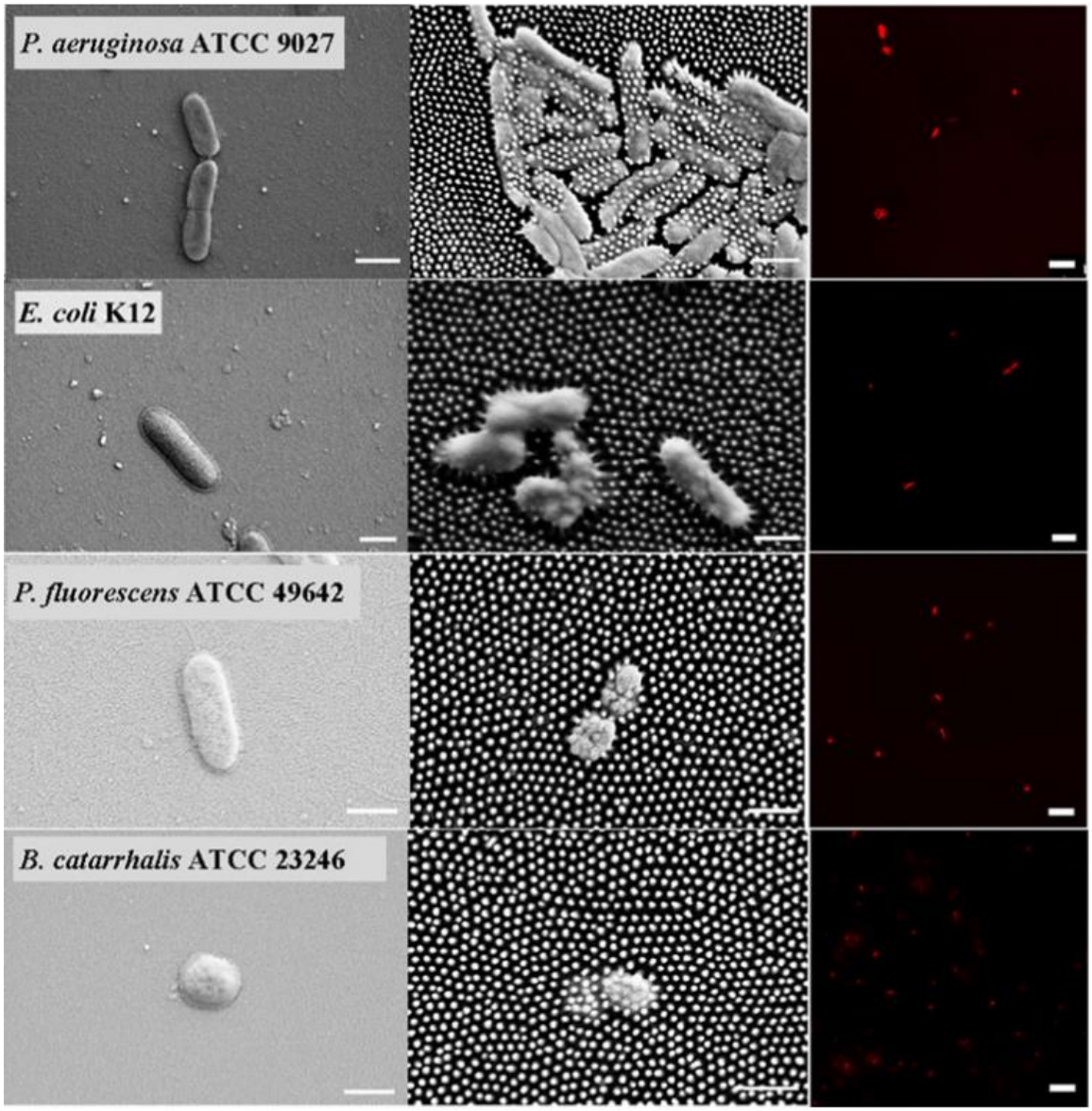

Figure 1.9 | Physical contact killing on cicada wings. Hasan and colleagues investigated the effects of cicada wing (*P. claripennis*) nanopillar arrays on the morphology and envelope integrity of Gram-negative (*B. catarrhalis*, *E. coli*, *P. aeruginosa* and *P. fluorescens*) and Gram positive (*B. subtilis*, *S. aureus*) bacteria following 18 h incubation. SEM and CLSM analysis indicated a selective bactericidal effect against Gram-negative bacteria (Hasan et al., 2013). Scale bars in electron micrographs = 1 µm; in CLSM images, scale bars = 5 µm.

In addition to cicada wings, dragonfly wings have been shown to possess efficient bactericidal properties. LIVE/DEAD staining and CLSM analysis of *Diplacodes bipunctata* wings revealed killing of both Gram-negative (*P. aeruginosa*) and Gram-positive (*S. aureus*, *Bacillus subtilis*) bacteria. It was hypothesised that the extended bactericidal activity against Gram-positive bacteria was caused by the capillary architecture of *D. bipunctata* wings, leading to enhanced cell wall stress, deformation and improved killing efficiency over cicada wings (Ivanova et al., 2013) (Figure 1.10). More recently, the nanopillar arrays on *Orthetrum villosovittatum* wings were reported to induce separation of the inner and outer cell membranes of *E. coli*, leading to envelope damage that resulted in killing rates of 4.99E+05 cells $min^{-1}cm^{-2}$ in the first hour of incubation. Of note, membrane separation was reported to occur without direct contact with the nanopillars. Instead, the adhesion forces between the substrate and bacterial EPS were proposed to have induced damage (Bandara et al., 2017). These findings are partly supported by earlier studies on *Progomphus obscurus* (sanddragon), which found a strong link between the adhesion force of *Saccharomyces cerevisiae* and the degree of rupturing (Nowlin et al., 2014). Although the wetting properties of dragonfly wings are similar to those of cicada (hydrophobic), these surfaces are not covered by periodic nanopillar arrays. Instead, they consist of randomly oriented nanoprotrusions, with variable size and spatial distribution. For example, *D. bipunctata* wing nanopillars are 240 nm in height, with diameters below 90 nm, and cluster spacings between 200 nm and 1800 nm (Ivanova et al., 2013). In contrast, the wings of *O. villosovittatum* were found to comprise two distinct nanopillar populations (short and tall) with heights starting from 80 nm and extending to 460 nm, and diameters varying from 20 nm to 74 nm (Bandara et al., 2017). Lastly, *P. obscurus* wings consist of nanopillars measuring 240 nm ± 35 nm in height, 53 nm ± 9.5 nm in diameter and spacings of 123 nm ± 50 nm (Nowlin et al., 2014).

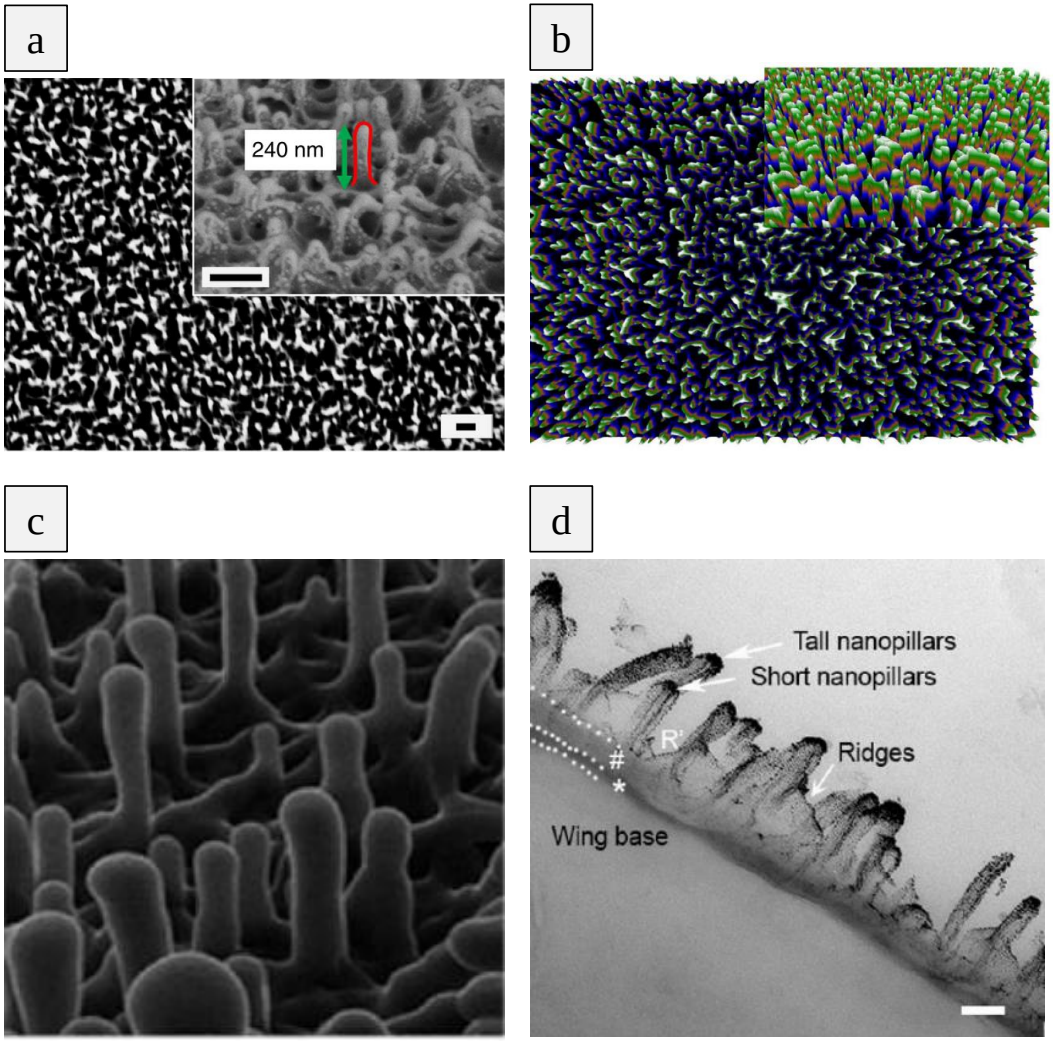

Figure 1.10 | Physical contact killing on dragonfly wings. The nanotopography of dragonfly wings (*D. bipunctata*) has been reported to exhibit bactericidal activity against Gram-negative (*P. aeruginosa*) and Gram-positive (*S. aureus*, *Bacillus subtilis*) bacteria. SEM and optical profilometry analysis of *D. bipunctata* wings reveals the random nature of the nanopillar arrays (a-b). Scale bar = 200 nm. Similarly, the wings of *O. villosovittatum* have been reported to possess bactericidal activity toward *E. coli*, and display random directions and variable heights (c-d) (Ivanova et al., 2013; Bandara et al., 2017). Scale bar = 200 nm.

Aside from insect wings, the skin of geckos (*Lucasium steindachneri*) have also been reported to possess antibacterial properties. Samples of gecko skin and smooth silicon wafers were incubated for 7 days in suspensions of *Porphyromonas gingivalis* (Gram-negative oral bacterium), and the proportion of live and dead bacteria were determined every 24 hours using LIVE/DEAD viability stains under CLSM. While the exact bactericidal activity of gecko skin was not stated in this study, red fluorescing bacteria were observed throughout the 7 days (Watson et al., 2015). In contrast to cicada and dragonfly wings, which possess ordered and random nanopillar arrays respectively, gecko skin consists of micro-spinules with lengths up to 4 μm and densities extending to 500 per 100 μm^2, while the tips range from 20 nm to 60 nm in diameter. This study builds on the existing literature reporting that nanotextured surfaces can mediate bactericidal effects, providing evidence that microtextured surfaces can also exhibit bactericidal activity.

The unique bactericidal properties of cicada and dragonfly wings have drawn significant research interest (Damiati et al., 2018; Lin et al., 2018; Modaresifar et al., 2019; Tripathy et al., 2017), as the physical nature of bacterial killing could provide an effective strategy to prevent biofilm formation and infection of indwelling and implantable devices, whilst avoiding the current need to use materials impregnated with antibiotics. For example, dragonfly mimetic nanoarrays have been generated on black silicon (bSi) wafers using a reactive ion etching (RIE) process. bSi wafers with comparable nanoarrays to *D. bipunctata* wings were immersed in cultures of *P. aeruginosa, S. aureus* or *B. subtilis* and incubated for up to 30 hours prior to LIVE/DEAD viability staining and imaging of the surfaces, alongside viable cell counts. A highly efficient bactericidal effect was observed against both Gram-positive and Gram-negative bacteria, with average killing rates of 450,000 cells min^{-1} cm^{-2} reported (Ivanova et al., 2013). Of note, the bactericidal effect was reported to decline after the first 3 hours, reducing to 50,000 cells min^{-1} cm^{-2}.

On pure titanium substrates, alkaline hydrothermal processing has been used to create titania nanowire arrays, resulting in nanotopographies described as brush or niche-types. The brush-type consisted of spike-like structures measuring 3 µm in length and 100 nm in diameter, while the niche-type comprised pocket-like formations with diameters extending to 15 µm. Using LIVE/DEAD viability staining, the brush-type nanotopography was shown to be effective in killing motile bacteria, including *P. aeruginosa, E. coli* and *B. subtilis,* with greater than 50% cell death reported within the first hour of incubation (Diu et al., 2014). Titanium dioxide (TiO_2) nanowires measuring approximately 1 µm in length and 20 nm in diameter have been successfully generated on titanium alloy (Ti-6Al-4V) using a thermal oxidation technique. Following 2 hour static incubation with *E. coli*¸ these surfaces were reported to effectively reduce *E. coli* viability by 40%. Furthermore, LIVE/DEAD staining revealed a higher proportion of dead bacteria on the nanowire surfaces compared to controls (Sjöström et al., 2016). More recently, colloidal lithography was used to produce cicada wing mimetic nanocone arrays on poly(ethylene terephthalate) (PET). By changing the parameters of this technique, namely the size of the polystyrene colloidal mask, and the etching time, it was possible to make nanoscale adjustments to the height, diameter and spacing of the PET. Nanocone arrays with sharper tips and higher aspect ratios were reported to achieve the greatest killing efficiency, with percentage kill values of close to 30% for *E. coli* and *K. pneumoniae* (Hazell et al., 2018b).

1.10 Current mechanistic understanding of physical contact killing

1.10.1 Theoretical models of contact killing

The discovery of natural surfaces with bactericidal properties led to the development of several theoretical models, each providing different interpretations of the killing process (Figure 1.11). In the case of cicada wings, a biophysical model was first proposed. This model outlined that bacterial sorption to nanopillar arrays results in physical stretching of the cell membrane, leading to rupture and lysis. The mechanistic basis of this process was compared to breaking a thin elastic layer under an applied stress, rather than piercing (Pogodin et al., 2013). This model was consistent with previous studies, in which killing of *P. aeruginosa* was observed on gold coated wing surfaces, suggesting that rupture was mediated via physical rather than chemical mechanisms (Ivanova et al., 2012). In a different study, *P. claripennis* wings were shown to mediate selective killing of Gram-negative bacteria (*B. catarrhalis, E. coli, P. aeruginosa, P. fluorescens*), while no effect was observed for Gram-positive bacteria (*B. subtilis, Planococcus maritimus, S. aureus*), indicating that envelope architecture was a key determinant of susceptibility (Hasan et al., 2013). This observation was explained by the biophysical model, indicating that Gram-positive bacteria were more resistant to nanoarray mediated killing due to their thicker cell wall, which provides increased rigidity (Pogodin et al., 2013).

Within the framework of the biophysical model, two additional models were developed. In one study, the degree of envelope stretching in Gram-positive and Gram-negative bacteria was compared in relation to the geometry of cicada wing nanopillar arrays. This led to the proposal of an elastic mechanical model. In general agreement with the biophysical model, the maximum stretching capacity of Gram-negative bacteria was shown to be greater than Gram-positive bacteria, leading to more deformation and increased susceptibility to rupture. The model further predicted that the antibacterial properties of nanoarrays could be enhanced by increasing nanopillar sharpness and spacing (Xue et al., 2015). In a different study, the equilibrium between adhesion energy and deformation energy was investigated for rod-shaped bacteria. In this case, a quantitative thermodynamic model was proposed, in which the bactericidal activity of a nanopatterned surface is directly related to the balance between adhesion energy and deformation energy. The model predicts that within certain dimensions (nanopillar radius 0 nm – 50 nm and nanopillar spacing 100 nm – 250 nm), the stretching degree applied across the bacterial envelope is enhanced by nanoarrays with greater nanopillar diameters (50 nm) and reduced nanopillar spacing (100 nm) (Li and Chen, 2016).

Despite the proposal of several theoretical models, there are a number of issues concerning their validity. Firstly, each model assumes that bacteria possess thin elastic membranes, which fails to account for the variations in envelope composition and structure that significantly impact the adhesion force to a surface (Nowlin et al., 2014). Furthermore, bacterial membranes are not thin elastic layers, instead they exhibit viscoelastic properties, whereby deformation occurs as a function of time (Vadillo-Rodriguez et al., 2009). Secondly, the effects of conditioning layers and bacterial surface-bound appendages are overlooked, yet are likely to play an important role in the overall interaction of bacteria with the cicada wing surface, even in the presence of gold coatings. Finally, the elastic mechanical model contributes envelope deformation to gravitational forces, without consideration for Brownian motion, bacterial motility and the extended DVLO theory (Berne et al., 2018). Thus, each model fails to produce accurate explanations for physical contact killing.

Aside from cicada wing nanopillar arrays, no models have been proposed to explain the physical contact killing properties of dragonfly wings. However, it is generally accepted that the bactericidal activity results from cell rupture. With respect to the dragonfly wing, bacterial cell death is thought to be induced by the capillary architecture, which can mediate increased deformation and cell wall stress compared to cicada wings (Ivanova et al., 2013). Contrary to all these hypotheses, one study proposed that dragonfly nanopillar arrays mediate bacterial envelope damage without direct contact, but through strong adhesion forces between the substrate and bacterial EPS (Bandara et al., 2017).

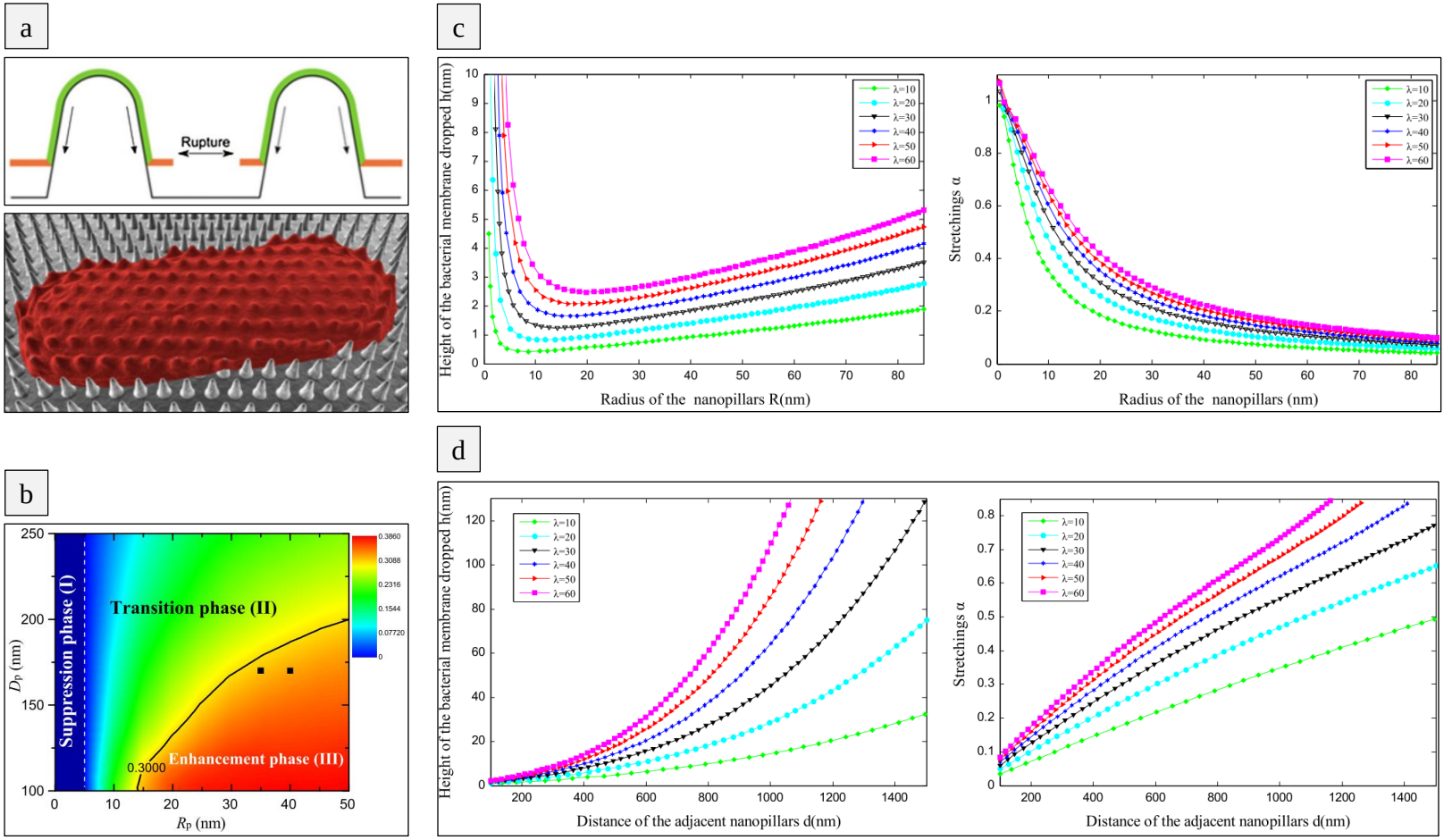

Figure 1.11 | Comparison of the different theoretical models for contact killing. The biophysical model proposed by Pogodin and colleagues suggests that bacterial sorption to nanopillar arrays results in physical stretching of the cell membrane, leading to rupture and lysis, analogous to breaking a thin elastic layer under an applied stress (a). Li and Chen developed a phase diagram to predict the bactericidal activity of a surface, where D_p denotes nanopillar spacing, R_p is nanopillar radius and the colour represents the degree of envelope stretching (red = high, blue=low) (b). The elastic mechanical model developed by Xue and colleagues indicated that the antibacterial properties of nanoarrays could be enhanced by increasing nanopillar sharpness and spacing. The relationship between nanopillar radius, bacterial membrane drop height and stretching degree was investigated for Gram-negative and Gram-positive bacteria (c-d) (Pogodin et al., 2013; Xue et al., 2015; Li and Chen et al., 2016).

1.10.2 Factors that contribute to bactericidal efficacy

In addition to the proposed mechanistic basis of nanopillar mediated killing, a number of factors are reported to influence the antimicrobial efficacy of natural and synthetic nanoarrays. The microbial adhesion force to a nanotopography has been shown to directly influence viability. *S. cerevisiae* rupturing was greatest in strains that adhered most strongly to cicada wing nanopillars (Nowlin et al., 2014). Similarly, strong adhesion between dragonfly nanopillars and *E. coli* EPS is reported to promote bacterial membrane damage (Bandara et al., 2017). The rigidity of bacterial cells has also been found to influence their susceptibility to mechanical rupture (Hasan et al., 2013; Pogodin et al., 2013), whereby Gram-negative bacteria were more sensitive to nanopillar mediated stretching. This observation is most likely to reflect differences in envelope architecture (Figure 1.12). Gram-negative envelopes consist of an outer and inner membrane, separated by a thin peptidoglycan cell wall (≈ 5 nm), which occupies the periplasmic space. By contrast, the peptidoglycan layer of the Gram-positive bacterial cell wall is significantly thicker (20 – 100 nm) (Silhavy et al., 2010), which may reduce susceptibility to stretching. In addition to this, nanotopography geometries, including aspect ratio and nanopillar density, have been shown to influence the efficiency of bactericidal activity (Hazell et al., 2018a; Hazell et al., 2018b; Kelleher et al., 2016; Nowlin et al., 2014).

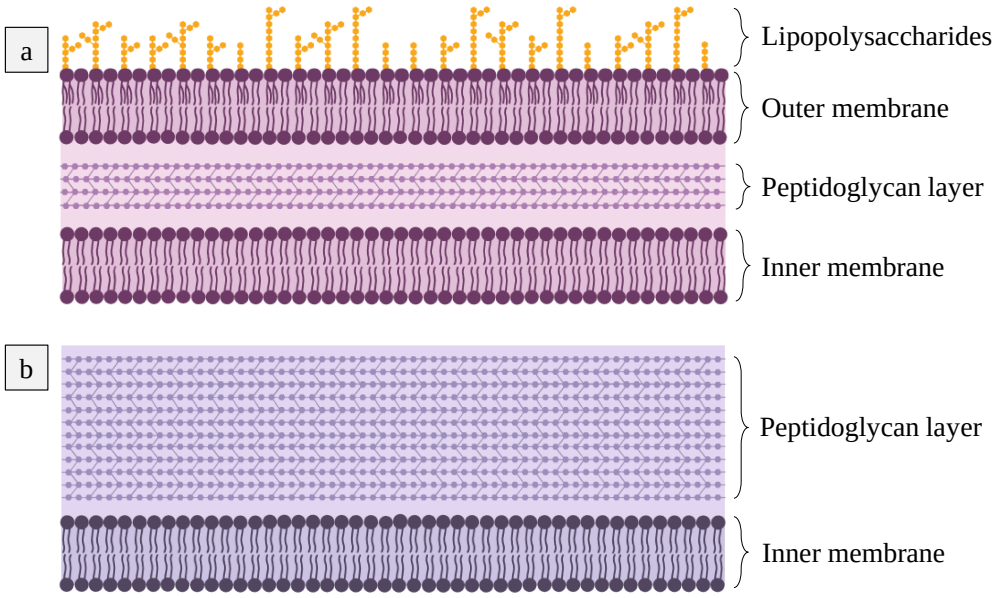

Figure 1.12 | Comparison of Gram-negative and Gram-positive envelope architecture. The Gram-negative envelope consists of an outer-membrane and cytoplasmic membrane, separated by the thin peptidoglycan layer (≈ 5 nm) (a). The Gram-positive envelope does not have an outer membrane, instead consisting of a thicker peptidoglycan layer (20 – 100 nm) with a cytoplasmic membrane (b). (Figure generated using BioRender software).

1.11 Fabrication of antibacterial nanostructured surfaces

The previous section has highlighted that a wide variety of fabrication techniques have been developed to modify the topography of surfaces at the micro- and nanoscale. As a general rule, these techniques are categorised as top-down or bottom-up approaches, depending on where the fabrication process begins. Top-down approaches involve the removal of material from an existing base substrate, to generate structures with desired geometries; such processes are generally used in the production of microelectronic devices. In contrast, bottom-up approaches involve generating structures from the assembly of atoms or small molecular building blocks; many natural processes can be described in this way, such as the growth of nanopillar arrays on cicada and dragonfly wings. Both top-down and bottom-up approaches have been used to create micro- and nanopatterned surfaces with antibacterial properties.

1.11.1 Top-down nanofabrication approaches

Lithography is the most widely used top-down approach for nanofabrication, and there are a number of methodological variants, including photolithography, electron and ion beam lithography, nanoimprint lithography, scanning probe lithography and block co-polymer lithography (Chen and Pepin, 2001). Although these methods vary with respect to the equipment and parameters used, the fundamental principles are the same, and each has the capacity to generate highly ordered and reproducible micro- and nanopatterns by selective partial removal of material. Nevertheless, these techniques often have high processing and maintenance costs and are low throughput, making them impractical for large-scale production (Sebastian et al., 2014). These limitations have led to the development of modified approaches, including projection lithography, immersion lithography, extreme ultraviolet lithography and Resolution Augmentation through Photo-Induced Deactivation “RAPID” (Biswas et al., 2012). These methods are a topic unto themselves and are generally outside the scope of this study. However, a select few examples of prominent lithography techniques are briefly discussed below in the context of bactericidal and/or mammalian cell promoting nanotopographies.

1.11.1.1 Mask lithography

In photolithography, also known as optical or UV lithography, a collimated beam of light passes through an optical mask to create a periodic pattern on a photoresist. A photoresist is a light sensitive material that is coated onto a planar (2D) substrate (i.e. silicon). In most cases a positive photoresist is used. The solubility of positive photoresists increases when exposed to UV light, and these regions are removed in developer solution. In contrast, the solubility of negative photoresists decreases when exposed to light, therefore the area not exposed to light will be dissolved. In subsequent stages, wet or dry etching processes are used to remove layers from the base substrate, with the photoresist acting as a protective mask. Once the final pattern has been created, the photoresist is removed. Again, this process can be performed by wet or dry etching processes (Biswas et al., 2012; Gates et al., 2005).

A colloidal lithography process was used to generate cicada mimetic nanocone arrays on PET. In this study, polystyrene microspheres measuring 200 nm or 500 nm in diameter were deposited onto PET films via spin coating (Figure 1.13). The resulting surfaces were comprised of hexagonally close packed polystyrene monolayers acting as the mask. The surfaces were then exposed to plasma-reactive ion etching (O_2) for up to 20 minutes, generating nanocone arrays with heights varying from 352 nm to 529 nm, tip width from 20 nm to 304 nm, and base diameters from 55 nm to 381 nm. The resulting nanocone arrays were shown to mediate bactericidal effects toward *E. coli* and *K. pneumoniae*, with nanocone density being identified as a key determinant of killing. Nanocone arrays generated from 200 nm polystyrene microspheres were reported to kill 24% and 27% of adhered *E. coli* and *K. pneumoniae* cells respectively, while this decreased to 12% and 15% on nanocone arrays generated from 500 nm polystyrene microspheres (Hazell et al., 2018b).

UV lithography was used to create microstructures on cp titanium and Ti-6Al-4V, to promote soft tissue integration. Spin coating was applied to transfer a positive photoresist to the titanium substrates. Chromium line masks with periodic spacings between 3 µm and 200 µm were then used to filter UV light (405 nm) onto the titanium substrates. A controlled etching process was used to transfer the resist pattern onto cp titanium and Ti-6Al-4V. This involved an etching solution containing hydrogen fluoride, hydrogen peroxide (H_2O_2) and water (ratio of 11:1:10). The resulting surfaces comprised of rectangular, spiked and sinus-shaped microgrooves of lateral dimensions of 2.5, 5, 10 and 50 µm (Doll et al., 2018a, 2018b).

The original method for nanoimprint lithography, also known as hot embossing, involves the transfer of a defined pattern from a mould into an imprint resist coated onto the desired substrate. In this type of imprint lithography, the resist is a thermoplastic polymer that can be shaped around the mould when heated above its glass-transition temperature and held under pressure. Following hot embossing, the sample is cooled, and the original mould is removed, leaving a thickness contrast in the resist. The pattern can then be transferred into the base substrate by wet or dry etching methods (Chou et al., 1996). In contrast to conventional photolithography and e-beam lithography, nanoimprint techniques are capable of high resolution and high throughput patterning at considerably lower costs (Biswas et al., 2012). However, such approaches are not without limitations. For example, the transfer of a nanopattern from the master mould does not always occur with high fidelity. The nanofeature imprints can become distorted in the transfer material and may not completely fill the moulded material due to trapped air bubbles, ultimately leading to variation in surface nanotopography (Gates et al., 2005).

In a recent study, nanoimprint lithography was used to create cicada wing mimetic nanopillar arrays on PMMA films. Silicone negative moulds of cicada wings were imprinted into PMMA films held above the glass transition temperature (170°C). Following 5-10 minutes of pressured contact (4.5 MPa), the samples were cooled to 50°C and the silicon moulds were removed, leaving a nanoarchitecture similar to the cicada wing imprinted in the PMMA. The resulting nanopillar surfaces were reported to induce higher levels of bacterial cell death (16%-141% higher than control), with the most efficient surfaces having smaller and more closely packed nanopillar arrays (Dickson et al., 2015). In a different study, thermal nanoimprint lithography was used to create nanostructured surfaces on PMMA. The resulting surfaces consisted of periodic nanostructures with 300 nm spacing, 490 nm height and 250 nm base diameter. In contrast to the previous study, these surfaces were not reported to kill bacteria. Instead, they were shown to significantly reduce the attachment of bacteria (*P. aeruginosa, E. coli*) and mammalian cells (myoblasts) over 7 days (Kim et al., 2015).

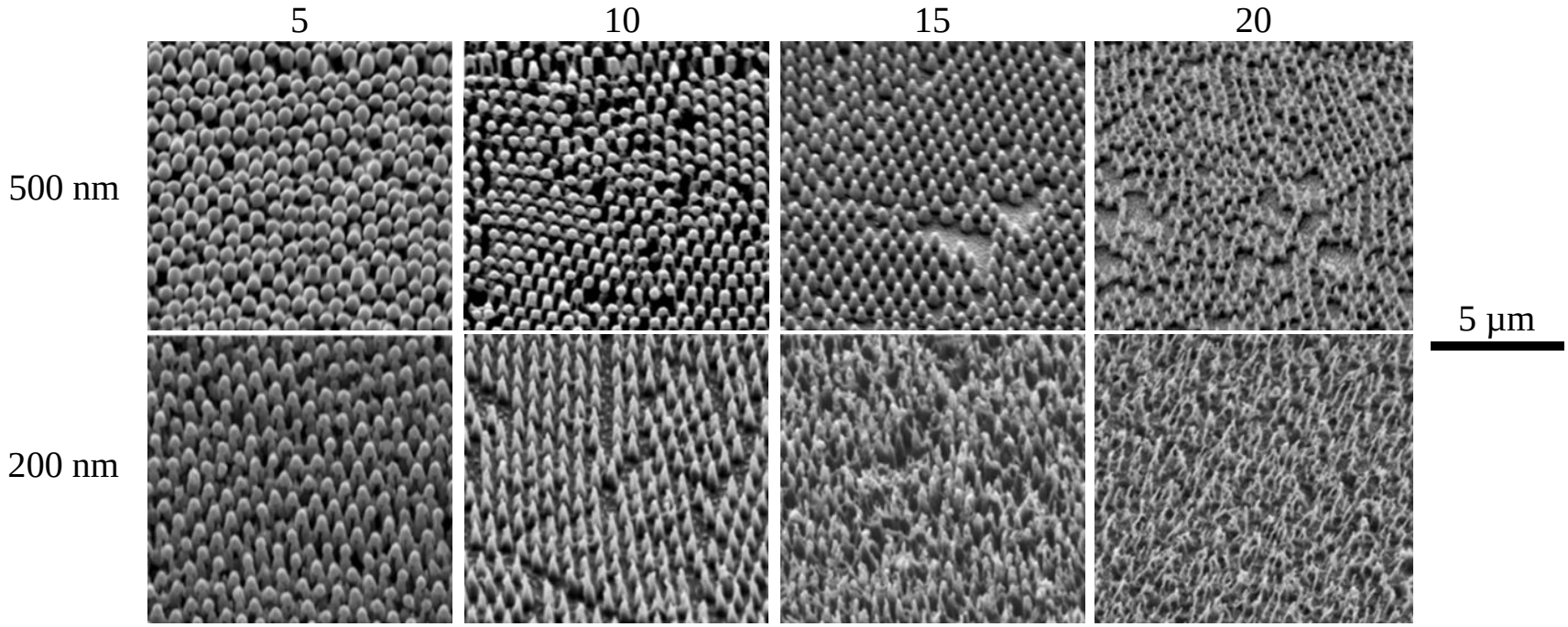

Structural parameter	Colloidal mask diameter (nm)							
	500				200			
	Etching time (mins)				Etching time (mins)			
	5	10	15	20	5	10	15	20
Base Diameter (nm)	381	316	272	187	155	129	118	55
Tip Width (nm)	304	280	193	99	54	33	22	20
Nanocone height (nm)	419	456	529	441	352	388	498	400

Figure 1.13 | Cicada mimetic nanocone arrays generated by colloidal lithography. Polystyrene microspheres measuring 200 nm or 500 nm in diameter were deposited onto PET films via spin coating and RIE was used for durations between 5 and 20 minutes to remove the regions of exposed PET, generating 8 distinct nanotopographies (Hazell et al., 2018b).

1.11.1.2 Maskless lithography

Maskless lithography techniques have also been used to generate bactericidal nanotopographies on a range of materials, including silicon and titanium. One example is RIE which involves bombarding a surface with a chemically reactive plasma, such as sulfur hexafluoride, chlorine or oxygen. The nanotopography can be modified by changing the etching time, pressure and gas phase. In one study, RIE was used to produce three different bSi nanotopographies, i) short needles (≈ 0.5μm), ii) medium needles (≈ 2.5μm) and iii) long needles (≈ 20μm) (Figure 1.14a). Short bSi needles were also denser and had sharper tips than medium and long needles. Following 1 hour incubation, a significant bactericidal effect was observed against *E. coli* on short, medium and long bSi needle surfaces compared to flat silicon. The percentage of dead cells was greatest on medium bSi needles, reported as 24-31%. In contrast, no effect was observed against Gram-positive cells (*Streptococcus gordonii*). This was attributed to the thicker peptidoglycan layer (Hazell et al., 2018a).

RIE techniques have been used to generate dragonfly mimetic nanotopographies. In one study, a five-minute etching process was applied to silicon wafers in the presence of sulfur hexafluoride and oxygen plasma. The resulting nanopillars showed a random size, shape and spatial distribution, similar to that of dragonfly wing nanoprotrusions, and were reported to possess highly efficient bactericidal activity (up to 450,000 cells $min^{-1}cm^{-2}$) toward both Gram-positive (*S. aureus*, *B. subtilis*) and Gram-negative cell types (*P. aeruginosa*) (Ivanova et al., 2013). Another study used a chlorine based RIE process to generate randomly orientated nanotopographies (≈1μm height) on cp titanium substrates. The resulting surfaces possessed significant bactericidal effects and were reported to achieve over 90% killing of *E. coli* and *P. aeruginosa* within 4 hours (Hasan et al., 2017). In another study, diamond nanocone arrays were fabricated by microwave plasma chemical vapour deposition (CVD) followed by RIE. Surfaces were etched for 2 hours using a gas mixture of 45% Ar and 55% H_2. By changing the potential of the substrate from -200V to -150V, two distinct nanocone arrays were created: surface A and surface B. Surface A nanocones varied in height from 800 nm to 2.5 μm while on surface B, the size of the diamond nanocones varied from less than 100 nm up to 5 μm (Figure 1.14b). The tips of nanocones on both surfaces varied from 10 to 40 nm. The density of nanocones on surface A was greater than surface B, measured at $4x10^8$ cm^{-2} and $1.7x10^8$ cm^{-2} respectively. A bactericidal effect was observed on both surfaces against *P. aeruginosa* following 1-hour static incubation, yet surface B was reported to possess the highest bactericidal activity (Fisher et al., 2016).

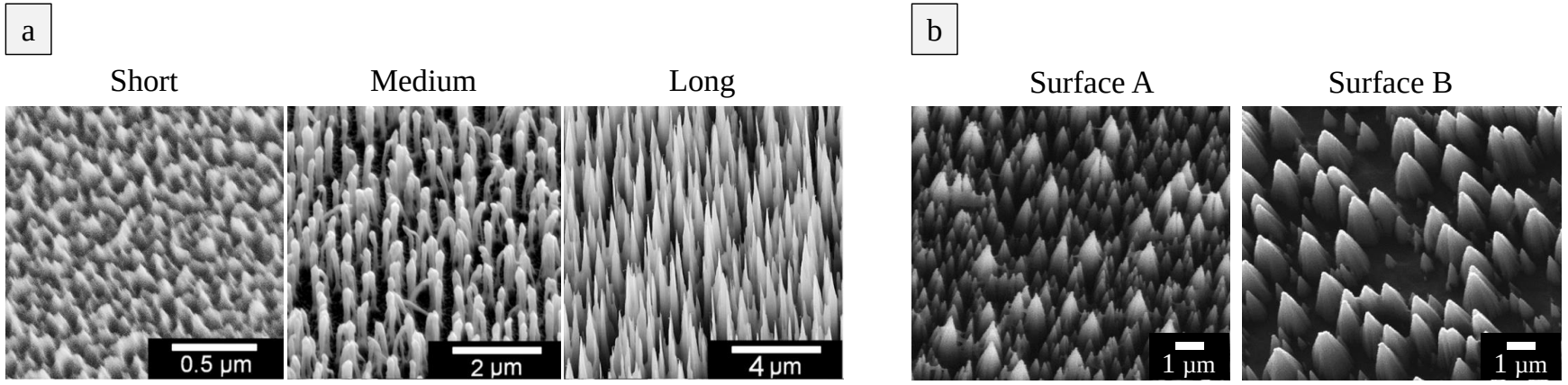

	bSi needles			Diamond nanocones	
	Short	Medium	Long	Surface A	Surface B
Length (µm)	0.5	2.5	18-20	0.8 - 2.5	0.1 – 5.0
Tip diameter (nm)	<30	100	<50	350-750	<100 - 1200
Density (per µm^2)	65	8	1.5	4	1.7

Figure 1.14 | Bactericidal nanotopographies generated by maskless lithography. Hazell and colleagues employed a RIE technique to generate nanoneedles on bSi wafers. Short, medium and long nanoneedles were generated by altering the conditions of RIE (duration and plasma constituents) (a). Fisher and colleagues utilised a RIE process to generate diamond nanocone arrays on silicon wafers (b) (Fisher et al., 2016; Hazell et al., 2018a).

1.11.2 Bottom-up nanofabrication approaches

The fundamental principle of bottom-up nanofabrication techniques is to generate functional nanotopographies from the self-assembly of atoms or molecules. As such, this approach is typically less wasteful as it removes the need for templates and resists commonly associated with top-down approaches (Biswas et al., 2012). Bottom-up nanofabrication can be broadly divided into liquid phase processing, that is, reactions that occur in aqueous solutions, or gas phase processing, in which a vapour phase is chemically or physically deposited onto a substrate (Sebastian et al., 2014).

1.11.2.1 Nanofabrication by liquid phase processing

The three most widely used liquid phase processing techniques include precipitation reactions, sol-gel processes and hydrothermal synthesis. By tuning the chemical and physical properties of these reactions, it is possible to control the size, morphology and crystallinity of the final nanotopography. Nevertheless, these approaches are often complex, involving multiple chemical processes, each of which needs to be precisely controlled to achieve the desired nanotopography (Sebastian et al., 2014). Nanofabrication by sol-gel processing involves the deposition of metal precursors onto a substrate that can then be sintered or oxidised to create the final product (Biswas et al., 2012). Such approaches have been widely used for the fabrication of metal oxide nanostructures, including silicon and titanium oxide (Hernández-Gordillo et al., 2014; Karami, 2010; Mohammadi et al., 2008). In contrast to the sol-gel method, hydrothermal processing uses mineralisers, such as sodium hydroxide, to dissolve and recrystallise a material. This process requires high pressures and is performed at temperatures between 100°C – 250°C. To facilitate this, hydrothermal processes are typically performed in Teflon lined stainless steel autoclaves that are chemically inert and can withstand degradation, thereby reducing the chance of contamination (Morgan, 2010). Hydrothermal processing has been used to generate needle shaped titania nanotubes with dimensions of 8 nm diameter and 100 nm length (Kasuga et al., 1999). Similar processes have been applied to the fabrication of cicada and dragonfly mimetic antibacterial nanowire arrays.

In one study, an alkaline hydrothermal process was used to generate cicada inspired titania nanowire arrays on cp titanium substrates. Polished titanium substrates were sealed inside an acid digestion vessel containing 1 M sodium hydroxide and heated to 240°C for durations of 3 hours or 8 hours. Following this hydrothermal step, additional heat treatment was performed at 300°C for 1 hour before ion exchange in 0.6 M hydrochloric acid. Finally, a calcination step was performed by heating the cp titanium samples for 2 hours at 600°C. The resulting 3 hour and 8 hour surfaces were termed brush-type and niche-type, respectively, reflecting the morphology of the nanowires (Figure 1.15a). Brush-type surfaces consisted of homogeneous nanowire arrays with average heights of 3 μm, while niche-type surfaces were characterised by pocket-like niches measuring 10-15 μm in diameter. These surfaces were reported to have strong bactericidal effects against motile bacteria *B. subtilis*, *E. coli* and *P. aeruginosa*, while no effect was observed for non-motile bacteria *Enterococcus faecalis*, *K. pneumoniae* or *S. aureus* (Diu et al., 2014). In a different study, spear-type and pocket-type titania nanowire arrays were generated using variations of the hydrothermal treatments previously outlined. In this case, the spear-type nanotopographies were ineffective at preventing *S. epidermidis* biofilm formation, while the pocket-type nanotopography showed anti-biofilm efficacy over 6 days *in vitro* (Cao et al., 2018). A different hydrothermal process was used to fabricate dragonfly inspired nanowire arrays (Figure 1.15b) (Bhadra et al., 2015). In this study, grade-2 titanium substrates were immersed in 10 M potassium hydroxide and heated to 121°C inside a steel autoclave maintained at 10-15 psi. Following hydrothermal treatment, samples were exposed to additional heating at 400°C for 3 hours. The resulting hydrothermally etched surfaces were reported to possess selective bactericidal activity, achieving percentage kill rates of 50% in *P. aeruginosa* and 20% in *S. aureus.*

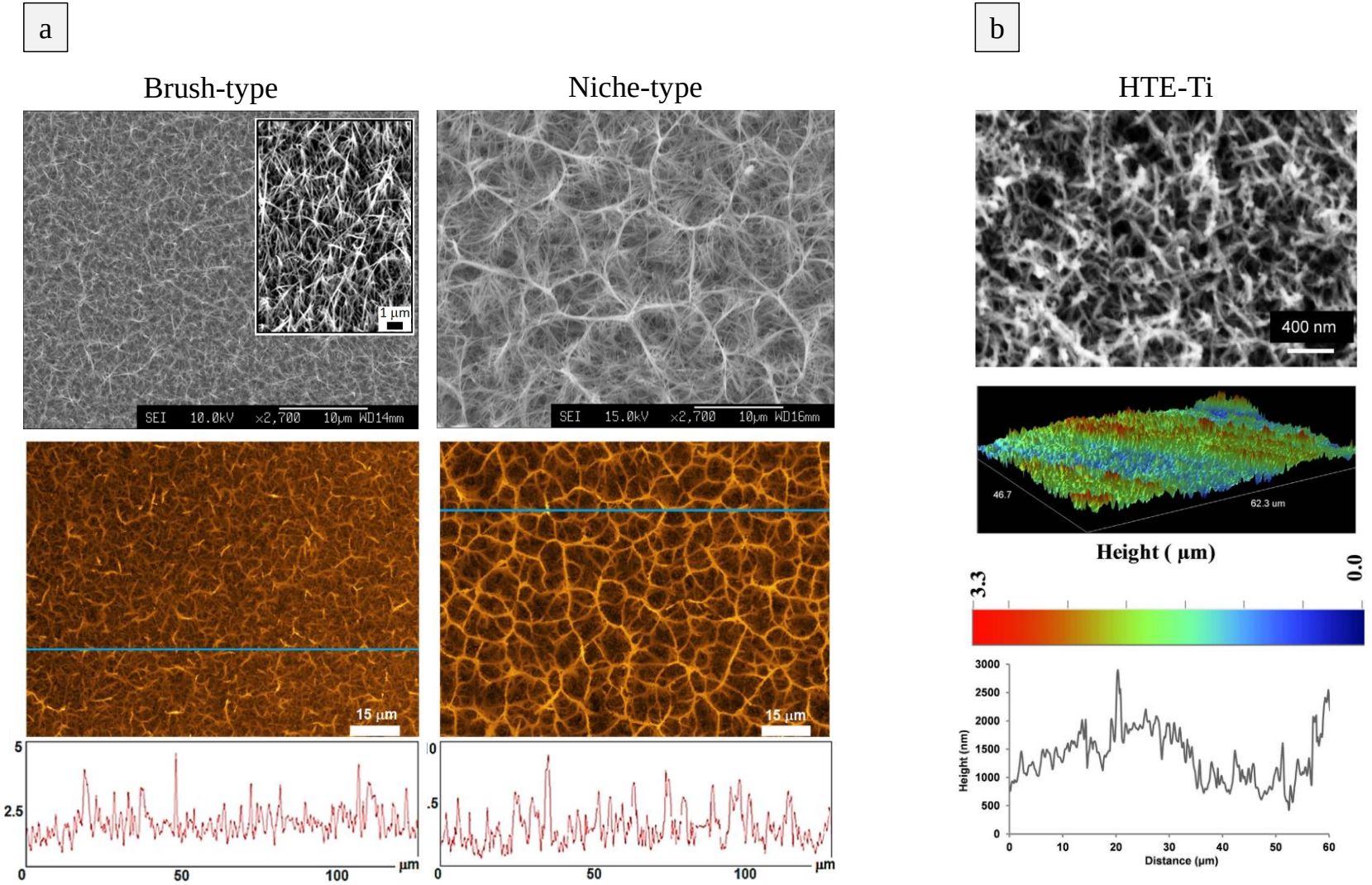

Figure 1.15 | Bactericidal nanotopographies generated by liquid phase processing. Diu and colleagues used alkaline hydrothermal treatments to generate brush- and niche-type nanowire arrays on cp titanium substrates (a). Bhadra and colleagues employed hydrothermal etching techniques to generate TiO_2 nanowires on cp titanium substrates (b) (Bhadra et al., 2015; Diu et al., 2014).

1.10.2.2 Nanofabrication by vapour phase processing

Vapour phase processing is frequently used for large-scale manufacturing of nanomaterial powders and thin films on metallic and ceramic substrates (Sebastian et al., 2014). It is also the most widely used approach for nanowire fabrication (Mohammad, 2009). Vapour phase processing is largely achieved by two methods: CVD and PVD. The key difference between these methods lies in the vapour phase constituents and the processing steps that are used to deposit them. For CVD, a source material is vaporised into a gaseous phase and mixed to form volatile precursors. These precursors are transported into a reaction chamber where deposition occurs by chemical reaction with the substrate (Biswas et al., 2012). In contrast, PVD involves the high energy evaporation of a pure source material that is transported by carrier gas into the reaction chamber, where physical deposition occurs. There are numerous variants of CVD and PVD, most of which are driven by thermal activation. However, they can also be initiated by photo- and plasma assisted methods (Mubarak et al., 2005). Several techniques which utilise vapour phase processing have been applied to the fabrication of nanostructured antibacterial surfaces.

Vertically aligned carbon nanotubes (VACNT) were fabricated using a combination of PVD and CVD followed by plasma treatment. Firstly, PVD was used to seed a catalyst layer comprised of 10 nm aluminium oxide and 1 nm iron. Next, carbon nanotubes (CNTs) were grown by CVD under atmospheric pressure and at 800°C. This step was performed for 20 s to create short nanotubes and 60 s to create long nanotubes. Additional oxygen and tetrafluoromethane plasma etching treatments were applied to short and long VACNT. The length of VACNT was reported to have a significant impact on *S. aureus* cell death, with 1 µm VACNT showing upward of 50% killing rates compared to less than 20% on 30 µm VACNT (Linklater et al., 2018). The diameter of CNTs is also reported to influence bacterial viability. In one study, single walled CNTs (SWCNTs) induced significantly more *E. coli* envelope damage than multiwalled CNTs (MWCNTs) (Kang et al., 2008). In general agreement with these findings, one study investigated the antibacterial efficacy of different SWCNT and MWCNT surfaces against *Lactobacillus acidophilus*, *Bifidobacterium adolescentis*, *E. coli*, *E. faecalis*, and *S. aureus*. Although each CNT surface inhibited the growth of the test bacteria, the diameter and length of CNTs was found to play an important role in the degree of membrane disruption observed. Envelope damage and piercing was greatest for SWCNTs, while longer CNTs were reported to wrap around bacteria (Chen et al., 2013).

In addition to CVD methods, a PVD method called glancing angle deposition was used to create cicada mimetic nanopillars on silicon. Firstly, silicon substrates were sputter coated with 450 nm titanium film using a magnetron sputter deposition system. titanium nanopillars were fabricated on top of this layer using glancing angle deposition. In this study, proliferation of adhered *E. coli* cells was reported to have caused envelope damage, leading to cell death (Köller et al., 2018).

1.12 Nanofabrication by thermal oxidation

The vapour phase processes discussed to this point, including CVD and PVD generally involve multiple processing steps and require the use of specialised equipment and vacuum pressure, thereby increasing fabrication costs. A simpler and less expensive route to generate nanowires in a vapour phase is by thermal oxidation, where nanowire growth is mediated by oxidation of a substrate at high temperatures (400°C-900°C). To date, thermal oxidation has been used to fabricate nanowires on a variety of substrates, such as copper (Jiang et al., 2002; Kaur et al., 2006; Mema et al., 2011; Xu et al., 2008, 2004), zinc (Li et al., 2005), cp titanium (Peng et al., 2005; Peng and Chen, 2004) and titanium alloys (Arafat et al., 2013; Dinan, 2012; Hu et al., 2010; Huo et al., 2008; Lee et al., 2010; Zhang et al., 2012), to name a few. In this study, thermal oxidation was used to generate nanowires on Ti-6Al-4V alloy. The following provides an overview of the oxidation process in titanium and the current literature relating to the use of thermal oxidation to generate nanowire arrays on titanium and its alloy substrates.

1.12.1 Titanium oxide formation

Titanium spontaneously reacts with oxygen to form a stable oxide layer. At standard room temperature and pressure, this layer is normally between 3 and 10 nm thick, which is sufficient to create a chemically passive and corrosion resistant barrier (Viteri and Fuentes, 2013). The most common oxide to form is TiO_2. In recent decades, TiO_2 has found use in a wide range of applications including biosensors, batteries, self-cleaning coatings and anti-corrosion coatings, wastewater management, biomedical implants and antimicrobial surfaces (Diebold, 2003; Peng and Chen, 2004; Sjöström et al., 2016). These useful properties are attributed to the crystal structure of TiO_2, of which anatase and rutile are the most important. Anatase and rutile TiO_2 have tetragonal crystal systems, whereby a central titanium atom is surrounded by six oxygen atoms arranged into an octahedral configuration, these constitute one unit cell (Figure 1.16). Although anatase and rutile are both tetragonal, the spacings between each unit cell (lattice constants) are different. For anatase a = b = 0.373 nm and c = 0.937 nm while in rutile a = b = 0.458 nm and c = 0.295. Furthermore, the stacking arrangement of these systems differ, in rutile, one corner is shared between neighbouring octahedra, in [110] type directions, and these are stacked with the long axis alternating by 90°. In contrast, neighbouring octahedra in anatase form [001] planes (Diebold, 2003).

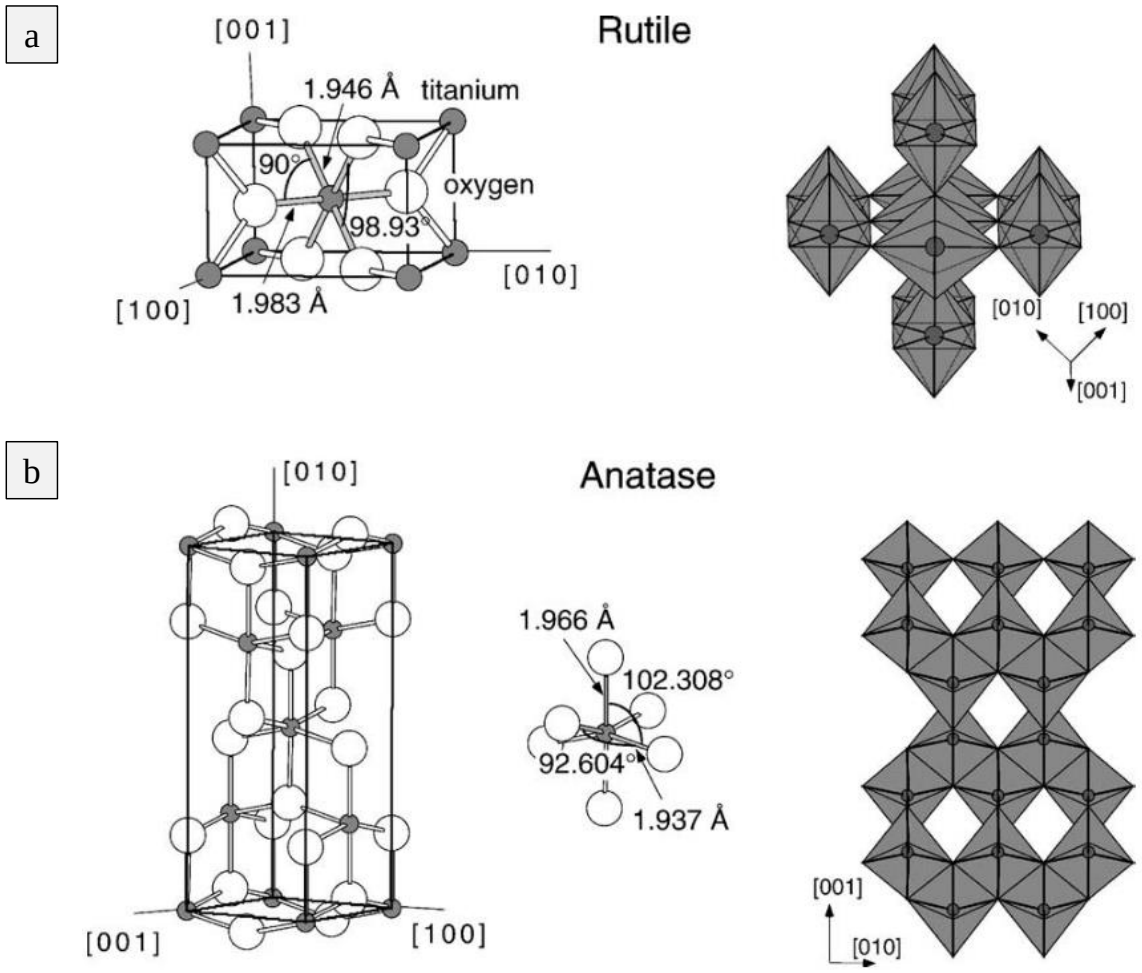

Figure 1.16 | Anatase and rutile TiO_2 unit cell structures and stacking arrangement. Both rutile and anatase have tetragonal unit cell arrangements with slightly different lattice constants. Rutile has the dimensions, a = b = 0.458 nm and c = 0.295 while for anatase a = b = 0.373 nm and c = 0.937 nm. The basic building units of anatase and rutile are slightly distorted octahedra, the stacking arrangements for which are shown on the right. The bond lengths and angles for anatase and rutile octahedra are shown (Diebold et al., 2003).

1.12.2 Thermal oxidation of titanium and its alloys

The physical properties of TiO_2 can be easily modified by changing the reaction conditions of thermal oxidation (Figure 1.17). One study reported the effects of temperature, flow rate and crystal phase on nanowires grown on cp titanium and its alloys (Ti-6Al-4V and β-Ti). Briefly, titanium samples were placed in a quartz tube, inside a horizonal tube furnace. After purging the tube for 1 hour with 5% hydrogen balanced with Ar gas (1000 mL min^{-1}) the furnace temperature was increased to 700-900°C at a rate of 30°C min^{-1}, these temperatures were maintained for time periods between 6 and 10 hours under Ar flow rates of 200, 500 and 1000 mL min^{-1}. For cp titanium, high aspect ratio nanowires with lengths ranging from 50 nm to 400 nm were generated after 8 hours at 600°C and 200 mL min^{-1}. In contrast, for titanium alloys (Ti-6Al-4V and β-Ti) nanowire growth was observed over a wide range of temperatures (600°C-800°C) while flow rate had a negligible effect. As for cp titanium, high temperatures (800°C-900°C) promoted the growth of larger, multifaceted crystals on titanium alloys (Lee et al., 2010). This study also indicated that nanowire growth was most prominent within β-phase crystals, that are present in titanium-alloys. This is most likely attributed to the higher diffusion coefficient of oxygen within β-phase crystals compared to α-phase crystals (Dinan, 2012), thus, nanowire growth is faster.

The type of oxidising environment used during thermal oxidation has been shown to strongly effect nanowire growth. In one study, thermal oxidation was performed under different oxygen atmospheres; i) pure oxygen, ii) low oxygen and iii) acetone. In all cases, cp titanium samples were oxidised at 850°C for 1.5 hours prior to natural furnace cooling. In pure oxygen, the resulting surfaces comprised of multifaceted crystal structures, while low oxygen concentrations generated randomly oriented nanofibers. In contrast, the use of acetone resulted in aligned nanorod arrays. These differences were attributed to the variable diffusion rates of oxygen. In the presence of acetone, the availability of oxygen is lower than in pure and low oxygen conditions, therefore, the diffusion of titanium to the oxide surface will likely dominate the oxidation reaction. In contrast, oxidation at the Ti-TiO_2 interface dominates in pure oxygen. Thus, the following mechanism of growth was proposed where acetone is the pure oxygen source: Firstly, a thin oxide layer is formed, followed by the diffusion of titanium cations to the surface via a grain boundary within the oxide layer, which then results in a reaction with adsorbed acetone (Peng and Chen, 2004). This model was supported by time duration studies, whereby the nanorods were observed to evolve from small crystals to larger nanorods after

longer durations (Peng and Chen, 2004). These findings were validated in subsequent investigations (Peng et al., 2005).

In another study, titanium foils were oxidised for 1.5 hours at 850°C and 150 SSCM, using acetone as the oxygen source. These conditions led to the generation core-shell nanocone structures. The core was found to comprise of rutile TiO_2 while the shell consisted of amorphous carbon (Huo et al., 2008). Of note, a carbon shell was not reported in the previous studies (Peng et al., 2005; Peng and Chen, 2004). The proposed mechanism by which core-shell nanocones formed is as follows: Under high temperature, acetone is thermally decomposed to generate gaseous phases of carbon monoxide (CO) and methyl radicals ($\cdot CH_3$). Following decomposition of acetone, CO absorbs to the titanium surface where it reacts to form TiO_2 and carbon in the shell. The sustained epitaxial growth of TiO_2 is believed to occur by the diffusion of titanium atoms through the TiO_2 layer, which react with CO upon reaching the solid-gas interface. Simultaneously, the decomposition of $\cdot CH_3$ results in the precipitation of carbon, which is deposited as a shell (Huo et al., 2008).

The mechanism of nanowire growth is reported to be different on Ti-6Al-4V substrates. Hu and coworkers performed thermal oxidation of Ti-6Al-4V substrates under acetone vapour at 800°C, which resulted the formation of uniform nanofibers with diameters between 70-90 nm and lengths of several micrometres. In similarity to the previous study, transmission electron microscopy (TEM) analysis identified a core-shell structure, with a consistent core diameter of 40-50 nm and a shell of 15-20 nm thickness. However, the core was reported to comprise of single crystalline titanium carbide (TiC) and the shell comprised of partially crystallised carbon. In light of these findings, the mechanism of growth was proposed to be slightly different: Following the decomposition of acetone, CO absorbs onto the Ti-6Al-4V where it reacts to form TiC nanoparticles and an aluminium oxide layer. TiC nanoparticles are deposited epitaxially with time, meaning that longer oxidation durations should generate larger nanostructures. During this surface reaction, $\cdot CH_3$ radicals are degraded into hydrogen and carbon. The deposition of carbon onto the TiC core results in a core-shell structure (Hu et al., 2010). In another study, thermal oxidation was performed on both titanium foils and aluminium ion implanted titanium foils. The oxidation conditions were similar to the previous studies (800°C in the presence of acetone for 2 hours). In general agreement with previous studies, this resulted in the formation of core-shell TiO_2/C on titanium foils and TiC/C nanofibers on aluminium ion implanted titanium foils (Zhang et al., 2012).

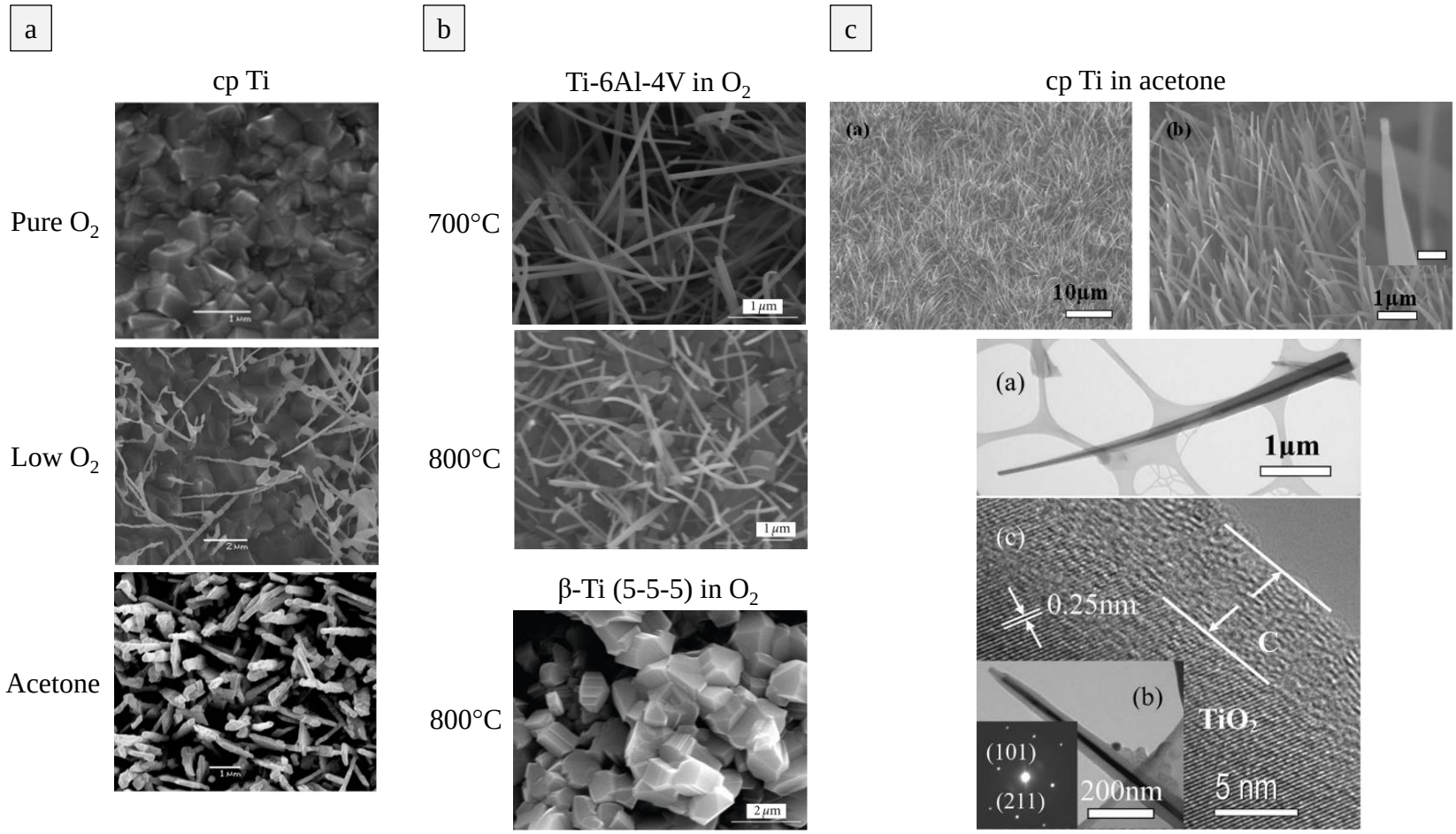

Figure 1.17 | Nanowires grown by thermal oxidation. Chen and Peng oxidised cp titanium at 850°C for 1.5 h using 3 different oxidising environments i) pure oxygen, ii) low oxygen and iii) acetone (a). Nanowire growth was most prominent in acetone. Lee and colleagues oxidised cp titanium and titanium alloys (Ti-6Al-4V and β-Ti (5-5-5)) at different temperatures using an oxygen environment. Nanowire growth occurred over a broader range of temperatures on Ti-6Al-4V (b). Huo and colleagues utilised acetone as the oxygen source to thermally oxidise cp titanium (c). The resulting surfaces consisted of nanowires with core-shell structures; TiO_2 was identified in the core while carbon was found in the shell (Huo et al., 2008; Lee et al., 2010; Peng & Chen, 2004).

1.12.3 Osteogenic and antimicrobial properties of thermally oxidised titanium

In recent years, many studies have reported on the enhanced osteogenic potential of titanium surfaces that have undergone thermal oxidation. In one study, a combination of acid etching and thermal oxidation were applied to cp titanium foil and rods. Oxidation was performed at 450°C under ambient atmosphere for durations of 2, 4 and 6 hours (TO2, TO4, TO6) prior to natural furnace cooling. The microstructure of each surface was comparable, consisting mainly of rutile TiO_2. *In vitro*, the attachment of bone marrow mesenchymal stem cells was enhanced on TO surfaces compared to control and had reached full confluence on each surface after 7 days. The expression of osteogenic-related genes, namely alkaline phosphatase (ALP), osteocalcin (OCN), osteopontin (OPN) and bone sialoprotein (BSP) were significantly up-regulated on TO6 after 14 days, and displayed the best matrix mineralisation after 21 days (Wang et al., 2016).

In another study, the adhesion, proliferation, differentiation, mineralisation and osteogenic response of primary osteoblasts was investigated on control surfaces compared to TiO_2 nanowires generated by thermal oxidation. TiO_2 nanowire arrays were reported to promote initial osteoblast adhesion and spreading compared to control, as well as induce higher levels of proliferation. The expression of osteogenesis-related genes, including ALP, BSP, OCN, OPN, runt-related transcription factor (Runx2) and extracellular mineralisation were significantly upregulated in the presence of TiO_2 nanowires (Tan et al., 2014). TiO_2 nanowire surfaces created by thermal oxidation have also shown promising results *in vivo* (rat calvarial model). Computer tomography based analysis of the interface between TiO_2 nanowire surfaces and the calvarial bone showed increased bone volume after 8 weeks *in vivo*, with significant differences observed after 4 weeks. Histology analysis after 8 weeks provided evidence of increased new bone formation on nanowire surfaces compared to control (Goriainov et al., 2018). The antibacterial properties of TiO_2 nanowire arrays created by thermal oxidation have also been reported (Figure 1.18). In one study, Ti-6Al-4V of oxidised at 850°C for 45 minutes, using acetone as the oxygen source. The final characteristics of the TiO_2 nanowires could be modified by changing the oxidation parameters, namely the Ar flow rate. TiO_2 nanowires with tip diameters of 20 nm were generated. Bacterial viability testing with PrestoBlue indicated a 40% reduction in *E. coli* viability following 2-hour static incubation (Sjöström et al., 2016). In combination, these studies indicate that thermal oxidation is an effective method for generating surfaces that impair bacterial growth, whilst enhancing the osteogenic properties of titanium and its alloys.

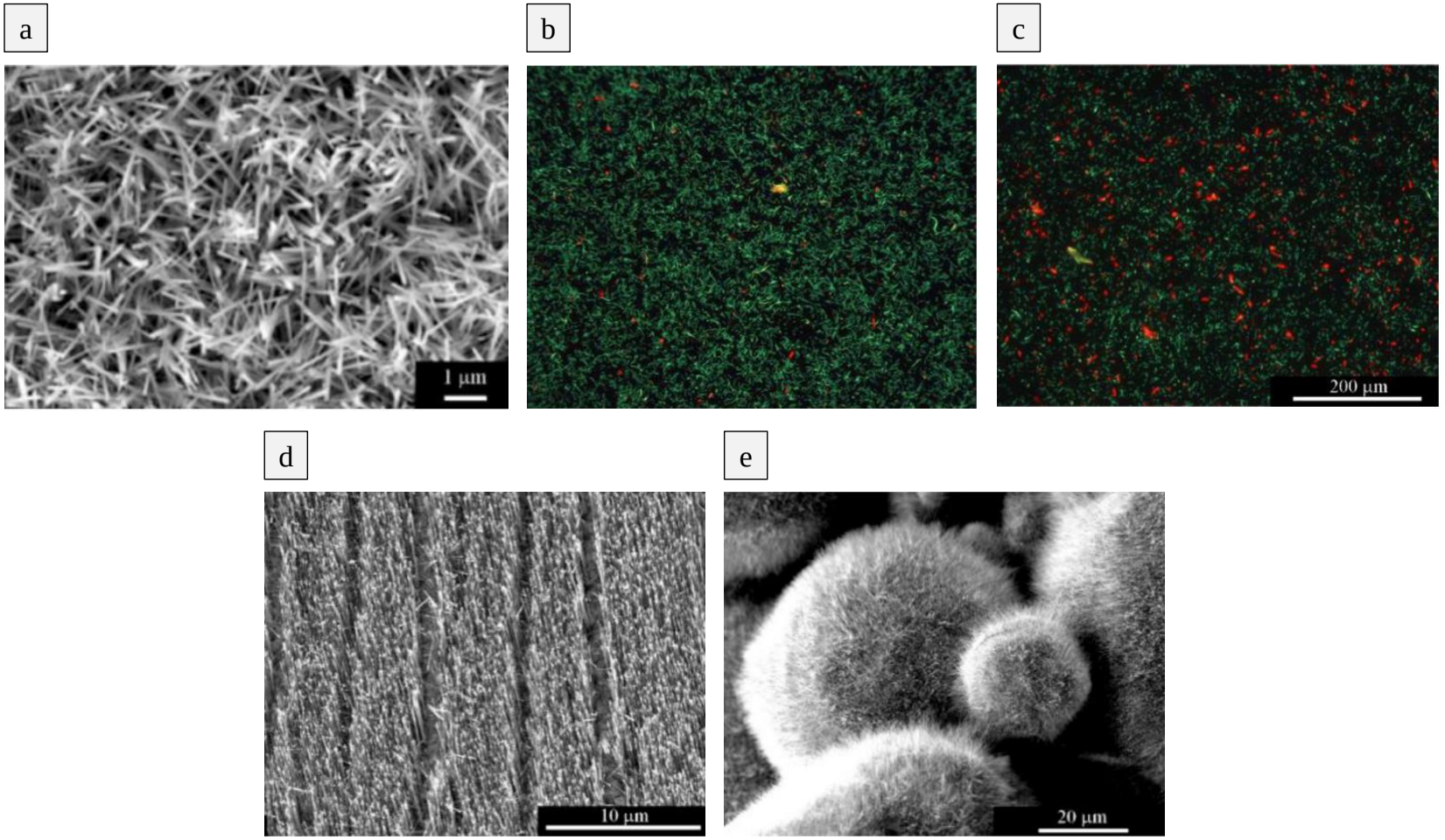

Figure 1.18 | Bactericidal nanotopographies generated by thermal oxidation. Sjostrom and colleagues utilised thermal oxidation to generate TiO_2 nanowire arrays on planar Ti-6Al-4V substrates (a). The resulting nanowire surfaces were shown to exhibit bactericidal activity toward *E. coli* (b) compared to control (c). The crystal structure of Ti-6Al-4V was manipulated to generate uniform arrays of nanowires (d). Thermal oxidation was also used to generate TiO_2 nanowires on 3D substrates (e) (Sjostrom et al., 2016).

1.12.4 Strengths and limitations of thermal oxidation

There are a number of advantages for using thermal oxidation over more conventional nanofabrication methods such as CVD and lithography. Firstly, thermal oxidation provides a simple and straightforward method to synthesise large areas of uniform nanowires, in a single step, and directly onto the device of choice. A further advantage of this technique is that specialised equipment, such as that used in lithography and the high vacuum chamber used in CVD, are not required, thereby reducing the cost of fabrication and negating the need for highly trained personnel. As an example, copper oxide nanowires have been synthesised directly onto copper substrates purely by furnace heating in air (Jiang et al., 2002). TiO_2 nanowires have been grown directly onto titanium alloy substrates in a carbon-rich thermal oxidation condition (Hu et al., 2010; Huo et al., 2008; Zhang et al., 2012). Additionally, thermal oxidation can be used to fabricate nanowires on both planar (2D) substrates and more complex (3D) shapes (Sjöström et al., 2016), whereas many conventional lithography techniques are restricted to fabrication on planar substrates (Gates et al., 2005). Additionally, thermal oxidation does not require an external catalyst to mediate growth, thereby eliminating the need for additional processing steps to remove the spherical cap that is commonly associated with the vapour-liquid solid (VLS) growth mechanisms (Dinan, 2012; Mohammad, 2008). Nevertheless, there are some limitations associated with thermal oxidation. Firstly, because of the high processing temperatures, this can change the physical structure and properties of the material, which may affect the desired end application. Furthermore, metal oxide nanowires are prone to damage. Again, this may restrict the suitability for some applications.

1.13 Thesis aims

Although a significant amount of research has investigated the bactericidal properties of natural and synthetic nanoarrays, our understanding of the underlying mechanism(s) that cause bacterial cell death remains unclear. Many studies have reported that nanowires mediate mechanical rupture of bacterial cells (Hasan et al., 2013; Ivanova et al., 2013, 2012; Pogodin et al., 2013). However, this has largely been inferred from LIVE/DEAD analysis and thus, has not been shown conclusively. Dragonfly wings are reported to possess antimicrobial activity against bacteria (Gram-positive and Gram-negative) (Bandara et al., 2017; Ivanova et al., 2013) and fungi (Nowlin et al., 2014). Given their broad spectrum activity, this study sought to generate dragonfly mimetic nanoarrays directly on Ti-6Al-4V, a material widely used for orthopaedic implants. A thermal oxidation method was employed for this purpose, since preliminary reports indicated that nanowire surfaces generated by thermal oxidation possess bactericidal activity (Sjöström et al., 2016). For such technologies to be translated into clinical applications, better understanding of the exact causes of bacterial cell death is required. Taking steps to address this fundamental knowledge gap was therefore the overall aim of this study.

The specific objectives of this study were as follows:

1. Fabricate dragonfly mimetic TiO_2 nanowire arrays on Ti-6Al-4V using a thermal oxidation technique.
2. Determine whether TiO_2 nanowire arrays possess antibacterial properties, using a range of viability indicator assays and molecular techniques.
3. Investigate the effects of TiO_2 nanowire arrays on bacterial morphology, using several advanced imaging techniques.

CHAPTER 2

Materials and Methods

2.1 Fabrication of TiO_2 nanowires on titanium alloy (Ti-6Al-4V)

2.1.1 Polishing

Square discs (25 cm^2) of grade 5 titanium alloy (Ti-6Al-4V) (Titanium Metals Ltd) were mechanically polished (Struers® TegraForce-1) on MD-Largo discs mounted with silicon carbide (SiC) paper (Struers®). Polishing was performed in 2-minute cycles, using decreasing SiC grit sizes (#80, #500, #1200, #2000, and #4000). Following mechanical polishing, several disc sizes were generated: 1) 0.64 cm^2 discs were used for bacterial cell viability testing, electron microscopy and end-point fluorescence microscopy, 2) 0.06 cm^2 discs were used for CLSM, and 3) 25 cm^2 discs were used in proteomic studies. To remove surface contaminants, titanium discs were placed inside a digital ultrasonic bath (Grant Scientific XUB series) in distilled water (dH_2O) and the samples were cleaned at 40°C for 15 minutes using 100% power. Following ultrasonication, titanium discs were placed in analytical reagent grade (99.99%) ethanol (Fisher Scientific, MA, USA) for 10 minutes before air drying.

2.1.2 Thermal oxidation

Polished and cleaned titanium discs were sealed inside a horizontal alumina tube (120 cm x 11 cm outer x 9 cm inner) positioned within a furnace (Elite Thermal Systems Ltd). Prior to thermal oxidation, the furnace was purged with Ar gas (BOC, Guildford, UK) for a duration of 30 minutes, this ensured a one-directional flow and minimised the concentration of atmospheric oxygen. Following Ar purging, furnace heating was initiated at a rate of 15°C/min until a pre-defined maximum was reached (Figure 2.1a); temperatures between 650°C-900°C were used in this study. Upon reaching the final temperature, Ar was redirected into a gas bubbler containing analytical reagent grade (99.99%) acetone (Fisher Scientific, MA, USA) (Figure 2.1b). The evaporation temperature of acetone was maintained using a water bath set to 25°C. The flow rate of Ar carrier gas was varied from 50 to 500 standard cubic centimetres per minute (SCCM) to control the concentration of acetone within the tube furnace. In this study, thermal oxidation was performed under different oxygen atmospheres however, for most of the experiments, acetone was used as the oxygen source. Upon completion of oxidation, the production of acetone vapour was stopped, and the furnace was cooled to room temperature under a constant flow of Ar (300 SCCM).

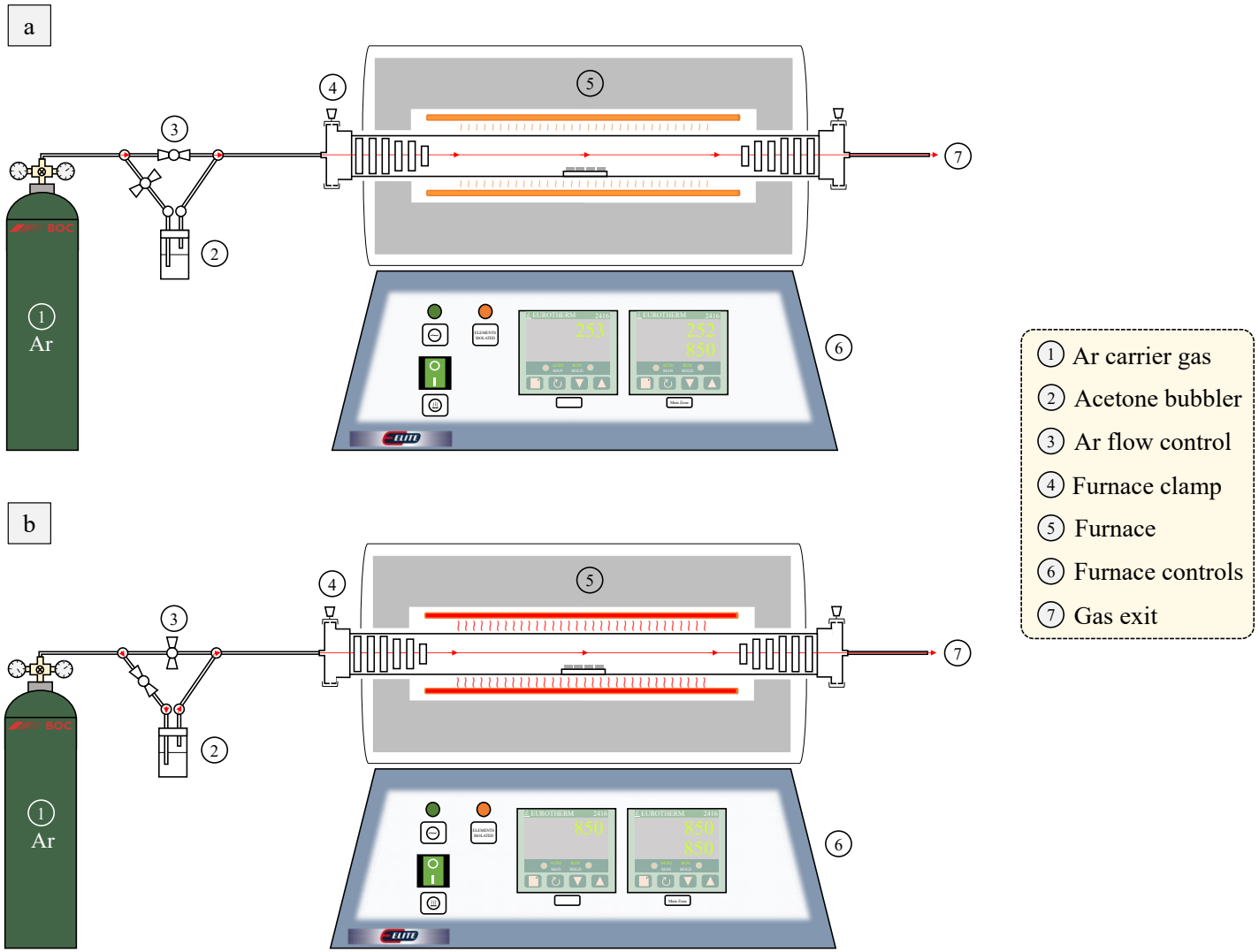

Figure 2.1 | Thermal oxidation experimental setup. Ar carrier gas is used to purge the alumina tube during furnace heating (a). Once a pre-defined temperature had been reached (850°C), Ar is redirected into an acetone bubbler, leading to the production of a vapour (b). Vaporised acetone was transported into furnace, leading to the oxidation of titanium discs and growth of nanowires.

2.1.3 Post-annealing

Thermal decomposition of acetone led to carbon deposits forming on nanowire arrays. To remove the carbonaceous layer, as-synthesised nanowire arrays were transferred to a muffle furnace (Elite Thermal Systems Ltd) and heated to 600°C at a rate of 10°C/min. Annealing was performed for 30 minutes before furnace cooling was initiated.

2.1.4 Pre-annealing

To determine the effect of grain size and orientation on nanowire growth, annealing was performed prior to thermal oxidation, at temperatures exceeding the beta transus of Ti-6Al-4V (996°C); 1000°C, 1100°C and 1200°C were used. Polished titanium discs were sealed inside a horizontal alumina tube (120 cm x 11 cm outer x 9 cm inner) positioned within a furnace (Elite Thermal Systems Ltd). The alumina tube was connected in series to a vacuum pump (Edwards Vacuum® RV8 pump) fitted with a vacuum gauge (INFICON® Pirani Standard Gauge PSG550 Tungsten). To limit the concentration of oxygen, the tube was pumped to a negative pressure of 5×10^{-2} mbar before purging with Ar gas to equalise the negative pressure. Once a positive pressure of 1.020×10^{3} mbar was established, furnace heating was initiated at a rate of 15°C/min until a pre-defined maximum was reached. Annealing of titanium discs was performed for a duration of 1 hour, prior to furnace cooling under constant Ar flow.

2.2 Determination of nanowire dimensions

A Quanta 200 field emission gun (FEG) SEM (FEI, Oregon, USA) equipped with an Everhart-Thornley detector (ETD) was used to characterise nanowires produced by thermal oxidation. Firstly, to establish nanowire homogeneity and reproducibility between thermal oxidation batches, top view electron micrographs were taken of discs from three independent batches; micrographs were taken at three locations per disc. The find maxima function within Fiji software was used to calculate the number of nanowires per micrograph (*nw*); *nw* was divided by the micrograph area (*a*), to quantify the average density of nanowires per μm^2 (*d*). Reported nanowire densities (*D*) show the average nanowire densities from three independent batches (Equation 2.1).

Equation 2.1: **Determination of nanowire density per μm^2.**

$$d = nw \div a \ \therefore D = average(d)$$

The straight-line tool within Fiji was also used to measure the tip-to-tip spacing of 20 nanowires per micrograph (*snw*) {1}. These values were averaged per micrograph (*sm*) and used to calculate the average spacing per batch (*s*) {2}. Reported nanowire spacings (*S*) {3} show the averages from three independent batches (Equation 2.2).

Equation 2.2: **Determination of nanowire tip-to-tip spacing.**

$$\{1\}: sm = average(snw)\ \{2\}: s = average(sm)\ \{3\}: S = average(s)$$

Tilted (40°) electron micrographs were used to estimate the length and tip diameter of nanowires; micrographs were taken at three locations per disc, from three independent batches. The straight-line tool within Fiji was used to measure the length (*lnw*) and tip diameter (*rnw*) of 20 nanowires per micrograph. These values were averaged per micrograph (*lm* and *rm*) {1} and used to calculate the average length and tip diameter per batch (*l* and *r*) {2}. Reported nanowire lengths (*L*) and tip diameters (*R*) {3} show the averages from three independent batches (Equation 2.3-2.4).

Equation 2.3 and 2. 4: **Determination of nanowire length and tip diameter.**

$$\{1\}: lm = average(lnw)\{2\}: l = average(lm)\ \{3\}: L = average(l)$$

$$\{1\}: rm = average(rnw)\{2\}: r = average(rm)\ \{3\}: R = average(r)$$

2.3 Contact angle measurements

Surface wettability describes the spreading behaviour of a liquid placed in contact with a solid. This interaction can be directly quantified by measuring the contact angle (θ) that forms at the three-phase point (Figure 2.2a). The sessile drop method is widely used to measure the contact angle of solids and can be used to derive the surface free energy via Youngs equations (Figure 2.2b).

In this study, the sessile drop method was performed using a Drop Shape Analyser (DSA)100 Goniometer (Kruss instruments, Hamburg, Germany). Dynamic dosing was used to transfer 2 µl droplets of dH_2O onto each titanium disc. Four categories were used to describe the wetting behaviour of titanium discs: 1) Superhydrophilic ($\theta < 5°$), 2) Hydrophilic ($\theta > 10°$ and $< 90°$), 3) Hydrophobic ($\theta = 90°$- $150°$) and 4) Superhydrophobic ($\theta = >150°$) (Zhang et al., 2013). Drop shape analysis was performed in triplicate per disc. The contact angle formed at the three-phase point was determined according to different geometrical models: 1) Circle method, and 2) Young-Laplace-Fit. The Circle method assumes the drop shape is a circular arc, which is suited to measuring small contact angles (0°- 20°). As such, the Circle method was used to determine the contact angle on post-annealed titanium discs, since these surfaces were generally superhydrophilic. In contrast, the Young-Laplace-Fit assumes an ideal sessile drop shape and can be used to determine wettability over a broader range of contact angles (10° - 180°). The Young-Laplace Fit was used to determine the contact angles on as-synthesised (core-shell) and control titanium discs, which are generally ≤90°.

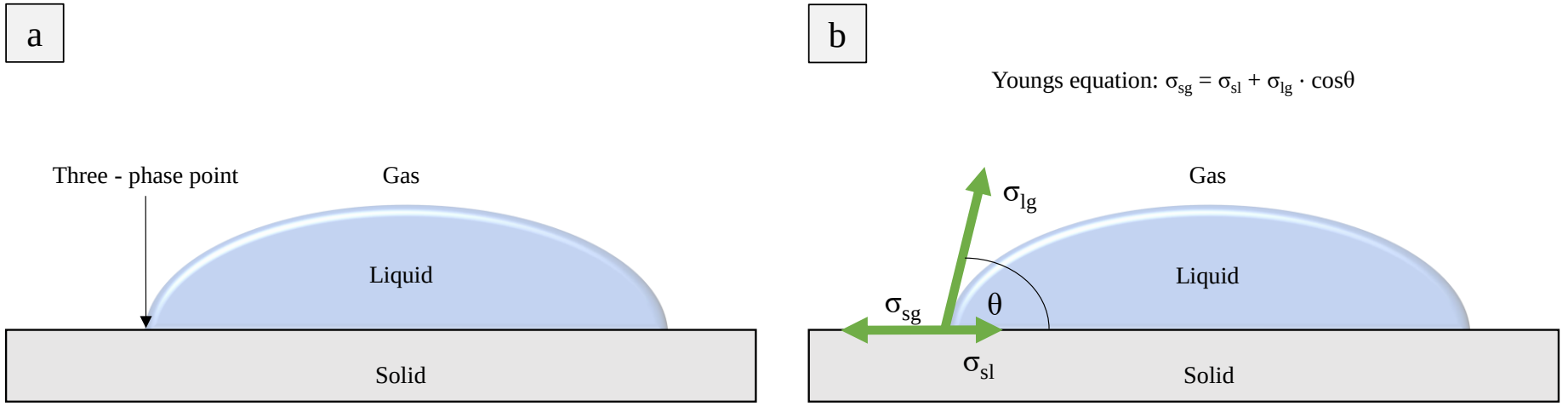

Figure 2.2 | Principles of contact angle measurements. The spreading behaviour of a liquid in contact with a solid can be described via Youngs equation, which shows the relationship between the contact angle (θ) and the three phases (solid, liquid and gas). The ratio between surface tension (liquid) and surface free energy (solid) determines the contact angle; solid interfaces displaying high surface free energy will often have low contact angles, whereas solids displaying low surface energy often exhibit high contact angles. (Adapted from Kruss instruments - https://www.kruss-scientific.com/services/education-theory/glossary/contact-angle/).

2.4 Determination of nanowire elemental composition

2.4.1 Energy Dispersive X-ray Spectroscopy (EDX)

Electron microscopes can be fitted with additional detectors to characterise the elemental composition of samples; EDX is one of these techniques. The fundamental principle of EDX is as follows: The sample is bombarded with a high energy beam of charged particles (usually electrons), resulting in the emission of ground state electrons and subsequent formation of an electron hole. Electrons occupying higher energy levels may fill this hole, and the energy difference between these shells results in the emission of an X-ray of specific energy (Figure 2.3) (Hafner, 2006). A scalpel blade was used to scrape nanowires into analytical reagent grade (99.99%) ethanol. The detached nanowires were transferred into a digital ultrasonic bath (Grant Scientific XUB series) and were sonicated for 5 minutes at 100% power to create a homogeneous suspension. Nanowire suspensions (1.5 µL) were then aliquoted onto copper grids with lacey and holey carbon support films (EM resolutions Ltd, Sheffield, UK) and ethanol was evaporation. EDX was performed in line-scanning and point analysis modes on a JEOL JEM-2100F FEG TEM. Elemental compositions were determined at multiple positions per nanowire. Data collection was carried out by Dr. Sean Davis, University of Bristol, Bristol, UK.

2.4.2 X-ray photoelectron spectroscopy (XPS)

XPS analysis is widely used to determine the elemental composition of a materials surface (1 – 10 nm depths). Briefly, mono-energetic (soft) X-rays are focused onto a sample, resulting in the emission of core electrons; this process is known as the photoelectric effect (Figure 2.4). The kinetic energy of photoelectrons is dependent on the electron binding energy, and the incident X-ray energy. Because each element has a distinct electronic configuration, the kinetic energy of photoelectrons is characteristic of the element from which it came. It is also possible to determine the chemical environment from which the electron was emitted, and the electron orbital (Figure 2.4). XPS measurements were carried out in an ultrahigh vacuum set-up equipped with a high-resolution Specs PHOIBOS 150 2D-DLD. A monochromatic Al K_α X-ray source (photon energy 1486.6 eV; anode operating at 15 kV) was used as incident radiation. The base pressure was around 2×10^{-10} bar. XPS spectra were recorded in the fixed transmission mode. Scans were collected from 10 to 1100 eV with a pass energy of 30-40 eV, resulting in an overall energy resolution of 0.1-0.5 eV. The data collection was carried out by Dr. Michael Wagstaffe at the DESY NanoLab, Hamburg, Germany.

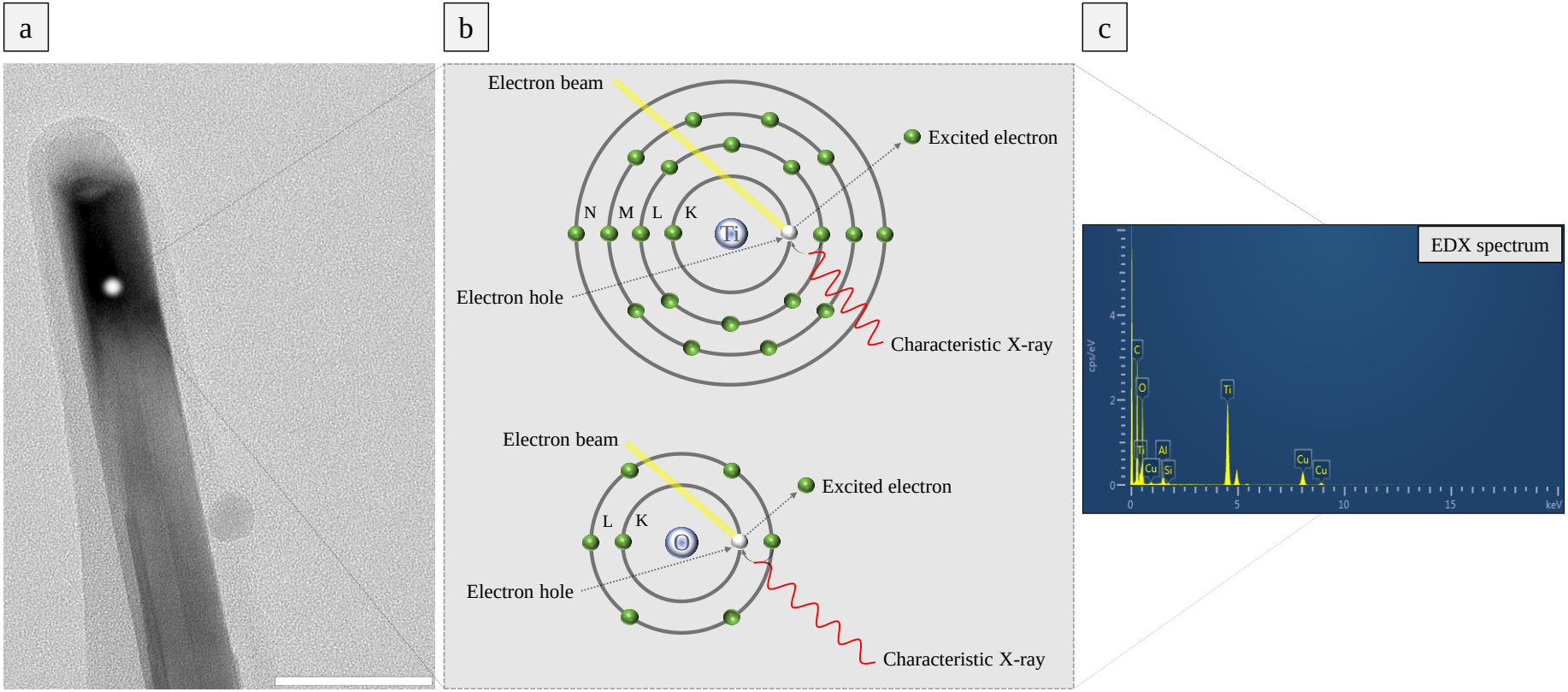

Figure 2.3 | Principles of EDX analysis. When high energy electrons are focussed onto a sample, such as a TiO_2 nanowire (a), ground state electrons (in low energy shells) may receive enough energy to be ejected from the shell, creating a positively charged electron hole. Electrons occupying higher energy shells may fill this hole, leading to the emission of an X-ray (b). The energy of emitted X-rays is dependent on the atomic structure, which is determined by the energy difference between the low and high energy shells. As can be seen from the EDX spectrum (c), the X-rays emitted from a sample are characteristic of its elemental composition. Scale bar = 50 nm (Hafner, 2006).

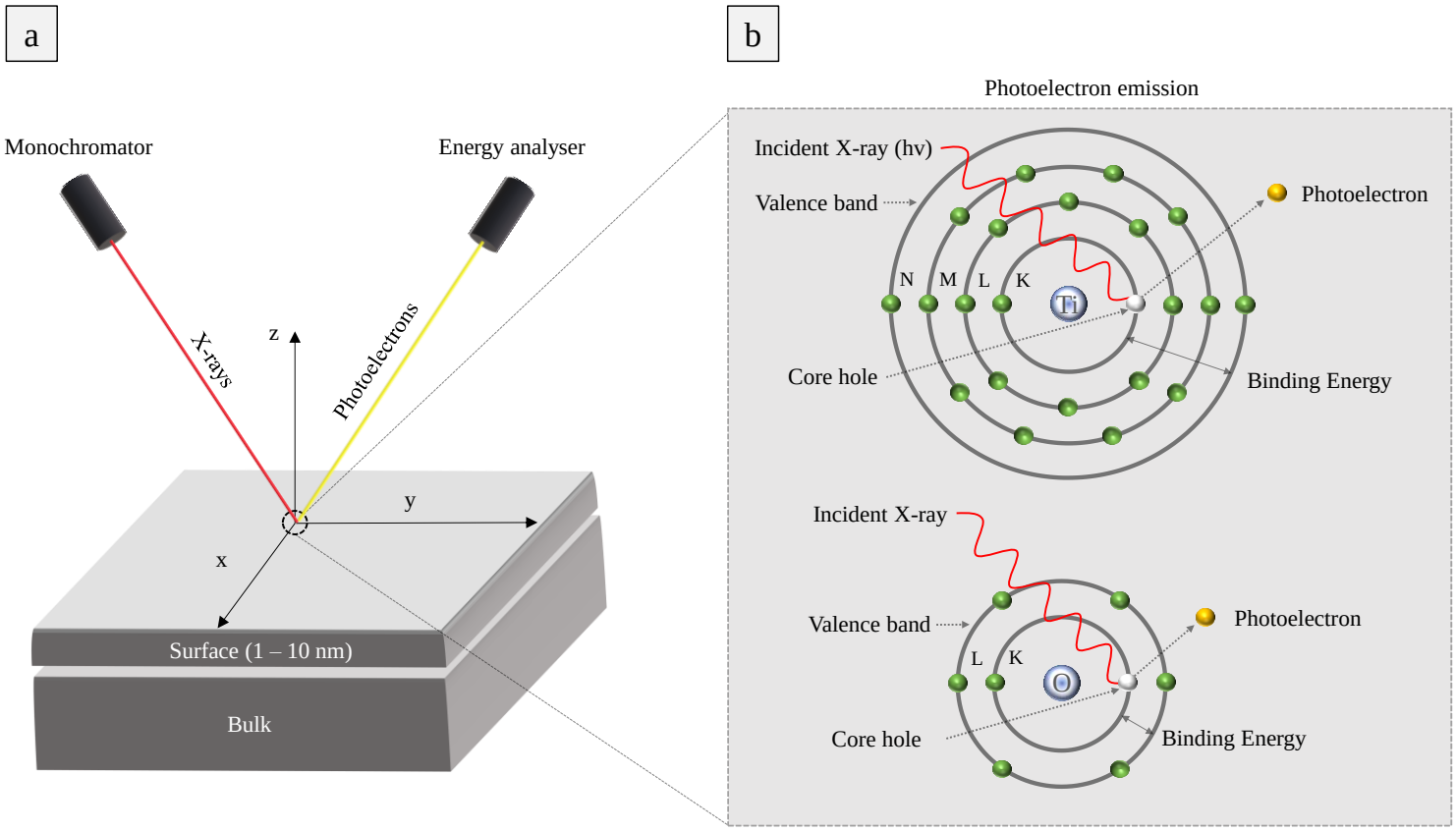

Figure 2.4 | Principles of XPS analysis and the photoelectric effect. Monoenergetic X-rays stimulate the emission of photoelectrons from the material surface (1 – 10 nm) (a-b). The kinetic energy and number of photoelectrons are quantified to determine the elemental composition of a surface and the chemical environment (c). (Adapted from ThermoFisher - https://xpssimplified.com/whatisxps.php).

2.5 Determination of nanowire crystal structure and orientation

2.5.1 Grazing-incident X ray diffraction (GIXD)

X-ray diffraction methods are routinely used to study the structure of crystalline materials. However, the large penetration distances of X-rays mean that conventional methods are not surface sensitive (Dutta, 2000). By changing the angle of incidence (<1°), X-rays can provide information relating to the surface. GIXD measurements were performed with the beamline BM28 (XMaS) at the European Synchrotron Radiation Facility in Grenoble, France. The sample was mounted 0.243 m from the detector and tilted at 0.7°. X ray beams (λ = 885.7 nm) were shot at the sample and the diffracted X rays were detected and imaged at two positions (8° and 30°). The images were converted into 1D profiles using azimuthal integration within the pyFAI package. The data collection and conversion were carried out by Patryk Wasik, University of Bristol, Bristol, UK. Peaks for all the samples were cross referenced with previous literature (Dinan, 2012; Wysocki et al., 2017) and the ICSD web from the CDS National Chemical Database service (Figure 2.5).

2.5.2 Electron backscatter diffraction (EBSD)

The microstructure of annealed titanium discs was analysed using EBSD. Prior to imaging, each disc was polished with colloidal silica using a vibratory polisher (VibroMet2, Buehler Ltd.). EBSD analysis was performed on a Zeiss Sigma™ HDVP field emission SEM with a Gemini electron source and Digiview high-speed camera. Titanium samples were tilted to 70° from the horizontal and imaged with an accelerating voltage of 20 kV. Kikuchi bands were automatically indexed and associated with corresponding crystal grains using OIM Analysis™ v7 software (EDAX, Cambridge, UK) (Figure 2.6). The data collection was carried out by Dr. Ian Griffiths and Dr. Peter Martin at the Interface Analysis Centre, University of Bristol, Bristol, UK.

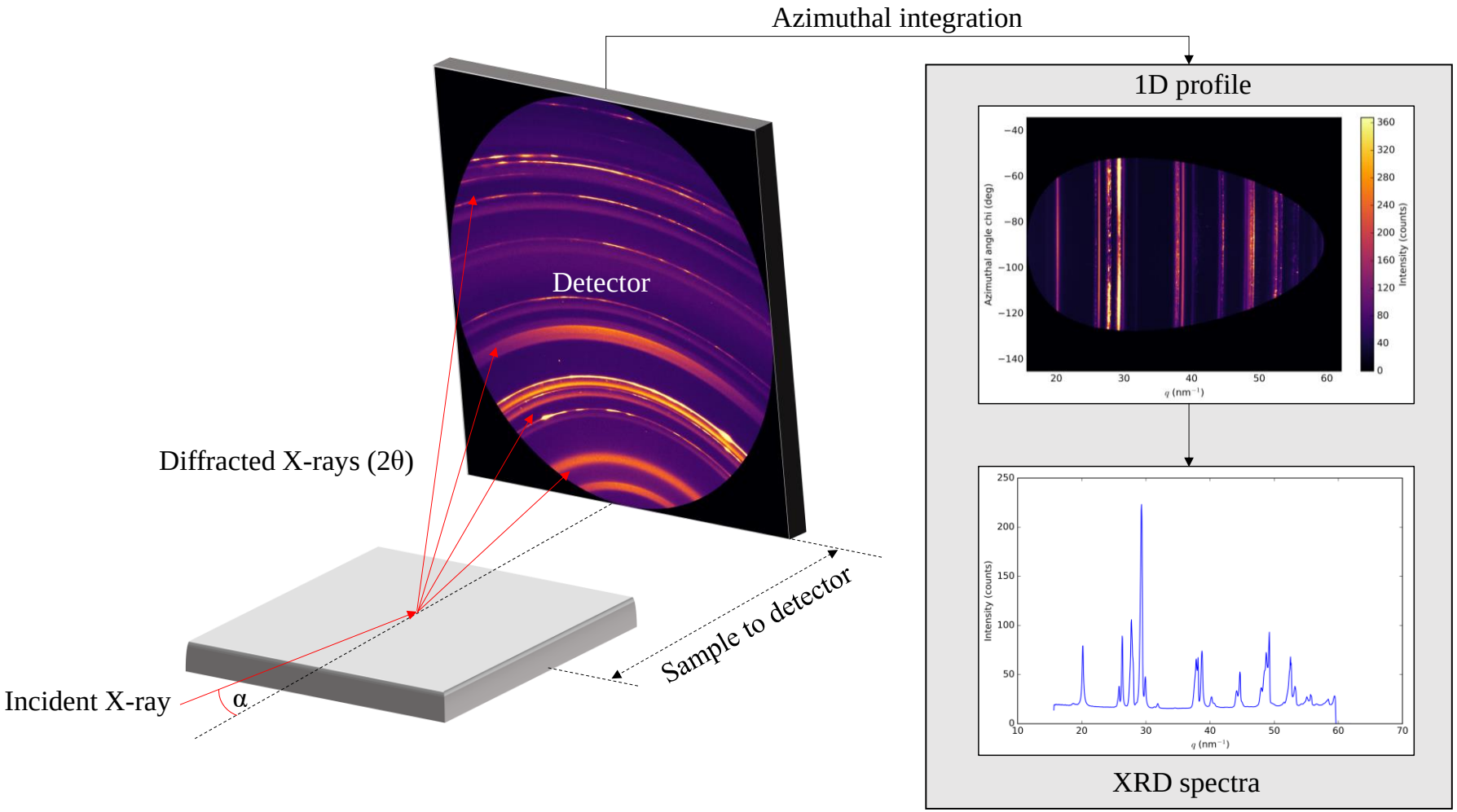

Figure 2.5 | Principles of GIXD. Grazing incident X-rays were focused onto titanium discs tilted at 0.7°. The resulting diffraction patterns formed on the detectors were converted into 1D profiles, by integrating the pixel intensity over the azimuthal angle (Azimuthal integration). XRD spectra were cross referenced against previous literature and the ICSD (Dutta, 2000).

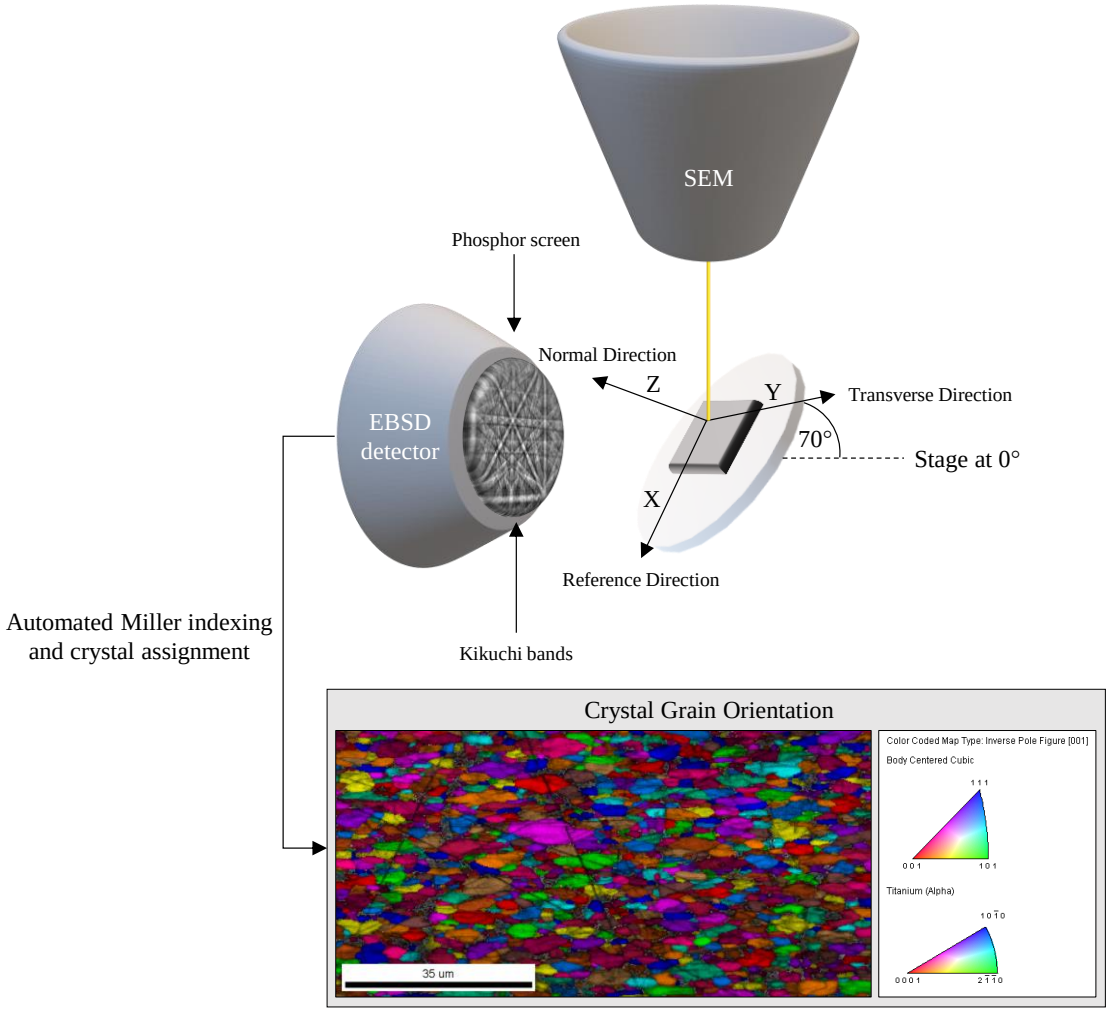

Figure 2.6 | Principles of EBSD analysis. The SEM stage holding the titanium sample was tilted to 70° from the horizontal. When the incident electron beam interacts with the sample, a proportion of the electrons may leave at the interface between atomic planes (satisfying the Bragg equation) and form a pattern of intersecting bands on a phosphor screen. Kikuchi bands were automatically indexed using Miller indices and used to determine the orientation of crystals within the scanning area. (Adapted from Oxford Instruments - http://www.ebsd.com/ebsd-for-beginners).

2.6 Bacterial strains and culture conditions

Bacteria from glycerol stocks (Table 2.1) were inoculated into 10 mL of LB broth (BD biosciences, New Jersey, USA) and incubated for 16 h at 37°C, 220 rpm. Bacteria were then sub-cultured into fresh, pre-warmed Luria Bertani (LB) broth (or Mueller Hinton (MH) Broth (Sigma-Aldrich, Missouri, USA) for BacTiter-Glo assays) to OD_{600} 0.1 and grown to exponential phase.

Table 2.1 | Bacterial strains.

Strain	Genotype/characteristics	Source/reference
S. aureus SH1000	$pCL55_{agr\ IR\ P3\text{-}GFP}$	James et al., 2013
S. aureus Newman	-	Provided by T. Foster
S. epidermidis RP62A	-	Provided by M. Upton
E. coli TOP10	pZEP08*gfp*$^{+}$	Hautefort et al., 2003
E. coli K12	-	Provided by A. Edwards
K. pneumoniae IS-2662A	-	Provided by M. Avison
P. aeruginosa PAO1	-	Provided by J. Spencer

2.7 Determination of bacterial viability on TiO_2 nanowire arrays

Titanium samples were sterilised in absolute ethanol, washed in dH_2O and dried prior to inoculation with bacterial suspensions. The viability of bacteria adhered to TiO_2 nanowire arrays was determined using a range of culture based methods, microscopical investigations and biochemical assays. The rationale for using several techniques was to ensure that multiple aspects of bacterial cell biology were studied and to compensate for the limitations of each individual approach.

2.7.1 Colony forming unit analysis

Direct quantification of the number of viable bacteria present on TiO_2 nanowire arrays was determined by CFU analysis, using a modified version of the international standard ISO-22196. The ISO-22196 outlines a methodology for quantifying antimicrobial activity on polymer and other non-porous surfaces. In this methodology, *S. aureus* or *E. coli* strains are diluted in nutrient broth (NB) to obtain final concentrations of 10^{5}-10^{6} cells per mL. Test inoculums are pipetted (400 µL) onto test specimens (40 mm x 40 mm) before covering with a sterile film to spread the test inoculum to the edges of the test specimen. Petri dishes containing the inoculated test specimens are then incubated for 24 h ± 1h, at a temperature of 35°C ± 1°C and relative humidity of 90%. Following incubation, test specimens are washed in soybean casein digest broth with lecithin and polyoxyethylene sorbitan monooleate (SCDLP broth) to recover bacteria. Viable bacteria are then enumerated by performing 10-fold serial dilutions of SCDLP in phosphate buffered physiological saline before plating onto nutrient agar plates (Standard, 2007)

In this study *S. aureus* Newman or *E. coli* K12 were diluted in LB to obtain final concentrations of 10^{6} cells per 25 µL. Bacterial suspensions (25 µL) were pipetted onto titanium discs (8 mm x 8 mm) and were placed in opaque 24-well plates (PerkinElmer, Massachusetts, USA) and were sealed inside a chamber containing a water reservoir. In this case, bacterial suspensions were not spread to the edges of the sample using a sterile film, which could have influenced nanotopography mediated killing. Inoculated titanium discs were incubated for 24 h, at a temperature of 37°C. Following incubation, titanium discs were transferred into a Tris-HCl suspension (1 mL) and a P200 Gilson pipette was used to remove the biofilms. Viable bacteria were then enumerated by performing 10-fold serial dilutions of recovered suspensions in Tris-HCl before plating onto LB agar plates and incubating at 37°C for 18 h.

The number of viable bacteria per titanium disc was calculated using the Miles and Misra method (Miles and Misra, 1938). Although the original volume of bacteria on each surface was 25 µL, the number of viable bacteria were calculated per mL, since each titanium disc was immersed in a final volume of 1 mL Tris-HCl. Therefore, a multiple of 50 was used, rather than 1.25. All CFU data are presented as the mean values calculated from three experimental replicates (n=3), each experimental replicate was performed in triplicate. Final volumes of 20 µL were plated in triplicate for each dilution.

Equation 2.5: **Determination of viable bacteria.**

$$CFU\ per\ ml = \ average\ number\ of\ colonies \times 50 \times dilution\ factor$$

2.7.2 Determination of bacterial recovery

To determine the efficiency of bacterial recovery by washing in Tris-HCl, the emission of SYTO9 from each titanium disc was measured in a microplate reader before and after washing in Tris-HCl (1 mL). The percentage change in fluorescence emission was used to estimate bacterial recovery. A stock of SYTO9 (2X) was prepared by diluting 3 µL of 3.34 mM SYTO9 in 1 mL of Tris-HCl. The 2X SYTO9 stock was then transferred to the meniscus atop each titanium disc (25 µL), making a final SYTO9 concentration of 1X (50 µL), in line with the manufacturer's recommendations. Titanium discs were then placed in the dark for 15 minutes to enable SYTO9 to permeate bacterial envelopes and intercalate with DNA. An Infinite® 200 PRO microplate reader (Tecan, Männedorf, Switzerland) was set up to measure the fluorescence intensity at 25 locations per well. Measurements were performed in a filled circular pattern using optimal gain and a 20 µs integration time. A wavelength of 485 nm ± 20 nm was used to excite SYTO9 and the emission was detected at a wavelength of 535 nm ± 25 nm. Fluorescence measurements were performed inside a black 24-well plate, recording measurements in top mode. Once the initial RFU had been recorded, titanium samples were washed in Tris-HCl (1 mL) before applying 25 µL of 1X SYOT9 stock (1.5 µL of 3.34 mM SYTO9 in 1 mL of Tris-HCl) for 15 minutes. The RFU post-washing were then recorded for each well using the same measurement parameters. Each titanium disc was also visualised by fluorescence microscopy.

2.7.3 Confocal laser scanning microscopy

The growth of *S. aureus* and *E. coli* strains containing green fluorescent protein (GFP) reporter constructs were monitored by *in-situ* CLSM. Sterile titanium discs (0.06 cm^2) were mounted in triplicate to the base of a transparent well modified from a 24-well plate (Greiner Bio-One, UK). Once mounted, the final distance between the top of the well and the titanium discs was approximately 1 mm. To facilitate bacterial attachment, titanium discs were inoculated with 10^6 bacterial cells (1 mL final volume) and incubated for one hour at 37°C under static conditions. Following this pre-incubation, the suspension was removed and then surfaces were immersed in fresh LB media, before sealing the well with a circular glass cover slip (25 mm diameter). Wells containing titanium discs were placed in a Petri dish (94 mm by 16 mm) and transferred onto a Scientifica IntraVital motorised stage inside an environmental chamber (Life Imaging Services, Basel, Switzerland) maintained at 37°C. The growth of *S. aureus* and *E. coli* was then monitored up to 18 h using a Leica SP8 AOBS CLSM attached to a Leica DM6000 upright epifluorescence microscope with multiphoton and confocal lasers.

Automated image acquisition was set up in LAS X software (Leica Microsystems, Wetzlar, Germany) to ensure the entire area of each titanium disc was viewed every 2 hours. The following parameters were used: surface areas between 1.34 cm^2 – 1.5 cm^2 were imaged in bidirectional scanning mode, at a scanning frequency of 400 Hz. Due to the large area, imaging was performed in sequential area scans (tile scanning), each measuring 1.47 mm in X and 1.47 mm in Y, leading to a resolution of 2.8 µm. Within each area scan, images were captured in 10 µm step sizes in Z, generating Z-stacks between 200 – 250 µm in depth (Figure 2.7). Following 18 h incubation the suspension of LB was removed and then surfaces were immersed in 1 mL of 1X propidium iodide (PI) stock (1.5 µL of 20 mM in 1 mL Tris-HCl) before continuing with image acquisition. Post-imaging, tile scans were merged together using Fiji, and dual fluorescence images were superimposed. GFP emission from *S. aureus* and *E. coli* was detected between 498 nm – 550 nm, and the signal from PI (ThermoFisher Scientific, MA, USA) was detected between 600 nm – 670 nm. Images were taken using a HC PL APO CS 10x/0.40 DRY objective lens.

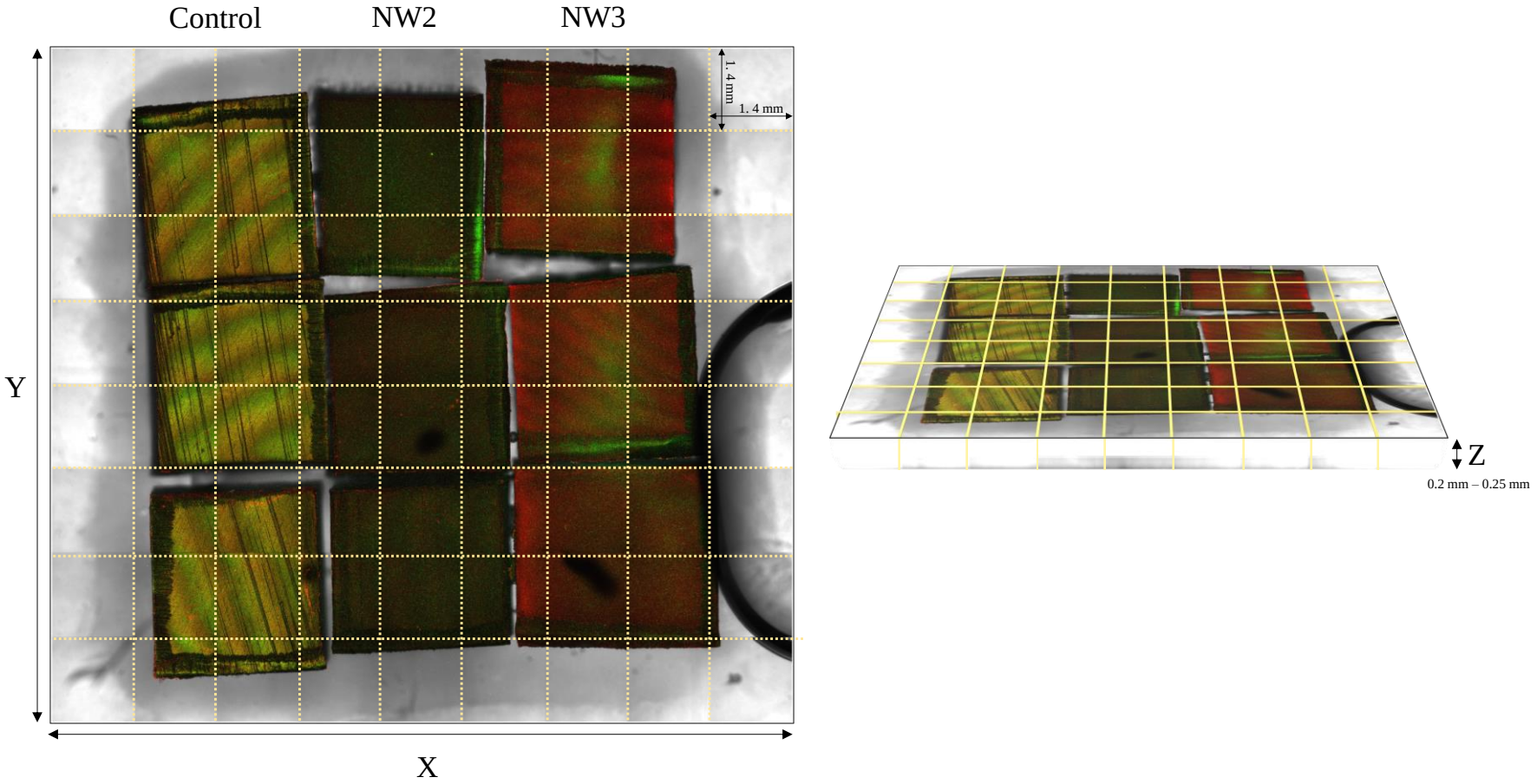

Figure 2.7 | *In-situ* CLSM set up. Sterile titanium discs (0.06 cm^2) were mounted in triplicate to the base of a transparent well and inoculated with *S. aureus* or *E. coli* expressing GFP. Automated image acquisition was set up in LAS X software. This enabled the entire surface area to be covered in sequential tile scans, each tile measuring 2.16 mm^2. Between 20-26 images were captured in Z, every 10 µm, generating final Z-stacks between 0.2 mm – 0.25 mm.

2.7.4 LIVE/DEAD™ *BacLight*™ Bacterial Viability Kit

Sterile titanium discs (0.64 cm^2) were placed into black 24-well plates (Greiner Bio-One, UK) and equilibrated to 37°C. Bacterial suspensions (10^6 cells; 25 µL aliquots) were transferred to each surface and incubated for 3 hour at 37°C under static conditions, inside a humidity chamber. A 2X LIVE/DEAD stock was prepared by combining 3 µL of 3.34 mM SYTO9 with 3 µL of 20 mM PI and diluting in 1 mL of Tris-HCl. The 2X LIVE/DEAD stock was then transferred to the meniscus atop each titanium disc (25 µL), making a final SYTO9 concentration of 1X (50 µL), in line with the manufacturer's recommendations (Figure 2.8). Titanium discs were then incubated in the dark for 15 minutes. For plate reader analysis, an Infinite® 200 PRO microplate reader was set up to measure the fluorescence intensity at 25 locations per well. For both SYTO9 and PI, measurements were performed in a filled circular pattern using optimal gain and a 20 µs integration time. For SYTO9, emission/excitation wavelengths of (485 nm ± 20 nm/535 nm ± 25 nm) were used, and for PI, (535 nm ± 25 nm/620 nm ± 20 nm) were used. Fluorescence measurements were performed inside a black 24-well plate, recording measurements in top mode.

For end-point fluorescence microscopy, titanium discs were dip-transferred into a solution of Tris-HCl to remove non-adhered bacteria and unbound, excess fluorophores. Titanium discs were transferred to glass slides and glass coverslips were placed atop each disc, which facilitated focussing onto surface-attached bacteria and preventing desiccation. Titanium discs were then imaged using a Leica DMLB fluorescence microscope, and images were acquired using CellSense software (Olympus corporation).

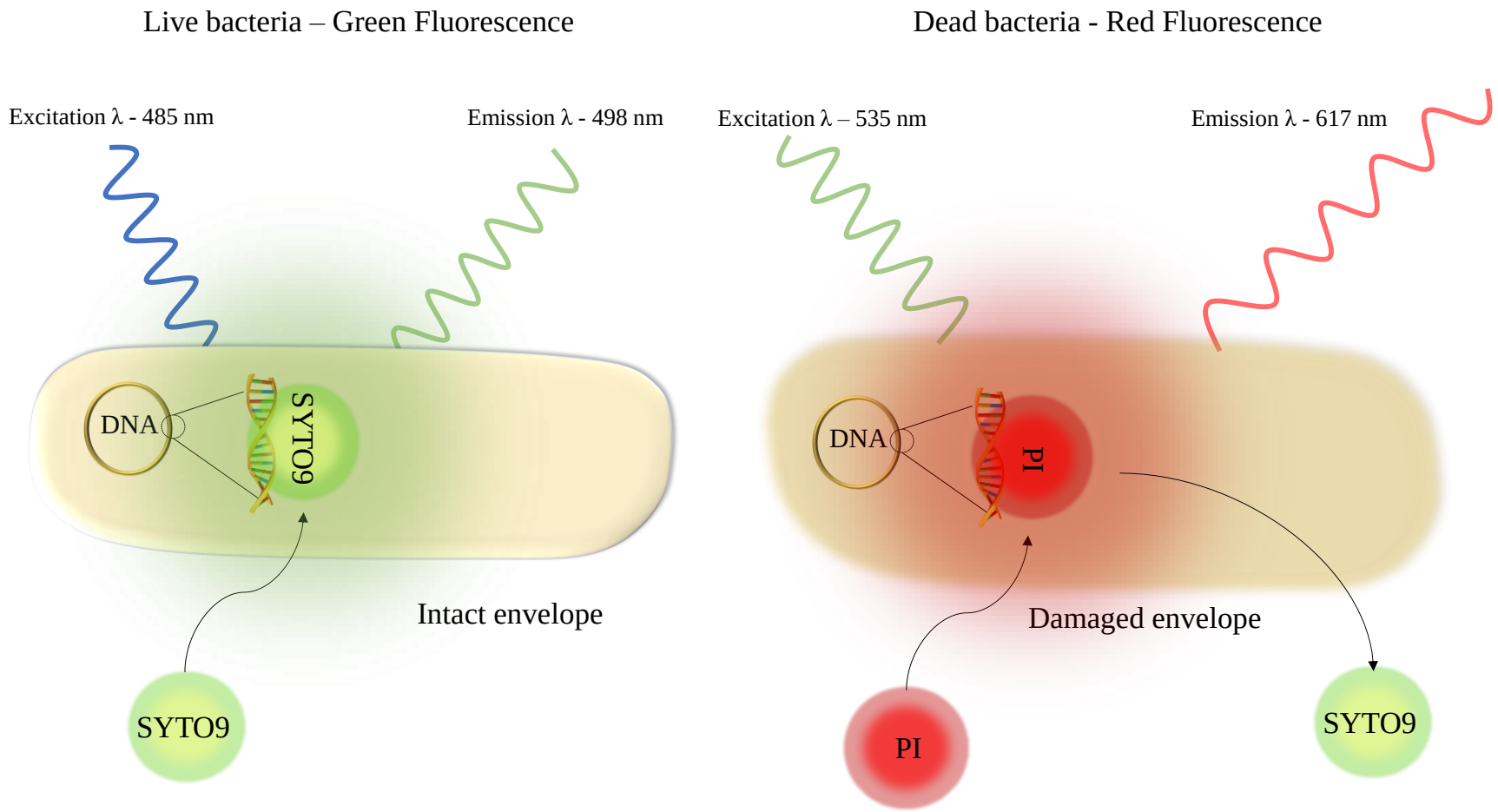

Figure 2.8 | Principles of LIVE/DEAD™*BacLight*™ assay. LIVE/DEAD provides an indication of viability based on the structural integrity of the bacterial envelope. SYTO9 fluorophore can permeate all bacteria, and while the exact interaction is unknown, SYTO9 is believed to intercalate with the minor groove of DNA. When the bound fluorophore is exposed to wavelengths of 485 nm, SYTO9 emits a fluorescent signal at 498 nm. In contrast, PI can only enter bacteria with compromised cell envelopes. Once inside the cell, PI displaces SYTO9 and binds to DNA within the major groove. When bound PI is exposed to wavelengths of 535 nm, PI emits a fluorescent signal at 617 nm (Stocks, 2004).

2.7.5 BacTiter-Glo™ Microbial Cell Viability Assay

The metabolic activity of bacterial cells is closely related to the intracellular concentration of adenosine triphosphate (ATP). BacTiter-Glo™ (BTG) is a lytic, end-point assay, containing a luciferase enzyme that generates a bioluminescent signal proportional to cellular ATP levels, which is directly proportional to bacterial cell number (Figure 2.9). BTG reagent was prepared according to the manufacturer's protocol (Promega Corporation, WI, USA). Standard curves were generated to determine the sensitivity of BTG reagent with different bacteria. Mid-exponential phase cultures of *S. aureus, S. epidermidis, E. coli* and *K. pneumoniae* were serially diluted (1:4) and 100 µL of each dilution was then transferred to a white, opaque 96-well plate (Greiner Bio-One, UK). BTG reagent was then added to each dilution in a 1:1 ratio. An Infinite® 200 PRO microplate reader was used to measure the glow based luminescent signal from each well. For non-established luminescence applications, such as measurements from titanium discs, it is recommended that measurments are performed using the automatic attenuation function. Automatic attenuation increases the dynamic range of the plate reader, thereby reducing the likelihood of "OVER" values in the data output, while maintaining assay sensitivity. The duration of signal acquisition (integration time) was set to 1 s per well with a settle time of 0.15 s between measurements, this ensures the fluid inside each well is not moving, which can negatively affect the precision of the luminescence measurements (Tecan Group Ltd, 2010). Following luminescence measurements, each dilution was plated out and enumerated using the Miles and Misra method (Miles and Misra, 1938). The relative luminescent units (RLU) recorded for each dilution were then plotted against the corresponding CFU per 100 µL, to generate standard curves.

To determine bacterial viability on TiO_2 nanowire compared to control, sterile titanium discs (8 mm x 8 mm) were placed inside white 24-well plates (PerkinElmer, MA, USA) and inoculated with 25 µL of bacterial suspension (10^6-10^7), forming a meniscus. Discs were incubated for 0.5, 1, 3 and 10-hour time points at 37°C under static conditions inside a humidity chamber. Following incubation, equilibrated BTG reagent was added in a 1:1 ratio with the bacterial suspension and following 5 minutes incubation (in the dark), the luminescent signal was measured via an Infinite® 200 PRO microplate reader, using the same parameters as above. Quantification of the total number of bacterial cells on each titanium disc was then calculated using the equation from the trendline on each standard curve.

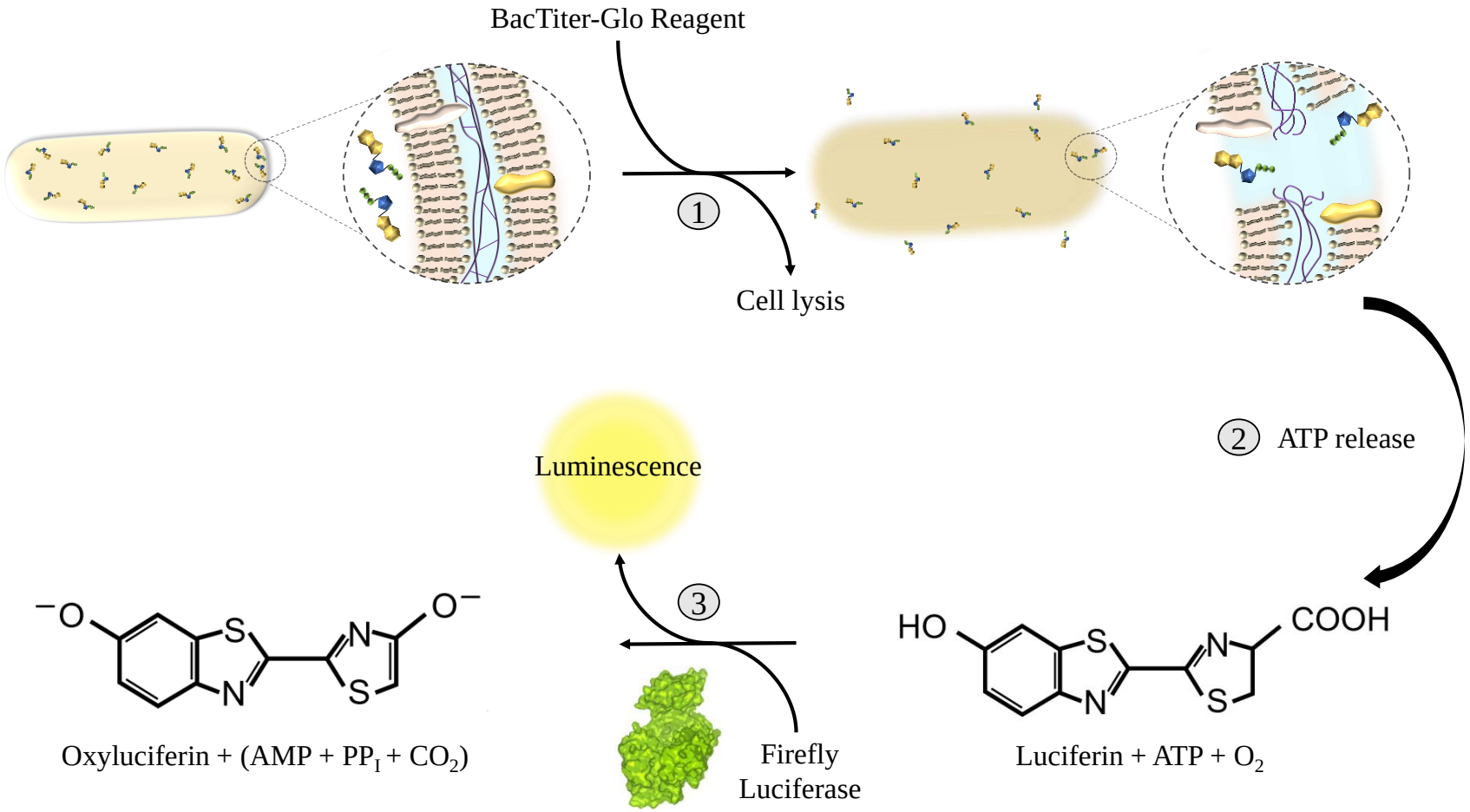

Figure 2.9 | Principles of BacTiter-Glo™ Microbial Cell Viability Assay. BTG is a lytic, bioluminescence end-point assay that provides an indication of viability based on the quantification of ATP. The assay works in three stages: 1) The addition of BTG reagent results in the lysis of all bacteria; 2) Cell lysis ensures the release of intracellular ATP; 3) ATP is utilised by the Firefly Luciferase to oxidise luciferin. Luminescence is a by-product of this reaction and is proportional to the concentration of ATP and cell viability. The luminescent signal can be detected using a plate reader. (Adapted from Promega - https://www.promega.co.uk/products/cell-health-assays/cell-viability-and-cytotoxicity-assays/bactiter_glo-microbial-cell-viability-assay/?catNum=G8230).

2.7.6 RealTime-Glo™ MT Cell Viability Assay

RealTime-Glo™ (RTG) monitors biochemical reduction reactions occurring within the cytoplasm of cells. These reactions lead to the production of a luminescent signal that is proportional to the number of metabolically active bacteria. The RTG assay contains a pro-substrate that is reduced to a substrate by metabolically active bacteria. This substrate is utilised by a luciferase enzyme that produces a luminescent signal proportional to pro-substrate turn over (Figure 2.10). RTG reagent was prepared according to the manufacturer's protocol (Promega Corporation, Madison, WI, USA).

Bacterial suspensions were supplemented with 1X MT Cell Viability Substrate and 1X NanoLuc® Enzyme and then incubated in the dark for 1 hour at 37°C, 220 rpm. Sterile titanium discs were placed inside white 24-well plates (PerkinElmer, MA, USA) and bacterial suspensions (50 µL, 10^6-10^7 cells) were placed on top of each disc, forming a meniscus. Each 24-well plate was sealed using transparent adhesive film and incubated for 10 hours at 37°C under static growth conditions. Luminescence measurements were recorded in real time using an automated Infinite® 200 PRO microplate reader. The luminescent signal from each well was recorded every 10 minutes, using automatic attenuation, 1 s integration time and 0.15 s settle time.

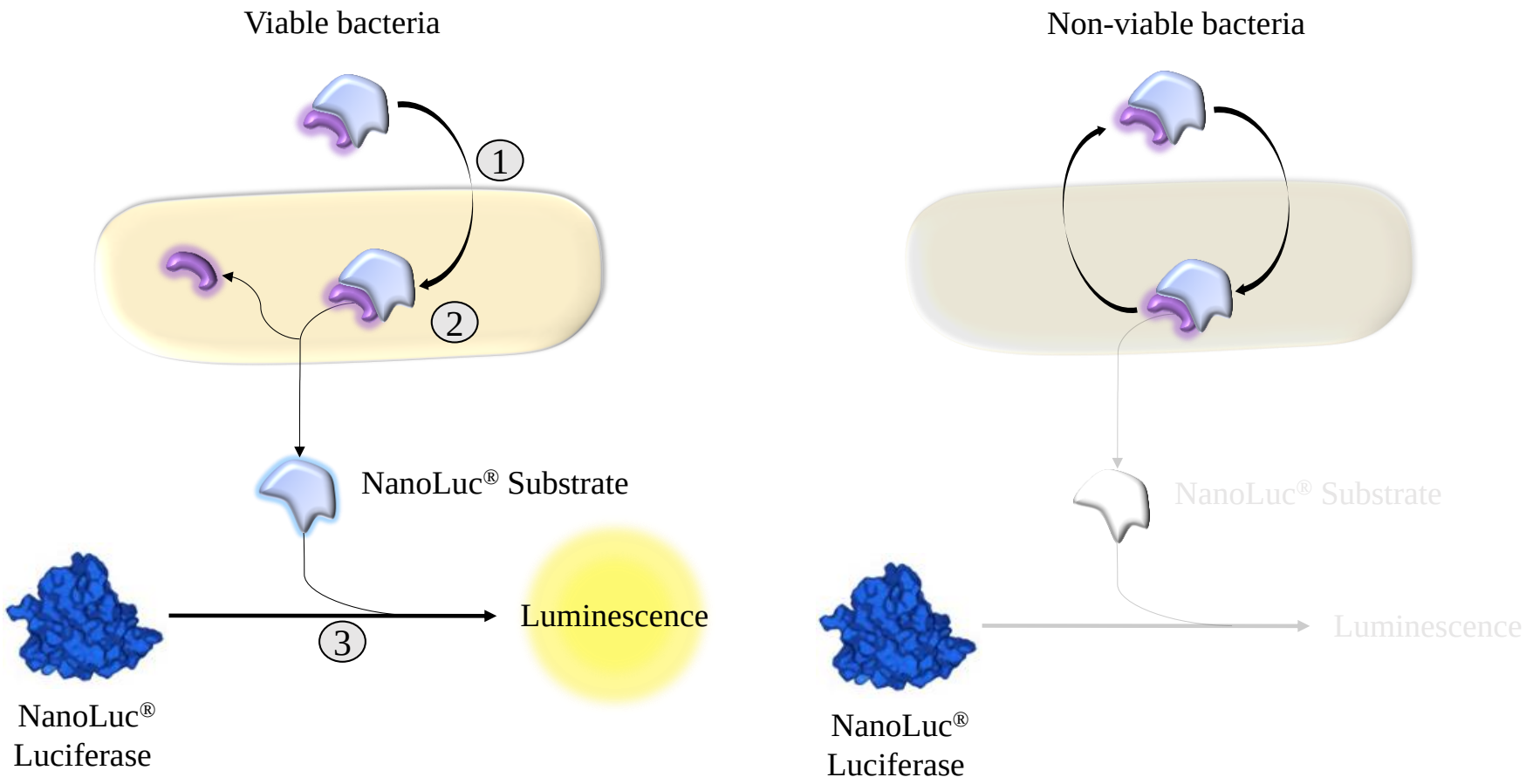

Figure 2.10 | Principles of RealTime-Glo™ MT Cell Viability Assay. RTG is a non-lytic, bioluminescent method that provides an indication of cell viability based on the reducing capacity of bacteria. The process occurs in three stages: 1) The MT Cell Viability Substrate diffuses into viable and non-viable cells; 2) Viable bacteria reduce the substrate, resulting in the production of NanoLuc Substrate; in contrast, non-viable bacteria are unable to reduce the substrate, which exits the cell unchanged; 3) The NanoLuc Luciferase catalyses the production of a luminescent signal using the NanoLuc Substrate. The luminescent signal is recorded using a plate reader format and is proportional to the number of viable cells. (Adapted from Promega - https://www.promega.co.uk/products/cell-health-assays/cell-viability-and-cytotoxicity-assays/realtime_glo-mt-cell-viability-assay/?catNum=G9711).

2.7.7 Proteomic analysis

2.7.7.1 Protein extraction and purification from *E. coli*

Titanium discs (25 cm^2) were placed inside sterile Petri dishes (94 mm by 16 mm), inoculated with 1 mL *E. coli* suspension (10^7-10^8 cells), and incubated for 24 hours at 37°C under static conditions inside a humidity chamber. Following incubation, titanium samples were vigorously rinsed in 20 mL of Tris-HCl (pH 7.2) buffer to recover bacteria, which were then harvested by centrifugation at 5000 rpm for 10 minutes. Cell pellets were resuspended in 500 µL of Tris-HCl supplemented with 1X Protease Inhibitor Cocktail and 1 mM phenylmethylsulfonyl fluoride (Sigma-Aldrich, MO, USA). To extract *E. coli* proteins, bacterial suspensions were snap-frozen in liquid nitrogen and transferred to a pre-cooled 5 mL Teflon shaking flask containing one tungsten carbide bead. Homogenisation was performed at 2000 rpm for 2.5 minutes, using a Micro-Dismembrator (Sartorius, Göttingen, Germany). This process generated a white bacterial powder that was resuspended in 1 mL of Tris-HCl. Cellular debris was then removed by centrifugation at 13,300 rpm for 20 minutes at 4°C. This left the soluble protein fraction, which was transferred into a fresh Eppendorf tube and stored at -80°C.

2.7.7.2 Protein extraction and purification from *S. aureus*

S. aureus suspensions (10^7-10^8 cells) were used to inoculate titanium discs and subsequently recovered, as described above. Cell pellets were then resuspended in 200 µL of Tris-HCl supplemented with 200 µg/mL of lysostaphin (Sigma-Aldrich, MO, USA) and incubated for 1 hour at 37°C. Cellular debris was removed by centrifugation at 13,300 rpm for 20 minutes at 4°C, and the soluble protein fraction transferred to a sterile Eppendorf tube and stored at -80°C.

2.7.7.3 TMT Labelling and High pH reversed-phase chromatography

An equal volume of each bacterial protein extract (ensuring that no sample contained more than 100 µg of protein) was digested overnight with 2.5 µg trypsin at 37°C, labelled with Tandem Mass Tag (TMT) ten plex reagents according to the manufacturer's protocol (Thermo Fisher Scientific, Loughborough, LE11 5RG, UK), and pooled. Pooled samples were evaporated to dryness, resuspended in 5% formic acid and then desalted using a SepPak cartridge according to the manufacturer's instructions (Waters, Milford, Massachusetts, USA). Eluate from the SepPak cartridge was again evaporated to dryness and resuspended in buffer A (20 mM ammonium hydroxide, pH 10) prior to fractionation by high pH reversed-phase chromatography using an Ultimate 3000 liquid chromatography system (Thermo Scientific). In brief, the sample was loaded onto an XBridge BEH C18 Column (130 Å, 3.5 µm, 2.1 mm X 150 mm; Waters, UK) in buffer A and peptides eluted with an increasing gradient of buffer B (20 mM ammonium hydroxide in acetonitrile, pH 10) from 0-95% over 1 hour. The resulting fractions were evaporated to dryness and resuspended in 1% formic acid prior to analysis by nano-LC MSMS using an Orbitrap Fusion Tribrid mass spectrometer (Thermo Scientific). TMT labelling and high pH reversed-phase chromatograph was performed at the Proteomics Facility, University of Bristol, Bristol, UK.

2.7.7.4 Nano-LC Mass Spectrometry

High pH reversed-phase fractions were further fractionated using an Ultimate 3000 nano-LC system in line with an Orbitrap Fusion Tribrid mass spectrometer (Thermo Scientific). In brief, peptides in 1% (vol/vol) formic acid were injected onto an Acclaim PepMap C18 nano-trap column (Thermo Scientific). After washing with 0.5% (vol/vol) acetonitrile/0.1% (vol/vol) formic acid, peptides were resolved on a 250 mm × 75 µm Acclaim PepMap C18 reverse phase analytical column (Thermo Scientific) over a 150 min organic gradient, using 7 gradient segments (1-6% solvent B over 1 minute, 6-15% B over 58 minutes, 15-32% B over 58 minutes, 32-40% B over 5 minutes, 40-90% B over 1 minute, held at 90% B for 6 minutes and then reduced to 1% B over 1 minute) with a flow rate of 300 nl min^{-1}. Solvent A was 0.1% formic acid and Solvent B was aqueous 80% acetonitrile in 0.1% formic acid. Peptides were ionized by nano-electrospray ionization at 2.0 kV using a stainless-steel emitter with an internal diameter of 30 µm (Thermo Scientific) and a capillary temperature of 275°C. Nano-LC mass spectrometry was performed at the Proteomics Facility, University of Bristol, Bristol, UK.

All spectra were acquired using an Orbitrap Fusion Tribrid mass spectrometer controlled by Xcalibur 2.0 software (Thermo Scientific) and operated in data-dependent acquisition mode using an SPS-MS3 workflow. FTMS1 spectra were collected at a resolution of 120,000, with an automatic gain control (AGC) target of 200,000 and a max injection time of 50 ms. Precursors were filtered with an intensity threshold of 5000, according to charge state (to include charge states 2-7) and with monoisotopic precursor selection. Previously interrogated precursors were excluded using a dynamic window (60 s ± 10 ppm). The MS2 precursors were isolated with a quadrupole mass filter set to a width of 1.2 m/z. ITMS2 spectra were collected with an AGC target of 10,000, max injection time of 70 ms and CID collision energy of 35%. For FTMS3 analysis, the Orbitrap was operated at 50,000 resolution with an AGC target of 50,000 and a max injection time of 105 ms. Precursors were fragmented by high energy collision dissociation at a normalised collision energy of 60% to ensure maximal TMT reporter ion yield. Synchronous precursor selection was enabled to include up to 5 MS2 fragment ions in the FTMS3 scan.

2.7.7.5 Proteomic Data Analysis

The raw data files were processed and quantified using Proteome Discoverer software v2.1 (Thermo Scientific) and searched against the UniProt *Staphylococcus aureus* (strain Newman) database (downloaded October 2018; 2584 entries) or the Uniprot *E. coli* (strain K12) database (downloaded February 2019; 4469 entries) using the SEQUEST algorithm. Peptide precursor mass tolerance was set at 10 ppm, and MS/MS tolerance was set at 0.6 Da. Search criteria included oxidation of methionine (+15.9949) as a variable modification, and carbamidomethylation of cysteine (+57.0214) and the addition of the TMT mass tag (+229.163) to peptide N-termini and lysine as fixed modifications. Searches were performed with full tryptic digestion and a maximum of 2 missed cleavages were allowed. The reverse database search option was enabled, and all data were filtered to satisfy false discovery rate (FDR) of 5%. Based on the protein abundance values from three biological replicates of each sample, a Student's *t*-test was used to determine the significance of protein abundance fold changes between *S. aureus* or *E. coli* incubated on nanowire versus control titanium discs. Proteins with $p \leq 0.05$ were deemed significant and were accordingly defined as differentially expressed proteins (DEPs). Blast2Go software was used to categorise *S. aureus* and *E. coli* DEPs based on Gene Ontology (GO). DEPs were grouped by Level 2 GO. Protein–protein interactions were investigated using the functional protein association network tool (STRING v11) within Cytoscape (Shannon et al., 2003; Szklarczyk et al., 2019).

2.8 Oxidative stress assays

2.8.1 GSH-Glo™ Glutathione Assay

GSH-Glo is a luminescence based, non-lytic assay used to detect and quantify glutathione (GSH) levels in cells. GSH-Glo reagent was prepared according to the manufacturer`s protocol (Promega Corporation, Madison, WI, USA). *S. aureus* and *E. coli* were incubated on titanium discs (NW3 or control) under static conditions for 24 hours at 37°C. Following 24 hours, 2X GSH-Glo reagent was transferred to each surface and incubated at room temperature for 30 minutes. After 30 minutes, a firefly luciferase was added and incubated for a further 15 minutes at room temperature. Luminescence measurments were recorded using an automated Infinite® 200 PRO microplate reader. Luminescence was recorded using automatic attenuation, 1 s integration time and 0.15 s settle time. Quantification of GSH on each titanium disc was then calculated using the equation from the trendline on the GSH standard curve. To generate a standard curve, GSH (5 mM stock) was diluted (1:100) in LB media before serially diluting (1:1) to the 8th dilution. The luminescence was then recorded from each well.

2.8.2 ROS-Glo™ H_2O_2 Assay

ROS-Glo is a luminescence based, non-lytic assay for the measurement of H_2O_2 within culture media. ROS-Glo reagent was prepared according to the manufacturer`s protocol (Promega Corporation, Madison, WI, USA). *S. aureus* and *E. coli* were incubated on titanium discs (NW3 or control) for 24 hours. After 18 hours, the H_2O_2 substrate solution was added to the discs before placing back into the incubator at 37°C for the remaining 6 hours. During this time, the H_2O_2 substrate reacts with H_2O_2, forming a luciferin precursor. After 24 hours, the ROS-Glo detection reagent was added. This converts the luciferin precursor into luciferin, which is then used by the Ultra-Glo™ Recombinant Luciferase to generate a luminescent signal that is proportional to the quantity of H_2O_2. Luminescence measurments were recorded using an automated Infinite® 200 PRO microplate reader. Luminescence was recorded using automatic attenuation, 1 s integration time and 0.15 s settle time.

2.9 Preparation of bacteria for electron microscopy

2.9.1 SEM sample preparation and imaging

Bacteria on titanium discs were fixed at 4°C in 2.5% EM grade glutaraldehyde (Agar Scientific Ltd. Essex, UK) buffered with 0.1 M sodium cacodylate (Acros Organics, New Jersey, USA). Following overnight fixation at 4°C, samples were washed in 0.1 M sodium cacodylate buffer (3 x 5 minutes) and dehydrated in a graded ethanol series of 25%, 50%, 70%, 90% and 100% (Sigma-Aldrich, St. Louis, MO, USA). Samples were then critically point dried using a Leica CPD300, following an established protocol for microbial cells (Yu et al., 2014). Titanium discs were mounted onto 0.5" aluminium stubs using colloidal silver paste (Agar Scientific Ltd. Essex, UK), before being coated with a 10 nm chromium layer using an Emitech K757X sputter coater system. Samples were loaded into the vacuum chamber of a Quanta 200 FEG-SEM (FEI). For image acquisition, electron beam accelerating voltages of 20 kV and beam current of 158 µA were used. Secondary electron emission was detected using an ETD (Figure 2.11).

2.9.2 Sample preparation for cross sectional analysis

Following overnight fixation in 2.5% EM grade glutaraldehyde at 4°C, samples were washed in 0.1 M sodium cacodylate buffer (3 x 5 minutes) prior to *en bloc* Osmium tetraoxide – Thiocarbohydrazide – Osmium (OTO) processing. Briefly, post fixation was performed in equal volumes of 4% osmium tetraoxide (Agar Scientific Ltd. Essex, UK) and 3% potassium ferrocyanide (Sigma-Aldrich, MO, USA) for 1 hour on ice. Following post-fixation, samples were washed in dH_2O (3 x 5 minutes) before incubating with thiocarbohydrazide (Sigma-Aldrich, MO, USA) for 20 minutes. Additional dH_2O washing steps (3 x 5 minutes) were applied before incubation in 2% aqueous osmium for 30 minutes at room temperature. Following OTO processing, bacterial samples were stained in 1% aqueous uranyl acetate (1 hour at 4°C) followed by lead aspartate (200 µM) for 30 minutes in the dark. Between these steps, washing with dH_2O was performed. After the final washing step, bacterial samples were dehydrated and dried as previously outlined. Titanium discs to be analysed using focused ion beam scanning electron microscopy (FIB-SEM) were mounted onto 0.5" aluminium stubs using colloidal silver paste before being coated with a 10 nm chromium layer using an Emitech K757X sputter coater system.

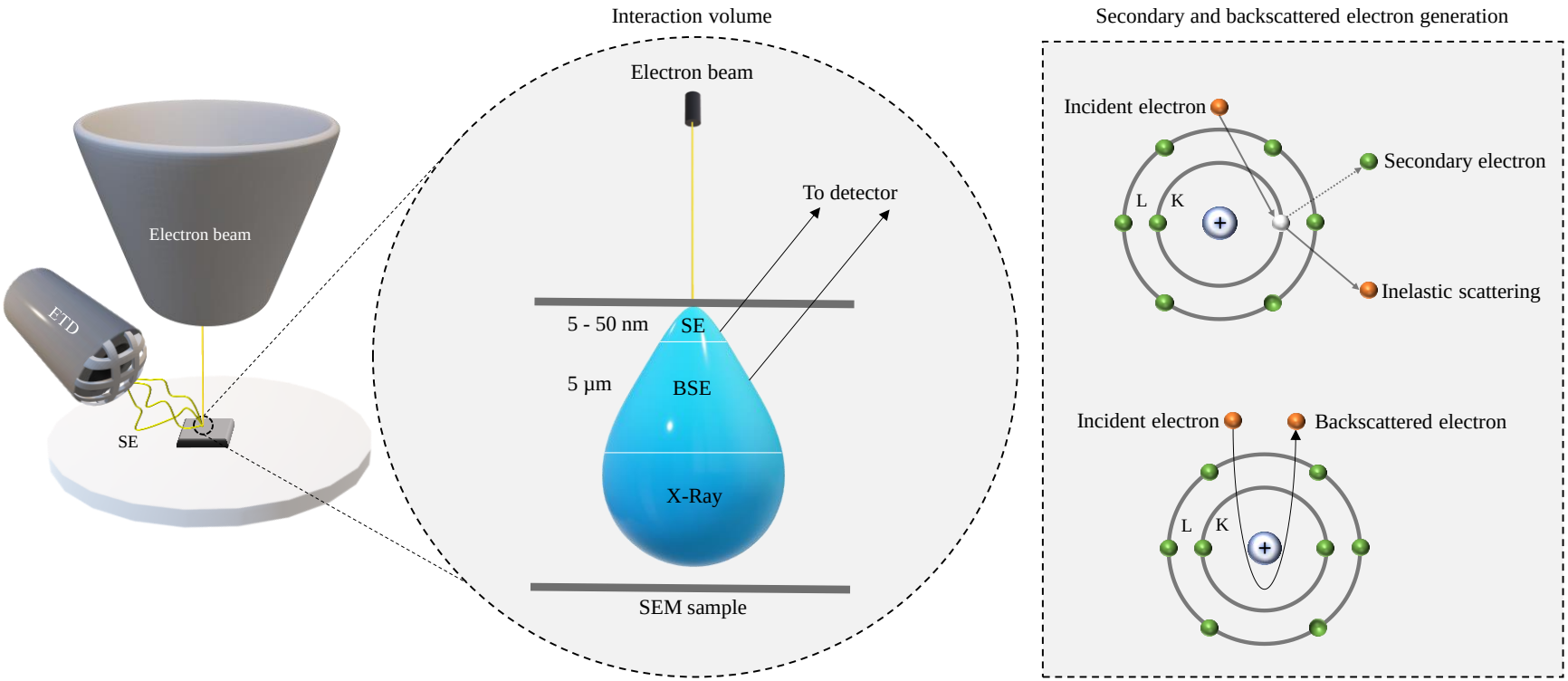

Figure 2.11 | Principles of SEM. The incident electron beam interacts with the sample, forming a three-dimensional space known as the interaction volume. The size of the interaction volume is dependent on the atomic configuration of the material, and electron beam energy. Multiple signals are generated within the interaction volume, as a result of inelastic and elastic scattering, the most common events are as follows: 1) Secondary electrons are generated by the energy transferred from the incident electron beam to atoms within the material; this leads to the emission of a secondary electron, which typically escapes from the first 50 nm of the material; 2) Backscattered electrons are also produced from the interaction between the incident electron beam and the material. However, backscattered electrons are generated from elastic scattering of incident electrons and can escape from depths 100 times greater than secondary electrons (Hafner, 2007).

2.9.3 Sectioning and imaging Epon® embedded samples

Bacteria incubated on control titanium discs were recovered and harvested by centrifugation prior to staining, whereas bacteria incubated on TiO_2 nanowire arrays were processed while attached to the titanium disc. All samples to be analysed using TEM were embedded in Epon® 812 resin (TAAB Laboratories Equipment Ltd. Berkshire, UK) for 90 minutes on a TAAB rotator type N, held at 2 rpm. Samples were then placed at 60°C for 48 hours to allow resin polymerisation. Resin embedded samples were sectioned by Dr. Chris Neal (Wolfson Bioimaging Facility, University of Bristol, UK) using an Ultra Diamond Knife (DiATOME) on a Leica EM UC6 ultramicrotome. These were transferred to pioloform coated TEM grids for microscopy. To analyse the ultrastructure of bacterial cells adhered to TiO_2 nanowire arrays, samples were loaded into a Tecnai 12 FEI 120kV BioTwin Spirit TEM. An electron beam with an accelerating voltage of 120 kV was used to capture images. For tilt series acquisition, TEM samples were transferred to a Fischione tomography holder and loaded into a Tecnai 20 (T20) - FEI 200kV Twin Lens TEM. Dedicated FEI tomography software was used to capture the tilt series data.

2.9.4 FIB sectioning and imaging

To date, most published data pertaining to bacteria-nanowire interactions have used SEM. However, this approach is limited to resolving surface morphology. In this thesis, FIB-SEM was used to generate cross sections through bacteria, thereby enabling the interface between nanowires and the bacterial envelope to be clearly visualised. Two microscopes were used to perform ion beam milling: 1) Strata FIB201 (University of Manchester); 2) FEI Scios (DESY NanoLab). The fundamental principle of FIB-SEM is outlined in Figure 2.12. Titanium discs were loaded into the chamber and the system was pumped to create a vacuum. Before cross sectional analysis, the stage was tilted by 52°, moving the titanium discs perpendicular to the gallium ion beam. While using the Strata 201, area scans were performed using an electron beam with an accelerating voltage of 5 kV and current of 98 pA. To preserve bacterial morphology, electron and ion assisted platinum deposition was performed to create a protective layer 500 nm thick. Once coated, rough cut trenches were milled around the bacteria to depths of 250 nm using an accelerating voltage of 30 kV and current of 6.5 nA. Auto Slice and View software (FEI) was used to carry out sequential sectioning of *S. aureus* and *E. coli* in 30–50 nm slices. This was performed with an accelerating voltage of 30 kV and beam current of 47.5 pA. Images of each section were acquired using electron beam accelerating voltages of 5 kV and current of 98 pA.

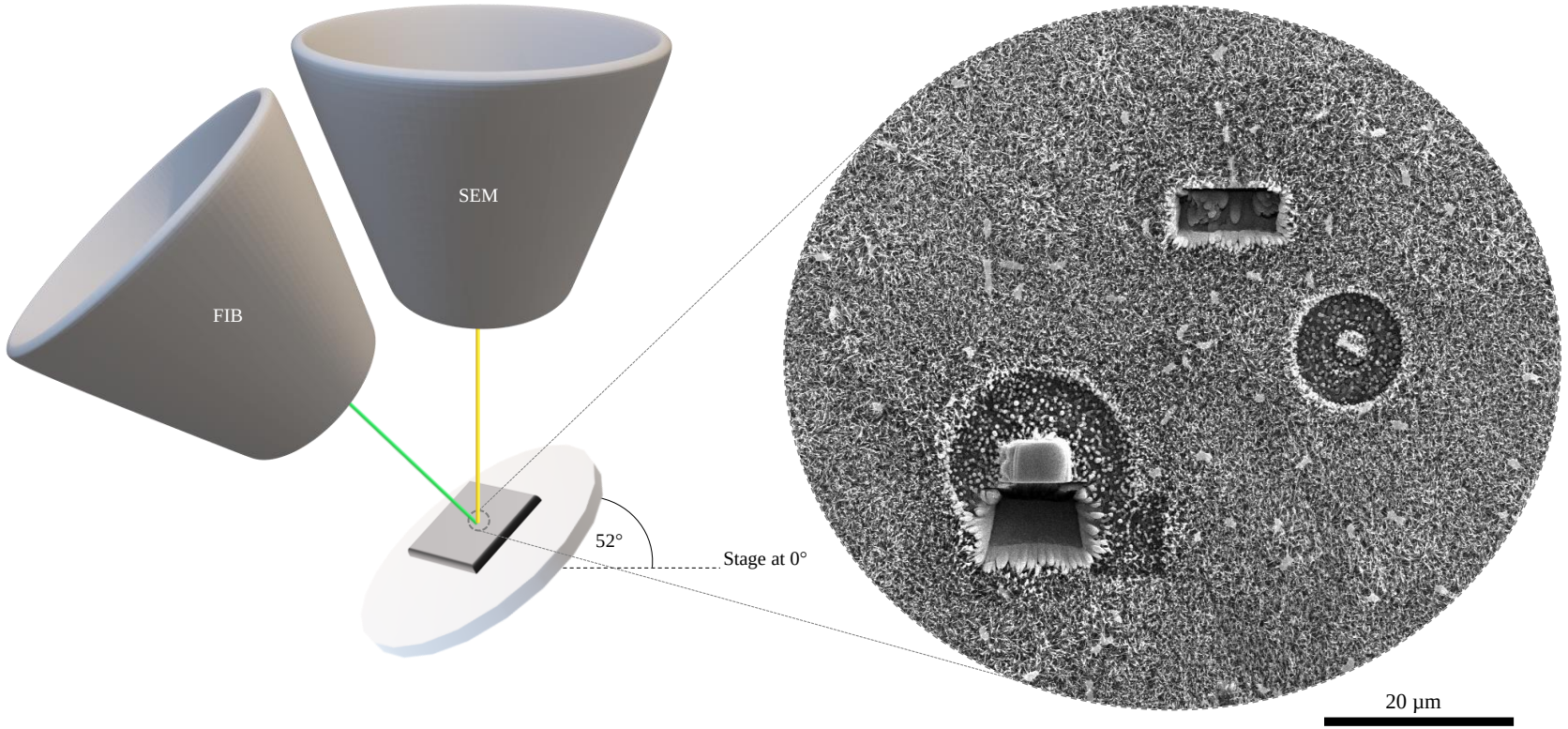

Figure 2.12 | Principles of FIB-SEM. The SEM stage holding the sample is tilted to 52° from the horizontal, positioning the sample perpendicular to the ion beam (FIB), and 38° from the electron beam (SEM). When working with delicate samples, such as tissue and cells, it may be necessary to protect the interface. This is generally achieved by coating the sample with a layer of platinum. Once positioned and coated, a beam of gallium ions are focused onto the region of interest, resulting in surface ablation and the formation of a trench. This process can be performed manually, or automatically using slice and view software. The electron beam is used to generate a micrograph of the region of interest from secondary electron emission. Examples of circular and square FIB milling patterns are highlighted.

Area scans on the Scios DualBeam were performed at an accelerating voltage of 5 kV and current of 50 pA. Prior to ion beam milling, a protective platinum layer (500 nm) was deposited on each bacterium. Rough cut trenches were milled around coated bacteria to depths of 250 nm using an accelerating voltage of 30 kV, and current of 1 nA. Auto Slice and View software was used to carry out sequential sectioning of *E. coli* in 30 nm slices. This was performed with an accelerating voltage of 30 kV and beam current of 30 pA. Images of each section were acquired using electron beam accelerating voltages of 5 kV and current of 50 pA.

2.9.5 TEM image processing and 3D volume reconstruction

Tilt series acquisition was performed by Judith Mantell (Wolfson Bioimaging Facility, University of Bristol, UK). To construct tomograms of bacteria, tilt series data sets were processed using 3Dmod in eTomo software. Tomograms were uploaded into Avizo v9.7.0 (FEI), and the segmentation editor was used to generate 3D volumes of each tomogram.

2.9.6 FIB-SEM image processing and 3D volume reconstruction

Slice and view FIB data acquisition was performed by Dr. Ali Gholinia (University of Manchester, UK) and Satishkumar Kulkarni (DESY NanoLab, Germany). The slice and view data acquired from sequential FIB milling was processed using the FIB-stack wizard tool in Avizo v9.7.0 (FEI). Briefly, this tool facilitates aligning the FIB-stack and correcting geometrical artefacts such as stage tilt foreshortening and/or vertical shift. Avizo segmentation editor was utilised to reconstruct 3D volumes of bacteria and to visualise interactions with TiO_2 nanowires.

2.10 Statistical analysis

Statistical analysis was performed using IBM SPSS statistical package (version 25). For bacterial viability testing, statistically significant differences were determined using one-way analysis of variance (ANOVA), with a Tukey HSD post-hoc test. For proteomic and oxidative stress response analysis, statistically significant differences were determined by students T-test. Statistically significant differences were attributed to variables with p-values ≤ 0.05. Unless otherwise stated, all data are expressed as mean ± standard deviation and are representative of three experimental replicates (n=3), performed in triplicate.

CHAPTER 3

Nanowire fabrication by thermal oxidation

3.1 Introduction

Thermal oxidation is a bottom up approach for nanofabrication, involving the reaction of an oxygen bearing gas phase with a substrate. The relative simplicity, low cost and scalability of thermal oxidation have made it a favourable method for generating nanowire arrays on a variety of substrates, such as copper, zinc, cp titanium and titanium alloys (Dinan, 2012; Jiang et al., 2002; Li et al., 2005; Peng and Chen, 2004). The possible applications of nanowire arrays generated by thermal oxidation are wide ranging. In particular, thermal oxidation has been highlighted as a versatile method to generate titanium implant surfaces that can promote osseointegration whilst impairing biofilm formation (Goriainov et al., 2018; Sjöström et al., 2016). It is for these reasons that thermal oxidation was chosen for the fabrication of biomimetic nanoarrays.

In general, thermal oxidation is performed in a horizontal tube furnace, through which the temperature, duration and oxidising atmosphere can be controlled and modified; the set-up used in this study is shown in section 2.1.2. A number of factors are reported to influence the growth of nanowires by thermal oxidation, including temperature, duration of heating, oxygen concentration, gas flow rate and the substrate crystal structure. From the examples discussed in Chapter 1, it is clear that some parameters impact nanowire growth more strongly than others. For example, controlled changes in temperature have been shown to influence surface morphology more strongly than duration or gas flow rate (Lee et al., 2010). Nevertheless, the precise effect of different parameters could be expected to vary depending on the exact equipment used; thus, it is necessary to optimise each processing condition related to a specific instrument. This optimisation should, in turn, help to finely tune nanowire growth and facilitate the generation of bioinspired nanowire arrays that closely mimic the nanoprotrusions of dragonfly wings.

In this chapter the influence of oxidation temperature, heating duration, gas flow rate, surface processing and crystal structure of substrate on nanowire growth are investigated systematically. Thermal oxidation was performed in a temperature window between 650°C and 900°C, at 50°C increments; the duration of the oxidation process was varied from 5 minutes to 60 minutes while the temperature increase was maintained at 15°C min^{-1}, the flow rate of Ar carrier gas was varied from 50 SCCM to 500 SCCM, thereby changing the concentration of acetone available for oxidation. The effects of surface polishing and crystal structure on nanowire growth were also investigated. Thermal oxidation was performed on grade 5 titanium alloy (Ti-6Al-4V) using acetone as the oxygen-bearing source; Ti-6Al-4V was the chosen substrate based on its widespread use for dental and orthopaedic implants.

3.2 Nanowire fabrication and characterisation

3.2.1 The effect of oxygen atmosphere on nanowire growth

Thermal oxidation of titanium and titanium alloys has been performed using a variety of oxygen-bearing sources, such as acetone, acetaldehyde, ethanol, formic acid and pure oxygen (Hu et al., 2010; Huo et al., 2008; Peng et al., 2005; Peng and Chen, 2004; Zhang et al., 2012). The source of oxygen used during thermal oxidation has been shown to significantly affect the growth of nanowires and thus, the final surface morphology (Dinan, 2012; Peng et al., 2005; Peng and Chen, 2004). To investigate the effect of oxidising atmosphere on the growth of nanowires in this study, and elucidate the possible mechanism of nanowire growth, thermal oxidation was performed under four different atmospheric conditions: 1) ambient air, 2) Ar, 3) acetone and 4) acetic acid. As a starting point to these investigations, Ti-6Al-4V substrates were oxidised at 850°C for a duration of 45 minutes, using a flow rate of 300 SCCM; these conditions have previously been used to successfully fabricate nanowires on planar (2D) and more complex (3D) Ti-6Al-4V substrates (Sjöström et al., 2016).

Thermal oxidation of Ti-6Al-4V substrates in ambient air led to the formation of a bulk oxide scale, displaying significant agglomeration and discontinuity. Upon closer inspection of surface morphology, the growth of nodular oxide particles was apparent, which were dispersed among the bulk oxide (Figure 3.1a). These findings are consistent with published literature (Kumar et al., 2010). In the presence of Ar gas, the Ti-6Al-4V substrates consisted of densely packed multifaceted crystals; each crystal had a distinct growth direction, indicating a polycrystalline surface layer (Figure 3.1b). Interestingly, this type of morphology has been observed on Ti-6Al-4V substrates thermally oxidised under pure oxygen atmospheres (Peng and Chen, 2004) and using low acetone concentrations (Sjöström et al., 2016). This observation indicated that some oxygen had entered the tube over the course of the heating programme; nevertheless, this did not appear to have interfered with the formation of nanowire arrays in the presence of acetone and acetic acid.

Although nanowire growth was observed in both acetone and acetic acid atmospheres, the coverage and homogeneity were significantly improved using acetone as the oxygen-bearing source (Figure 3.1c). In the presence of acetic acid, a combination of nanowires and larger crystal facets were observed (Figure 3.1d). These results are consistent with previous literature (Peng et al., 2005; Peng and Chen, 2004), indicating that nanowire growth in this study was attributed to the reduced diffusion of oxygen from the vapour phase, thereby enabling oxidation to occur mostly at the TiO_2-gas interface.

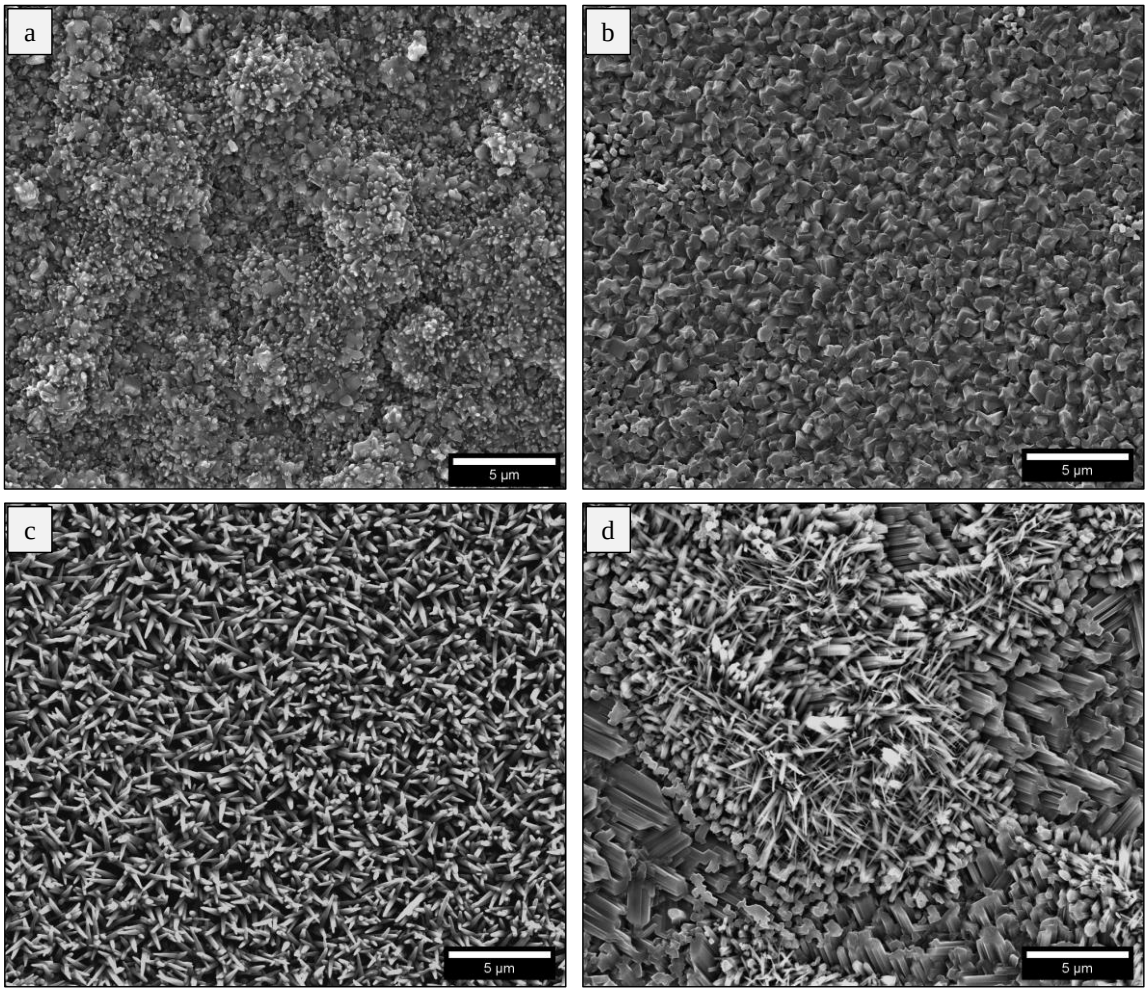

Figure 3.1 | The effect of oxygen atmosphere on nanowire growth. Scanning electron micrographs revealing the surface morphology of Ti-6Al-4V substrates oxidised in (a) ambient air, (b) Ar, (c) acetone, and (d) acetic acid. Nanowire growth was only observed when acetone and acetic acid were used as the oxygen sources.

3.2.2 Core-shell nanowire morphology

Based on the previous finding that nanowire growth was most prominent under acetone atmosphere, this was selected as the oxygen-bearing source for subsequent investigations. As-synthesised nanowires displayed a conical shape, with a general decrease in diameter from base to tip (Figure 3.2). SEM and TEM analysis revealed the presence of a core-shell structure; this was initially observed by SEM, which showed a subtle difference in contrast between the edge and centre of each nanowire that was particularly noticeable at higher magnification (Figure 3.2b). Evidence of a core-shell structure was further supported by imaging under backscattered detector (Figure 3.2d) where heavier elements appear brighter. The increased brightness of nanowire cores relative to the shell indicates a difference in elemental composition. Conclusive evidence of a core-shell structure was provided by TEM analysis (Figure 3.2e-f). Previous studies have reported similar core-shell morphologies following thermal oxidation with acetone (Hu et al., 2010; Huo et al., 2008). The core and shell of each nanowire was found to reduce in diameter from base to tip and the shell thickness was generally symmetrical around the core. The relative core and shell thickness were measured for nanowires highlighted in Figure 3.2e-f.

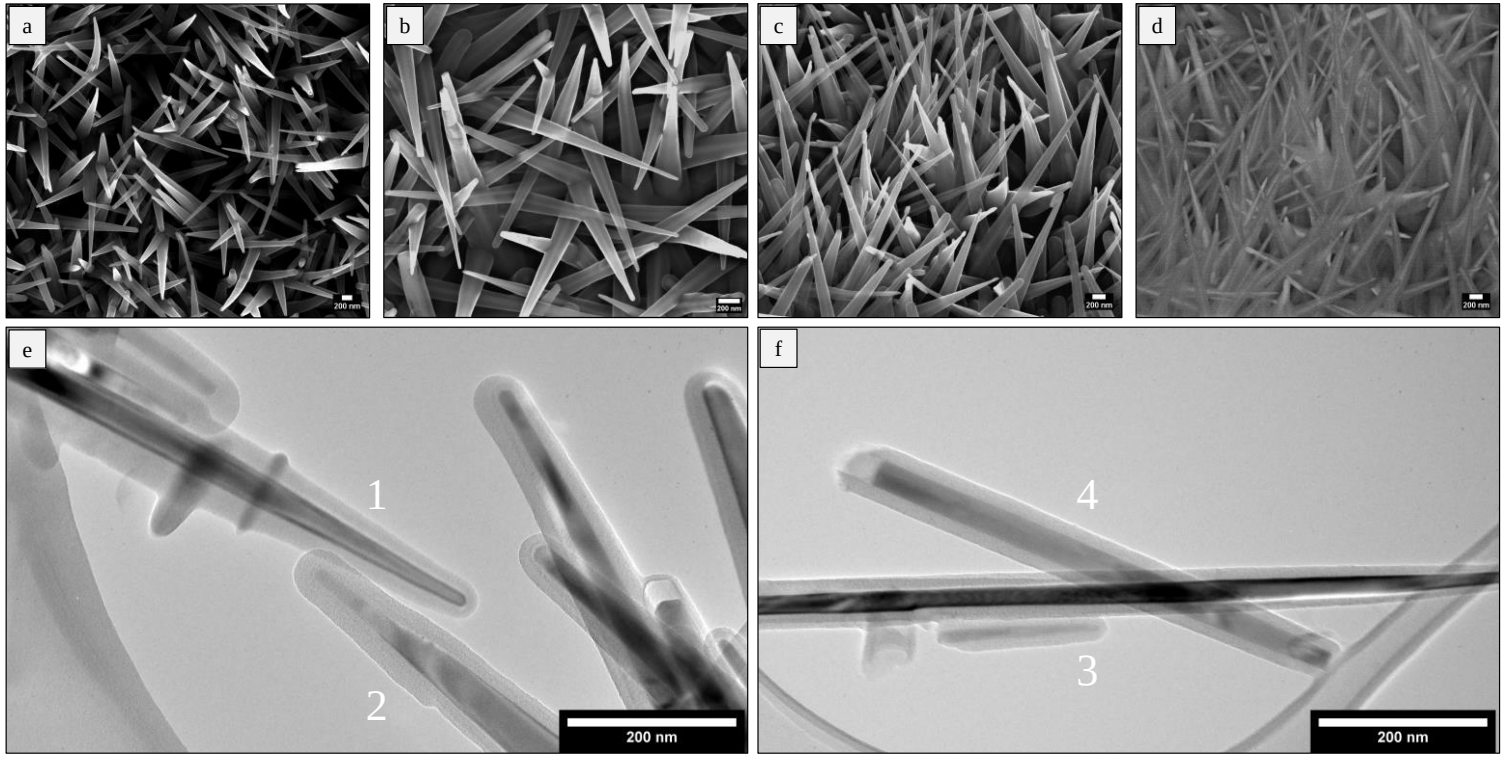

	Core diameter (nm)			Shell diameter (nm)		
Nanowire	*Tip*	*Middle*	*Base*	*Tip*	*Middle*	*Base*
1	12.46	38.09	43.86	13.93	31.303	37.21
2	15.02	20.72	30.43	13.68	16.11	19.24
3	20.49	33.19	32.21	11.71	21.49	24.39
4	31.17	49.10	48.49	16.67	21.92	23.58

Figure 3.2 | SEM and TEM analysis of core-shell nanowires. Top view SEM highlighting the conical shape of core-shell nanowires (a). The outline of the core and shell can be seen at higher magnification (b). Tilted SEM analysis of the same area of core-shell nanowires imaged using secondary electrons (c) and backscattered electrons (d); the core of nanowires appeared brighter than the shell, indicating different elemental compositions. TEM analysis of core-shell nanowires (e-f). The relative core and shell thickness of selected nanowires (1-4) is provided.

EDX was employed to identify the elemental composition of the core and shell layers within nanowires. EDX analysis in line scanning mode revealed that titanium (blue trace), oxygen (yellow trace) and carbon (green) were present within the core. Of note, the signal intensity of titanium and oxygen was greatest within the core, this is most likely attributed to TiO_2. In contrast, only carbon was identified within the shell. The signal intensity of carbon was lower in the core than in the shell, which is likely to originate from TiC and the carbon shell (Figure 3.3). These analyses indicate that a mixture of TiO_2 and TiC are present within the core and that carbon is present in the shell. This is in general agreement with previous studies, which have reported the presence of TiO_2 or TiC within the core and carbon within the shell, when using acetone as the oxygen source for thermal oxidation (Hu et al., 2010; Huo et al., 2008; Zhang et al., 2012).

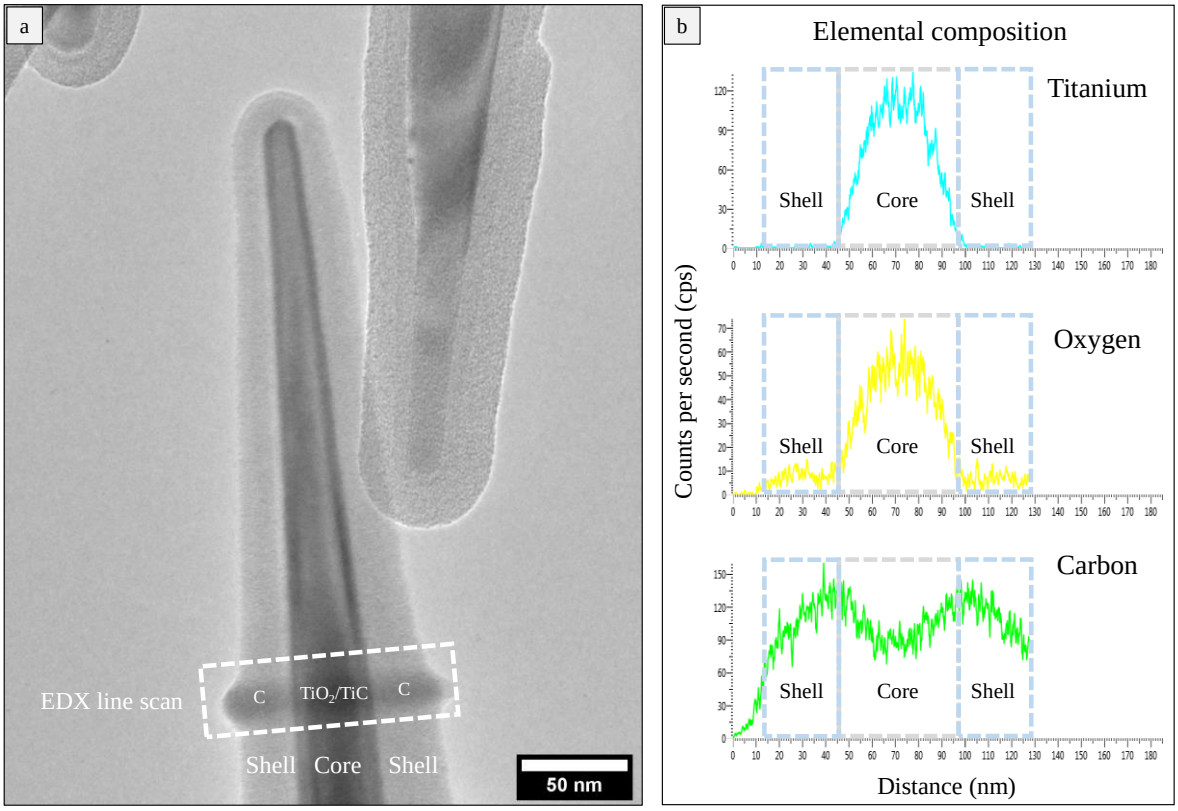

Figure 3.3 | TEM-EDX analysis of core-shell nanowires. EDX was used in line-scanning mode to reveal the elemental composition of as-synthesised nanowires, with the scanned region highlighted (a). EDX scanning revealed that titanium, oxygen and carbon were present in the core, and carbon was present in the shell; graphs show counts per second (cps) [y] versus distance (nm) [x] (b).

3.2.3 The effect of post-annealing on nanowire morphology and composition

3.2.3.1 Surface wettability

Surface wettability is an important factor that influences the attachment of bacteria to solid interfaces (Zhang et al., 2013). In one study, a superhydrophobic surface comprised of silicon elastomer was reported to greatly reduced the adhesion of *E. coli* and MRSA. This was proposed to occur by the Cassie-Baxter wetting regimen, which prevented contact between the bacteria and surface (Crick et al., 2011). Furthermore, nano- and microtextured materials with high surface roughness (R_a – arithmetic average) have been shown to enhance hydrophobicity (Shiu et al., 2004; Yoshimitsu et al., 2002; Zhang et al., 2004). Although reduced adhesion of bacteria would be a beneficial surface property, this could also impair the contact killing abilities of nanowire arrays. Furthermore, superhydrophobicity could also be expected to prevent the attachment of mammalian cells, which would be detrimental to the proposed applications of these surfaces as novel implant materials. Indeed, nanostructured PMMA surfaces with hydrophobic wetting have been shown to reduce the attachment of myoblasts compared to flat PMMA surfaces (Kim et al., 2015). With this in mind, the surface wettability of core-shell nanowire surfaces was compared to control Ti-6Al-4V substrates.

To determine surface wettability, contact angle measurements were performed using the sessile drop method. The average contact angle measured on control titanium discs was 88.63° ± 5.20°, giving rise to a slightly hydrophilic surface (Figure 3.4a). Core-shell nanowire substrates possessed hydrophobic wetting, with an average contact angle of 125.20 ± 7.26° (Figure 3.4b). Hydrophobic contact angles have been observed in other investigations of titanium nanostructured surfaces (Bhadra et al., 2015; Peng and Chen, 2004); in these cases, hydrophobicity was attributed to trapping of air between TiO_2 nanowires, as is described by the Cassie-Baxter model. However, owing to the non-polar properties of carbon, it was also considered that the shell could lead to hydrophobicity. To test this hypothesis, the carbonaceous layer surrounding nanowires was removed by annealing at 600°C for 30 minutes under ambient atmosphere. Interestingly, annealed titanium discs displayed superhydrophilic properties, with complete wetting occurring in less than a second (Figure 3.4c).

Owing to the hydrophobic nature of core-shell nanowire arrays, this could be expected to interfere with bacterial attachment, thereby hindering the investigation of bacteria and nanowire interactions. Thus, in all subsequent investigations, the carbon shell was removed, generating a superhydrophilic nanowire surface comprised of TiO_2.

Surface type	Contact angle [°]	Surface wettability
[a] Control (titanium alloy)	88.63 ± 5.20	Hydrophilic
[b] Core-shell nanowire	125.20 ± 7.26	Hydrophobic
[c] Annealed nanowire	< 10	Superhydrophilic

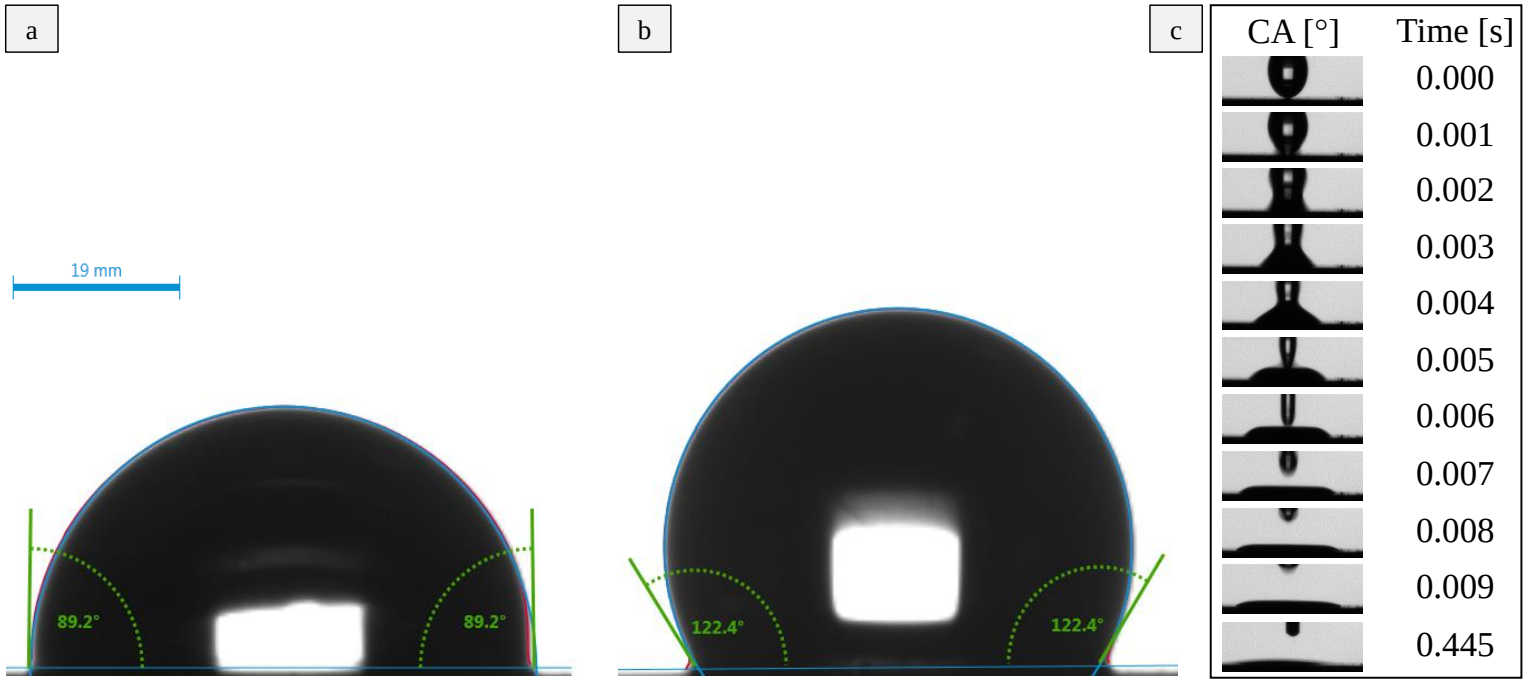

Figure 3.4 | Contact angle measurements and surface wettability. Control titanium surfaces were marginally hydrophilic, with an average contact angle just below 90° (a). In contrast, the wettability of core-shell nanowire surfaces was hydrophobic (≥90°) (b). The wettability of titanium surfaces changed significantly post-annealing, from hydrophobic to superhydrophilic (c).

3.2.3.2 Nanowire morphology and composition

In addition to the transition from hydrophobic to superhydrophilic surface wetting, annealing also resulted in a visible colour change of the surface from black to light brown, further indicating the removal of carbon. Furthermore, several aspects of nanowire morphology had been altered by annealing; most noticeably, the tapered morphology of core-shell nanowires had transformed into two distinct types. The first comprised of rod-like nanowires (RLNW) with a constant diameter apart from the very tip, where the diameter had decreased slightly (Figure 3.5a-b). This morphology was consistent with the core of core-shell nanowires. In contrast, some nanowires had an increasing diameter from the base to tip, bearing close resemblance to horseshoe nails. These structures were called horseshoe nail-like nanowires (HSNLNW) (Figure 3.5c-d). Although nanowire morphology had changed, qualitative observations indicated no significant deviation in nanowire density or coverage (Figure 3.5e-f). Both nanowire morphologies were prominent across the surface and displayed random growth directions, as had previously been observed with core-shell nanowires.

To determine whether annealing had changed the elemental composition of nanowires, EDX analysis was used. Line scanning EDX analysis showed that annealed nanowires were comprised of titanium (green trace) and oxygen (blue trace) (Figure 3.6), confirming that carbon had been removed. EDX was also used in point analysis mode to establish whether the elemental composition changed along the length of nanowires. This revealed that nanowire composition was consistent with length, as strong signals of titanium and oxygen were identified in each spectrum. EDX point analysis was also used to detect alloying elements, aluminium and vanadium. While vanadium was not found, a weak signal was generated for aluminium. The presence of carbon, chromium and silicon are likely attributable to background contamination, while the presence of copper originates from the TEM grid (Figure 3.7).

To further investigate the elemental composition of RLNW and HSNLNW compared to core-shell nanowires, HR-TEM was used to measure the lattice spacings within nanowires (Figure 3.8). RLNW displayed inter planar spacings of approximately 0.3 nm, which is comparable to the *c* lattice constant value of the (001) plane of rutile TiO_2 (c = 0.295 nm) (Diebold, 2003; Peng and Chen, 2004) (Figure 3.8a). In contrast, HSNLNW displayed spacings of approximately 1 nm, which is consistent with the *c* lattice constant of anatase TiO_2 (c = 0.937 nm) (Figure 3.8b). The lattice spacing of the core of core-shell nanowires was not resolved; however, the amorphous structure of the carbon shell is clear from the disordered lattice spacings (Figure 3.8c).

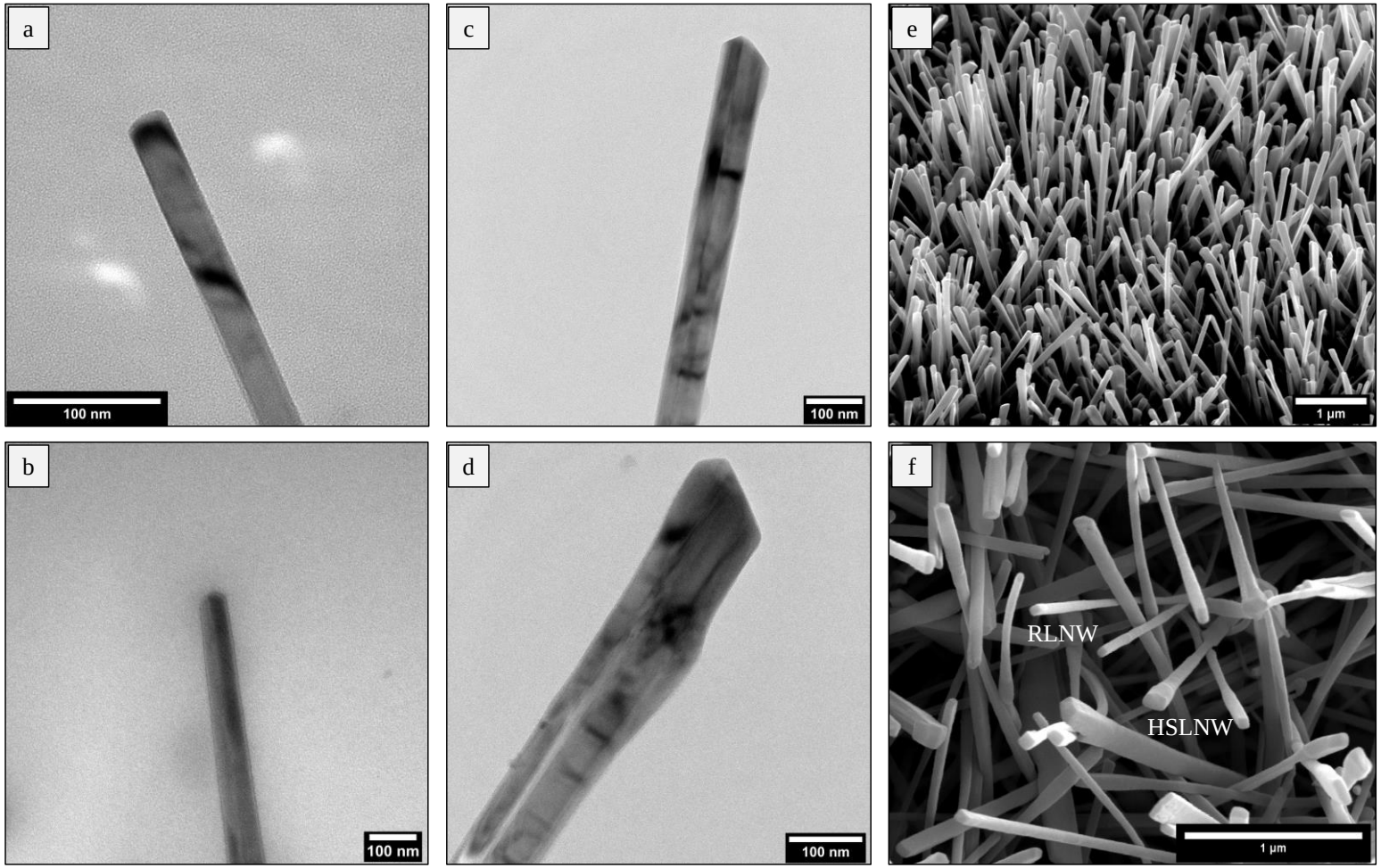

Figure 3.5 | SEM and TEM analysis of post-annealed nanowires. Two nanowire morphologies were observed following annealing. The first were rod-like nanowires (a-b), which generally displayed a uniform diameter from base to tip. The second type of nanowire closely resembled the shape of horseshoe nails (c-d). SEM analysis revealed that both RLNW and HSNLNW predominated across the surface (e-f).

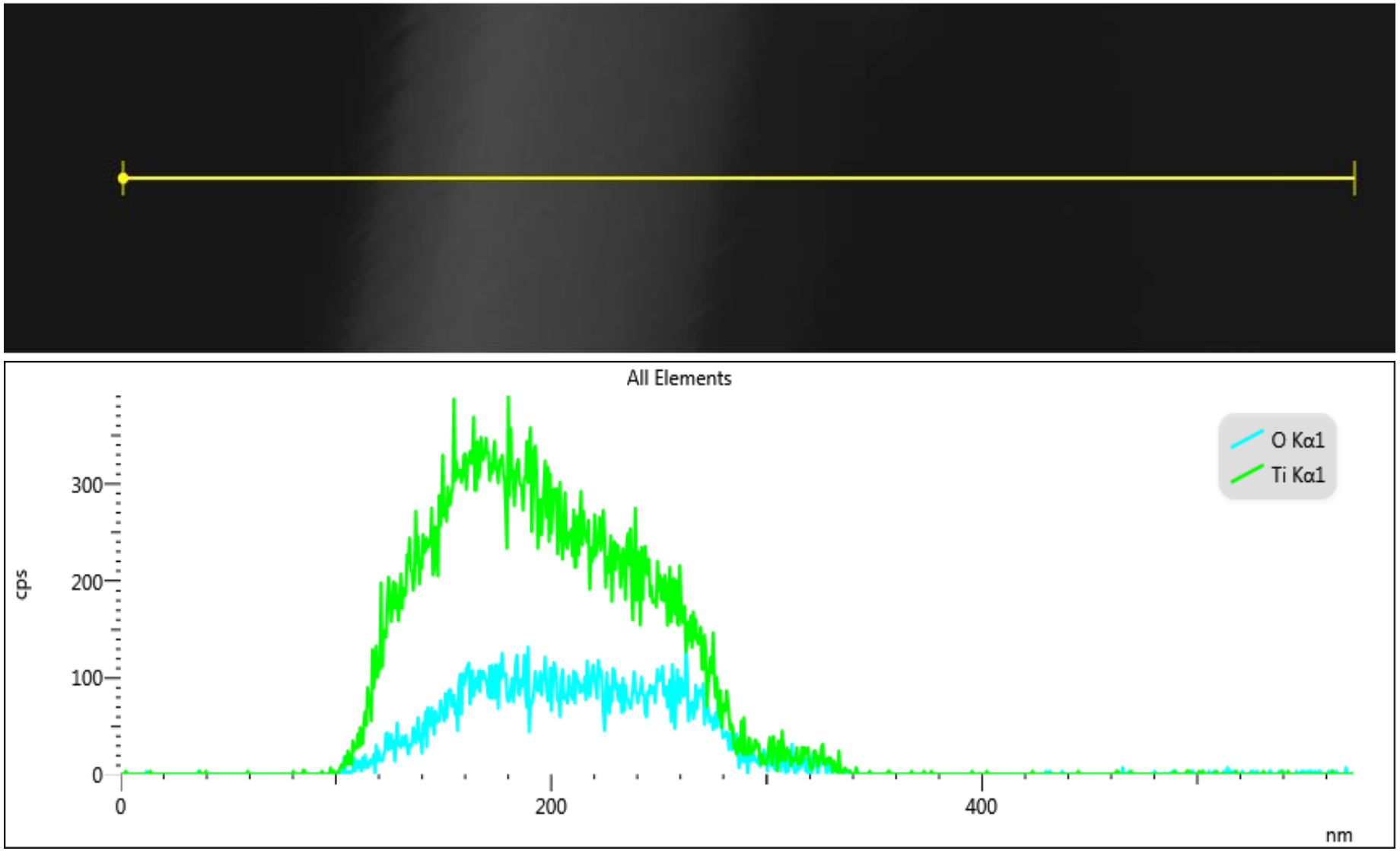

Figure 3.6 | Line-scanning EDX analysis of post-annealed nanowires. EDX line-scanning was performed in dark field mode, across the width of a single nanowire to determine the elemental composition; signals were detected from titanium and oxygen.

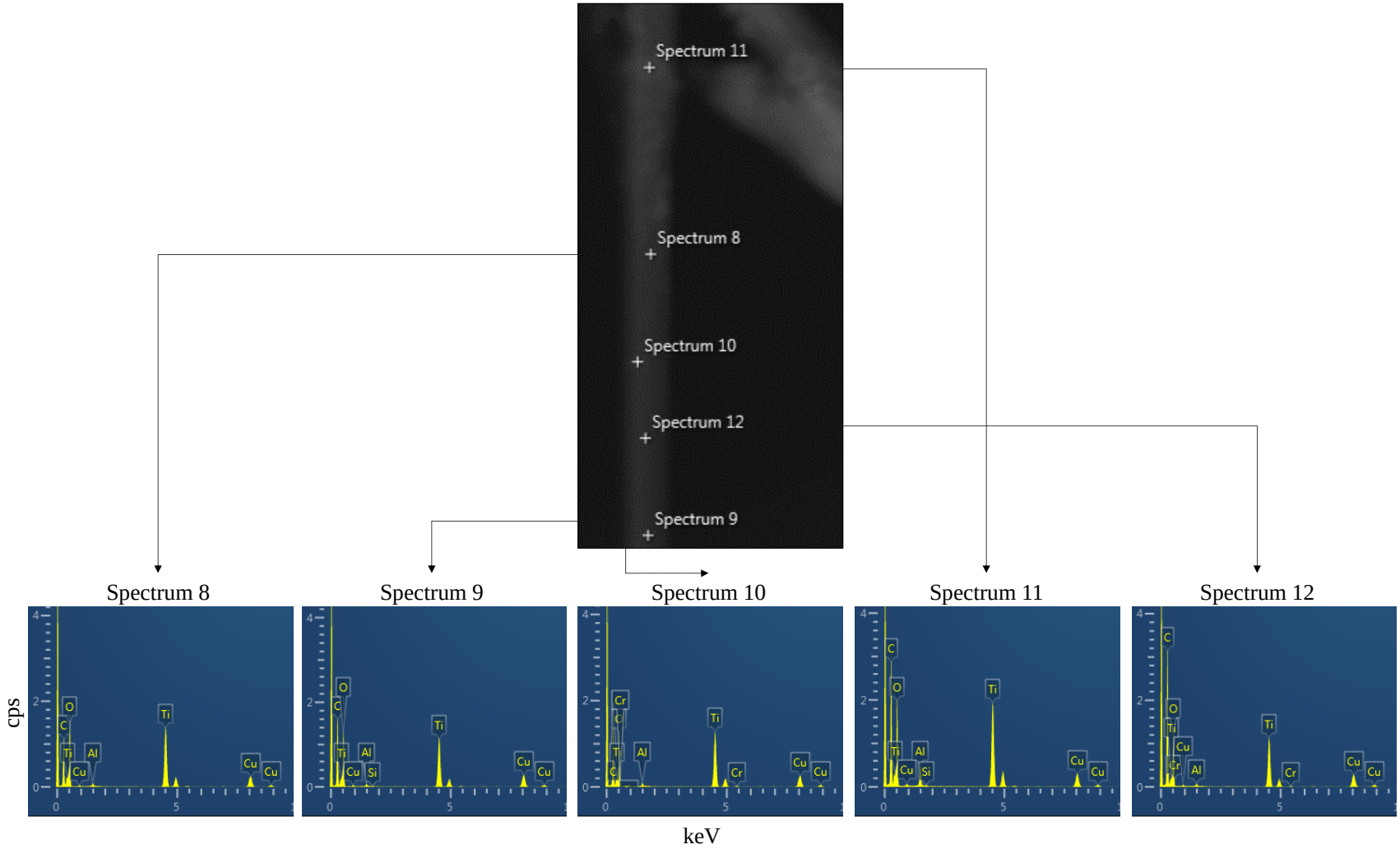

Figure 3.7 | EDX point analysis of post-annealed nanowires. EDX mapping was performed in dark field mode at five points along a single nanowire, titanium and oxygen were detected consistently in each EDX spectra. The presence of copper is attributed to the TEM grid while the presence of carbon, chromium and silicon is likely to be background contamination. Aluminium was also found at a low intensity in each spectrum, which could suggest its incorporation into the nanowire as Ti-6Al-4V contain 6% aluminium by weight.

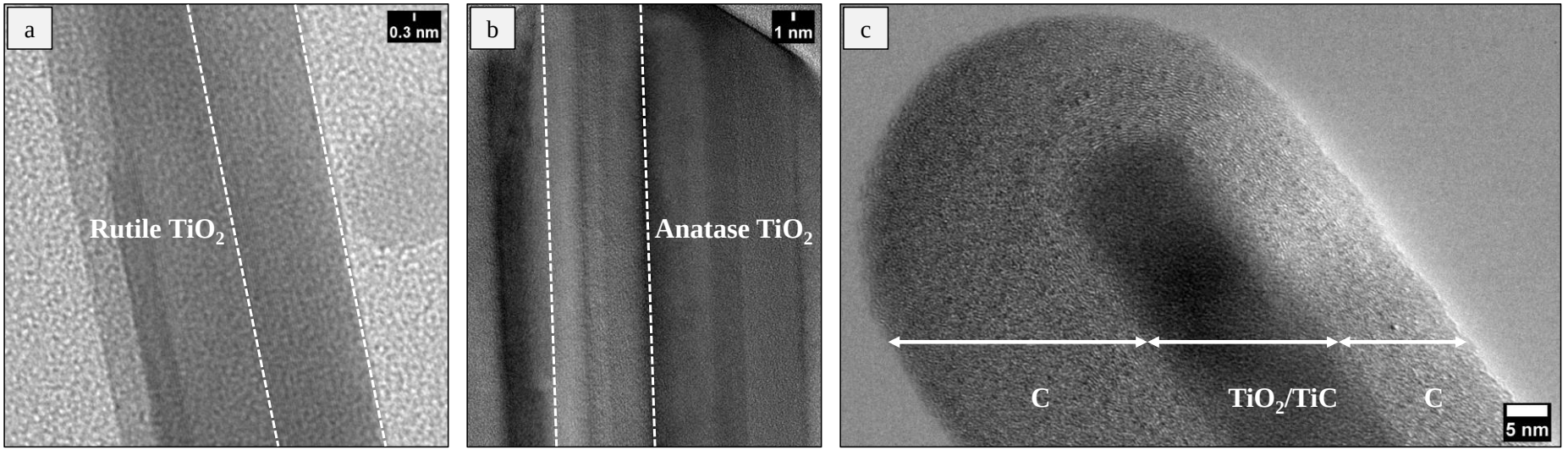

Figure 3.8 | HR-TEM analysis of nanowire lattice spacings. The lattice spacings observed in RLNW were comparable to the (001) plane of rutile TiO_2 (c = 0.295 nm) (a). In contrast, HSNLNW displayed spacings consistent with the c lattice constant of anatase TiO_2 (c = 0.937 nm) (b). The lattice spacings for the core of core-shell nanowires could not be resolved. One possible explanation for this is the shielding effect of the carbon layer, which exhibited discontinuous lattice spacings, characteristic of amorphous carbon (c). Regions where lattice planes are visible are denoted between dashed lines.

3.3 Optimisation of nanowire growth parameters

A number of factors are reported to influence the growth of nanowires by thermal oxidation, including the crystal phase, temperature, duration, gas flow rate, the initial oxide thickness and impurities. Therefore, in addition to the effects of oxidising atmosphere, nanowire growth was also investigated at different temperatures, durations, gas flow rates and with different initial surfaces (i.e. oxide thicknesses and crystal phases). By systematically changing the oxidation conditions, this enabled parameters to be selected that generated biomimetic nanotopographies.

3.3.1 The effect of oxidation temperature on nanowire growth

Oxidation temperature has been widely reported to influence the rate of nanowire growth on titanium and titanium alloys by thermal oxidation (Arafat et al., 2013; Dinan, 2012; Lee et al., 2010). Furthermore, it has been shown to influence nanowire growth on copper substrates (Jiang et al., 2002; Xu et al., 2004). As such, temperature was chosen as the starting point for these investigations. In line with previous studies, oxidation temperatures between the ranges of 650-900°C were selected in 50°C increments, while duration and flow rate remained constant at 45 minutes, and 300 SCCM respectively.

In agreement with previous literature (Dinan, 2012; Lee et al., 2010), temperature significantly affected nanowire formation (Figure 3.9-3.10). At 650°C, nanoprotrusions with an average length of 73 nm ± 18 nm, and diameter of 28 nm ± 3 nm had formed. The small and rounded morphology of these structures created a high packing density (169 per μm^2 ± 12 per μm^2), and low spacing (50 nm ± 5 nm) (Figure 3.10a). As the temperature was increased to 700°C, structures resembling nanowires began to form (Figure 3.10b), and while the length of nanoprotrusions had doubled (154 nm ± 43 nm), no significant change in diameter was seen (27 nm ± 5 nm). The increasing length of nanowires led to a reduced density (99 per μm^2 ± 44 per μm^2) and increased spacing (84 nm ± 15 nm). Interestingly, nanowire growth occurred in specific areas at 650°C and 700°C, with a formation resembling the outline of crystal grains. One possible explanation for this is the preferential growth of nanowires on certain crystal phases. Previous studies have reported that nanowire growth is more prominent in β-phase than α-phase (Lee et al., 2010). This morphology led to poor nanowire coverage across the surface. Due to the poor coverage, oxidation temperature was increased to 715°C, and this led to a more uniform and homogeneous nanowire formation. The average length, diameter, density and spacing of nanowires at 715°C were as follows: 350 nm ± 52 nm, 27 nm ± 4 nm, 58 per μm^2 ± 3 per μm^2 and 115 nm ± 10 nm (Figure 3.10c).

The length of nanowires continued to increase at 750°C, 800°C and 850°C (Figure 3.10d-f), with average measurements of 372 nm ± 33 nm, 726 nm ± 184 nm and 1700 nm ± 347 nm respectively. In addition to this, incremental changes to tip diameter were observed at these temperatures, and were recorded at 33 nm ± 1 nm, 48 nm ± 7 nm and 114 nm ± 26 nm respectively. As was previously seen between 650°C and 700°C, the increases in length resulted in decreased packing density and increased spacing from 750°C to 850°C. Densities were recorded as 71 per μm^2 ± 23 per μm^2, 12 per μm^2 ± 23 per μm^2 and 8 per μm^2 ± 1 per μm^2 respectively, and the average nanowire spacings were observed to be 132 nm ± 27 nm, 278 nm ± 52 nm, and 494 nm ± 73 nm. Contrary to the lower temperatures, at 900°C, larger multifaceted crystals had formed (Figure 3.10g).

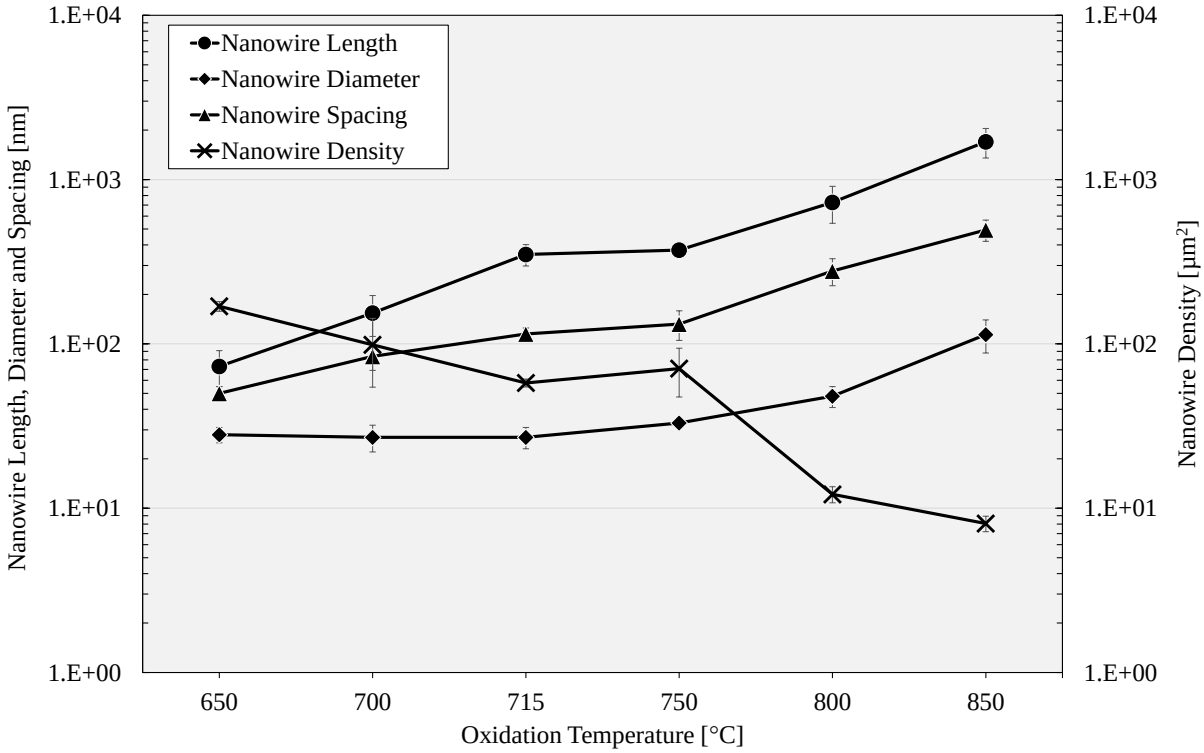

Figure 3.9 | The effect of oxidation temperature on nanowire growth. Thermal oxidation of Ti-6Al-4V discs was performed at different temperatures (650-900°C) at a constant duration (45 minutes) and flow rate (300 SCCM). The average nanowire length, diameter, tip spacing, and density (per μm^2) are shown ± standard deviation. These dimensions were measured in Fiji using top down SEMs for tip spacing and density measurements and tilted SEMs to approximate nanowire length and diameter. A more detailed outline is provided in section 2.2.

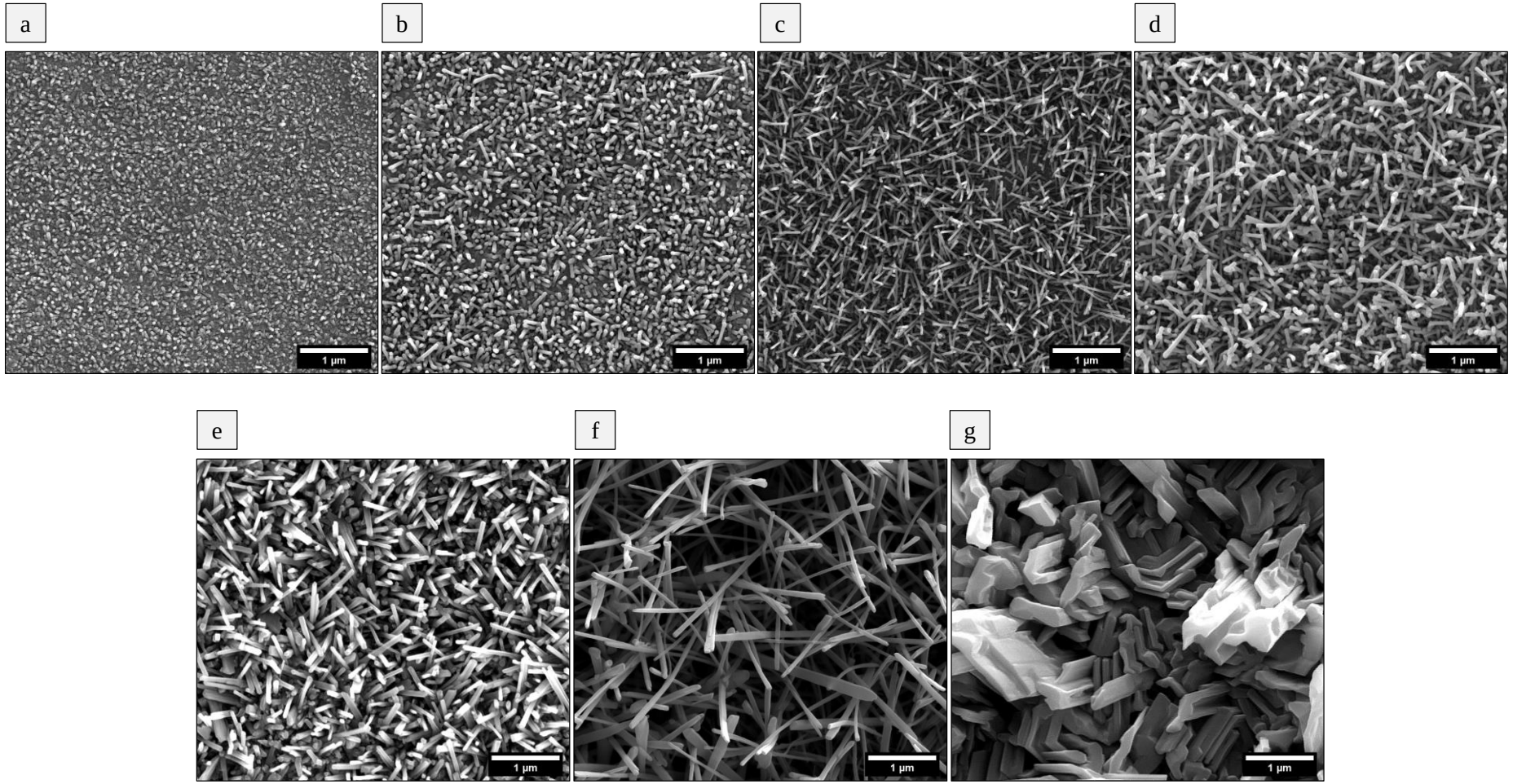

Figure 3.10 | The effect of oxidation temperature on nanowire morphology. Thermal oxidation of Ti-6Al-4V discs was performed at different temperatures (650-900°C) at a constant duration (45 minutes) and flow rate (300 SCCM). Representative SEM micrographs of each nanotopography are shown; 650°C (a), 700°C (b), 715°C (c), 750°C (d), 800°C (e), 850°C (f), 900°C (g). Scale bar = 1 µm**.**

3.3.2 The effect of oxidation duration on nanowire growth

Nanowires were shown to nucleate in temperature ranges between 650°C and 850°C, with the most prominent growth observed at 850°C. As such, this temperature was chosen to investigate the effect of oxidation duration on nanowire growth. The formation of nanowires at 850°C was studied at five additional durations: 5, 10, 15, 30 and 60 minutes, all of which occurred under a constant flow rate of 300 SCCM.

The length and diameter of nanowires was found to increase from 5 minutes to 60 minutes, but the differences between each time point were not as large as those seen for changes in temperature (Figure 3.11). After 5 minutes oxidation, nanowires averaged 851 nm ± 80 nm in length and 68 nm ± 24 nm in diameter. The morphology of nanowires after 5 minutes resembled cone structures, with a decreasing diameter from base to tip and spherical cap. This morphology is referred to as cone-like nanowires (CLNW) (Figure 12a). Following an additional 5 minutes, the average length of nanowires had increased to 974 nm ± 81 nm while the diameter had not changed significantly, measured at 61 nm ± 10 nm. CLNW morphologies were less pronounced after 10 minutes, while RLNW morphologies were more prominent (Figure 12b). Nanowire length and diameter continued to increase from 15 to 60 minutes; average nanowire lengths were recorded at 1135 nm ± 102 nm, 1227 nm ± 228 nm, and 1858 nm ± 126 nm, while nanowire tip diameters were observed to be 82 nm ± 19 nm, 85 nm ± 10 nm and 102 nm ± 17 nm, at 15, 30 and 60 minutes respectively. Of note, CLNW morphologies were largely absent after 15 minutes (Figure 12c) and had disappeared between 30 and 60 minutes (Figure 12d-f). As was observed for changes in oxidation temperature, increasing the oxidation duration led to gradual decreases in nanowire density while spacing steadily increased. The average nanowire densities for 5, 10, 15, 30 and 60-minute oxidations were 23 per μm^2 ± 6 per μm^2, 17 per μm^2 ± 1 per μm^2, 14 per μm^2 ± 5 per μm^2, 10 per μm^2 ± 1 per μm^2 and 7 per μm^2 ± 1 per μm^2 respectively, and the average nanowire spacings were measured at 185 nm ± 17 nm, 195 nm ± 19 nm, 228 nm ± 46 nm, 296 nm ± 55 nm and 558 nm ± 117 nm.

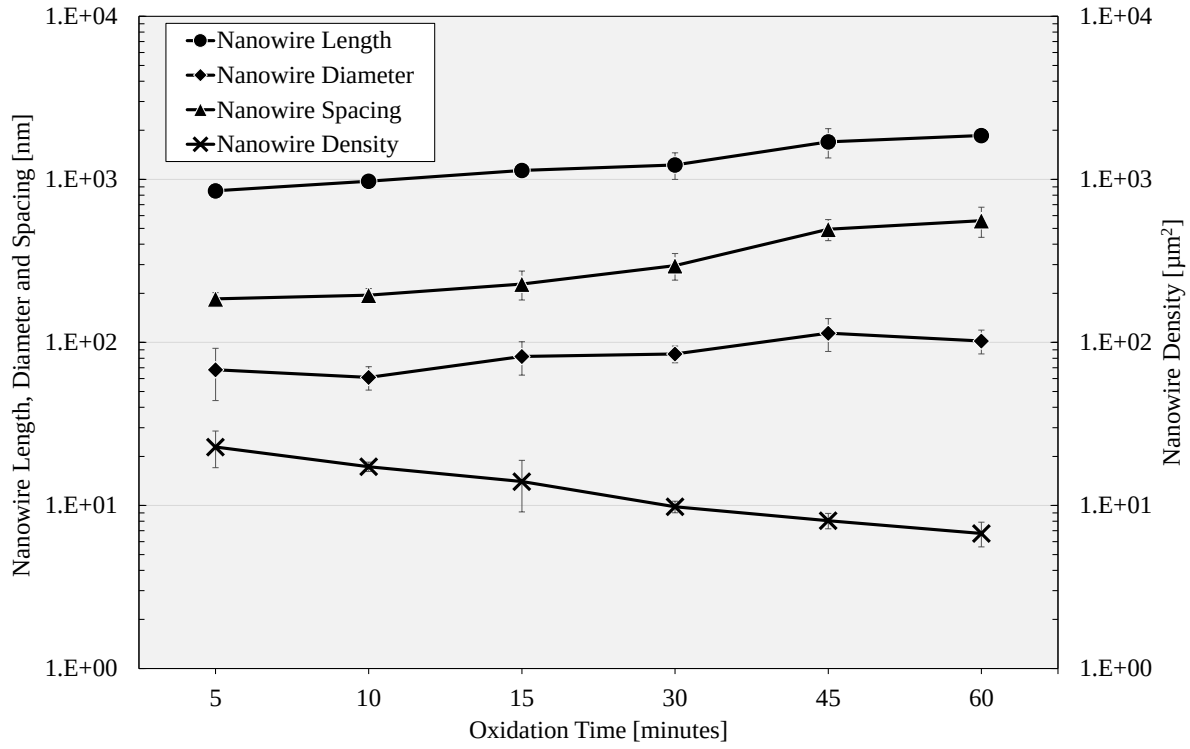

Figure 3.11 | The effect of oxidation time on nanowire growth. Thermal oxidation of Ti-6Al-4V discs was performed at different durations (5 – 60 minutes) at a constant temperature (850°C) and flow rate (300 SCCM). The average nanowire length, diameter, tip spacing, and density (per μm^2) are shown ± standard deviation. These dimensions were measured in Fiji using top down SEMs for tip spacing and density measurements and tilted SEMs to approximate nanowire length and diameter. A more detailed outline is provided in section 2.2.

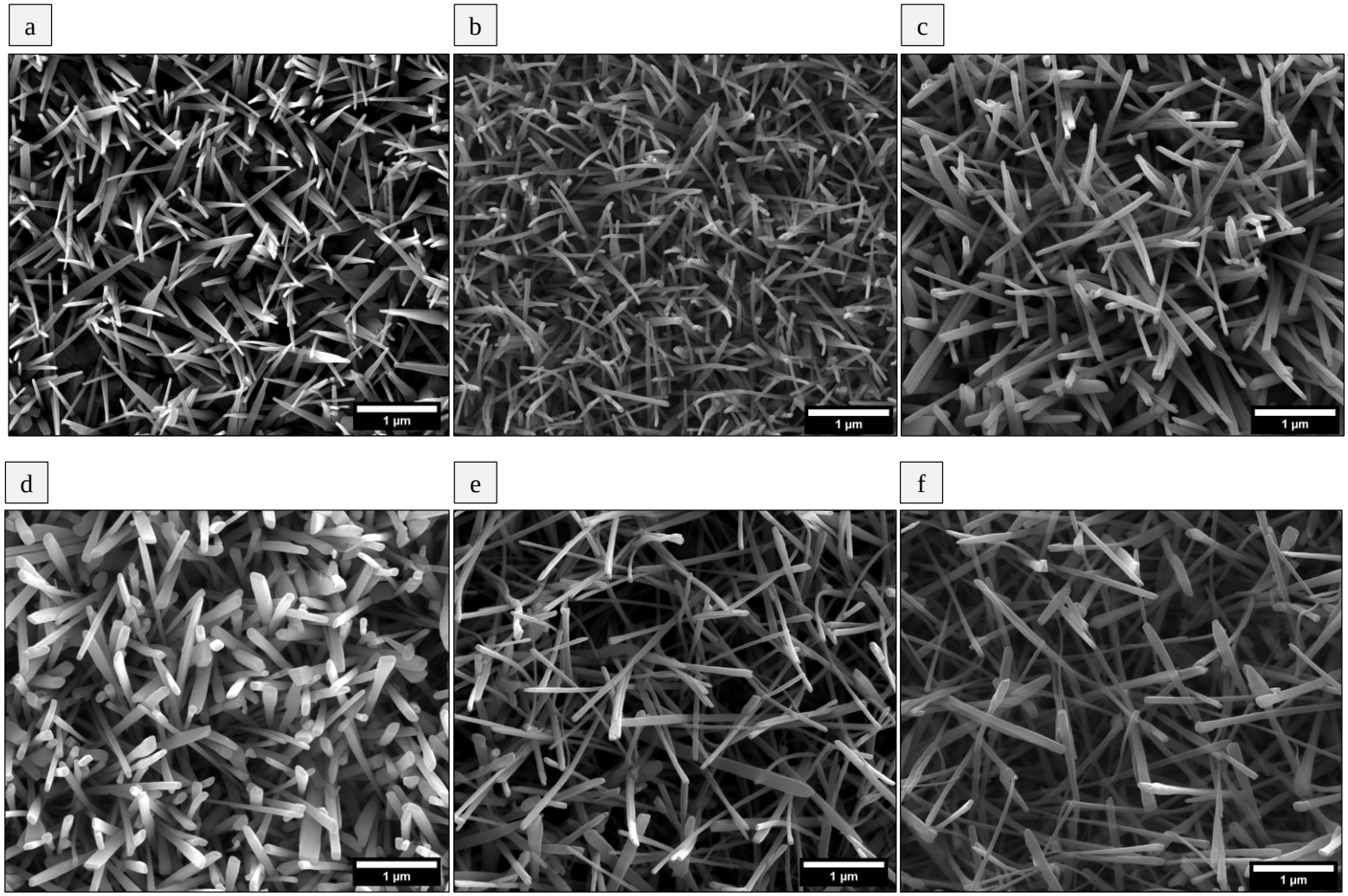

Figure 3.12 | The effect of oxidation time on nanowire morphology. Thermal oxidation of Ti-6Al-4V discs was performed at different durations (5 – 60 minutes) at a constant temperature (850°C) and flow rate (300 SCCM). Representative SEM micrographs of each nanotopography are shown. 5 (a), 10 (b), 15 (c), 30 (d), 45 (e) and 60 minutes (f). Scale bar = 1 µm.

3.3.3 The effect of flow rate on nanowire growth

As was shown in section 3.2.1, the type of oxygen source used during thermal oxidation can have a significant effect on the availability of oxygen and thus, the growth of nanowires. Therefore, the flow rates of Ar carrier gas could be expected to have a comparable influence, as this would also affect the concentration of oxygen within the vapour phase. To investigate the effect of Ar flow rate on nanowire growth, thermal oxidation was performed at five additional flow rates: 50, 100, 200, 400 and 500 SCCM. All of these occurred at a constant temperature of 850°C and for a duration of 45 minutes.

At 50 SCCM, equiaxed crystals had formed on the bulk substrate (Figure 3.13a). These shared a close morphology to Ti-6Al-4V substrates oxidised in the absence of acetone. The formation of TiO_2 nanowires was observed between 100 SCCM to 500 SCCM; however, qualitative analysis revealed no significant change to nanowire morphology or coverage (Figure 3.13b-f). These observations are consistent with published literature, showing minimal changes to nanowire growth following changes in flow rate on titanium substrates (Lee et al., 2010).

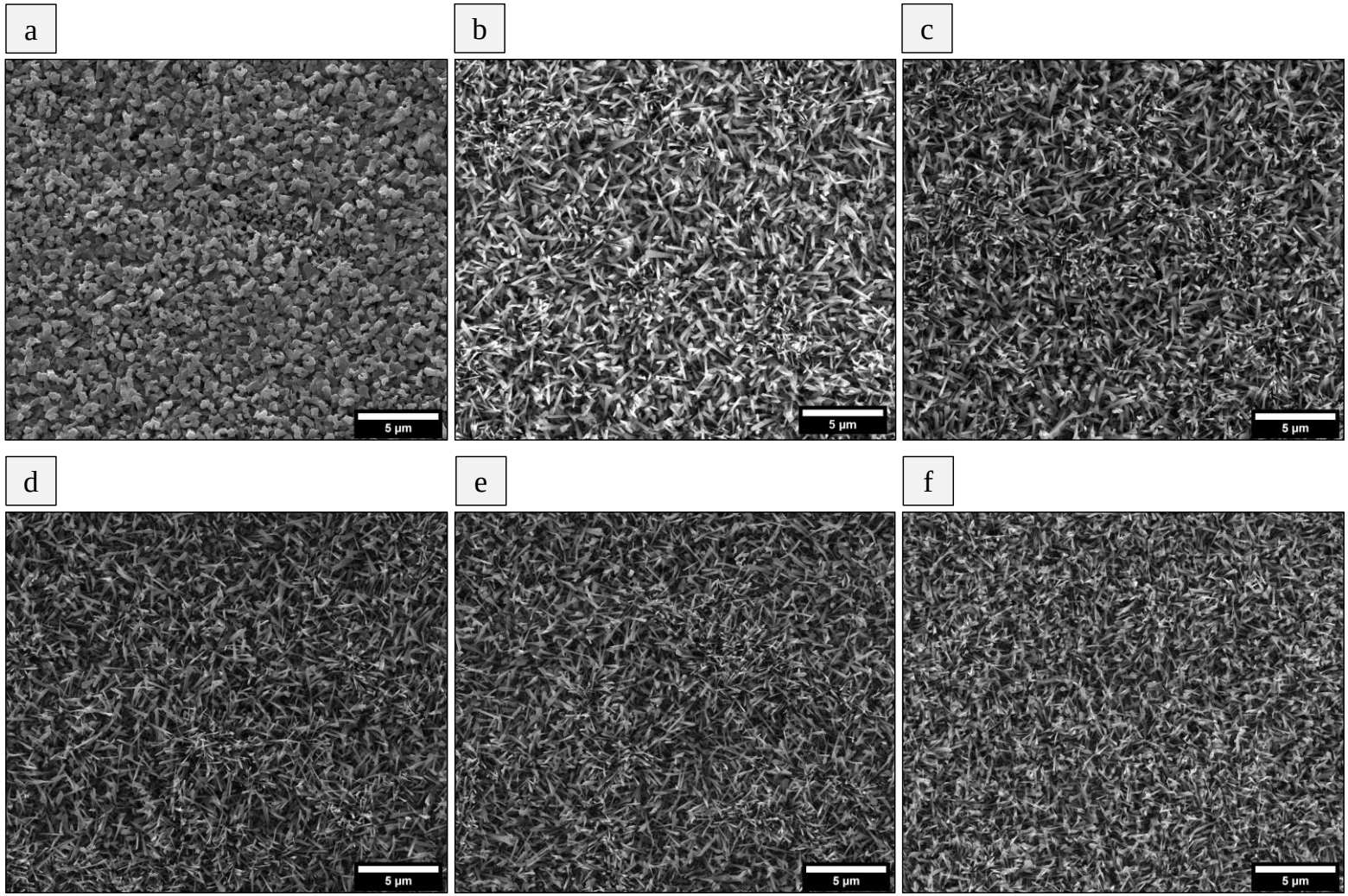

Figure 3.13 | The effect of oxidation flow rate on nanowire growth. Thermal oxidation of Ti-6Al-4V discs was performed at different flow rates (50 – 500 SCCM) at a constant temperature (850°C) and duration (45 minutes). Representative SEM micrographs of TiO_2 nanowire arrays generated under different Ar flow rates 50 (a), 100 (b), 200 (c), 300 (d), 400 (e) and 500 SCCM (f). Scale bar = 1 µm.

3.3.4 The effect of crystal grain structure on nanowire growth

Titanium and titanium alloys are allotropic, meaning that their crystal phase can be altered through heating. In the context of nanowire growth, certain crystal phases, namely β-phases, have been shown to enhance the growth and coverage of nanowires (Lee et al., 2010), which could improve the efficiency of nanowire fabrication by thermal oxidation. Furthermore, heating Ti-6Al-4V beyond its β-transis (980°C) has been shown to increase nanowire alignment following thermal oxidation, which could be expected to influence bactericidal activity (Sjöström et al., 2016). To investigate the effect of pre-annealing on nanowire growth by thermal oxidation, the microstructure of Ti-6Al-4V was first manipulated by heating to temperatures exceeding the beta-transus of Ti-6Al-4V, namely 1000°C, 1100°C and 1200°C. Thermal oxidation was then performed at 850°C for 45 minutes at 300 SCCM.

Pre-annealing of Ti-6Al-4V substrates led to a significant increase in the average crystal grain size. This was observed both qualitatively by optical microscopy (Figure 3.14), and quantitatively by EBSD (Figure 3.15). At 1000°C, the cross sectional diameter of crystal grains varied from 0.34 mm to 3.2 mm; for samples heated at 1100°C, the crystal size varied from 0.67 mm to 3.79 mm; at 1200°C, the diameters varied from 0.41 mm to 3.9 mm. Qualitatively, the average size of crystal grains appeared to increase with temperature. This is likely to be attributed to the transformation of smaller crystals into larger, more energetically favoured crystal grains as described by Ostwald ripening (Yao, 1993). To determine the average grain size before pre-annealing and thus determine the effect of heating on grain enlargement, EBSD mapping was used to compare the grain size, orientation and phase within control Ti-6Al-4V substrates and Ti-6Al-4V discs that had undergone pre-annealing at 1200°C. In the scanning areas shown, the average size of crystal grains with control Ti-6Al-4V discs varied from 0.29 µm to 8.2 µm and were predominantly alpha phase (93%), with only 7% beta phase. This is to be expected, as Ti-6Al-4V is an α-β alloy and comprises mostly α-phase at room temperature. In contrast, the average grain size increased significantly following pre-annealing, with some in mm range, which is consistent with observations from optical microscopy. While average grain size had increased following pre-annealing, the relative proportions of alpha and beta phases remained comparable (99% alpha, 1% beta) when cooled to room temperature.

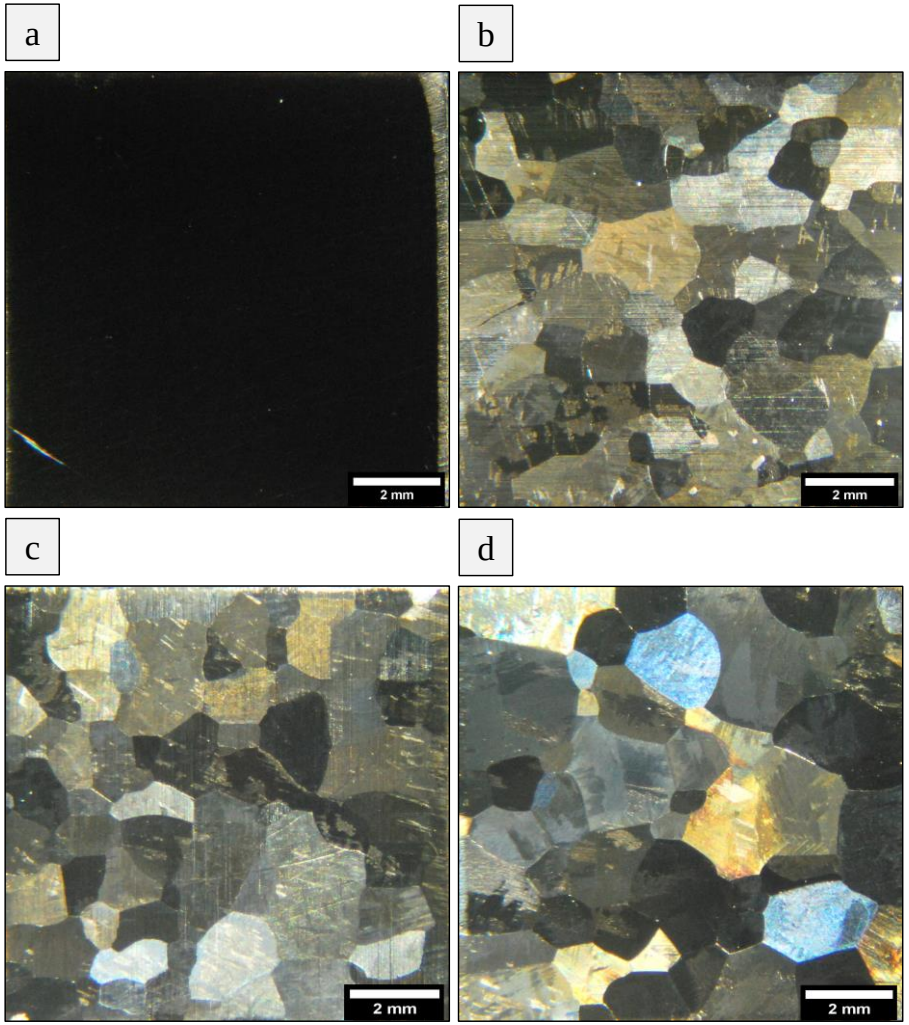

Figure 3.14 | The effect of pre-annealing on Ti-6Al-4V crystal size. The microstructure of Ti-6Al-4V discs was manipulated by heating to temperatures exceeding the beta-transus (1000°C, 1100°C and 1200°C) for 1 hour. Optical micrographs of annealed Ti-6Al-4V substrates reveal a significant increase in the average grain size compared to control (a), with a general increase with temperature, 1000°C (b), 1100°C (c), 1200°C (d).

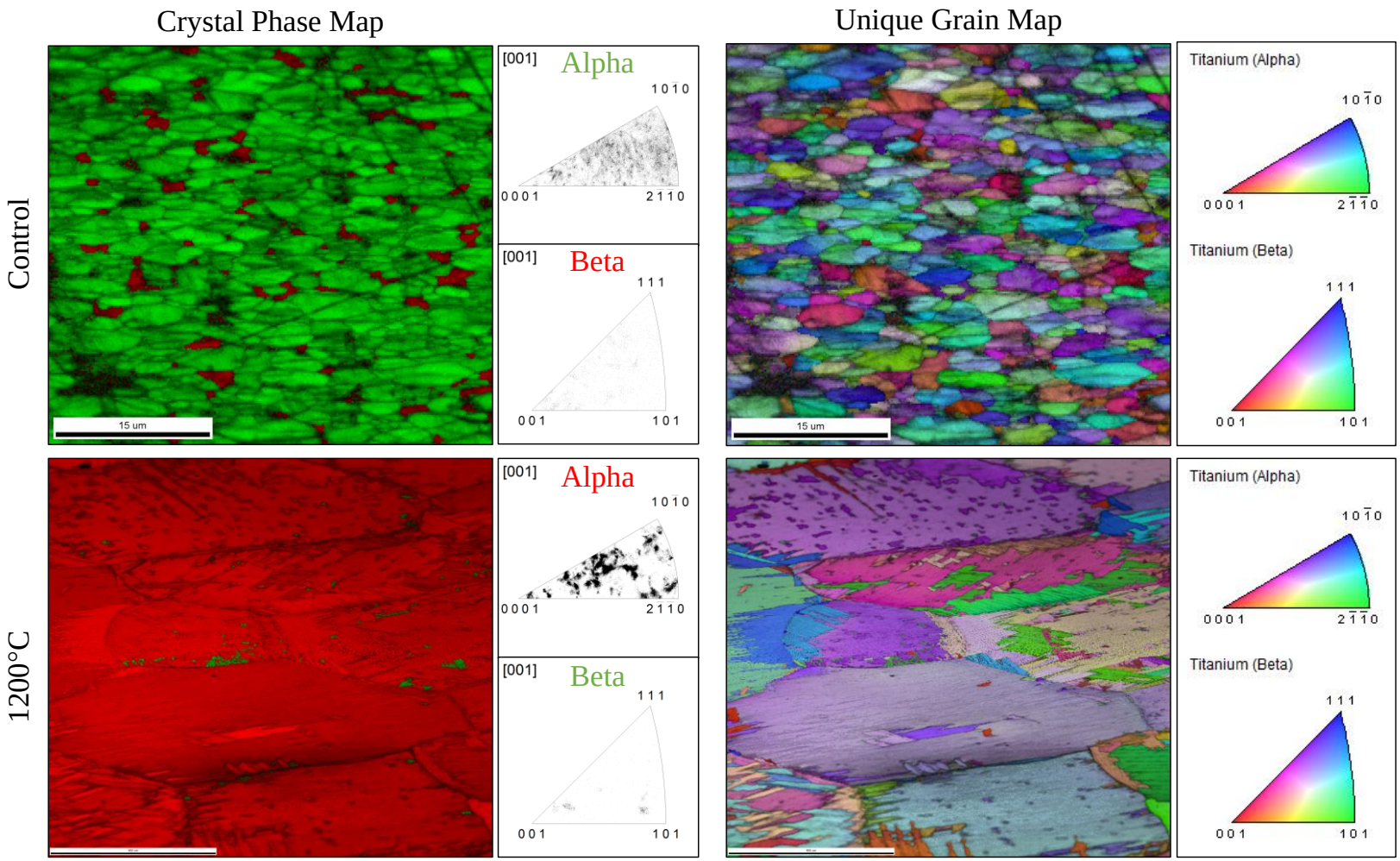

Figure 3.15 | The effect of pre-annealing on Ti-6Al-4V crystal size, orientation and phase. EBSD maps show the crystal phase (alpha or beta) and orientation within control Ti-6Al-4V and pre-annealed Ti-6Al-4V (1200°C for 1 hour). Corresponding inverse pole figures show the crystal orientation with respect to the specimen normal direction [001].

Thermal oxidation of pre-annealed Ti-6Al-4V led to the formation of nanowire arrays with three distinct morphologies: 1) Nanowire rows, 2) aligned nanowires and 3) randomly oriented nanowires. Nanowire rows, characterised by repeating laths of nanowires, were observed at each pre-annealing temperature tested (1000°C-1200°C) (Figure 3.16a-c). Nanowire rows were widespread across the surface and are most likely attributable to the presence of secondary α-lamella, which form within β crystals during cooling (Gammon et al., 2004). Aligned nanowires had formed in some regions, as reported in previous literature (Sjöström et al., 2016). Figure 3.16d shows the intersection of three crystal grain boundaries, denoted by the white-hashed lines. The orientation of nanowire growth is clearly different on each crystal. The formation of alpha lamella appeared to disrupt nanowire alignment, with repeating nanowire rows interrupting aligned areas (Figure 3.16e). Some regions of nanowires displayed high levels of alignment, but nanowires with random growth directions were still observed in these areas (Figure 3.16f). Nanowires with random growth orientations were also observed, similar to those seen on surfaces that had not been annealed prior to thermal oxidation. Although pre-annealing had changed the orientation of nanowires, this was only true for selected regions that could not be fully controlled. Furthermore, there was no evidence that nanowire growth had been enhanced. For these reasons, pre-annealing was not used for routine surface processing.

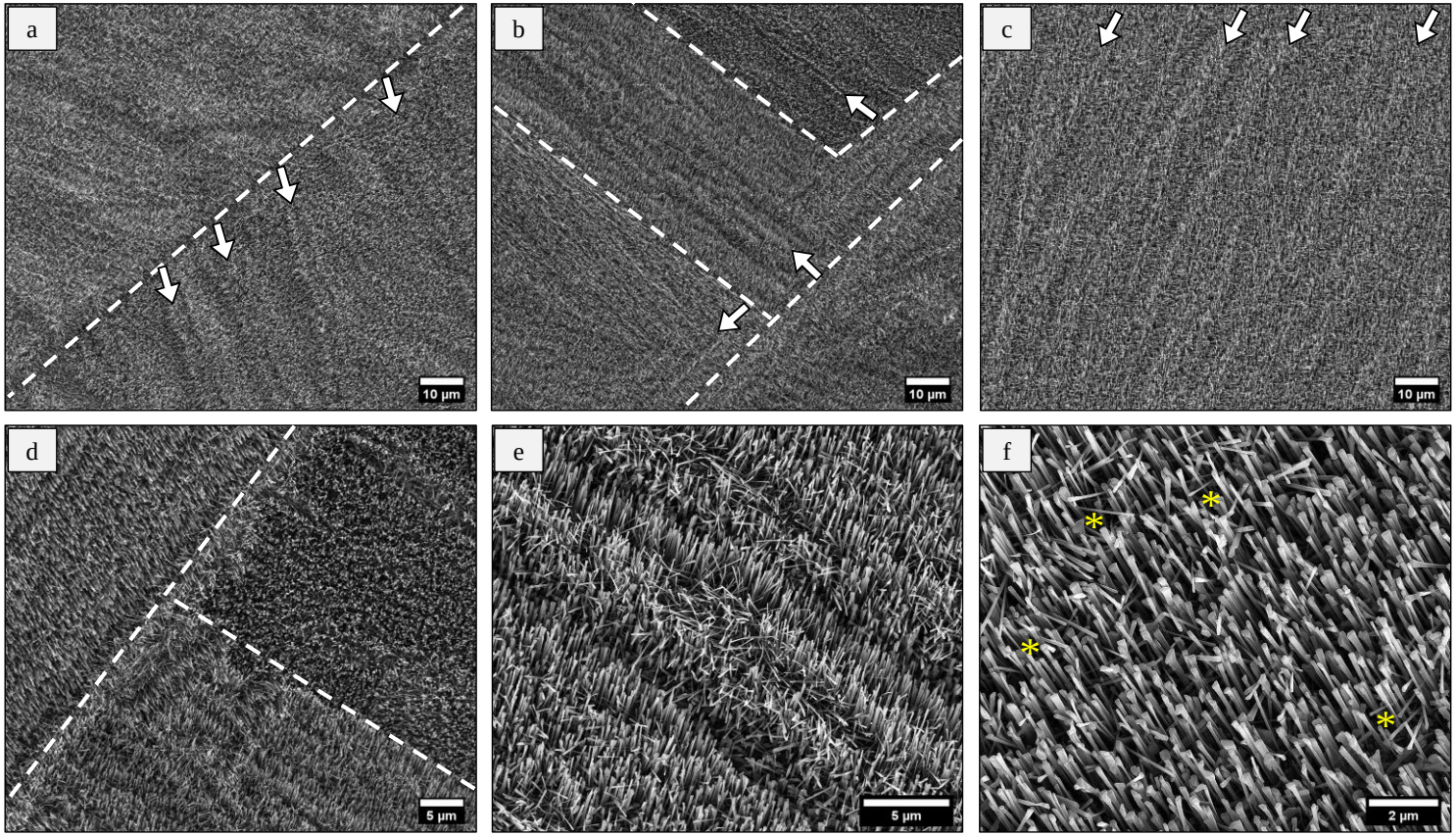

Figure 3.16 | The effect of pre-annealing on nanowire growth. Pre-annealing of Ti-6Al-4V led to the formation of three nanowire morphologies: 1) Nanowire rows, 2) aligned nanowires and 3) randomly oriented nanowires. Nanowire rows were identified at each pre-annealing temperature (a) 1000°C, (b) 1100°C, and (c) 1200°C and were characterised by repeating nanowire laths. Selected nanowire rows are indicated by white arrows and white-hashed lines denote what appear to be crystal boundaries. The growth direction of nanowires appeared to be dependent on the underlying crystal structure (d) with nanowires inside the top left and top right crystals displaying mostly unidirectional growth, while nanowires within the bottom crystal had nucleated in rows. The formation of alpha-lamella appeared to disrupt the continuous formation of aligned areas of nanowires (e). The area of aligned nanowires could not be controlled, nanowires with random growth directions were interspaced between aligned nanowires, these regions are indicated by yellow asterixis (f).

3.3.5 Nanotopography selection

Four nanowire arrays were selected for additional characterisation and viability testing: 650°C, 715°C, 850°C (5 minutes) and 850°C (45 minutes). There were two reasons for choosing these surfaces. Firstly, these nanotopographies possessed biomimetic feature sizes with properties similar to those found in nature, while also covering a range of nanowire dimensions to help identify parameters that may be promoting antibacterial effects. Secondly, all nanotopographies were reproducible, helping to ensure that the bacterial response would be consistent. For the remainder of this thesis, these nanowire surfaces will be referred to as NW1 (650°C), NW2 (715°C), NW3 (850°C (5 minutes)) and NW4 (850°C (45 minutes)) respectively (as shown in Figure 3.17), where NW is the abbreviation of nanowire. The respective colours of NW1-NW4 were light yellow, purple/blue, blue and beige. This is likely to be attributable to the increased thickness of the oxide layer and the change in the surface topography, which interfere with the incident light radiation (Kumar et al., 2010).

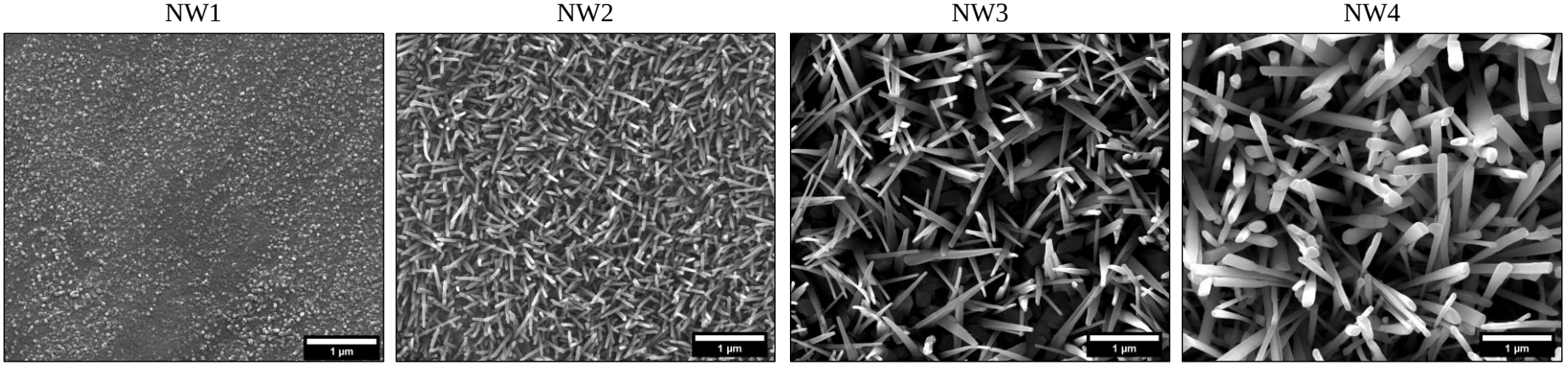

Nanotopography	Processing conditions				
	Oxidation temperature (°C)	Oxidation time (minutes)	Flow rate (SCCM)	Ramp rate (°C/min)	Ar purging (minutes)
NW1	650	45	300	15	30
NW2	715	45	300	15	30
NW3	850	5	300	15	30
NW4	850	45	300	15	30

Figure 3.17 | Nanotopography selection. Representative SEM of NW1-NW4 and table summarising the corresponding processing conditions used to fabricate each nanotopography. In each case, the initial Ti-6Al-4V substrate was machine polished using increasingly fine SiC grit sizes (50#, 500#, 1200#, 2000#, 4000#). All batches were annealed following thermal oxidation at 600°C for 30 minutes, using a ramp rate of 10°C/min. Pre-annealing was not performed. All batches were performed using acetone as the source of oxygen.

3.3.6 The effect of polishing on TiO_2 nanowire formation and homogeneity

The rate of oxide growth is known to decline with time, because the diffusion distance for oxygen species increases (Dinan, 2012). Therefore, surfaces with thicker initial oxide scales could be expected to show reduced nanowire growth compared to substrates with thinner oxide layers. As such, the effect of polishing on nanowire growth was investigated to identify the optimal processing conditions to generate homogeneous nanowire arrays reproducibly. This would also ensure consistency when investigating the bacterial response to nanowire arrays. Different polishing techniques were applied to Ti-6Al-4V discs before thermal oxidation. Thermal oxidation was performed using as-received Ti-6Al-4V, SiC polished Ti-6Al-4V and nano-diamond mirror polished Ti-6Al-4V. The formation and homogeneity of nanowires was compared on NW1-NW4 (Figure 3.18).

The surface topography of as-received Ti-6Al-4V substrates was found to consist of crater-like formations, several microns in diameter, and therefore a non-uniform surface on which to form nanowires. In contrast, SiC polished Ti-6Al-4V and nano-diamond polished Ti-6Al-4V displayed increasing smoothness. On NW1 nanoprotrusions had formed on all the titanium substrates, but the resulting morphologies were very different. On as-received Ti-6Al-4V, nanoprotrusions had formed around the edges of each crater, with little to no growth inside. Preferential growth was also observed on polished Ti-6Al-4V, where nanoprotrusions seemed to form in regions that resembled the outline of a crystal face. Interestingly, the coverage of nanoprotrusions appeared to be most uniform on SiC polished Ti-6Al-4V. This was somewhat unexpected as the starting nanotopography was not as smooth as polished Ti-6Al-4V.

On NW2, the formation of nanowires was more widespread on each titanium substrate. Nanowire growth on as-received Ti-6Al-4V had now taken place within the crater like structures, as well as around the edges. Interestingly, nanowires within the craters were more uniform and shared the same growth direction. Nanowire growth was more pronounced on nano-diamond polished Ti-6Al-4V, with nanowires having a greater homogeneity than on SiC polished Ti-6Al-4V. Nanowire growth had increased significantly on NW3 as-received Ti-6Al-4V but was not uniform in height and density. While nanowire growth was less pronounced on nano-diamond polished Ti-6Al-4V, the density and height profiles of nanowires were more uniform. Furthermore, the diameter of nanowires were more consistent on as-received and SiC polished Ti-6Al-4V than compared to nano-diamond polished Ti-6Al-4V. Comparable trends were observed in nanowire growth and homogeneity on NW4.

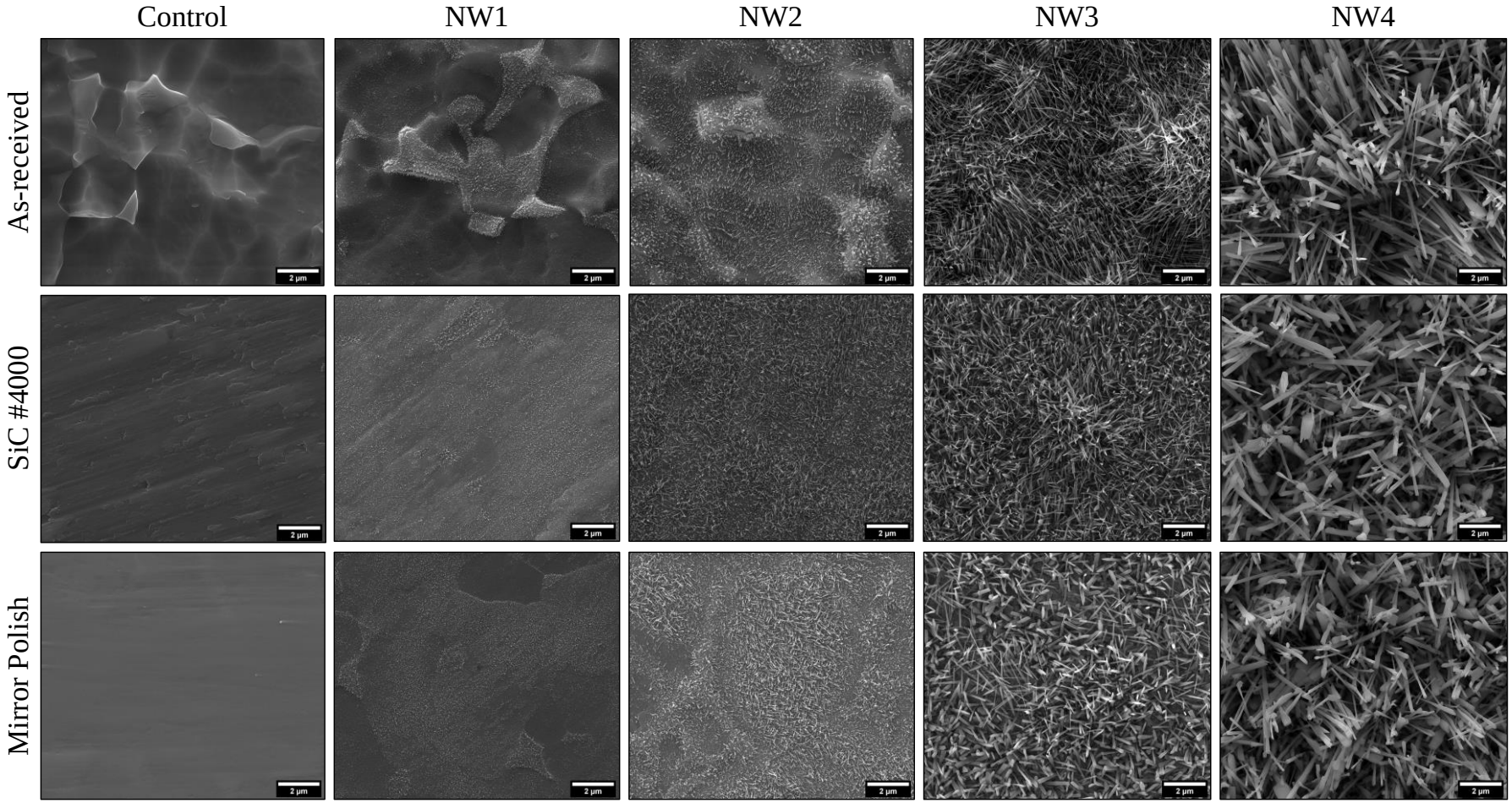

Figure 3.18 | The effect of titanium polishing on nanowire growth. Thermal oxidation was performed using as-received Ti-6Al-4V, SiC polished Ti-6Al-4V and nano-diamond mirror polished Ti-6Al-4V. The formation and homogeneity of nanowires was compared under the oxidation conditions for NW1-NW4. Representative micrographs of nanowire arrays NW1-NW4 grown on as-received Ti-6Al-4V, SiC #4000 paper polished and nano-diamond slurry polished are shown.

3.4 Discussion

The proposed mechanism of nanowire growth in this study is indicated in Figure 3.19. At high temperature, acetone decomposes into CO and $\cdot CH_3$. CO absorbs onto the Ti-6Al-4V oxide layer where TiO_2 and TiC nanoparticles may form. TiO_2 and TiC nanoparticles are deposited epitaxially with time, meaning that longer oxidation durations result in larger nanostructures. During this surface reaction, $\cdot CH_3$ radicals are degraded into hydrogen and carbon. Carbon is deposited onto the TiO_2/TiC core, forming a shell.

3.4.1 The effect of oxygen atmosphere on nanowire growth

The growth of nanowires on Ti-6Al-V4 substrates by thermal oxidation was strongly influenced by the type of oxidising atmosphere. Nanowire growth was most prominent when acetone was used as the oxygen-bearing source. This was followed by acetic acid, which generated a mixture of nanowires and multifaceted crystals. In contrast, nanowire formation was not observed under ambient air or Ar atmospheres. In the case of ambient air, agglomerated oxide scales had formed across the entire surface, while in the presence of Ar, surfaces were dominated by multifaceted crystals. These differences are most likely attributable to the availability of oxygen within the gaseous phase. There are three regions where oxidation reactions could take place: 1) Ti-TiO_2 interface, 2) TiO_2 surface or 3) within the TiO_2 film. Considering that temperature and oxide thickness were the same here, the diffusion rate of titanium atoms and oxygen species may be assumed as constant, leaving only the concentration of oxygen as a determining factor. Thus, the following model could explain the differences in observed morphology. Under ambient air the diffusion of oxygen species is expected to dominate the growth process. This is because the relative quantity of oxygen species in the vapour phase is higher, meaning that oxidation mainly occurs at the Ti-TiO_2 interface, resulting in a highly agglomerated oxide scale. In contrast, under acetone and acetic acid atmospheres, the availability of oxygen species in the vapour phase is much lower. This means that diffusion of titanium atoms from the bulk substrate governs the growth process, resulting in preferential oxidation at the TiO_2-gas interface. Furthermore, acetone has fewer oxygen species per molecule than acetic acid, and therefore is predicted to generate the lowest concentration of oxygen species within the vapour phase, which may account for nanowire growth being most pronounced under acetone. These results are consistent with previous studies (Peng et al., 2005; Peng and Chen, 2004). Regarding the growth of multifaceted crystals in Ar, it is clear that some oxidation had occurred. Nevertheless, this did not hinder the fabrication of nanowires using acetone vapour.

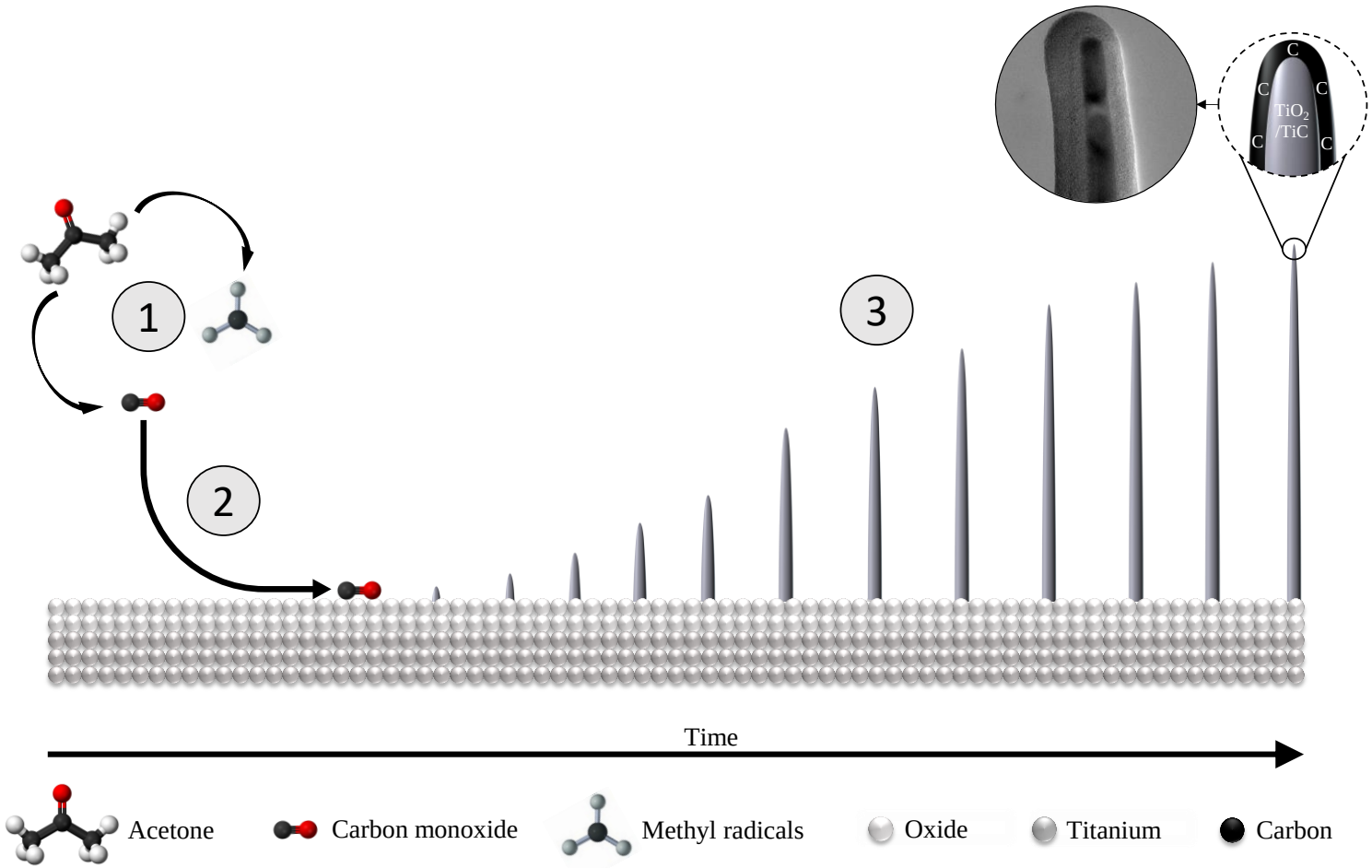

Figure 3.19 | Schematic illustration of the proposed mechanism of nanowire growth on Ti-6Al-4V. 1) Thermal decomposition of acetone results in the production of CO and $\cdot CH_3$. 2) CO is adsorbed on to the Ti-6Al-4V substrate where titanium reacts with carbon or oxygen to form TiC and TiO_2. 3) Provided that a continuous source of oxygen is supplied, nanowires will continue to grow epitaxially with time. Aluminium oxide is proposed to restrict nanowire growth to the vertical direction and carbon is deposited as a decomposition by product (Hu et al., 2010; Zhang et al., 2012).

3.4.2 Core-shell nanowire morphology

Individual nanowires displayed conical shapes, owing to the decreasing diameter of the core and shell from the base to the tip. These findings are contrary to previous studies, which have reported that the width of the core remained constant while the diameter of the shell reduced (Hu et al., 2010; Huo et al., 2008). Line scanning EDX analysis confirmed the presence of titanium, oxygen and carbon within the core, most likely attributable to a combination of TiO_2/TiC. These findings are broadly consistent with previous studies. Huo and colleagues performed thermal oxidation of cp titanium in the presence of acetone and generated nanowires with TiO_2 in the core and carbon in the shell (Huo et al., 2008). By comparison, thermal oxidation of Ti-6Al-4V has been reported to generate nanowires with TiC in the core and carbon in the shell (Hu et al., 2010; Zhang et al., 2012). On the basis of these data, it is likely that titanium reacts with both oxygen and carbon, forming a mixture of TiO_2 and TiC. However, the exact ratio of these was not determined in this study.

Regarding the formation of conical shape nanowires by thermal oxidation, two mechanisms have been proposed: 1) carbon precipitation rate and 2) hydrogen etching rate. The decomposition rate of $\cdot CH_3$ radicals is temperature dependent, thus, the precipitation of carbon atoms occurs faster at the base of nanowires where the temperature is higher than at the tip. As such, the deposition of carbon reduces from base to tip. Furthermore, hydrogen atoms generated from the thermal decomposition of $\cdot CH_3$ radicals will move upwards owing to their light mass, thereby resulting in a stronger etching effect at the tip (Huo et al., 2008).

Interestingly, while a carbon shell was observed in this investigation and has been reported in other studies using comparable thermal oxidation processes (Hu et al., 2010; Huo et al., 2008; Zhang et al., 2012), one study reported no carbon layers following thermal oxidation of titanium substrates using acetone as the oxygen source (Peng and Chen, 2004). This suggests that acetone was not the sole oxygen source, since thermal decomposition of acetone generates carbon, which could not have been removed without sufficient oxygen.

3.4.3 The effect of post-annealing on nanowire morphology and composition

Following the removal of carbon by post-annealing, the density and coverage of nanowires did not appear to change significantly, but the individual morphologies of nanowires had changed. Of note, core-shell nanowires had transformed into two distinct types: RLNW with uniform diameter, and HSNLNW with increasing diameter from base to tip. Of note, nanotopographies generated by 5 minutes oxidation comprised largely of CLNW that are more desirable shapes for bactericidal surfaces. Although the elemental composition of RLNW and HSNLNW was the same, the lattice spacings appeared to differ, displaying lattice constants of rutile and anatase planes respectively. Although XRD analysis would be required to confirm this, it does not rule out the possibility that annealing may transform the crystallinity of TiO_2 nanowires from rutile to anatase, since anatase is typically formed at lower temperatures than rutile (Diebold, 2003) However, as the lattice spacings of core-shell nanowires could not be measured, the precise reason for this is unclear.

3.4.4 Surface wettability

Antibiofouling surfaces have been proposed as a non-drug based strategy to prevent bacterial adhesion and biofilm formation on medical implants (Banerjee et al., 2011). This concept is based on the Lotus effect, which describes the process by which water droplets easily roll off the Lotus leaf. The self-cleaning mechanism of Lotus leaves is caused by their hierarchical micro and nanotopography combined with the cuticle wax layer, which instil superhydrophobic wetting (WCA≥150°) (Marmur, 2004). Superhydrophobicity has been reported to reduce the force of adhesion between bacteria and solid surfaces (Zhang et al., 2013) and prevent bacterial contact (Crick et al., 2011), furthermore, increased surface roughness has been shown to reduce the wetting properties of nano- and microtextured materials (Shiu et al., 2004; Yoshimitsu et al., 2002; Zhang et al., 2004). Thus, the wettability of nanowire arrays was determined, as this could have influenced the attachment behaviour of bacteria to nanowires, and in turn, the contact killing properties. To investigate this, contact angle measurements were performed to determine the wettability of core-shell nanowire surfaces compared to control surfaces. Control surfaces generally displayed hydrophilic contact angles (<90°), while core-shell nanowire surfaces displayed hydrophobic wetting (>90°). Following the removal of carbon, the nanowire surface became superhydrophilic (<5°) (Zhang et al., 2013).

There are two models used to describe the contact angle formed on a rough surface, the Wenzel model and the Cassie-Baxter model (Shiu et al., 2004; Zhang et al., 2013):

The Wenzel model:

$$cos\theta^* = r'cos\theta$$

compares the WCA formed on rough (θ^*) and smooth versions (θ) of the same material, and links them by a roughness coefficient (r`). This model predicts that when the smooth surface is hydrophilic (WCA<90°), then increasing the surface roughness will enhance the wettability. In contrast, when the smooth surface is hydrophobic (WCA>90°), then increasing the roughness will reduce wettability. Thus, the Wenzel model is not suitable to explain the wetting behaviour of core-shell nanowire surfaces in this study, because the wettability decreases in comparison to the hydrophilic control Ti-6Al-4V surface. In contrast, the post-annealed nanowire surface can be explained by the Wenzel model, since wetting had switched from hydrophilic to superhydrophilic. Peng and Chen observed hydrophilic contact angles on TiO_2 nanowire arrays generated by thermal oxidation; however, the surface hydrophobicity increased with longer oxidation times (increased roughness) (Peng and Chen, 2004). Similarly, Bhadra and colleagues reported an increase in the WCA between as-received titanium discs (33°) and TiO_2 nanowire discs (73°) (Bhadra et al., 2015). In both of the above studies, the reduced wetting of nanowire surfaces was attributed to the ability of TiO_2 nanowires to trap air, as described by the Cassie and Baxter model.

The Cassie-Baxter model:

$$cos\theta^* = f\,(cos\,\theta + 1) - 1$$

has been proposed for cases where only parts of the solid interface are in contact with the liquid, where f denotes the proportion of wetted surface. In this case, the hydrophobic properties of a surface are attributed to the trapping of air between the nanostructures. Although this could partly explain the hydrophobic properties of core-shell nanowires in this study, it fails to clarify how nanowire surfaces became superhydrophilic following the removal of carbon, without significant changes in nanowire coverage and dimensions. Thus, we propose that it is the chemical composition of core-shell nanowire surfaces that influence wettability. The spreading of polar H_2O is more energetically favourable on TiO_2 as this is also polar, while carbon in non-polar.

3.4.5 Optimisation of nanowire growth parameters

By systematically changing the temperature and duration of oxidation, it was possible to modify the type of nanowire array formed. In general, the average length and diameter of nanowires could be increased by raising the temperature and duration. This also led to reductions in nanowire density, thereby increasing the tip-to-tip spacing. Nevertheless, nanowire growth did not occur indefinitely, and beyond 850°C, larger multifaceted crystals had formed. Nanowire growth was generally confined between 650°C and 850°C.

The effects of temperature on nanowire growth are likely attributable to the relative diffusion rates of titanium and oxygen species at different temperatures. As temperature is increased, the diffusion of titanium species is expected to rise, meaning that oxidation is more likely to occur at the TiO_2 surface, which could account for enhanced nanowire growth from 650°C to 850°C. The formation of larger multifaceted crystals at 900°C suggests that the high temperatures favour oxidation at the Ti-TiO_2 interface, which could be due to the increased availability of oxygen in the vapour phase or the increased diffusion of oxygen through the oxide layer. These observations are consistent with the reported literature. Lee and colleagues observed comparable nanowire morphologies on Ti-6Al-4V. At 600°C, shorter nanowires were observed, and these had increased in length at 700°C. However, at 800°C, a combination of nanowires and faceted crystals were seen, while at 900°C, only faceted crystals were noted (Lee et al., 2010). Arafat and colleagues also noted the temperature dependent transition from nanowires to large multifaceted crystals between the ranges of 700°C to 900°C (Arafat et al., 2013).

The effect of oxidation duration on nanowire growth was less pronounced than oxidation temperature. Nevertheless, the same general trends were observed. Examples of the effects of oxidation duration on nanowire growth are limited, and most studies report on oxidation of titanium and titanium alloys at single time points (Arafat et al., 2013; Hu et al., 2010; Huo et al., 2008; Lee et al., 2010; Peng et al., 2005; Peng and Chen, 2004; Zhang et al., 2012). In contrast to oxidation temperature and duration, the flow rate of Ar carrier gas through liquid acetone was found to have negligible effects on the growth of nanowires between 100-500 SCCM. These observations are consistent with previous studies that have investigated the effect of Ar flow rate on nanowire growth. Lee and colleagues reported no significant change to nanowire growth on both Ti-6Al-4V and β-Ti (5-5-5), using flow rates of 200, 500 and 1000 mL/min (Lee et al., 2010). However, at lower flow rates of 50 SCCM, larger crystals were generated, similar to the morphologies observed on Ti-6Al-4V oxidised under Ar atmosphere.

Pre-annealing of Ti-6Al-4V substrates at temperatures exceeding the beta-transus (980°C) resulted in a general increase in the crystal grain size. This is attributable to Ostwald ripening, which describes the process in which smaller crystal grains are dissolved at high temperature, leading to a release of atoms that are redeposited onto larger, more energetically favourable crystals, thus resulting in a general grain enlargement (Yao, 1993). Although there was an increase in the average size of crystal grains between 1000°C to 1200°C, the exact size, shape, phase and orientation of crystals was variable and could not be precisely controlled. This is due to the dynamic changes in crystal structure that occur during heating and cooling. For example, upon cooling from temperatures above the beta-transus, secondary alpha phases will begin to nucleate within the beta phase crystals, such as acicular and lamella alpha (Gammon et al., 2004). This grain structure was evident on nanowire surfaces, which had periodic nanowire rows, typical of aforementioned secondary alpha crystals. Furthermore, it is likely that the formation of secondary alpha phases prevented the large-scale formation of aligned nanowires. Therefore, pre-annealing Ti-6Al-4V did not improve the efficiency of nanowire growth and was not able to reproducibly increase nanowire alignment. As such, this step was not included in routine surface fabrication.

The initial surface topography was found to strongly influence the growth of nanowires by thermal oxidation. In general, nanowire growth on as-received titanium substrates was non-uniform, while SiC polished surfaces led to more homogeneous nanowire arrays. This is likely to have been caused by the crater-like formations on as-received substrates. An interesting observation was made at 650°C, whereby nanowire growth appeared to be enhanced in specific regions on all surfaces, but most notably on as-received and polished substrates. Preferential growth could be attributed to the different α/β phases within Ti-6Al-4V. Indeed, nanowires have been shown to grow more within β phase crystals (Lee et al., 2010). Alternatively, the oxide scale thickness may vary across the substrates, which could be expected to result in less nanowire growth in regions of increased oxide thickness (Dinan, 2012). These effects were less pronounced at other temperatures, which is likely due to the increased growth of nanowires across the entire surface. SiC polished Ti-6Al-4V was selected as the initial surface for oxidation reactions, as this provided optimal nanowire coverage, uniformity and reproducibility.

CHAPTER 4

Bacterial response to titanium dioxide nanowire arrays

4.1 Introduction

Bacterial viability is broadly defined as the percentage of living cells within a whole population. Determination of this parameter is essential for identifying candidate materials for novel antibacterial implants. As such, a number of *in vitro* methods have been developed to determine bacterial viability on nanostructured materials; these are broadly classified as culture based, biochemical and microscopic investigations (Doll et al., 2016). While it is common for antimicrobial agents to induce bacterial cell death, this is not always the case; in many instances, the physiological capabilities of bacteria may be impaired without directly causing cell death; this impacts bacterial vitality (Kwolek-Mirek and Zadrag-Tecza, 2014). To gain a comprehensive understanding of the antibacterial properties of nanotopographies, it is important to investigate both viability and vitality. In this study, to determine whether TiO_2 nanowire arrays possessed antibacterial properties, a range of culture based, biochemical and microscopic investigations were employed, including commercially available assays such as LIVE/DEAD™*BacLight*™ staining, BacTiter-Glo™ and RealTime-Glo™.

To date, LIVE/DEAD staining has been the most widely used assay to determine the bactericidal performance of natural or synthetic nanotopographies (Diu et al., 2014; Fisher et al., 2016; Hasan et al., 2013; Hazell et al., 2018a; Ivanova et al., 2013, 2012). This assay utilises two fluorophores, SYTO9 and PI, which intercalate with DNA leading to the emission of green and red fluorescent signals respectively. SYTO9 is able to permeate live and dead bacterial cells, upon which DNA binding results in strong green fluorescence (λ=498 nm). PI displays a higher affinity for DNA but can only enter bacteria with structurally compromised envelopes, upon which SYTO9 is displaced from DNA and PI binding results in a strong red fluorescence (λ=617 nm) (Stocks, 2004). Thus, LIVE/DEAD staining determines the permeability of bacterial envelopes, which is an indicator of bacterial viability. Given its mechanism of action, this assay has been widely used for testing the bactericidal activity of natural and synthetic nanotopographies that are proposed to physically rupture the bacterial cell envelope (Ivanova et al., 2012; Pogodin et al., 2013). In this context, LIVE/DEAD staining has exclusively been used for end point fluorescence microscopy, where fluorescence micrographs are used to count the relative proportions of green (live) and red (dead) bacteria, which can provide an estimation of killing efficacy per unit area (Figure 4.1).

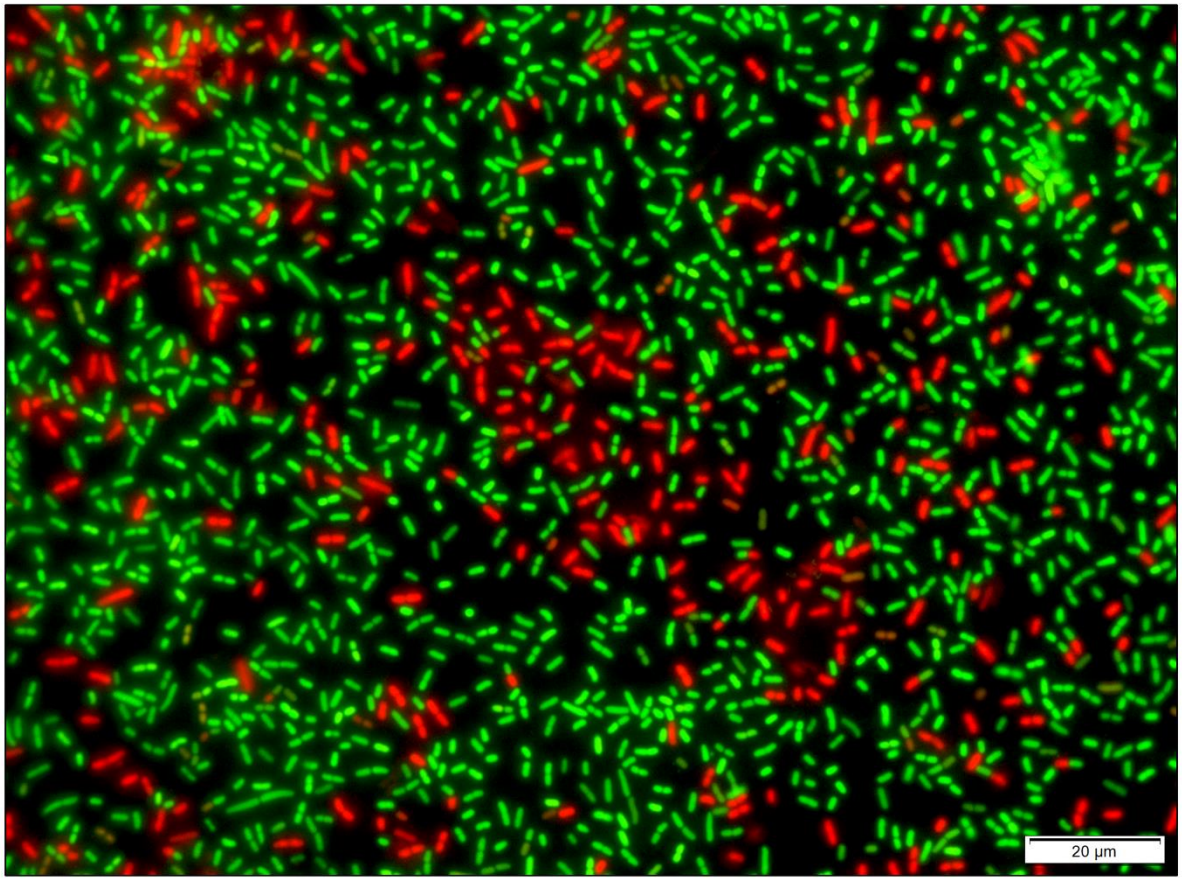

Figure 4.1 | Fluorescence micrograph of *K. pneumoniae* stained with LIVE/DEAD fluorophores SYTO9 and PI. Bacterial viability is inferred by envelope permeability. Green cells are categorised as live, or viable, while red cells are considered to be dead, or non-viable.

Determination of bacterial viable counts by colony forming unit (CFU) analysis (culture based method) is the second most common approach that has been used to determine the bactericidal performance of natural and synthetic nanotopographies (Ivanova et al., 2013; Mann et al., 2014; Nowlin et al., 2014). This method generally involves recovering bacteria from a test surface and plating serial dilutions of the suspension onto a suitable agar, which is then incubated to allow colonies to form and be counted. In contrast to LIVE/DEAD staining, CFU analysis measures the ability of bacteria to grow and divide, thereby providing a direct method to quantify the number of viable bacteria.

Very few studies have used biochemical methods to determine bacterial viability on natural and synthetic nanotopographies. Sjostrom and colleagues used PrestoBlue to determine *E. coli* viability on TiO_2 nanowire arrays produced by thermal oxidation (Sjöström et al., 2016). PrestoBlue contains a cell permeable resazurin molecule that forms a deep-blue solution. Inside metabolically active bacteria, resazurin is reduced by NADH, resulting in the formation of a red fluorescent molecule, resorufin. The accumulation of resorufin in solution is frequently assessed using a multi-well plate reader to measure the fluorescence emission (λ =590-615 nm), but it is also possible to measure absorbance (i.e. a colorimetric measurement), although this approach is far less sensitive (Riss et al., 2016).

In contrast to LIVE/DEAD and CFU analysis, PrestoBlue provides an indication of redox potential, which is directly related to metabolic activity. However, the quantity of resorufin is proportional to viable cell numbers and as such, PrestoBlue is marketed as a viability assay, not a vitality assay. Alternative biochemical methods, BTG and RTG, were employed in this study to determine bacterial viability on TiO_2 nanowire arrays. Like PrestoBlue, BTG and RTG provide an indication of metabolic activity, which can be directly related to the number of viable bacteria. However, rather than generating a fluorescent signal, these assays are luminescence based, involving luciferase enzymes. BTG is a lytic, end-point assay that generates a luminescent signal proportional to the intracellular concentration of ATP, which is directly proportional to the number of viable bacteria. Similarly, RTG produces a luminescent signal, which correlates to the number of viable cells. However, this assay is not lytic and generates luminescence based on cellular redox potential. To date, no studies have used BTG or RTG to determine the viability of bacteria in contact with natural or synthetic nanotopographies.

Although bacterial viability and vitality assays can aid in determining the antibacterial performance of different nanotopographies, in isolation they provide limited insight into the underlying mechanism of action. Genomic and proteomic methods could provide more detailed information regarding the molecular changes that occur in bacteria that attach to TiO_2 nanowires, providing new perspectives on the precise mechanistic basis of cell death. Nevertheless, only a small number of studies have used such approaches to date (Kang et al., 2008; Rizzello et al., 2012, 2011). This study utilised quantitative proteomic analysis to determine molecular changes in bacteria incubated on nanowire arrays.

4.2 The effect of TiO_2 nanowires on bacterial viability

4.2.1 Viable count analysis

CFU analysis is one of the most widely used microbiological tools to determine bacterial viability, forming the basis of most international standard protocols. In this study, viable counts were assessed using a modified version of ISO-22761, which outlines a standardised methodology for quantifying antimicrobial activity on polymer and other non-porous surfaces. Nanotopographies NW1-NW4 were incubated for 24 hours with 10^6 *S. aureus* or *E. coli* cells. Following incubation, bacterial suspensions were then recovered and plated for enumeration by viable count (Figure 4.2). Staining of bacteria with SYTO9 pre- and post-washing enabled the percentage recovery to be estimated (Figure 4.3-4.4).

Following 24 hours incubation, the numbers of viable *S. aureus* cells recovered from NW2 were approximately 10-fold lower than from the control while *S. aureus* cells recovered from NW3 and NW4 were approximately 100-fold lower than control, while comparable cell numbers were recovered from NW1 compared to control. For *E. coli*, significantly lower numbers of viable cells were recovered from NW1-NW4 than from the control, with approximately 10-fold fewer cells from each of the nanotopographies.

One potential limitation of this approach was that washing may have been insufficient to fully remove bacteria from the titanium surface, particularly in the presence of nanowires. To explore this possibility, the SYTO9 signal emitted from each titanium disc was measured in a microplate reader before and after washing, and the percentage change in fluorescence emission was used to estimate bacterial recovery. Each surface was also visualised by fluorescence microscopy. Bacterial recovery was found to be inversely proportional to nanotopography roughness, resulting in lower percentage recoveries from nanowire discs compared to control discs (Figure 4.3). The emission profiles for control and NW1 surfaces were comparable for both *S. aureus* and *E. coli*, but the signals emitted from NW3-NW4 implied that <50% of the bacteria were removed by washing. In general, fluorescence microscopy indicated a similar trend (Figure 4.4). Since it was clear that all surfaces remained heavily colonised following washing, this significantly diminished the accuracy of the viable count data.

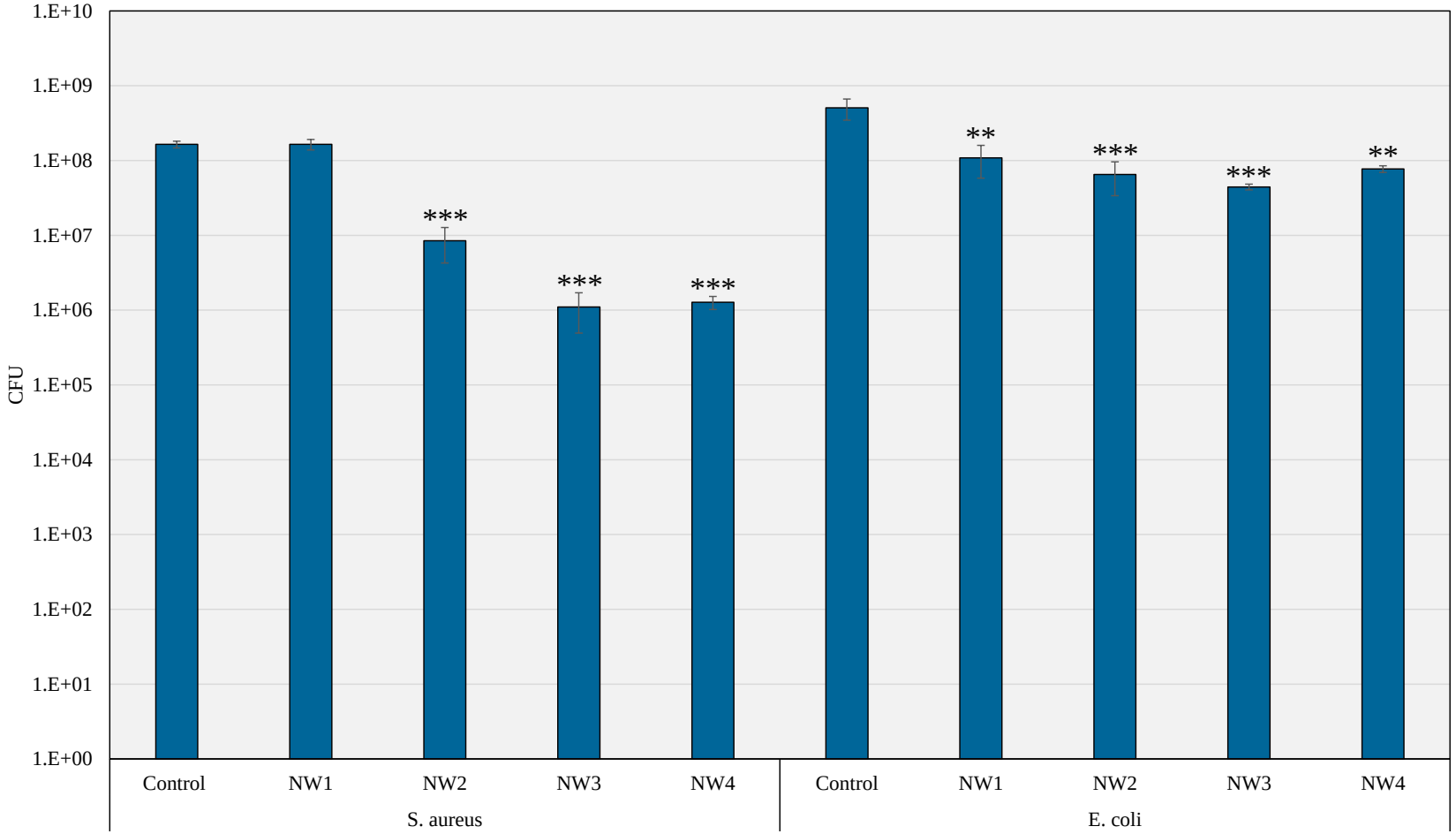

Figure 4.2 | Determination of viable bacteria from nanowire surfaces. *S. aureus* (a) or *E. coli* (b) were incubated for 24 h on control or nanowire (NW1-NW4) surfaces and then total viable counts were determined. Values given are mean ± standard deviation. **P<0.01, ***P<0.001 compared to control, as determined by one-way ANOVA with post-hoc Tukey HSD; n=3 performed in triplicate.

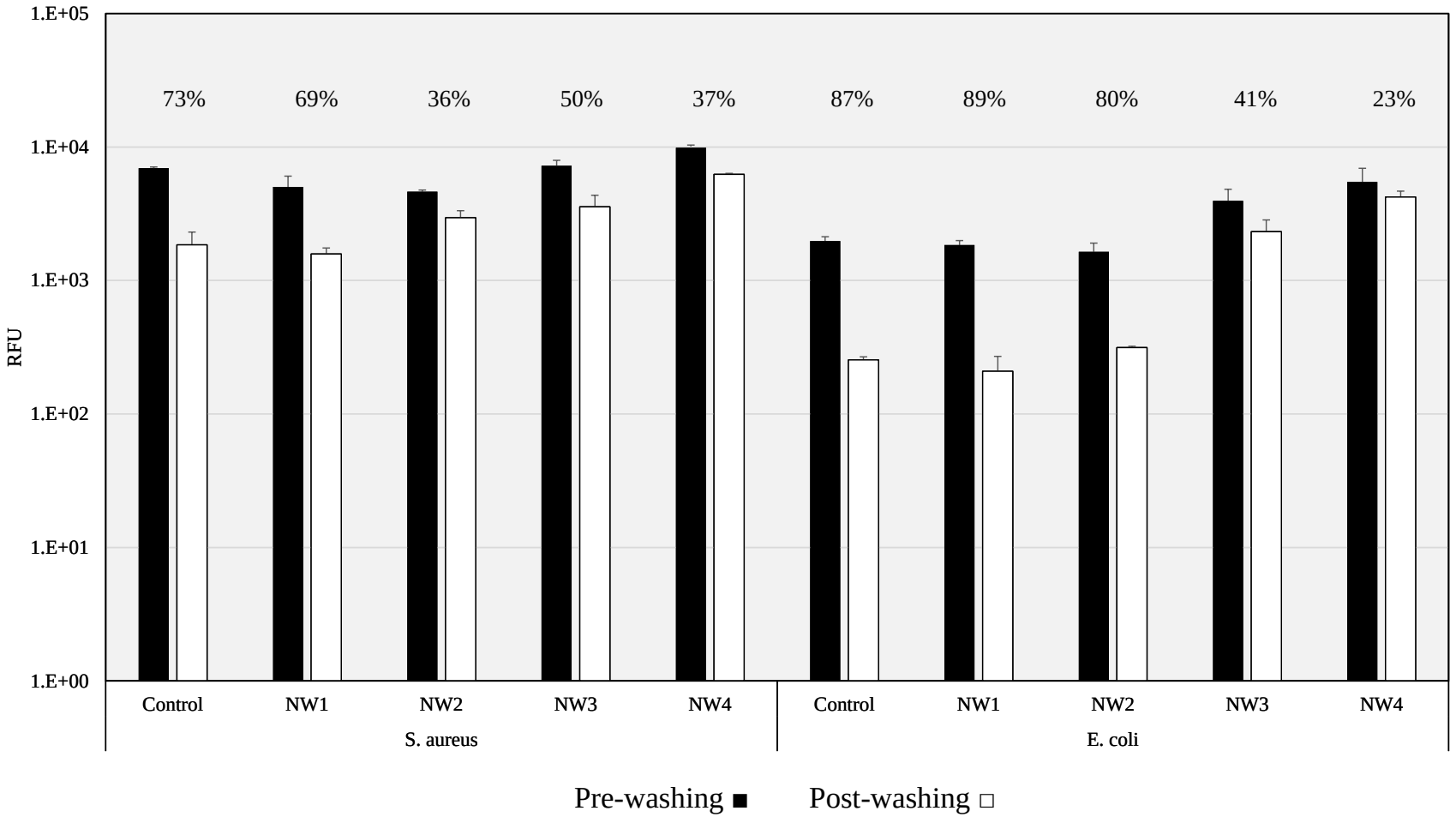

Figure 4.3 | Plate reader measurments for bacterial recovery from nanowire surfaces compared to control. *S. aureus* or *E. coli* were incubated for 24 h on control or nanowire (NW1-NW4) surfaces prior to washing. SYTO9 staining was used to measure total biomass before and after washing. The change in SYTO9 emission was used to estimate the percentage recovery of bacteria from each surface, as indicated. Values given are mean ± standard deviation; n=2 performed in triplicate.

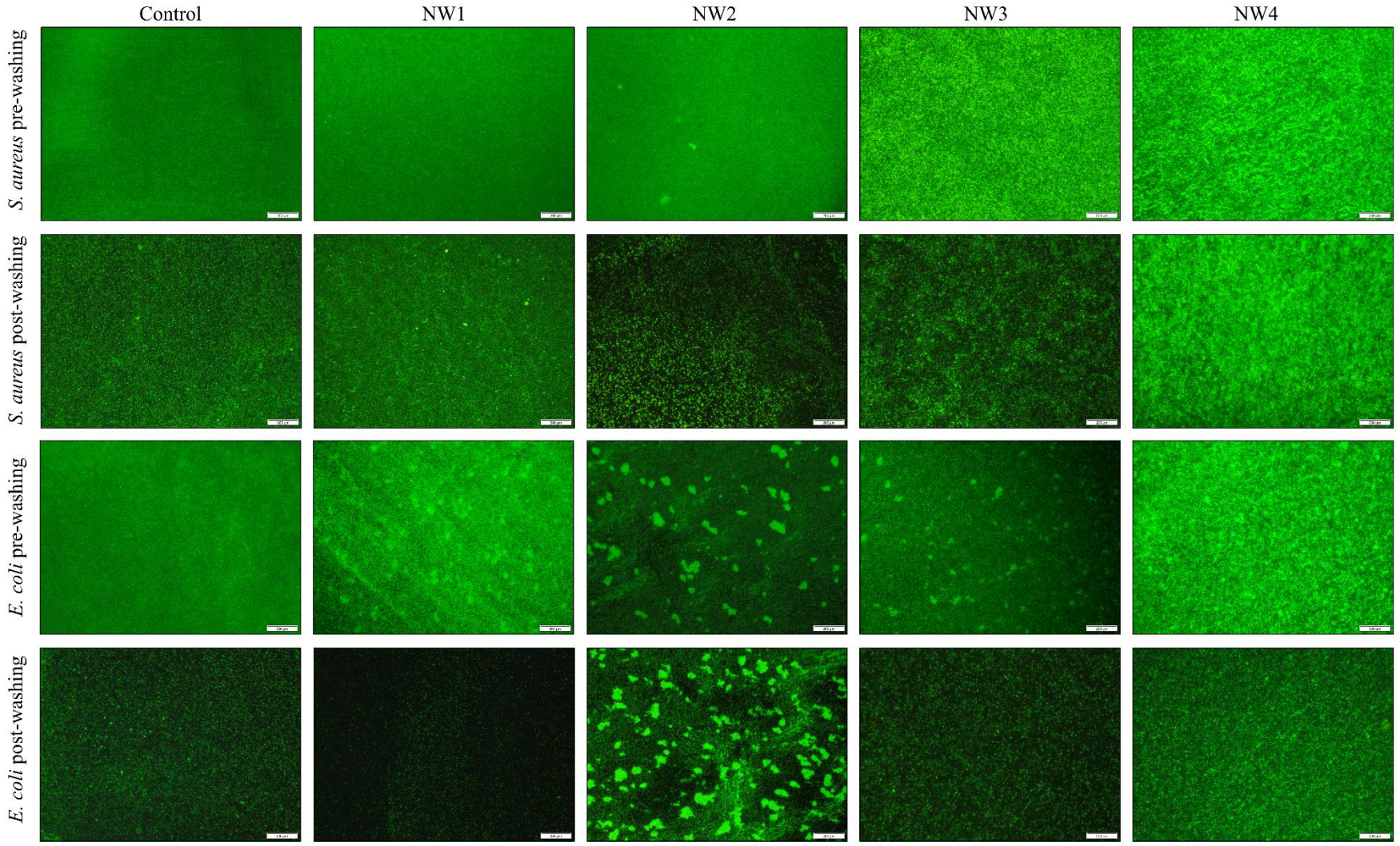

Figure 4.4 | Fluorescence microscopy for bacterial recovery from nanowire surfaces compared to control. *S. aureus* or *E. coli* were incubated for 24 h on control or nanowire (NW1-NW4) surfaces prior to washing. Fluorescence micrographs of each surface were taken pre- and post-washing. SYTO9 fluorescent labelling was used. Scale bar = 200 μm.

4.2.2 LIVE/DEAD™ *BacLight*™ analysis

The bactericidal effects of cicada wings were first observed in *P. aeruginosa*, where individual cells were found to have spread between the nanopillar arrays. This effect was reported to occur almost instantaneously, with the majority of cell death observed within 5 minutes of initial seeding (Ivanova et al., 2012). Furthermore, bacterial cell death observed on dragonfly wings was also found to be highest shortly after attachment (<3 hours), with average killing rates of 450,000 cells $min^{-1}cm^{-2}$ reported against Gram-negative (*P. aeruginosa*) and Gram-positive (*S. aureus* and *B. subtilis*) bacteria (Ivanova et al., 2013). Considering the high killing rates observed in previous studies, the biomimetic TiO_2 nanowires in this study could be expected to elicit bacterial cell death over similar time frames. As such, LIVE/DEAD staining was used to investigate the permeability of *S. aureus* and *E. coli* cells after 3 hours incubation, as a first possible indication of envelope damage and bactericidal action. *S. aureus* and *E. coli* were selected as model Gram-positive and Gram-negative bacteria respectively, as they are commonly isolated in PJIs (Pozo and Patel, 2009; Sendi et al., 2010). In line with the time points used in previous studies, *S. aureus* and *E. coli* were incubated on TiO_2 nanowire arrays (NW1-NW4) and flat control surfaces for 3 hours prior to dual staining with SYTO9 and PI. Prior to qualitative fluorescence microscopy, a multi-well plate reader was used to record the emission of SYTO9 and PI fluorescence from each surface, thereby providing a representative signal from the whole bacterial population.

4.2.2.1 Optimisation of LIVE/DEAD staining for plate reader measurements

Prior to fluorescence measurements, LIVE/DEAD fluorophores were optimised for plate reader analysis. Importantly, the background signals attributed to SYTO9 and PI auto-fluorescence, titanium surfaces, multiwell plates and nutrient media were determined. These signals could then be subtracted from the raw data to reveal the exact signal intensity originating from the bacterial populations. To begin, an empty black 24-well plate was exposed to the excitation wavelengths of SYTO9 and PI. Although no SYTO9 or PI were inside the wells, this determined whether there was any variation in signal detection across the plate reader, which could result in false positive or false negative data. A black 24-well plate was selected, as this minimised background signals and cross talk compared to white 24-well plates (https://www.promega.co.uk/resources/pubhub/which-plates-to-choose-for-fluorescence-and-luminescence-measurements/).

Figure 4.5a shows the relative fluorescence units (RFU) of SYTO9 and PI generated from each well inside an empty black 24-well plate. While the background RFU from SYTO9 and PI appeared to be quite high, it is important to note that these values were not normalised against a reference signal and therefore, are purely based on instrument response. Rather, more important is that the variation in signal emission was minimal between wells, as is evident from the low standard deviations from each row and column. The same measurements were performed in the presence and absence of TiO_2 nanowire arrays (NW1-NW4), flat titanium controls, SYTO9, PI and nutrient media (Figure 4.5b). There were several important findings from this: 1) In the presence of a reference signal (i.e. SYTO9 or PI only), the background RFUs from empty wells were low (<300 RFU). This was also observed for wells containing titanium surfaces only, which were generally lower than the RFUs of empty wells; 2) SYTO9 and PI autofluorescence was higher than the background RFUs from empty wells but the absolute signals remained comparatively low (<1600 RFUs). Furthermore, LB broth generated a comparable background signal. Together, these data indicate that autofluorescence from broth or fluorophores only would not have a significant effect on assay sensitivity or well cross-talk; 3) Cross signalling occurs when fluorophores have overlapping emission and excitation spectra; for example, an emission signal could be detected from PI under the excitation wavelength of SYTO9. In this study, under SYTO9 excitation wavelengths, the RFUs generated from PI remained below background RFUs. Furthermore, under PI excitation wavelengths, the RFUs generated from SYTO9 were comparable to background RFUs. This confirmed that background due to cross signalling was minimal. However, reductions in emission signal intensity were observed when SYTO9 and PI were added in combination; 4) When SYTO9 and PI fluorophores were added to LB broth only, the emission signal intensity of SYTO9 and PI increased substantially when excited at their respective wavelengths. This effect was further enhanced in the presence of titanium surfaces. Furthermore, it was evident that some titanium surfaces, particularly NW2, generated lower fluorescent signals than other titanium surfaces, suggesting a possible quenching effect. These findings highlighted the need to include internal controls for surface testing to account for variation in emission signal intensity between different titanium substrates, and to factor in the significant background signals that originated from LB broth in the presence of fluorophores.

a

SYTO9		Well column (RFU)						
Well row		1	2	3	4	5	6	SD
	A	35751	36220	36844	36058	36195	35475	426
	B	36277	37262	37043	36967	38099	35551	795
	C	35666	37080	36497	36026	37481	34985	841
	D	36645	36536	35897	36831	36085	34634	732
SD		399	417	435	431	854	374	

PI		Well column (RFU)						
Well row		1	2	3	4	5	6	SD
	A	38000	38023	38222	37790	37595	37544	242
	B	37369	37684	38067	37589	37947	37573	236
	C	37568	37587	37382	37143	37782	37196	226
	D	37603	37128	37957	38338	37220	37063	468
SD		229	320	317	429	271	220	

b

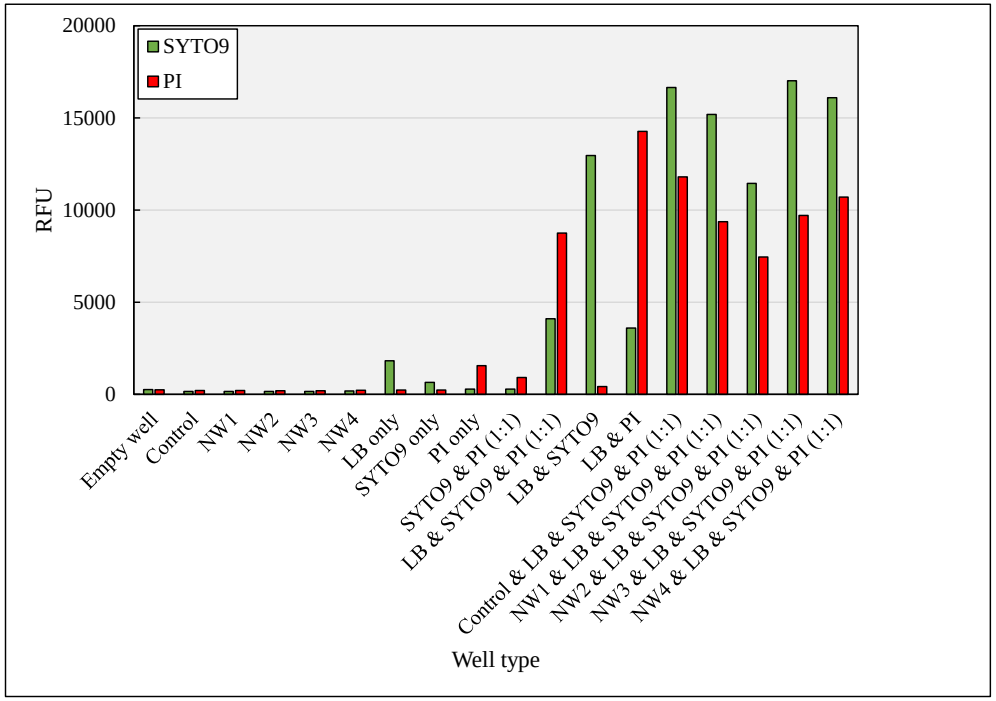

Figure 4.5 | Optimisation of LIVE/DEAD stain for multiwell plate reader measurements. The background fluorescence from a single empty, black 24-well plate was measured at the emission and excitation wavelengths of SYTO9 and PI (a). The standard deviation for each column and row is shown. The background emissions from a single well attributed to titanium discs (control, NW1-NW4), LB broth only, 1X SYTO9 only, 1X PI only and combinations thereof were measured inside a black 24-well plate (b). Equal ratios of SYTO9 and PI are denoted by 1:1.

4.2.2.2 LIVE/DEAD staining analysis by multiwell plate reader

Consistent with the findings in the previous section, high background signals were attributed to SYTO9 and PI fluorophores in the presence of LB broth. Therefore, normalising the raw data against these background signals resulted in low overall RFUs and in most cases, negative values (Figure 4.6). This was somewhat surprising, as the starting densities of *S. aureus* and *E. coli* were relatively high (10^6 per 25 µL) and were clearly visible under the fluorescence microscope (Figure 4.7).

For *S. aureus,* following normalisation of SYTO9 emissions, all titanium discs (NW1-NW4 and control) showed negative values, yet fluorescence microscopy revealed a significant covering of *S. aureus* on each surface. The same general trend was observed for normalised PI emissions, with the exception of control and NW3 discs, which displayed positive values. Nevertheless, it was clear from fluorescence microscopy that the level of envelope damage was negligible in *S. aureus*, as indicated by the absence of PI staining. In line with the findings of the previous section, there was significant variation regarding the background emission intensity from each titanium surface. For example, control titanium discs exhibited the highest background emission for both SYTO9 and PI fluorophores, while the background emissions observed on nanowire discs were generally lower. In contrast, the background signals attributed to SYTO9 and PI were marginally lower for *E. coli* measurements, meaning that positive RFU values were recorded for most surfaces. Regarding SYTO9 emission, control discs showed the greatest intensity, followed by NW3, NW4, NW1 and NW2. However, the differences in SYTO9 emission did not reach statistical significance. For PI, the highest emission intensity was recorded from NW4 and this was followed by NW1, NW3, NW2 and control discs respectively. Nevertheless, these differences were not significant.

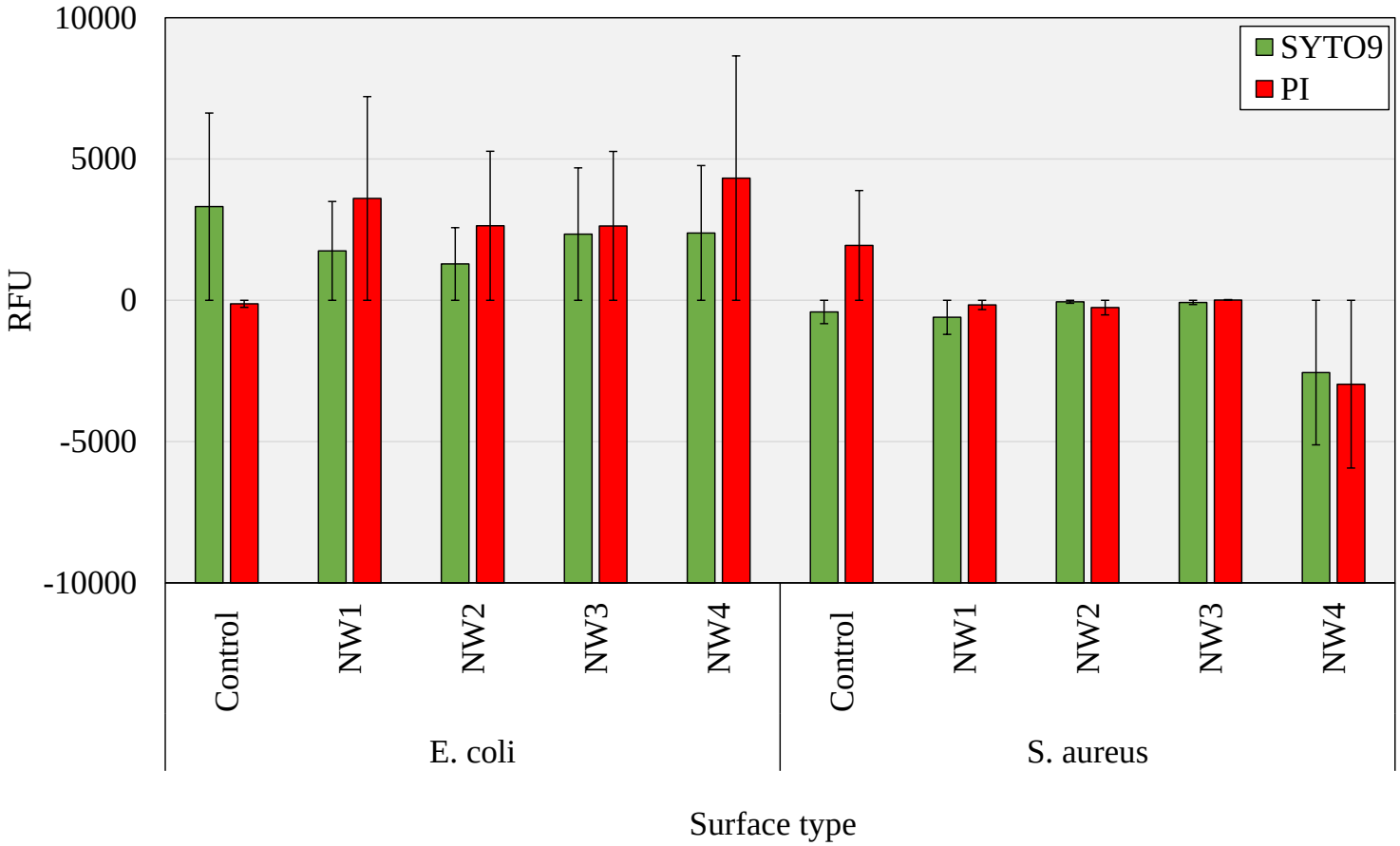

Figure 4.6 | Plate reader LIVE/DEAD staining analysis. SYTO9 and PI emissions from *E. coli* (n=3 performed in triplicate) and *S. aureus* (n=2 performed in triplicate) incubated on control and nanowire (NW1-NW4) discs for 3 h. RFU values are normalised against the background signals of SYTO9 and PI fluorophores in LB. Values given are mean ± standard deviation.

For *S. aureus*, the raw RFUs obtained for each surface type showed little intra- or inter-experimental variation, resulting in small standard deviations. Nevertheless, the high background signals attributed to SYTO9 and PI on each surface resulted in a low assay sensitivity (negative values). As a consequence, no meaningful conclusions could be derived from the multi-well plate reader data from *S. aureus.* In contrast, while the background signals for *E. coli* were lower, there was a greater degree of inter-experimental variation, resulting in larger standard deviations. Based on high background signals, and large inter-experimental variation, performing LIVE/DEAD analysis in a multi-well plate reader was deemed inaccurate, and could therefore not be used to make reliable conclusions on the antimicrobial efficacy of TiO_2 nanowire arrays. Nevertheless, fluorescence microscopy of surfaces was still considered for analysis.

4.2.2.3 LIVE/DEAD analysis by end point fluorescence microscopy

Titanium discs were visualised using a 10x objective lens to ensure a large area of the surface could be analysed. A total of three micrographs were taken per disc, which covered a surface area of 22.2 mm^2 and represented approximately 35% of the total disc area. For *S. aureus*, there was significant variation across individual titanium discs with respect to cell density, which further highlighted the need to acquire images of the entire surface to attain representative data. *S. aureus* density appeared to be highest on control titanium discs, followed by NW3. The coverage on NW1, NW2 and NW4 appeared to be comparable (Figure 4.7). The majority of the *S aureus* population emitted a green fluorescent signal, indicating that the envelope had not been damaged by TiO_2 nanowires; PI staining was negligible. Similarly, for *E. coli*, the majority of the population emitted a green fluorescent signal, suggesting that envelope integrity had not been compromised by TiO_2 nanowires. Furthermore, bacterial density was variable across individual surface types and different surface types. In general, NW4 displayed the greatest coverage and density, while control and NW2 showed the lowest (Figure 4.7). This was the direct opposite to the results for *S. aureus*. This discrepancy is most likely attributed to variation in experimental methodology. For example, prior to microscopy, to remove the non-adherent bacteria that were present within the meniscus, each titanium disc was dip-transferred into a solution of Tris/HCl. The manual nature of this step could be expected to influence the number of adherent bacteria, as the precise immersion force and time will likely have differed between each disc. Additionally, the differences in surface roughness and energy for each titanium disc will have introduced further variation. After the washing step, titanium discs were transferred to a glass slide and covered with a glass coverslip to prevent drying out and to arrange bacteria into a narrow focal plane at the surface. This step undoubtedly increased the hydrodynamic forces experienced at the interface, as bacteria were often seen to move under the microscope. Thus, it was unclear if those bacteria were representative of surface attached bacteria that had been removed, or bacteria in planktonic phase that were not removed by washing. It is also pertinent to consider the bleaching effects of SYTO9 and PI with time (Stiefel et al., 2015), meaning that the bacterial density may have appeared less, when in fact the fluorescence intensity had reduced. Although the differences observed in *S. aureus* and *E. coli* surface coverage were likely to be caused by the inherent variability of the end point methodology, it was clear that no bacterial envelope damage was observed in either *S. aureus* or *E. coli* after 3 hours.

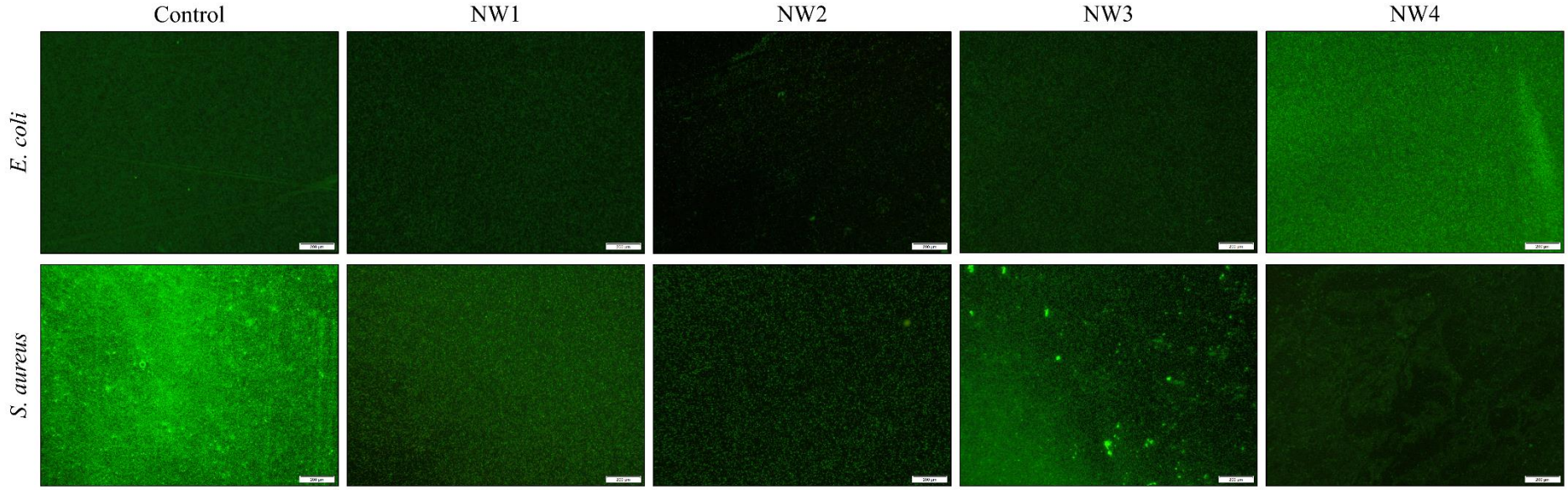

Figure 4.7 | End point fluorescence microscopy LIVE/DEAD staining. SYOT9 and PI dual colour fluorescence micrographs of *E. coli* and *S. aureus* incubated on control and nanowire (NW1-NW4) discs for 3 h. Micrographs were taken at three locations per disc, covering approximately 35% of the total surface area. Scale bar = 200 µm.

4.2.3 *In-situ* confocal laser scanning microscopy

Considering the limitations associated with LIVE/DEAD analysis for both plate reader measurements and end point fluorescence microscopy, a fluorescence microscope, equipped with automated tile scanning, image acquisition and environmental chamber, was used to monitor the growth of *S. aureus* and *E. coli* on TiO_2 nanowire arrays compared to control titanium surfaces at millimetre scales. Rather than using SYTO9, which is prone to bleaching effects (Stiefel et al., 2015), *S. aureus* and *E. coli* expressing GFP were utilised, meaning that the signal emission could be detected over time. The addition of an environmental chamber meant that titanium discs could be inoculated with bacteria and then left to incubate at 37°C under static conditions for up to 18 hours, thereby avoiding biofilm disruption caused by disc transfer and washing steps. Control and nanowire discs were imaged in triplicate, with the entire surface area being scanned every two hours. Following 18 hours, PI counterstaining was used to qualitatively measure bacterial envelope integrity. At this stage, NW2 and NW3 only were selected for further testing. There were two reasons for this: 1) The coverage of nanoprotrusions on NW1 was much lower than for NW2-NW4 and therefore, the bacterial response was likely to vary significantly based on surface location if using NW1; 2) The oxide layer present on NW4 was easily damaged and could often detach from the bulk Ti-6Al-4V substrate, resulting in significant intra-sample variability.

4.2.3.1 *In-situ* CLSM optimisation

At time point zero, the intensity of *S. aureus* and *E. coli* GFP signals was visibly stronger on control surfaces than nanowires, indicating that greater bacterial adhesion had occurred during pre-incubation to the controls (Figure 4.9-4.14). To determine whether this was a true effect, or if the fluorescence profile had been influenced by the nanotopography, the fluorescent signal emitted from control and nanowire discs was measured following inoculation with the same density of GFP expressing *S. aureus* or *E. coli* (Figure 4.8). The fluorescent signal detected from NW2 discs was consistently the lowest, for both *S. aureus* and *E. coli*. While these differences did not reach statistical significance, GFP detection was lower, which could indicate a possible GFP quenching effect. Of note, in the absence of any titanium disc, the fluorescent signal from *S. aureus* or *E. coli* was lowest, indicating that all surface types had enhanced the detection of GFP.

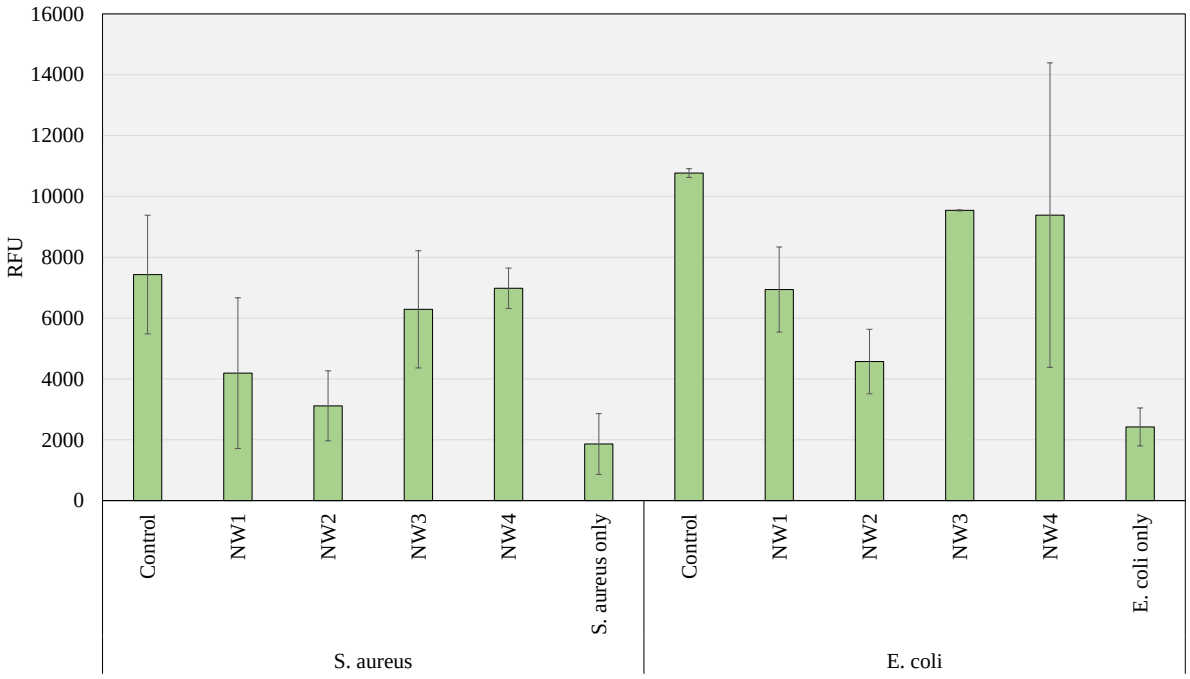

Figure 4.8 | GFP signal emission at time zero. *S. aureus* (a) or *E. coli* (b) strains expressing GFP were transferred to control or nanowire (NW1-NW4) surfaces and the fluorescence emission was measured immediately. Values given are mean ± standard deviation; n=3 performed in triplicate (*S. aureus*), n=2 performed in triplicate (*E. coli*).

4.2.3.2 *Staphylococcus aureus* time course

For *S. aureus*, GFP emission was most intense on control surfaces at time point zero. Between 0 hours and 10 hours, the GFP signal generated by *S. aureus* progressively decreased on control discs 1-3; this occurred simultaneously with marked reductions in density (Figure 4.9 – Figure 4.11, control disc 1-3). On control disc 1 and 2, *S. aureus* density appeared to reduce at the centre of each disc and gradually spread to the disc edge over 10 hours, as determined from the reduced intensity of GFP fluorescence at the centre of each disc (Figure 4.9-4.10). The density of *S. aureus* biofilm stabilised after 10 hours, with subtle increases in fluorescence observed around the edges until the end of the time course. A similar pattern had developed on control disc 3, but instead of the effect occurring at the disc centre, the intensity of GFP fluorescence was seen to reduce in the top right corner between 0 hours and 10 hours (Figure 4.11). Again, subtle increases in fluorescence were observed around this region between 10 hours and 18 hours. On control disc 1 and 2, PI staining had generally concentrated at the centre, corresponding to the regions of low GFP emission (Figure 4.9-4.10). In contrast, PI staining was strongest in the bottom left corner of control disc 3 (Figure 4.11). On all control discs, PI staining had also concentrated at the very edge.

The intensity of GFP fluorescence was noticeably lower in *S. aureus* that had been incubated on nanowire array NW2. Although the coverage and density of *S. aureus* did not visibly change throughout the time course, the fluorescence intensity reduced at each time point; however, this effect was very subtle due to the low GFP signal overall. In contrast to the control discs, the PI stain was observed across the entire surface of each NW2 disc, while the GFP signal remained low (Figure 4.9-4.11, Disc 1-3 NW2).

Throughout the time course, *S. aureus* GFP emission was least intense from nanowire disc NW3. In contrast to control and NW2 discs, for which *S. aureus* GFP emission was highest at 0 hours, the GFP signal appeared to be highest at 18 hours on NW3, yet the overall intensity of this signal was noticeably lower than for control and NW2. Like NW2, PI staining was more intense and widespread on NW3 than on the control discs, while the GFP signal was generally detected around the edges (Figure 4.9-4.11, Disc 1-3 NW3).

4.2.3.3 *Escherichia coli* time course

Likewise to *S. aureus*, the most intense GFP signal was detected from *E. coli* that had been incubated on control discs (Figure 4.12 – Figure 4.14, control disc 1-3). On all control discs, *E. coli* growth had steadily increased from 0 hours to 6 hours, with the GFP signal being most intense in lateral regions across the surface. This effect was most prominent on control disc 1, where *E. coli* had concentrated in an area spanning from the top left corner to the bottom right corner of the disc; similar formations were observed on control disc 2 and 3. Between 8 hours and 18 hours, the regions of highest *E. coli* density were seen to gradually disperse, leading to a more homogeneous distribution across the surface. Of note, between 8 and 18 hours, the density of *E. coli* on control disc 3 steadily declined in two areas within the bottom right quarter. This decline occurred in a similar fashion to the reductions observed for *S. aureus* that had been incubated on control discs. PI staining of *E. coli* resulted in an even distribution across the surface. This was in contrast to *S. aureus*, for which PI was seen to concentrate at the centre and edge of control discs.

The starting intensity of GFP fluorescence was noticeably lower for *E. coli* that had been incubated on nanowire discs NW2 and NW3 compared to control. The GFP signal emitted from *E. coli* was visible after 4 hours on NW2 discs (Figure 4.12-4.14, Disc 1-3 NW2). On NW2 disc 1, *E. coli* growth was initially seen along the bottom edge of the disc; this region displayed a uniform fluorescence intensity that continued to grow in size and spread vertically throughout the time course (Figure 4.12). A steady increase in *E. coli* growth was also observed on NW2 disc 2 and disc 3, with microcolonies being visible after 4 hours that exhibited greater levels of GFP fluorescence (Figure 4.13-4.14). *E. coli* microcolonies had increased in size and fluorescence by 6 hours and then were seen to progressively spread across the surface between 8 hours and 18 hours. Like on control discs, PI staining was evenly distributed on NW2 discs, but the intensity was lower. This is likely attributed to the reduced fluorescent signal from NW2 discs. As had previously been observed for *S. aureus, E. coli* GFP emission was most delayed on nanowire NW3 discs (Figure 4.12-4.14, Disc 1-3 NW3). The first signs of *E. coli* growth on NW3 discs were observed after 6 hours incubation. On NW3 disc 1, *E. coli* growth occurred laterally across the surface, spanning from the bottom left corner to the top right corner of the disc. While *E. coli* continued to grow, an air bubble had become visible after 8 hours and steadily increased in size, which may have impacted biofilm growth. On NW3 disc 2, microcolonies had formed on the surface after 6 hours and these continued to grow up to 10 hours before dispersing across the surface. On NW3 disc 3, *E. coli* growth occurred in a similar pattern to disc 1 and disc 2. In contrast to control and NW2 discs, PI staining intensity was noticeably higher on NW3.

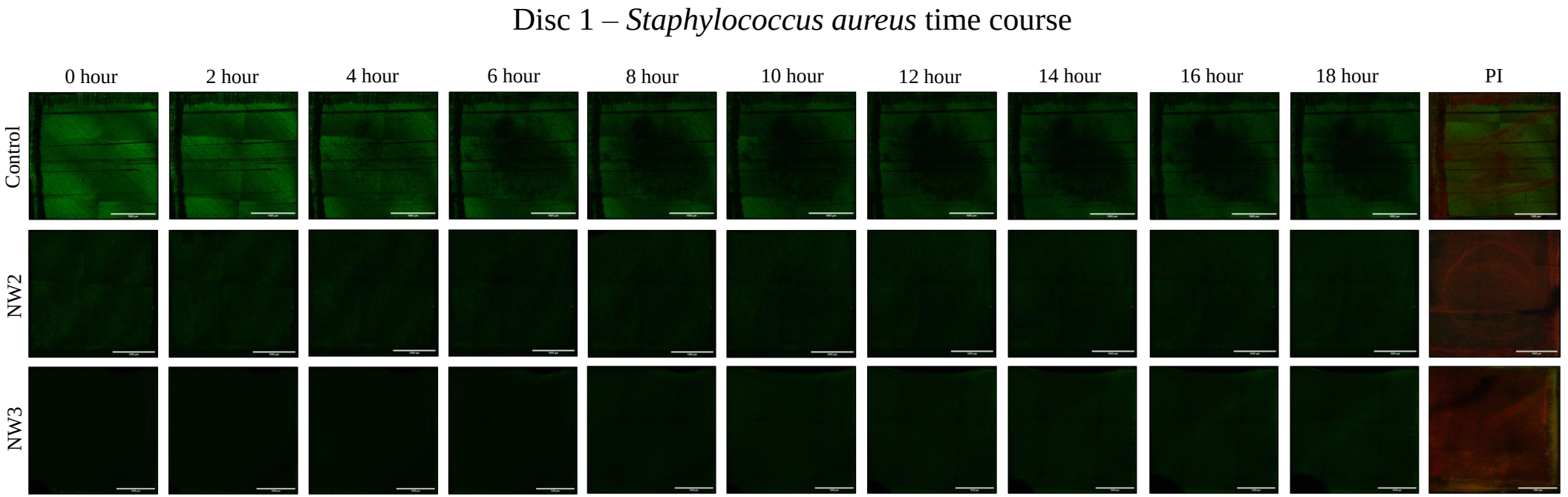

Figure 4.9 | Disc 1 – GFP *S. aureus* automated fluorescent microscopy. Fluorescence time course monitoring biofilm growth on control, NW2 and NW3 surface for 18 hours (2-hour increments). PI stain was added at 18 hours. Scale bar – 1000 µm.

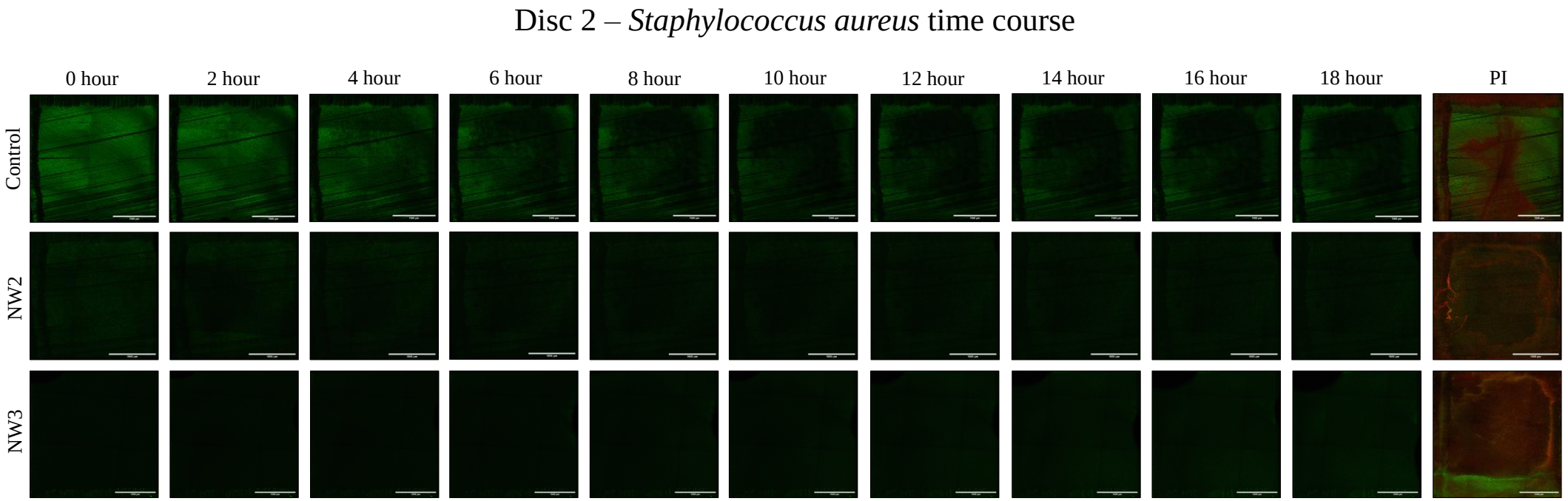

Figure 4.10 | Disc 2 – GFP *S. aureus* automated fluorescence microscopy. Fluorescence time course monitoring biofilm growth on control, NW2 and NW3 surface for 18 hours (2-hour increments). PI stain was added at 18 hours. Scale bar – 1000 µm.

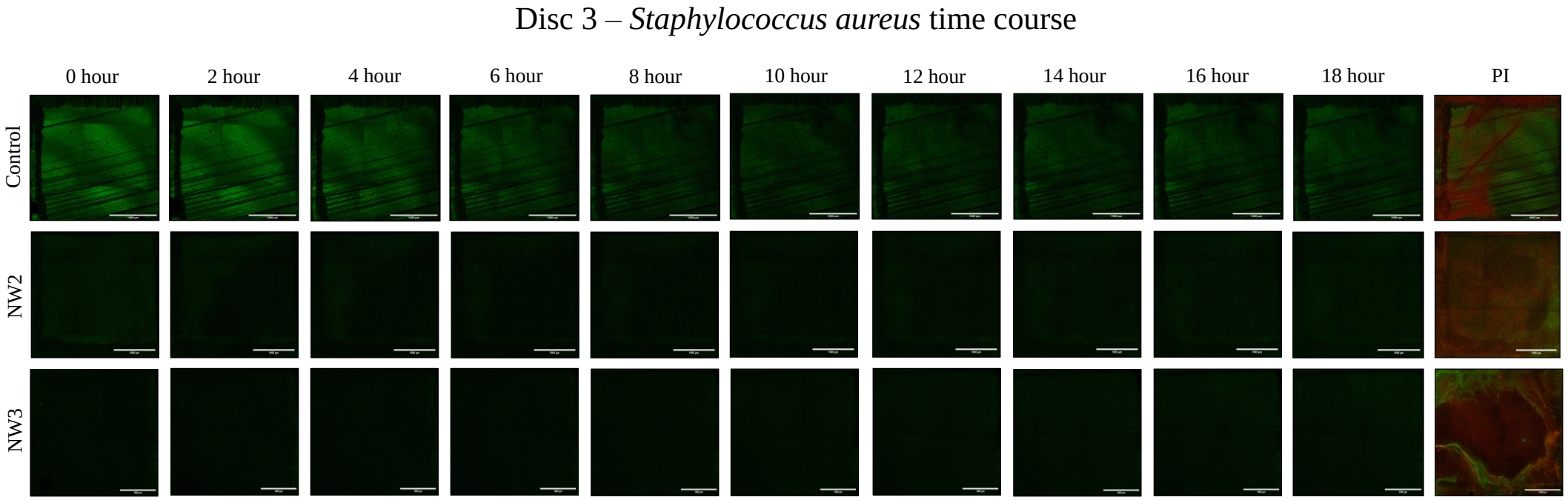

Figure 4.11 | Disc 3 – GFP *S. aureus* automated fluorescence microscopy. Fluorescence time course monitoring biofilm growth on control, NW2 and NW3 surface for 18 hours (2-hour increments). PI stain was added at 18 hours. Scale bar – 1000 µm.

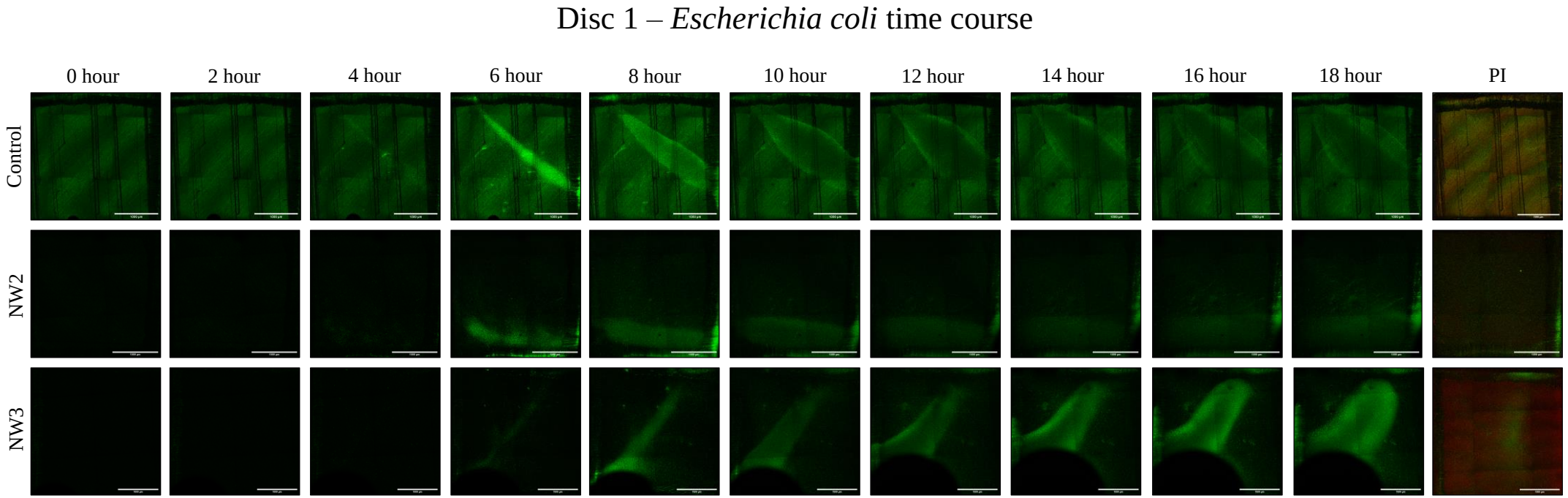

Figure 4.12 | Disc 1 – GFP *E. coli* automated fluorescence microscopy. Fluorescence time course monitoring biofilm growth on control, NW2 and NW3 surface for 18 hours (2-hour increments). PI stain was added at 18 hours. Scale bar – 1000 µm.

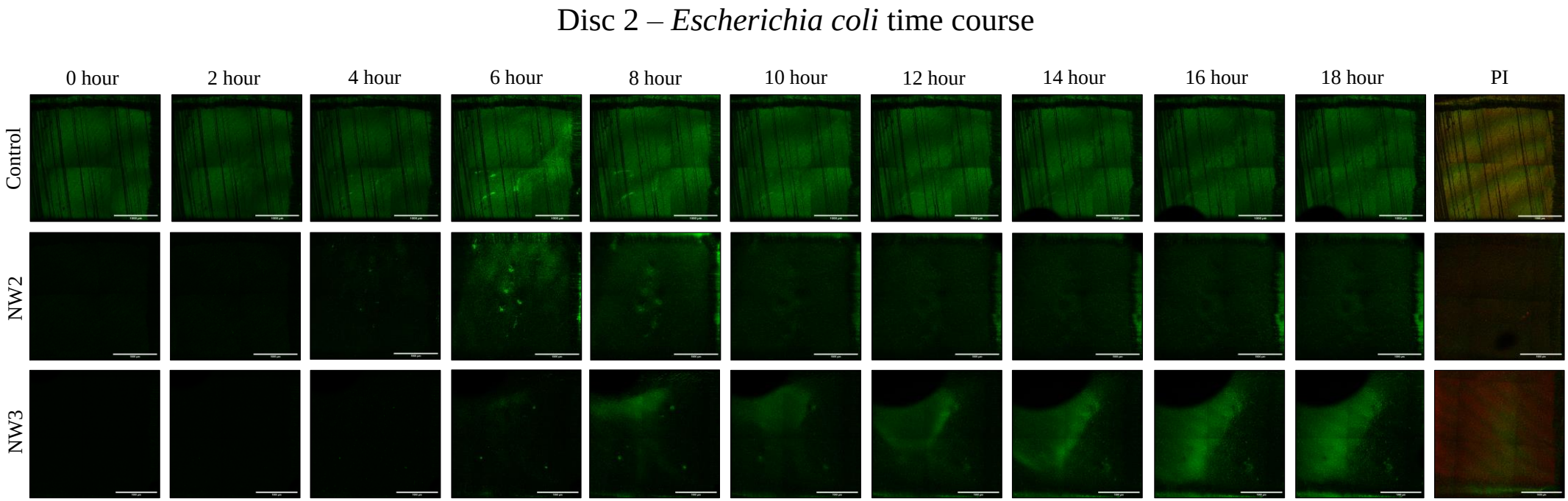

Figure 4.13 | Disc 2 – GFP *E. coli* automated fluorescence microscopy. Fluorescence time course monitoring biofilm growth on control, NW2 and NW3 surface for 18 hours (2-hour increments). PI stain was added at 18 hours. Scale bar – 1000 µm.

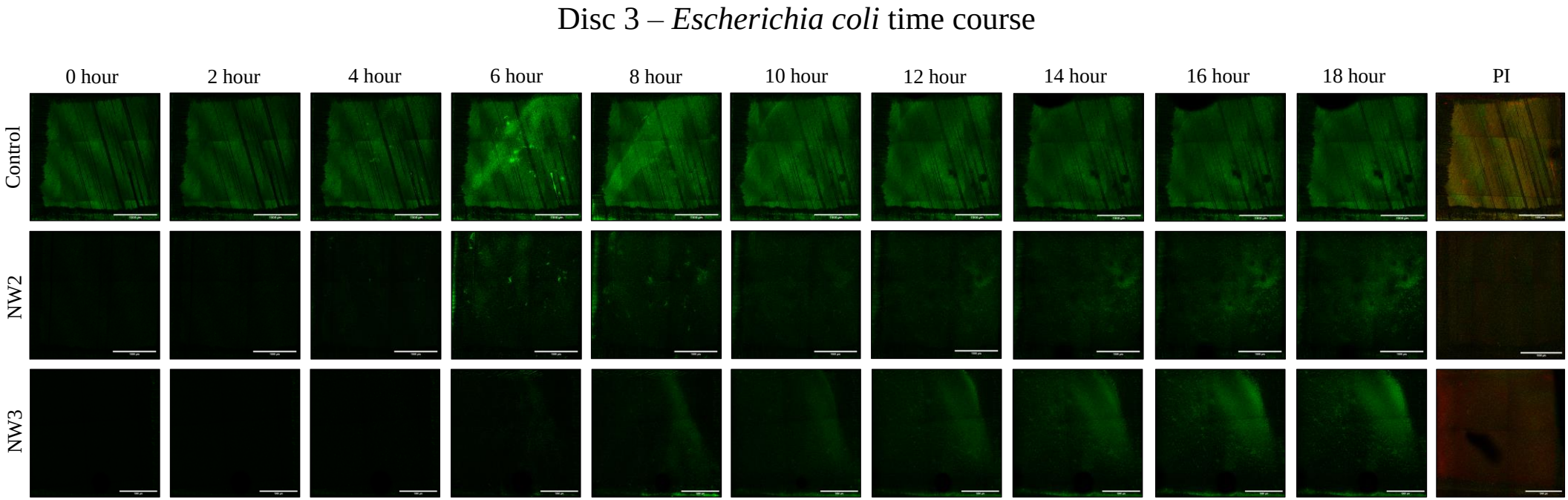

Figure 4.14 | Disc 3 – GFP *E. coli* automated fluorescence microscopy. Fluorescence time course monitoring biofilm growth on control, NW2 and NW3 surface for 18 hours (2-hour increments). PI stain was added at 18 hours. Scale bar – 1000 µm.

At this stage, culture based methods appeared to show significant reductions in *S. aureus* and *E. coli* viability after 24 hours on nanowires, but the quantitative accuracy of these data was compromised by reduced bacterial recovery from nanowire arrays compared to control. Contrary to previous studies, microscopic investigations implied that TiO_2 nanowires mediated envelope damage in a time-dependent manner. To better assess the antibacterial effects of the nanowire arrays in greater detail, assays that utilise biochemical indicators for determination of bacterial viability were exploited, namely RTG and BTG.

4.2.4 RealTime-Glo™ and BacTiter-Glo™ analysis

RealTime-Glo™ (RTG) is a luminescence based, non-lytic assay used to monitor cell redox potential continuously in a plate reader format. The reducing environment inside metabolically active bacteria facilitates in the conversion of a cell-permeable prosubstrate into a substrate. A NanoLuc® luciferase generates a luminescent signal that correlates to viable cell number. Non-viable cells do not produce a luminescent signal as the substrate is not reduced (Riss et al., 2016). In contrast, BacTiter-Glo™ (BTG) is a luminescence based, lytic assay used for end point measurements of bacterial viability in a plate reader format. The BTG reagent contains a detergent that lyses bacterial cells in suspension, which leads to the release of ATP. ATP is utilised by an Ultra-Glo™ recombinant luciferase, which generates a luminescent signal proportional to the concentration of ATP. This is directly proportional to the number of viable cells (Riss et al., 2016).

4.2.4.1 RealTime-Glo™ and BacTiter-Glo™ optimisation for plate reader measurements

Prior to antibacterial surface testing, RTG and BTG were optimised for measurements on a plate reader. In line with manufacture guidance, white, opaque-walled plates were selected as these maximise the luminescence output signal. During experiments, white plates were incubated in the dark, thereby minimising autophosphorescence from the emission of photons. To begin this set of studies, background luminescent signals were first measured from empty plates, titanium discs, growth media and RTG reagents. Figure 4.15a shows the relative luminescence units (RLU) measured from each well within an empty plate, highlighting that background luminescence was low, with little variation across the plate. Furthermore, the background signals were not enhanced by the presence of different titanium discs, RTG or BTG reagents, or growth media (Figure 4.15b), although there were slight increases in RLU when RTG and BTG were combined with growth media.

a

White-24 well plate		Well column (RLU)						
Well row (RLU)		1	2	3	4	5	6	SD
	A	19	13	13	14	19	34	7
	B	16	16	8	12	15	21	4
	C	11	23	25	11	22	25	6
	D	18	27	26	36	31	37	6
SD		3	6	8	10	6	6	

b

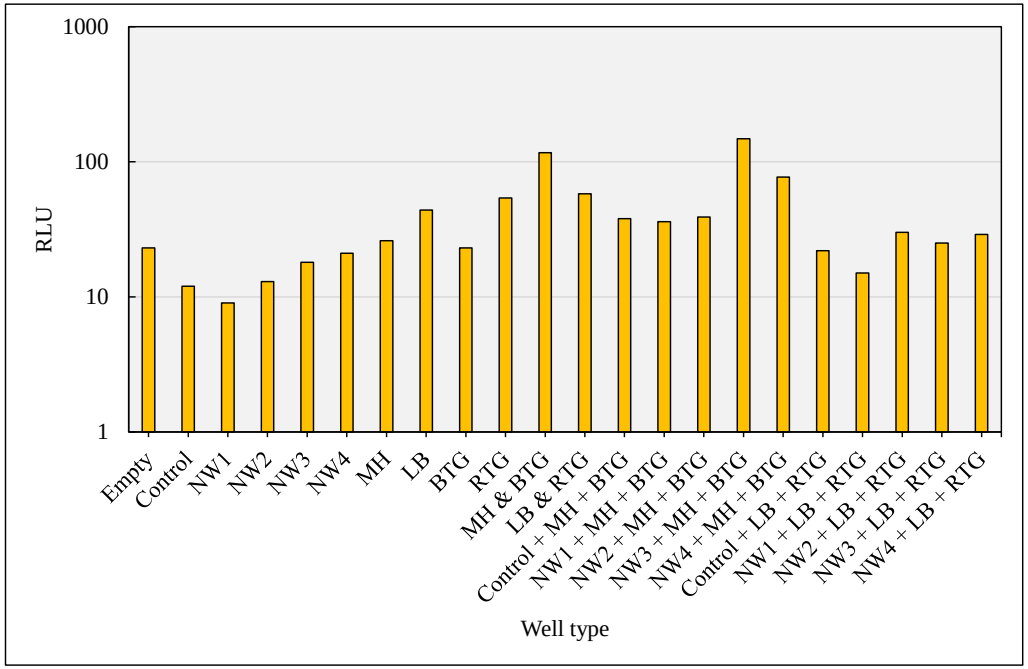

Figure 4.15 | Optimisation of RTG and BTG for multiwell plate reader measurements. The background luminescence from a single empty, white 24-well plate was measured (a). The standard deviation measured for each column and row across the plate are shown. The background emissions from a single well attributed to titanium discs (control, NW1-NW4), MH, LB, BTG, RTG and combinations thereof were measured inside a white 24-well plate (b).

Since bacterial growth in planktonic culture is affected by the type of growth medium, this could be expected to influence both the intensity and duration of the luminescent signal generated from RTG. As such, the luminescent signals produced from *S. aureus*, *S. epidermidis, E. coli* and *K. pneumoniae* were monitored in four growth media: Brain Heart Infusion (BHI), LB, MH and Tryptone Soya Broth (TSB), to identify the most suitable growth medium for continuous plate reader measurements. In contrast, MH growth media was selected for all BTG studies, since this was recommended by the manufacturer. For RTG, the type of growth medium was found to significantly influence the luminescent signal over time, and there were several key findings from this (Figure 4.16): 1) The total luminescent signal generated from Gram-negative bacteria (*E. coli* and *K. pneumoniae*) was generally 10-100 fold lower than from Gram-positive bacteria (*S. aureus* and *S. epidermidis*). This was true for all growth media; 2) For *E. coli* and *K. pneumoniae*, the rate of luminescence production was typically slower in BHI and TSB compared to MH and LB, while in *S. aureus* and *S. epidermidis*, the opposite was generally observed; 3) Based on the low RLU produced from *S. epidermidis* in MH, this was not selected as the growth medium, as it did not appear to support *S. epidermidis* growth as well as other media; 4) The RLU signals produced in BHI and TSB were undulating for all bacteria, and so BHI and TSB were not considered further; 5) The RLU produced in LB appeared to be the most consistent across all bacteria, showing the least deviation. As such, LB was selected for subsequent RTG experiments.

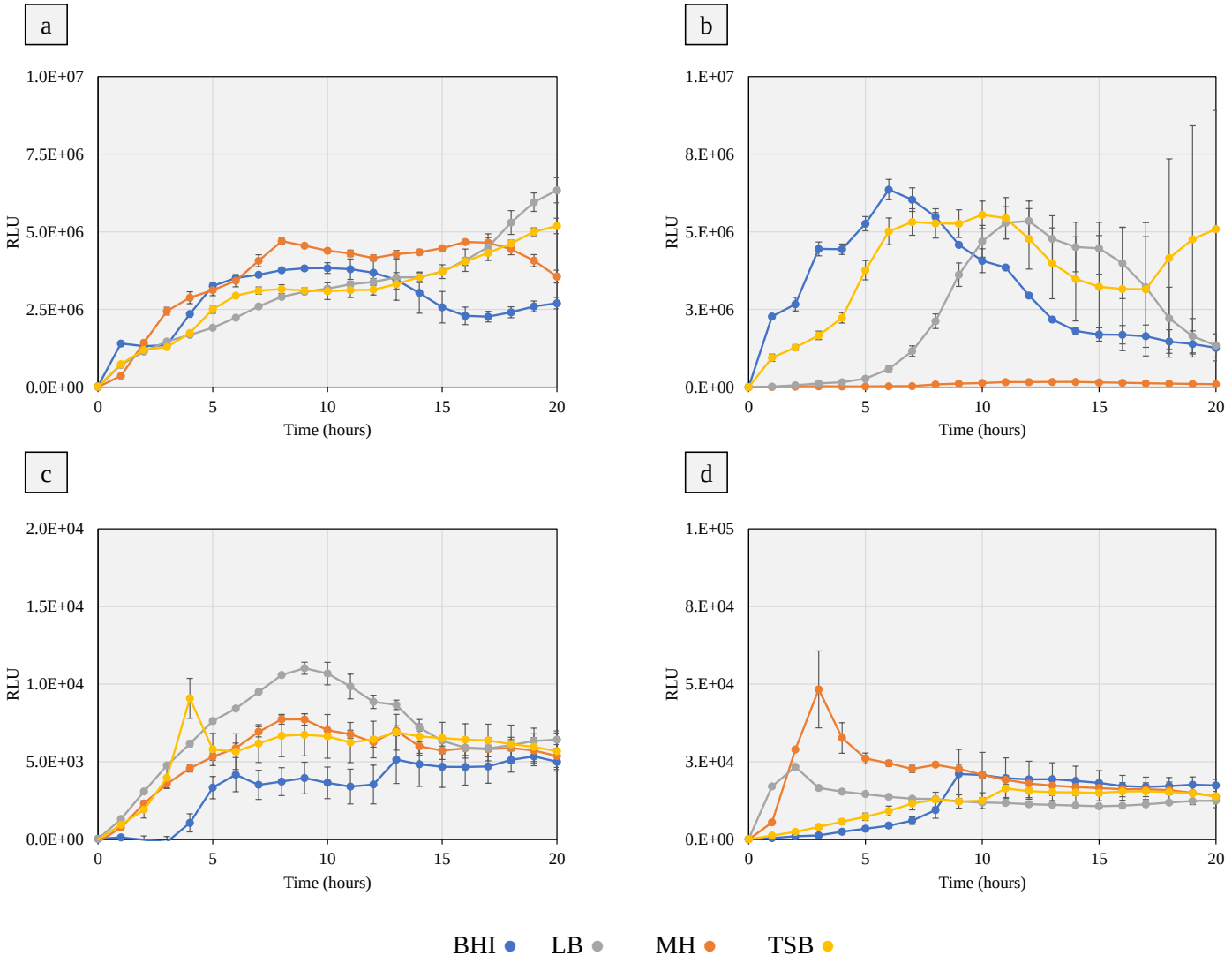

Figure 4.16 | The effect of growth media on luminescent signal from RTG reagent. RTG reagent was incubated with *S. aureus* (a), *S. epidermidis* (b), *E. coli* (c) and *K. pneumoniae* (d) and the RLU were measured up to 20 h. Four different growth media were used: BHI, LB, MH and TSB. To ensure no effect was missed, the RLU signal was measured every 10 minutes, although hourly data points are shown. Values given are mean ± standard deviation from one experiment (n=1) performed in triplicate.

The luminescence produced by RTG is reported to correlate with viable cell number and quickly diminish upon cell death (Riss et al., 2016). To check this, the luminescent signal produced from different starting densities of *S. aureus*, *S. epidermidis*, *E. coli* and *K. pneumoniae* was monitored. As anticipated, the luminescent signal correlated to the bacterial density, with the rate of luminescence production occurring more quickly at lower dilutions. Although higher dilutions emitted a reduced RLU, the luminescent signal was more linear over time. Thus, bacterial densities of approximately 10^6-10^7 per 50 µL were selected for subsequent optimisation, as this provided the best compromise between signal intensity and linearity over time (Figure 4.17).

Since the luminescence produced by NanoLuc® luciferase is dependent on the formation of a substrate from a prosubstrate, the concentration of the prosubstrate could be expected to become a limiting factor over longer durations. Thus, it was considered that increasing the concentration of prosubstrate may aid in extending the linear range, thereby enabling the effect of TiO_2 nanowire arrays on bacterial viability to be monitored for longer durations. Four different starting concentrations of cell permeable prosubstrate were investigated, 1X, 2X, 4X and 8X. For *S. aureus*, increasing the concentration of the prosubstrate did not improve assay linearity, and, of note, the intensity of the luminescent signal was generally inversely proportional to prosubstrate concentration. A similar trend was observed for *E. coli.* On the basis of these findings, the concentration of cell permeable prosubstrate was maintained at 1X (Figure 4.18).

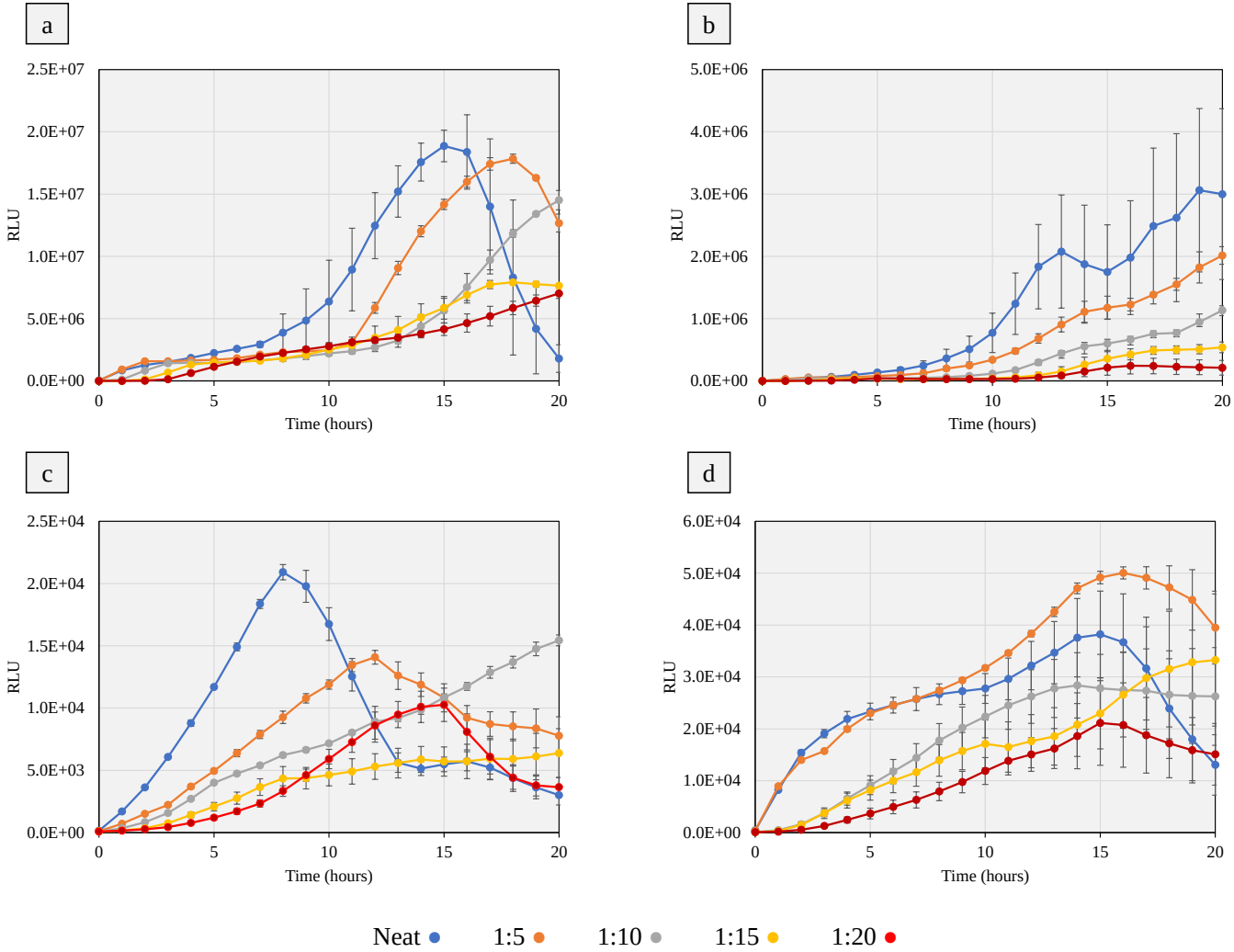

Figure 4.17 | The effect of bacterial density on luminescent signal from RTG reagent. RTG reagent was incubated with serially diluted (1:5) suspensions of *S. aureus* (a), *S. epidermidis* (b), *E. coli* (c) and *K. pneumoniae* (d) and the RLU were measured from each dilution up to 20 h. To ensure no effect was missed, the RLU signal was measured every 10 minutes, although hourly data points are shown. Values given are mean ± standard deviation from one experiment (n=1) performed in triplicate.

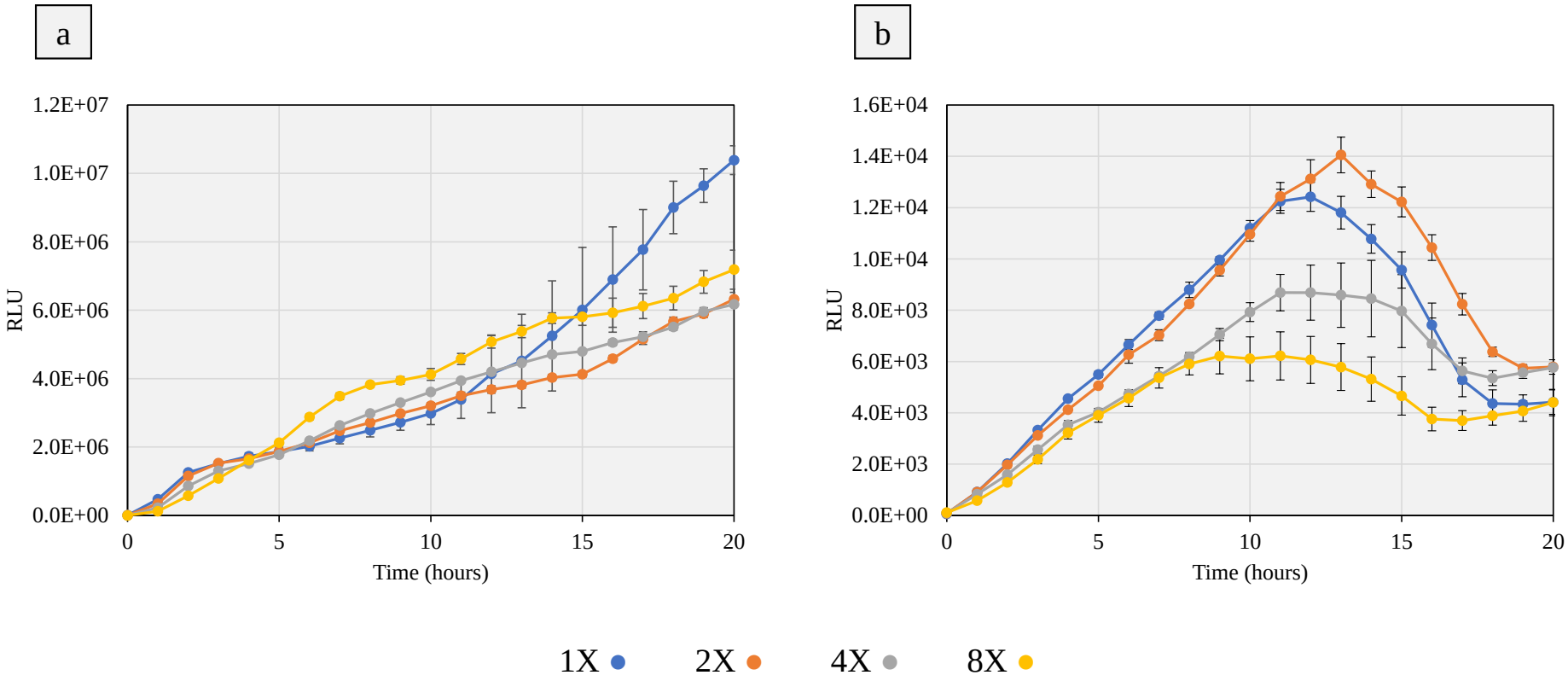

Figure 4.18 | The effect of prosubstrate concentration on luminescent signal from RTG reagent. RTG reagent was incubated with 10^6-10^7 *S. aureus* (a) and *E. coli* (b) and the RLU were measured from each dilution up to 20 h. To ensure no effect was missed, the RLU signal was measured every 10 minutes, although hourly data points are shown. Values given are mean ± standard deviation from one experiment (n=1) performed in triplicate.

4.2.4.2 Continuous plate reader measurements using RealTime-Glo

On the basis of optimisation experiments, continuous plate reader measurements using RTG were performed as follows: *S. aureus, S. epidermidis, E. coli* and *K. pneumoniae* were adjusted to cell densities of 10^6-10^7 per 50 µL of LB broth. These were supplemented with 1X NanoLuc® luciferase and 1X cell permeable prosubstrate, and incubated for 1 hour prior to being transferred onto titanium discs inside white, opaque 24-well plates. All assay reagents, plate reader and multiwell plate were equilibrated to 37°C prior to measurements. RLU were measured continuously in a temperature-controlled (37°C) plate reader over 10 hours. Use of this time period minimised the chance of recording bacterial cell death due to factors independent of the nanotopography e.g. nutrient depletion (Figure 4.19).

The rate of luminescence production by *S. aureus* was noticeably slower on NW2 and NW3 relative to control and plateaued after 6 hours, while on controls, the signal increased over the entire 10-hour incubation period. Levels of metabolic activity differed significantly from controls on NW2 and NW3 after 10 and 9 hours respectively (Figure 4.19a). Similar trends were observed for *E. coli* (Figure 4.19c), although the differences between nanowire and control surfaces did not reach statistical significance. As previously highlighted in optimisation experiments, a contributory factor to this was that the absolute RLU values were significantly (1000-fold) lower for *E. coli* than for *S. aureus*, which most likely reflects the lower reducing capacity of Gram-negative bacteria.

This variance between Gram-positive and -negative bacteria was further supported when additional Gram-positive (*S. epidermidis*) and Gram-negative (*K. pneumoniae*) bacteria were tested (Figure 4.19b, d). Significant differences in *S. epidermidis* viability relative to controls were observed after 4 hours on both nanowire arrays. For *K. pneumoniae*, the absolute RLU values were much lower and no significant differences were observed, although the luminescence profile for NW3 was distinct from that of the other two surfaces. Of note, *E. coli* and *K. pneumoniae* studies showed a reduction in luminescent signal from 10 and 3-5 hours respectively, even on control surfaces. This indicated that other factors, independent of the surface, may have been affecting bacterial growth after these times.

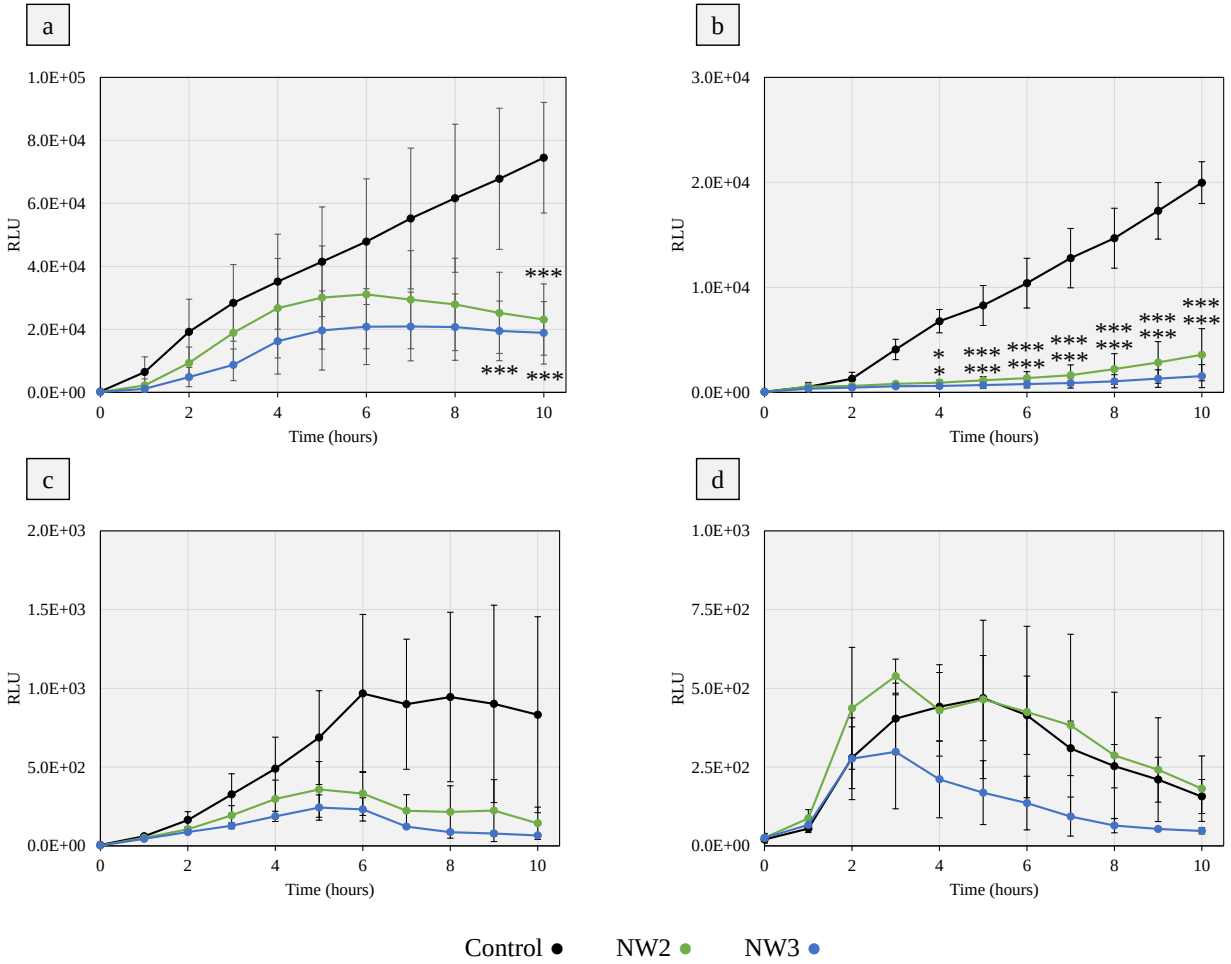

Figure 4.19 | The effect of TiO_2 nanowires on bacterial viability as measured using RTG. RTG reagent was incubated with *S. aureus* (a), *S. epidermidis* (b), *E. coli* (c), or *K. pneumoniae* (d) according to the manufacturers' instructions. Bacterial suspensions (50 µL) containing 10^6-10^7 cells were transferred to control, NW2 or NW3 surfaces inside a white, 24-well plate. To ensure no effect was missed, the RLU signal produced from each surface type was measured every 10 minutes for 10 h, although hourly data points are shown. Values are given as mean ± standard deviation. *P<0.05, ***P<0.001 relative to control, as determined by one-way ANOVA and Tukey HSD post hoc test; n=6 performed in triplicate (*S. aureus*, *S. epidermidis*), n=3 performed in triplicate (*E. coli*, *K. pneumoniae*).

4.2.4.3 BacTiter-Glo optimisation for plate reader measurements

Given the low sensitivity of RTG with Gram-negative bacteria in this study, viability testing was additionally performed using BTG. Prior to surface testing, BTG was optimised for measurements in white, opaque-walled plates. In line with manufacturers' instructions, measurements were performed in MH broth, as this generates low background luminescence and is reported to facilitate reproducible batch-to-batch measurements. As for RTG, the background RLU signals attributed to empty 24-well plates, titanium discs and growth media were low for wells containing BTG reagent only (Figure 4.15).

The sensitivity of BTG was determined by means of standard curve. Overnight cultures of *S. aureus, S. epidermidis, E. coli* and *K. pneumoniae* were sub-cultured into MH broth and incubated to mid-exponential phase. Mid-exponential phase cultures were serially diluted (1:4) and 100 µL of each dilution was then transferred to a white, opaque 96-well plate. BTG reagent that had been equilibrated to room temperature was then added to each dilution in a 1:1 ratio. The luminescent signal generated from each dilution was measured in a plate reader. Each dilution was also plated out and enumerated the following day using the Miles and Misra viable count method (Miles and Misra, 1938). The RLU recorded for each dilution were then plotted against the corresponding CFU to generate standard curves for *S. aureus, S. epidermidis, E. coli* and *K. pneumoniae* (Figure 4.20). The sensitivity of BTG was very high, and generally able to detect bacteria down to 100-1000s of cells.

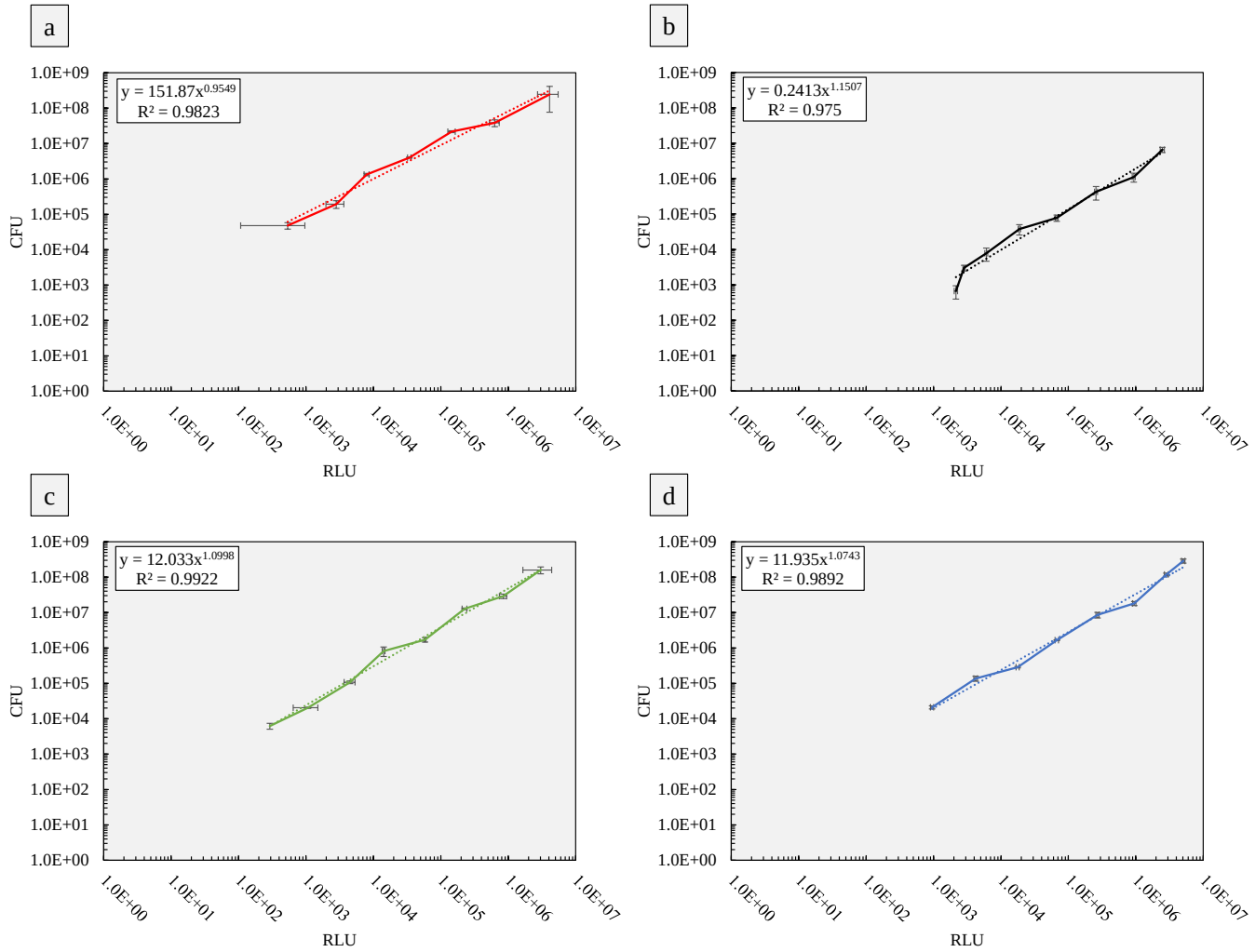

Figure 4.20 | Standard curves for correlation of luminescence with CFU using BTG. Bacterial viability on TiO_2 surfaces was semi-quantified by converting raw luminescence data (recorded from BTG experiments) into CFU. (a) *S. aureus*, (b) *S. epidermidis*, (c) *E. coli* and (d) *K. pneumoniae*. Displayed on each graph is the corresponding equation and coefficient of determination (R^2). Values given are mean ± standard deviation; n=3 performed in triplicate.

4.2.4.4 End point plate reader measurements using BacTiter-Glo

On the basis of manufacturers' instructions and optimisation experiments, end-point plate reader measurements using BTG were performed as follows: *S. aureus, S. epidermidis, E. coli* and *K. pneumoniae* were adjusted to cell densities of 10^6 -10^7 per 25 µL in MH broth. Aliquots (25 µL) of each bacterial suspension were transferred onto separate titanium discs inside white, opaque 24-well plates. In line with RTG analyses, BTG was performed at discrete time points up to 10 hours, including 0.5, 1, 3 and 10 hour incubations at 37°C. Following incubation, 25 µL of equilibrated BTG reagent was combined with the bacterial suspension on each titanium disc and RLU measurements were recorded in a plate reader. Standard curves were used to covert RLU into CFU.

For *S. aureus,* significant reductions in CFU relative to controls were observed on both NW2 and NW3 following a 10-hour incubation (Figure 4.21a), corroborating the RTG data. In contrast, while *S. epidermidis* CFU data were generally higher on control at each time point compared to nanowire surfaces, these differences did not reach statistical significance (Figure 4.21b). Contrary to RTG analyses, BTG revealed significant differences in *E. coli* viability on NW3 following 3- and 10-hour incubations relative to control. Significant differences were observed after 10 hours on NW2, and lower CFU were also seen at 3 h (Figure 21c). For *K. pneumoniae*, significant reductions in CFU were observed following 3-hour incubation on both NW2 and NW3 relative to control (Figure 21d). Although statistical significance was not achieved after 10 hours, the overall luminescent signals had dropped at this time point, along with the control, compared to 3 hours, as also seen for the RTG assay.

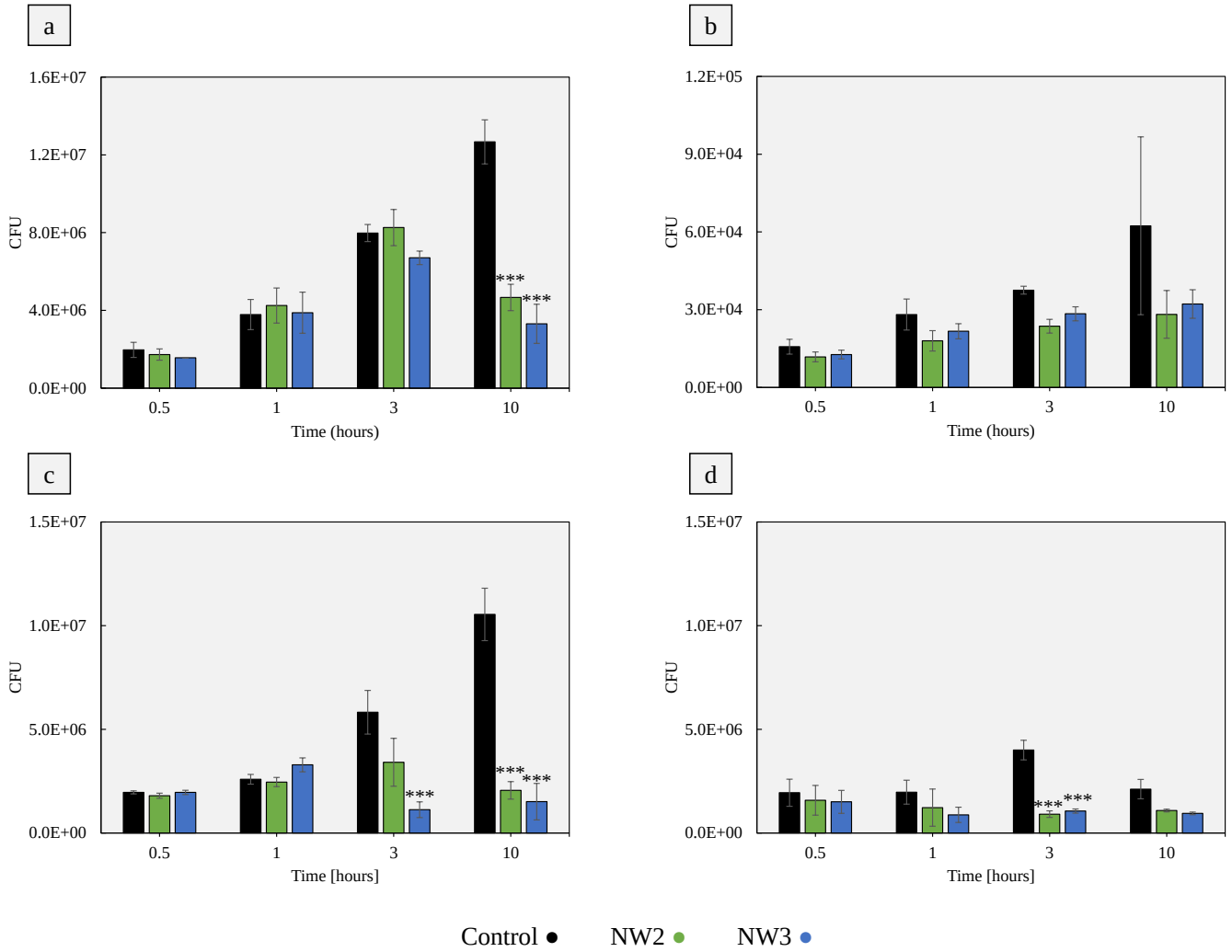

Figure 4.21 | The effect of TiO_2 nanowires on bacterial viability as measured using BTG. Aliquots (25 µL) of *S. aureus* (a), *S. epidermidis* (b), *E. coli* (c) or *K. pneumoniae* (d) suspensions, containing 10^5-10^6 cells, were incubated on control, NW2 or NW3 surface types for 0.5, 1, 3 or 10 hours. Following incubation, BTG reagent was added following the manufacturers' instructions. Values are given as mean ± standard deviation. ***P<0.001 relative to corresponding control, as determined by one-way ANOVA and Tukey HSD post hoc test; n=3 performed in triplicate.

4.3 Surface characterisation

To better determine if reductions in bacterial viability were mediated by physical contact, rather than chemically mediated, the surface chemistry of NW3 was analysed by XPS and GIXD. NW3 was selected on the basis that bacterial viability was consistently lower on this nanotopography compared to the other surfaces tested.

4.3.1 XPS analysis

XPS analysis was used to determine the elemental composition of NW3 surfaces. For comparison, XPS analysis was also performed on machine polished (SiC #4000 grit size) titanium discs and core-shell NW3 surfaces, to identify whether the elemental composition had changed significantly at each stage of fabrication. An XPS survey scan was performed over a binding energy range of 1100 eV and –10 eV using a pass energy of 40 eV, in energy steps of 0.500 eV and dwell times of 100 ms. Cross referencing against the CasaXPS elemental library identified four primary regions, Ti 2p, O1s, C1s, Al 2p. These elemental peaks are highlighted in green regions within the survey scans for control, core-shell NW3 and NW3 surfaces (Figure 4.22). Automated region generation within CasaXPS revealed that the relative quantities of titanium, oxygen, carbon and aluminium changed between control, core-shell NW3 and NW3 surfaces.

On control surfaces, oxygen was the most abundant element, accounting for 50%. Carbon and titanium were present in very similar quantities, 24 and 22 % respectively, while aluminium was present at much lower quantities (4%). NW3 surfaces displayed a very similar survey scan and elemental content. There was a slight increase in oxygen (55%) and aluminium (6%), while carbon had reduced slightly (17%) and titanium remained comparable (22%). In contrast, the elemental content of core-shell NW3 surfaces was predominantly carbon, accounting for over 90% of the total composition. This was attributed to the carbon shell.

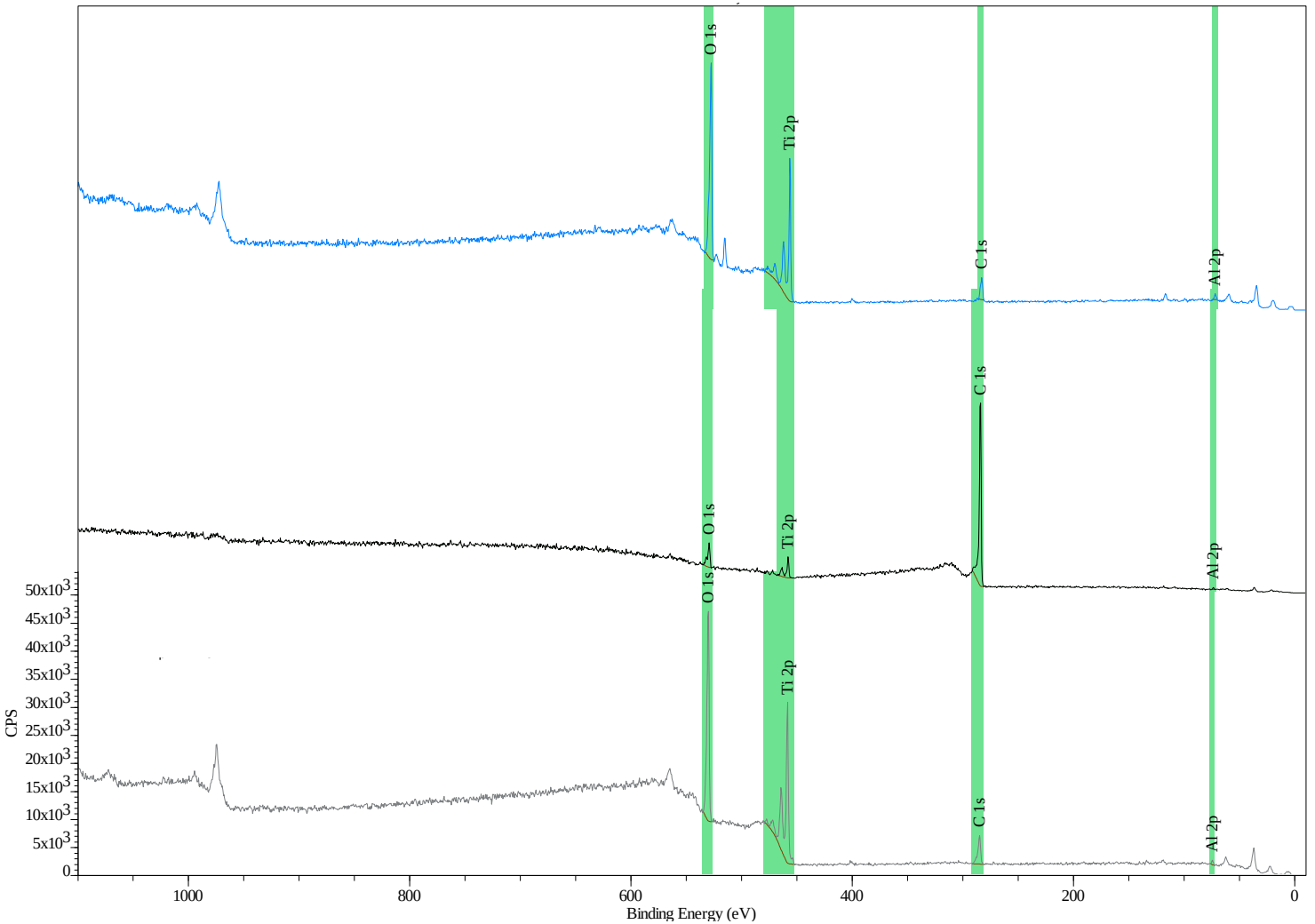

NW3	
Element	At%
O1s	55.55
C1s	16.74
Ti2p	21.50
Al2p	6.22

Core-shell NW3	
Element	At%
O1s	5.09
C1s	91.85
Ti2p	1.89
Al2p	1.16

Control	
Element	At%
O1s	50.03
C1s	23.88
Ti2p	21.86
Al2p	4.23

Figure 4.22 | Determination of surface elemental composition and quantity of titanium surfaces. XPS survey scans were performed on control, core-shell NW3 and NW3 surfaces to identify elemental peaks and the relative quantity of each. Scans were performed over a binding energy range of 1100 eV and -10 eV using a pass energy of 40 eV, in energy steps of 0.500 eV and dwell times of 100 ms. Cross referencing against the CasaXPS elemental library identified four primary regions, Ti 2p, O1s, C1s, Al 2p, highlighted in green regions within the survey scans.

4.3.2 GIXD analysis

The type of crystal polymorphs present in nanowires was determined by GIXD. The anatase TiO_2 polymorph has been reported to exhibit strong photocatalytic activity when exposed to ultraviolet radiation (Luttrell et al., 2014; Su et al., 2011). Given that photocatalytic activity leads to the production of free radicals, this could impart strong antimicrobial effects and so influence the mechanism of antimicrobial action of the nanowire arrays. Thus, XRD spectra of annealed TiO_2 nanowire arrays were obtained (Figure 4.23). The area underneath the anatase (101) and rutile (110) peaks was calculated and the polymorph composition was determined using the Spurr and Myers equation (Spurr and Myers, 1957). These analyses confirmed that rutile was the dominant polymorph, contributing to 98% of the TiO_2, while anatase was present in low quantities (2%). As rutile TiO_2 generally exhibits low photocatalytic activity (Luttrell et al., 2014), this indicated that the observed impairment of bacterial viability on NW3 was very unlikely to have been induced via free radical production via photocatalysis.

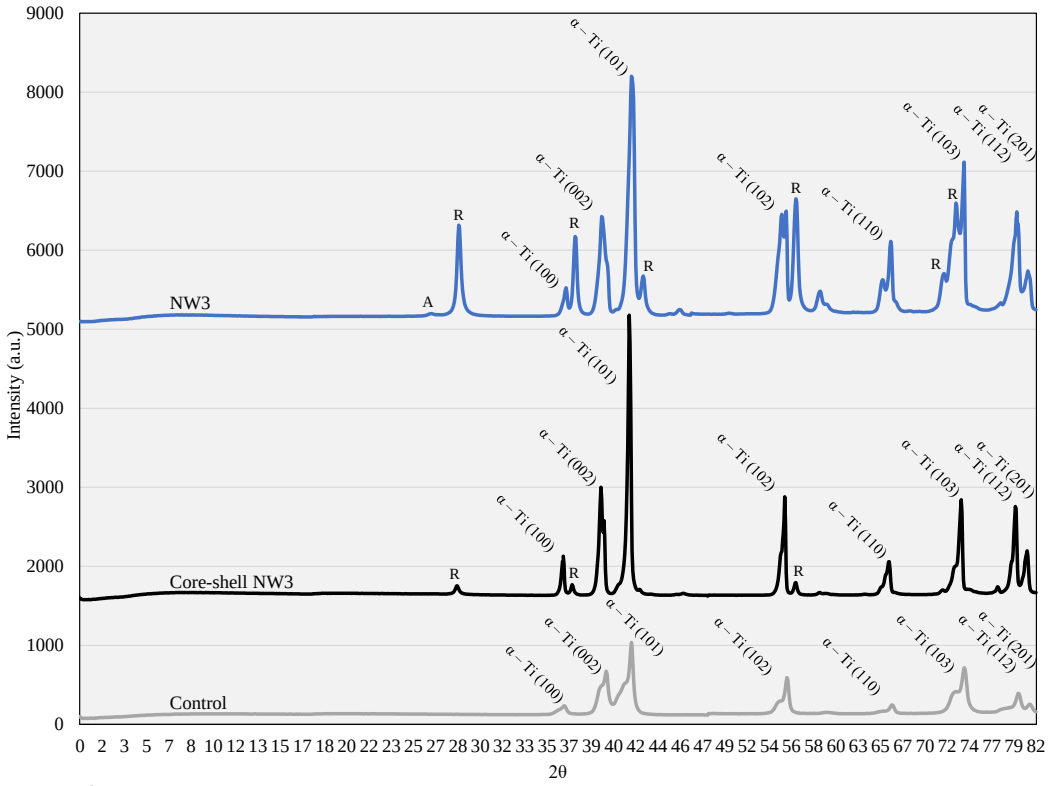

Figure 4.23 | Determination of NW3 crystal structure. GIXD spectra were obtained for NW3, alongside control and core-shell surfaces. Samples were mounted 0.243 m from the detector and tilted at 0.7°. X ray beams (λ = 885.7 nm) were shot at the sample and the diffracted X rays were detected and imaged at two positions (8° and 30°). The images were converted into 1D profiles using azimuthal integration within the pyFAI package. Peaks for all the samples were cross referenced and annotated based on published literature (Dinan, 2012; Wysoki et al., 2017).

4.4 Bacterial proteomic response to TiO_2 nanowires

The combined viability data and surface characterisation implied that nanowire arrays had capacity to reduce bacterial viability via physical contact. It was considered that such interactions might trigger envelope stress responses that, in turn, could have led to the apparent increased bacterial cell permeability and reduced viability. *E. coli* and *S. aureus* have evolved a number of two-component systems that facilitate their adaptation to environmental stresses such as antimicrobials, nutrient limitations, changes in pH, temperature, osmolarity or redox stress (Mitchell and Silhavy, 2019). For example, the σ^E and Cpx responses in *E. coli* alter gene expression in response to outer and inner envelope stress respectively, with analogous responses found in *S. aureus* (Jordan et al., 2008). To explore the bacterial response to nanowires at the molecular level, TMT labelling and mass spectrometry analysis was performed to enable a direct quantitative comparison of *S. aureus* and *E. coli* proteomes after 24 hours in the presence or absence of nanowires.

The results of Sequest searches against the Uniprot *S. aureus* and *E. coli* database identified 1231 and 1483 proteins respectively, at an FDR confidence of 5%. Following removal of contaminants, those proteins for which the relative abundance significantly differed for bacteria recovered from NW3 compared to control surfaces were identified. These are displayed as volcano plots in Figure 4.24. These analyses revealed that very few *S. aureus* and *E. coli* proteins had undergone significant ($P \leq 0.05$) changes in expression. A total of 90 *S. aureus* (Fig. 4.24a) and 27 *E. coli* (Fig. 4.24b) proteins exhibited differential expression with a *P*-value ≤ 0.05, corresponding to 7% and 2% of the total proteomes respectively. For *S. aureus,* the majority (90%) of DEPs recovered from bacteria on NW3 were present in elevated levels relative to control, with 81% displaying fold-changes greater than two. Of the 10% of *S. aureus* DEPs present at lower levels, only 1 DEP showed a decreased expression greater than two-fold. In contrast to *S. aureus,* the fold-changes in *E. coli* DEPs were more normally distributed around zero. Of the DEPs recovered from *E. coli* on NW3, 11 were present at lower levels than control, and 7 of these had decreased by two-fold or more. Among the 16 DEPs showing increased abundance, 11 had increased greater than two-fold.

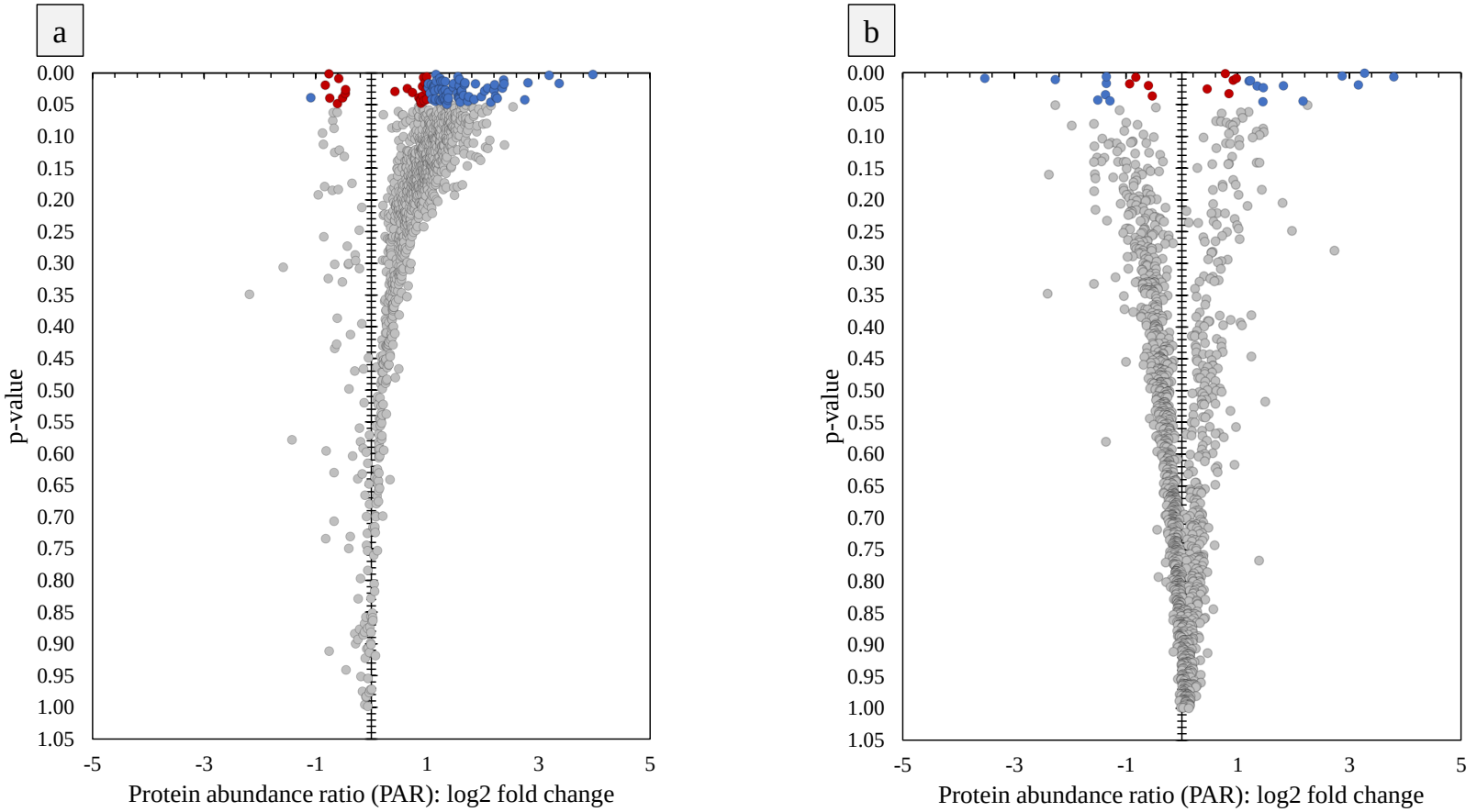

Figure 4.24 | Volcano plots indicating *S. aureus* and *E. coli* proteomic responses to TiO_2 nanowires. Volcano plots of *S. aureus* (a) or *E. coli* (b) proteins, as identified by TMT quantitative proteomic analysis following 24 hour incubation on control or NW3 surfaces. Proteins displayed are the result of Sequest searches against the *S. aureus* or *E. coli* Uniprot database (5% FDR). Proteins that had not changed significantly between the control and nanowire group are displayed in grey, whereas proteins showing significant abundance changes are highlighted by red (less than 2-fold changes) and blue (greater than or equal to 2-fold changes) points. Data is representative of one experiment (n=1) performed in triplicate.

To determine whether *S. aureus* and *E. coli* DEPs were biologically connected, protein-protein interactions were mapped using the STRING application within Cytoscape (Shannon et al., 2003; Szklarczyk et al., 2019). The DEP network generated for *S. aureus* consisted of 88 nodes and 421 edges; among these, 28 proteins displayed no interactions, while 60 proteins displayed at least one interaction at a confidence level between 0.46 and 1.00. The PPI enrichment *P*-value was < 1.0e-16 (Fig. 4.25). The *E. coli* DEP network comprised of 27 nodes and 14 edges. From these, 6 proteins had at least one interaction at a medium to high confidence. The PPI enrichment *P*-value was < 9.54e-06 (Fig. 4.26). In both instances, the number of interactions (edges) was significantly higher than would be expected for a random set of proteins of similar size drawn from the genome (203 or 3, respectively). This verifies that the *S. aureus* and *E. coli* DEP networks were biologically connected. To further investigate the function of *S. aureus* and *E. coli* DEPs, GO enrichment analysis was used to categorise each protein by molecular function, biological process and cellular component. NCBI BlastP and EMBL-EBI InterPro database searches generated 137 GO annotations for *S. aureus*, of which 113 corresponded to upregulated proteins and 14 to downregulated proteins (Fig. 4.27a). For *E. coli* there were 61 GO annotations, 34 of which were associated with upregulated proteins, and 23 from downregulated proteins (Fig. 4.27b).

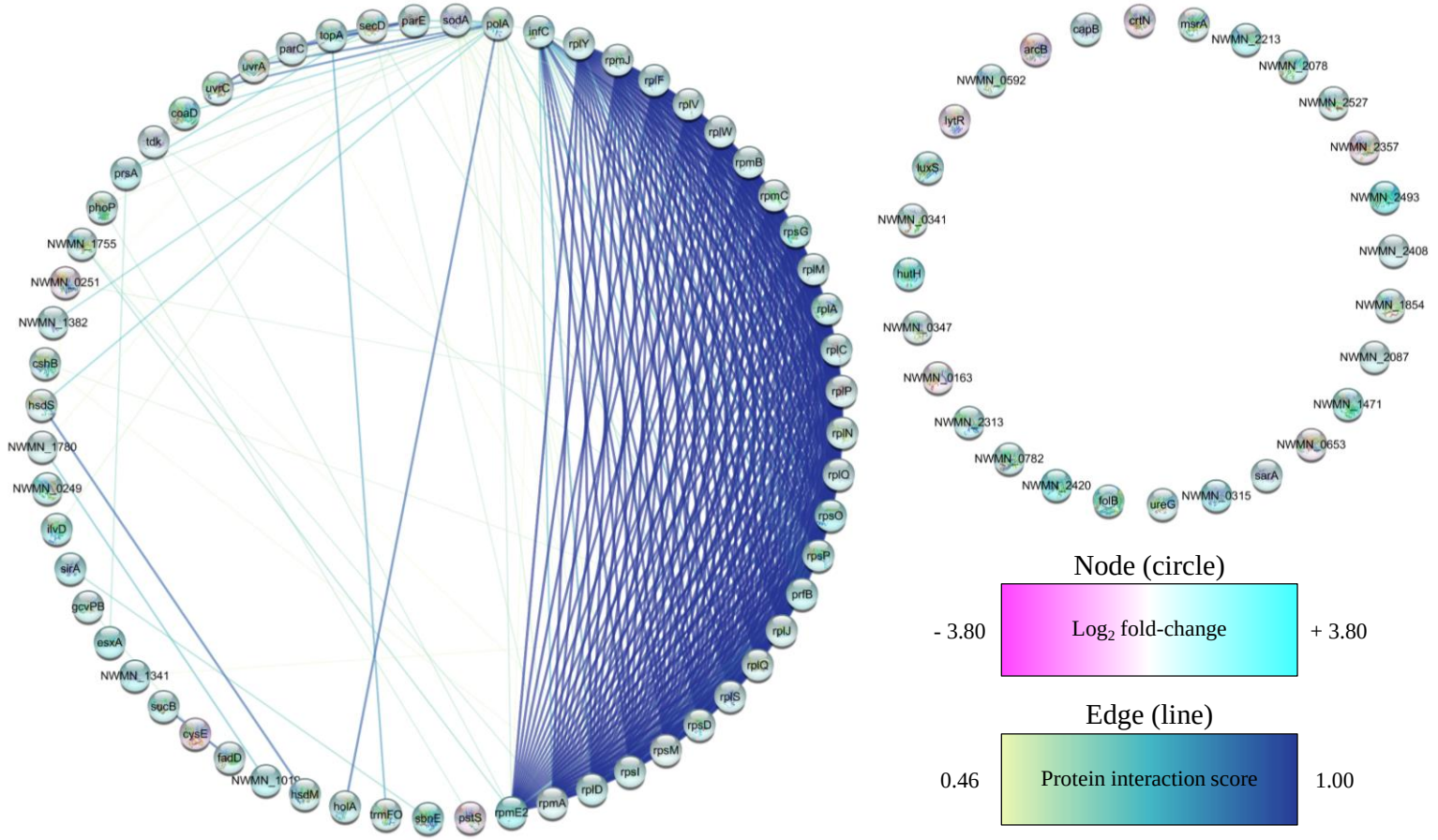

Figure 4.25 | *S. aureus* DEP protein-protein interactions. To investigate biological connections among DEPs, protein-protein interactions were established using the functional protein association network tool (STRING) within Cytoscape (v3.7.1). The predicated functional partners among *S. aureus* DEPs are shown, where individual proteins are represented in circles (nodes), and protein-protein associations are represented by the connecting lines (edges). DEPs have been coloured according to the log2 fold change in protein abundance, and node colour indicates the confidence of supporting interaction evidence (0.15 = low confidence, 0.40 = medium confidence, 0.70 = high confidence and 0.9 = highest confidence).

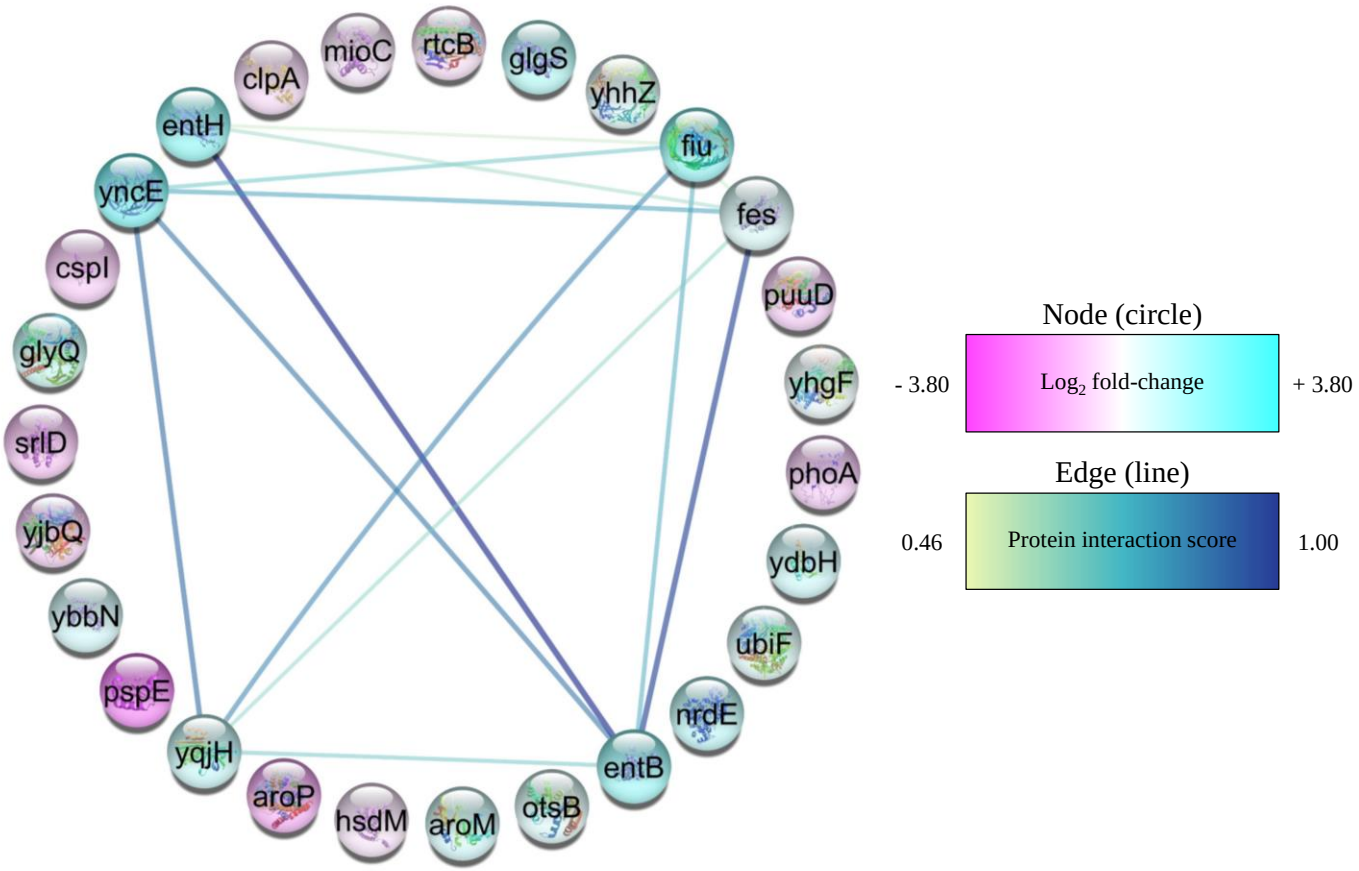

Figure 4.26│***E. coli*** **DEP protein-protein interactions.** To investigate biological connections among DEPs, protein-protein interactions were established using the functional protein association network tool (STRING) within Cytoscape (v3.7.1). The predicated functional partners among *E. coli* DEPs are shown, where individual proteins are represented in circles (nodes), and protein-protein associations are represented by the connecting lines (edges). DEPs have been coloured according to the log2 fold change in protein abundance, and node colour indicates the confidence of supporting interaction evidence (0.15 = low confidence, 0.40 = medium confidence, 0.70 = high confidence and 0.9 = highest confidence).

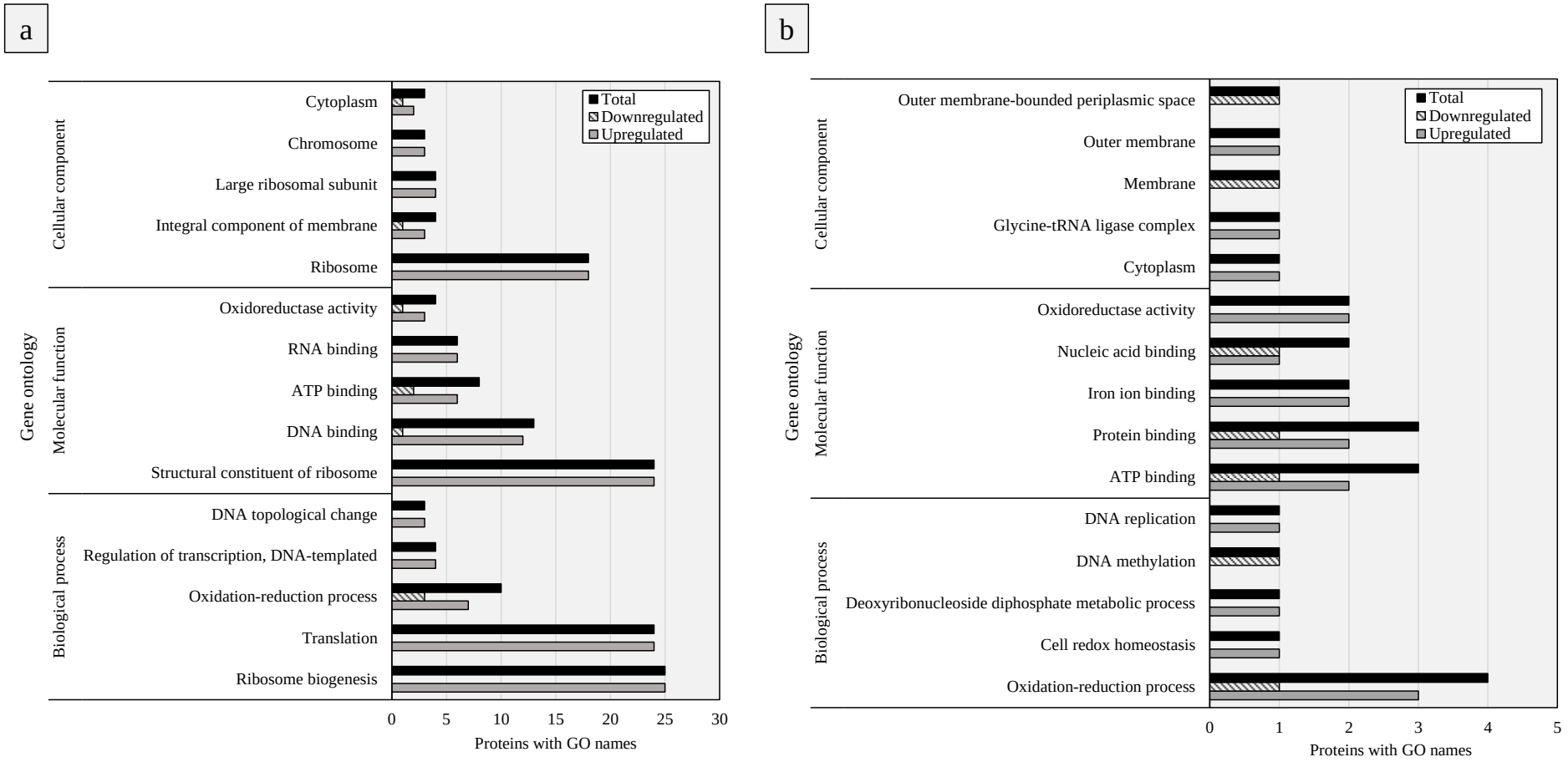

Figure 4.27 | Gene ontology enrichment analysis of *S. aureus* and *E. coli* DEPs. *S. aureus* (a) and *E. coli* (b) DEPs were categorised using gene ontology enrichment analysis, with the five most common GO annotations for up and down-regulated proteins according to Level 1 GO (Biological Process, Cellular Component and Molecular Function) indicated.

A number of the DEPs identified for *S. aureus* were associated with the oxidative stress response. Superoxide dismutase (SodA) is a key oxidative stress protein, responsible for the conversion of superoxide anions into oxygen and H_2O_2 within the cytoplasm (Arts et al., 2015). SodA had increased over two-fold in *S. aureus* recovered from NW3. The abundance of other oxidative stress proteins had also increased in *S. aureus*, namely methionine sulfoxide reductase (MsrA), responsible for repairing the oxidation of methionine residues (Ezraty et al., 2017), and bacterioferritin comigatory protein (Bcp), a thiol peroxidase involved in the reduction of H_2O_2 (Horsburgh et al., 2001). Furthermore, the NADH-dependent flavin oxidoreductase (NWMN_0315) had increased nearly 6-fold in the presence of NW3. Expression of such proteins is induced by H_2O_2 stress (Fitzpatrick et al., 2003). Additionally, proteins involved in L-glutamate and cysteine biosynthesis had been downregulated on NW3, namely ferredoxin dependent glutamate synthase (NWMN_2357) and serine acetyltransferase (CysE). The reaction between L-glutamate and cysteine is the rate-limiting step in GSH biosynthesis, which is a key antioxidant (Mytilineou et al., 2002). SOS response proteins UvrA and UvrC and bleomycin resistance protein had also increased significantly in the presence of NW3, which mediate repair of DNA damage (Silva et al., 2017; Sugiyama et al., 1995), along with Histone-like DNA-binding protein HU, which is involved in DNA stabilisation under extreme environmental conditions (Almarza et al., 2015). Taken together, these findings, while preliminary, suggested that TiO_2 nanowires had mediated an oxidative stress response within *S. aureus*.

In addition to oxidative stress, another key theme of *S. aureus* DEPs was protein expression. A significant proportion (33%) of DEPs were involved in protein translation, secretion and translocation, all of which had been upregulated in the presence of NW3. Additionally, the abundance of SarA (global transcriptional regulator), a key mediator of *S. aureus* biofilm formation (Archer et al., 2011; Beenken et al., 2004, 2003), had increased 2-fold in the presence of nanowires.

As for *S. aureus*, oxidative stress was a key theme of the DEPs identified for *E. coli*. Subunit A (ClpA) of the ATP-dependent protease (ClpAP), which mediates unfolding and translocation of abnormal proteins (Duran and Lucius, 2018), had decreased significantly in the presence of NW3. Oxidative stress is known to inactivate such chaperone proteins (Goemans et al., 2018). Concomitantly, chaperedoxin had increased in the presence of NW3, another recognised oxidative stress response that allows bacteria to protect against the aggregation and irreversible oxidation of proteins (Goemans et al., 2018). Similar to *S. aureus*, a protein involved in L-glutamate biosynthesis had been down regulated in *E. coli* recovered from NW3, gamma-glutamyl-gamma-aminobutyrate hydrolase (PuuD). PuuD is involved in the final step of the putrescine degradation pathway, which generates L-glutamate. Another notable DEP was surface composition regulator GlgS. This is a negative regulator of flagellum-dependent cell motility and biofilm formation on inanimate substrata (Rahimpour et al., 2013) and was increased significantly in *E. coli* recovered from NW3.

Another key theme identified in both *S. aureus* and *E. coli* DEPs was iron homeostasis. For *S. aureus*, this included three proteins involved in iron uptake and solubilisation, namely ferrichrome ABC transporter lipoprotein (NWMN_2078), siderophore compound ABC transporter binding protein (SirA*)* and siderophore biosynthesis family protein (SbnE). Among *E. coli* DEPs involved in iron homeostasis were proofreading thioesterase (EntH) and enterobactin synthase (EntB), which are required for the synthesis of iron-complexing siderophore enterobactin. Furthermore, *E. coli* proteins involved in iron uptake, namely catecholate siderophore receptor (Fiu) and the NADPH-dependent ferric-chelate reductase (YqiH), and one protein involved in iron metabolism, enterochelin esterase (Fes), had been upregulated.

4.5 Determination of oxidative stress response on TiO_2 nanowires

Proteomic analysis suggested that *S. aureus* and *E. coli* had experienced oxidative stress on NW3, with a number of upregulated proteins involved in DNA repair, protein repair and reactive oxygen species (ROS) detoxification. Additionally, enzymes involved in the production of L-glutamate and cysteine had been downregulated, which are required for GSH biosynthesis. On the basis of these data, it was considered that TiO_2 nanowires may have the capacity to induce oxidative stress-like responses in *S. aureus* and *E. coli.* To investigate oxidative stress as a possible mechanism for reduced viability and increased permeability,

GSH-Glo and ROS-Glo were used to measure the levels of oxidative stress markers GSH and H_2O_2 respectively.

GSH is a three amino acid antioxidant comprised of L-glutamate, cysteine and glycine (Mytilineou et al., 2002). Intracellular ROS can mediate oxidation of native GSH, leading to its depletion. Thus, GSH-Glo was used to measure the intracellular levels of GSH, as a first possible indication of oxidative stress. GSH-Glo is a luminescence based, non-lytic assay used to quantify GSH levels in a plate reader format. To quantify GSH levels, *S. aureus* and *E. coli* were incubated on NW3 and control discs for 24 hours, under the same conditions used for proteomic analysis. After 24 hours, 2X GSH-Glo reagent was transferred to each surface and incubated at room temperature for 30 minutes. During this step, a luciferin derivative (Luc-NT) is converted into luciferin by glutathione S-transferase; this reaction is dependent on the concentration of GSH. A firefly luciferase was added after 30 minutes and incubated for a further 15 minutes at room temperature. During this step, a luminescent signal is generated that is proportional to the amount of GSH in the sample. The luminescent signal was then measured in a plate reader and the GSH concentration was determined by means of a standard curve (Figure 4.28). For *S. aureus*, the average concentration of GSH on control surfaces was 14.44 µM while on NW3 discs the average concentration was 13.01 µM. Although the levels of GSH had reduced on NW3, this was not a significant reduction. The quantity of GSH was generally lower for *E. coli*, measured at 3.18 µM on control discs and 3.96 µM on NW3. As for *S. aureus*, this difference was not significant (Figure 4.29a).

To further investigate the possibility of an oxidative stress response, ROS-Glo was used, which generates a luminescent signal proportional to the quantity of H_2O_2, a stable by-product of ROS detoxification. As before, *S. aureus* and *E. coli* were incubated on NW3 and control discs for 24 hours, under the same conditions used for proteomic analysis. In line with manufacturers' instructions, after 18 hours, the H_2O_2 substrate solution was added to the discs before placing back into the incubator at 37°C for the remaining 6 hours. During this time, the H_2O_2 substrate reacts with H_2O_2, forming a luciferin precursor. After 24 hours, the ROS-Glo detection reagent was added. This converts the luciferin precursor into luciferin, which is then used by the Ultra-Glo™ Recombinant Luciferase to generate a luminescent signal, measured in a plate reader. The intensity of the luminescent signals emitted from *S. aureus* and *E. coli* were significantly higher on NW3 discs compared to control discs, corresponding to 1.6- and 3.8-fold increases respectively. This confirmed that the levels of H_2O_2 were greater on NW3 than on control discs

(Figure 4.29b). This supported the hypothesis that bacterial contact with NW3 was inducing an oxidative stress response within *S. aureus* and *E. coli*.

The increased quantity of H_2O_2 on nanowire surfaces could be expected to induce changes in bacterial envelope morphology, since ROS mediate damage of DNA, lipids and proteins (Hong et al., 2019; Silva et al., 2017). To investigate this, the morphology of *S. aureus* or *E. coli* was compared by SEM analysis, following 24 h incubation on control or NW3 discs. The cell density and coverage of *S. aureus* and *E. coli* was notably higher on control discs compared to NW3 (Figure 4.30a-d). At higher magnification the characteristic morphologies of *S. aureus* (coccoid) and *E. coli* (bacillus) were observed on control surfaces (Figure 4.30e, g), with evidence of microcolony and biofilm formation. In contrast, the morphology of *S. aureus* and *E. coli* on NW3 discs was less-rigid and did not conform to the defined shapes observed on control surfaces (Figure 4.30f, h). This was particularly evident in *E. coli*, which appeared to be deforming onto the nanowires, indicating a loss of turgor pressure. These morphologies are consistent with previous studies that have proposed ROS-mediated cell death on CNTs (Olivi et al., 2013).

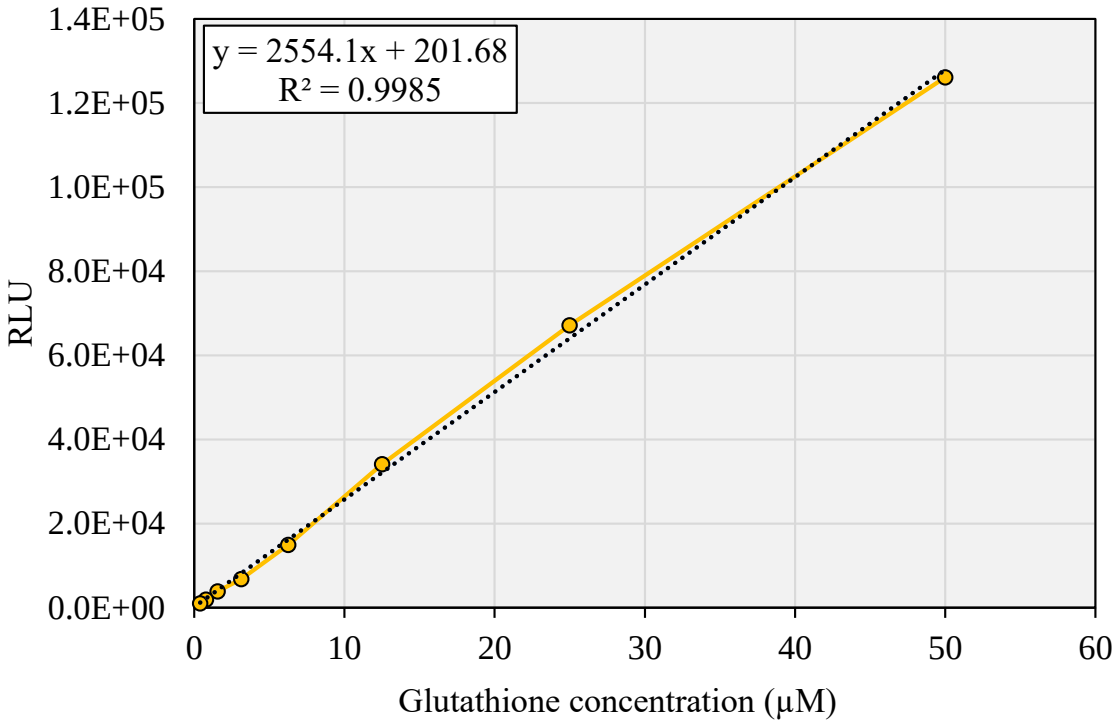

Figure 4.28 | Standard curves for correlation of GSH-Glo luminescence with GSH concentration. The production of GSH on NW3 was semi-quantified by converting raw luminescence data (recorded from GSH-Glo™ experiments) into GSH concentration (µM). Displayed on each graph is the corresponding equation and coefficient of determination (R^2) (dotted line – trend line).

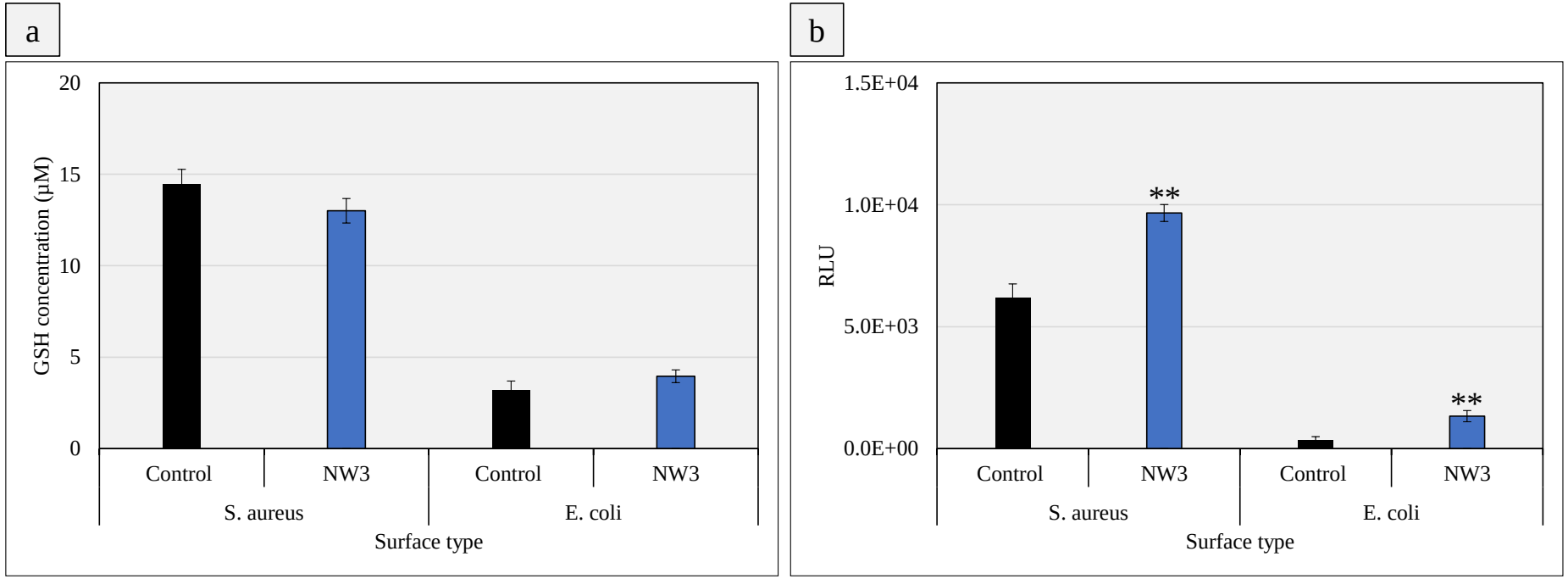

Figure 4.29 | Determination of *S. aureus* and *E. coli* oxidative stress responses to TiO_2 nanowires. *S. aureus* or *E. coli* were incubated for 24 h on control or NW3 surfaces under the same growth conditions used for proteomic analysis. Following 24 h incubation, GSH-Glo™ and ROS-Glo™ were used to determine the levels of intracellular GSH (a) or H_2O_2 (b) respectively. The concentration of GSH (µM) was determined by standard curve (Fig. 4.28), while the levels of H_2O_2 were inferred from RLU. Values given are mean ± standard deviation. **P<0.01 relative to control, as determined by Student's T-test; n=3 performed in duplicate.

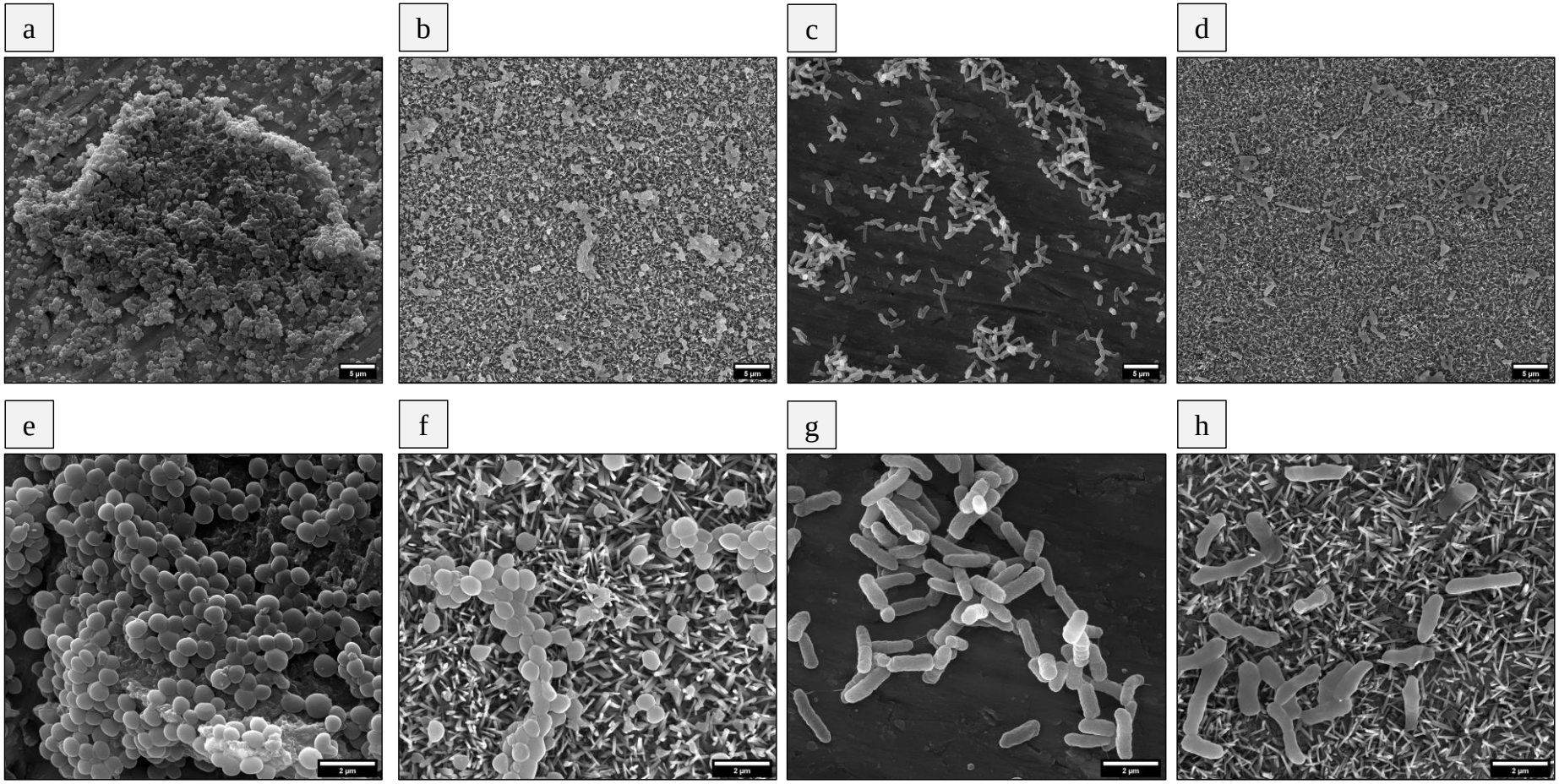

Figure 4.30 | Determination of *S. aureus* and *E. coli* morphology on NW3. *S. aureus* or *E. coli* were incubated for 24 h on control or NW3 surfaces under the same growth conditions used for proteomic analysis and oxidative stress assays. Following 24 h incubation titanium discs were processed for SEM analysis as outlined in section 2.9.1. The cell coverage and density of *S. aureus* and *E. coli* was higher on control (a, c) compared to NW3 (b, d). *S. aureus* and *E. coli* displayed characteristic coccoid and bacillus morphologies respectively on control (e, g), while on NW3, S. *aureus* and *E. coli* displayed less-rigid morphologies (f, h).

4.5 Discussion

The antibacterial performance of natural and synthetic nanotopographies has been the subject of many publications (Tripathy et al., 2017). Despite this, only a narrow range of microbiological tools have been used to investigate these interactions. As such, the antibacterial effects of nanowires, and their mechanistic basis, have not yet been fully characterised. Here, the effects of TiO_2 nanowire arrays on bacterial physiology were investigated using a number of approaches, including bacterial viability assays BTG and RTG, and the two most widely used methods, LIVE/DEAD staining and viable counts. Furthermore, to determine whether TiO_2 nanowire arrays could induce molecular changes within bacteria, the abundance of *S. aureus* and *E. coli* proteins were investigated using quantitative proteomic analysis.

4.5.1 Culture-based investigations

The effect of TiO_2 nanowires on bacterial viability were initially investigated by viable counts, which enabled antibacterial activity to be measured quantitatively based on the growth and proliferation of *S. aureus* and *E. coli.* This approach heavily relies on the ability to recover bacteria from the test surface. In this study a "soft" washing step was used as the detachment procedure, whereby samples were transferred into Tris-HCl (1 mL) and gentle pipetting action was used to remove bacteria. However, it was found that *S. aureus* and *E. coli* recovery had been strongly influenced by surface nanoroughness, resulting in fewer bacteria being recovered from nanowire arrays compared to control discs. Therefore, it was clear that this approach overestimated the antibacterial effect of TiO_2 nanowires, limiting the quantitative accuracy of these data. This trend is consistent with previous studies that have reported that increased surface roughness can enhance microbial retention (Bollen et al., 1997; Costa et al., 2016; Medilanski et al., 2002; Whitehead and Verran, 2006; Yoda et al., 2014). Alternative methods could have been employed to improve the removal of *S. aureus* and *E. coli* from nanowire arrays, such as sonication or enzymatic treatments (Doll et al., 2016). Nevertheless, the percentage recovery rates achieved by these approaches have also been shown to vary, depending on the type of surface, processing time, processing conditions and the initial number of bacteria (Doll et al., 2016).

Previous studies have reported that enzymatic treatments can increase the proportion of dead bacterial cells within the recovered suspension (Doll et al., 2016). These observations were determined by LIVE/DEAD staining, indicating that enzymatic treatments can weaken the bacterial envelope, which in turn, could increase the likelihood of nanowire-induced envelope penetration and cell death. Bacterial recovery via sonication methods could result in a similar false-positive effect and there are several routes by which this could occur: Firstly, the acoustic cavitations that are generated during sonication have been shown to induce envelope damage in *E. coli*. This is caused by the dissociation of water molecules into free radicals (e.g. ·OH), and is enhanced in the presence of TiO_2 (Rahman et al., 2010). Furthermore, sonication is likely to damage TiO_2 nanowire surfaces, leading to a suspension of nanowire fragments. Previous studies have reported that suspensions containing SWCNTs can induce bacterial envelope damage in Gram-positive (*S. aureus, B. subtilis*) and Gram-negative (*P. aeruginosa, E. coli*) bacteria. This is proposed to be caused by the "nano-dart" effect of SWCNT (Liu et al., 2009). Another fundamental issue with viable counts is that bacteria are removed from the test environment. *Salmonella typhimurium* has been reported to remain viable after repeated envelope penetration (Suo et al., 2009). As such, transferring bacteria from the nanowire arrays onto a nutrient rich agar could be expected to facilitate repair, resulting in the antibacterial properties of a surface being underestimated.

Despite the limitations of viable counts, this method has been utilised in several publications investigating the antibacterial efficacy of natural and synthetic nanotopographies. In one study, dragonfly wings and dragonfly mimetic bSi samples were immersed in 5 mL of PBS containing *P. aeruginosa, S. aureus* or *B. subtilis*. These suspensions were then sampled at discrete time intervals by removing 100 µL of the suspension and performing viable counts (Ivanova et al., 2013). This study reported average killing rates of up to 450,000 cells min^{-1} cm^{-2} against all tested bacteria. However, it is clear that this methodology could result in inaccuracy. Firstly, the viable counts will not be representative of the surface attached bacterial populations, due to the sampling method used. Secondly, bacteria were incubated in PBS, meaning that any signs of cell death may be attributed to nutritional starvation and not the nanotopography. Other studies have used similar methodologies to perform viable counts (Bandara et al., 2017; Nowlin et al., 2014). Irrespective of the methodology used to recover or sample bacteria, it is clear from this study that the final viable counts are strongly influenced by recovery of bacteria from the nanotopography. This brings into question the validity of existing published data that have reported significant reductions in viability using viable counts.

4.5.2 Microscopic investigations

To date, most studies have utilised LIVE/DEAD staining in conjunction with endpoint fluorescence microscopy, which enables bacterial viability to be calculated per area as a function of envelope integrity (Bhadra et al., 2015; Diu et al., 2014; Fisher et al., 2016; Hasan et al., 2013; Hazell et al., 2018a; Hazell et al., 2018b; Ivanova et al., 2013, 2012; Nowlin et al., 2014). In this study, LIVE/DEAD staining revealed no evidence that TiO_2 nanowires had induced envelope damage in *S. aureus* or *E. coli* after short incubations (3 hours). This finding is contrary to many previous studies, which have reported high killing rates on natural and synthetic nanotopographies within the same time frame (Ivanova et al., 2013, 2012). This inconsistency is most likely attributed to the different methodologies used. Firstly, in this study, approximately 35% of the total disc area was visualised by fluorescence microscopy. By comparison, the first study to report mechanical rupture of *P. aeruginosa* had visualised less than 1% (0.000256%) of the cicada wing surface (Ivanova et al., 2012). Similar approaches have been adopted in subsequent publications (Hasan et al., 2013; Ivanova et al., 2013). This finding highlights two important issues. First, microscopic investigations involving LIVE/DEAD staining must analyse the entire surface, to account for intra- and inter-disc variability, as was shown in this study with end point fluorescence microscopy and in-situ CLSM. Furthermore, without standardised methodologies, it is difficult to directly compare the antibacterial efficacies of nanotopographies across different studies, which hinders progression toward a performance benchmark.

LIVE/DEAD staining analysis was also performed using a multiwell plate reader. Although this approach enabled a signal to be detected from the entire surface, the assay was not sensitive enough to measure the signal originating from *S. aureus* and *E. coli*. This was attributed to the high background autofluorescence of SYTO9 and PI in the presence of LB broth. Consequently, no valid conclusions could be drawn from the multiwell plate reader data. Also, the signal intensity of SYTO9 and PI was reduced on nanowire surfaces compared to control, indicating that nanowires had the capacity to quench fluorophore emission. Further to the problems encountered in this study, the limitations of LIVE/DEAD analysis have been discussed elsewhere (Doll et al., 2016; Shi et al., 2007; Stiefel et al., 2015). First of all, the fluorescence intensity of SYTO9 has been reported to decrease significantly over time (4-8% per 5 minutes), in a process known as bleaching. This effect could be expected to cause significant variability in image quality. To minimise bleaching in this study, imaging of all

samples was restricted to 15 minutes. However, the caveat of this is that high throughput testing could not be performed.

Additionally, LIVE/DEAD staining must be critically evaluated to exclude false positive and negative data, as there are a number of routes through which this can arise. SYTO9 emission has been reported to occur at the emission wavelength of PI. This background cross signalling could be interpreted as increased levels of cell death when fluorophores are used in combination (Stiefel et al., 2015). The emission intensity of SYTO9 has been shown to be 18-times stronger in dead *P. aeruginosa* cells compared to live cells, which could lead to dead cells being mistaken for live cells (Stiefel et al., 2015). Rapidly dividing cells are more permeable to PI than stationary phase cultures, which can lead to higher reported killing rates in exponential phase cultures (Shi et al., 2007). Bacterial cells can also have intact envelopes whilst being unculturable and metabolically inactive, leading to an overestimation of live cells (Doll et al., 2016). Considering the limitations discussed, it is evident that LIVE/DEAD staining can result in unreliable and misleading data, if not critically evaluated for its accuracy. This raises serious questions over the validity of published data that have used LIVE/DEAD staining in isolation to determine the bactericidal properties of natural and synthetic nanotopographies.

LIVE/DEAD analysis does not indicate whether bacteria are capable of growth and division (Kwolek-Mirek and Zadrag-Tecza, 2014; Stiefel et al., 2015). As such, in this project, in-situ CLSM with automated image acquisition, tile scanning and environmental chamber was used to monitor the growth of *S. aureus* and *E. coli* expressing GFP across entire surfaces. As for SYTO9 and PI, the emission signal of GFP was generally lower on nanowire surfaces compared to control, while these differences did not reach statistical significance, it is possible that nanowires possesses GFP quenching properties. During in-situ CLSM analysis, the emission intensity of GFP was strongest on control surfaces at time point zero, while NW2 and NW3 discs showed comparatively weak emissions. Consequently, it was not possible to determine whether nanowire arrays impaired *S. aureus* or *E. coli* growth compared to control. The reduction in GFP emission from NW2 and NW3 is possibly an optical artefact caused by the presence of nanowires. In one study, Alexa Fluor 488 and 555 were used to stain f-actin filaments within embryonic mouse fibroblasts (NIH/3T3); the fluorescence intensities were quantified from cells that had been incubated on planar gold (pl-Au) or nanoporous gold (np-Au) surfaces. Fibroblasts on np-Au surfaces displayed a 3-fold decrease in Alexa Fluor 555 fluorescence and a 1.5-fold decrease for Alexa Fluor 488. This effect was attributed to

increased light scattering and localised surface plasmon resonance (LSPR) on the np-Au surface (Chapman et al., 2017).

LSPR is an optical phenomena caused by the trapping of light waves; this process is frequently observed on nanoparticle (NP) surfaces when the average feature size is less than the incident wavelength of light. Thus, when incident photons interact with the surface, electrons within the conduction band of NPs can resonate, these are known as surface plasmons. This interaction may result in a loss of photon emission intensity due to absorption or scattering. The ratio between photon absorption and scattering is strongly influenced by the shape and size of NP, with a general increase in scattering as the size of NPs increases. For example, for rectangular (rod-shaped) NPs, when the aspect ratio is increased, the amount of photon scattering increases markedly (Petryayeva and Krull, 2011). In this study, it is possible that photon scattering caused by LSPR led to the reductions in GFP emission from nanowire surfaces, since the average spacing of nanowires is < 200 nm and the aspect ratio is >10. Thus, as biofilms grows vertically away from the surface, the effects of photon scattering would diminish, which is mostly likely to manifest as delayed GFP detection. Furthermore, this effect is likely to have influenced the reduced SYTO9 and PI emission on nanowire surfaces compared to control, in the absence of bacteria.

Nonetheless, it was evident from CLSM analysis that the intensity of PI staining for *S. aureus* and *E. coli* was higher on nanowire discs, most noticeably on NW3. Therefore, even with the effects of photon scattering, it is evident that envelope damage had occurred. Furthermore, the distribution of red fluorescing *S. aureus* and *E. coli* cells was different between nanowire and control discs. On nanowire discs, PI staining was observed across the whole surface, whereas PI staining was in concentrated areas on control surfaces. These data support that structural damage was mediated by TiO_2 nanowires. Since PI staining was not observed after 3 hours using LIVE/DEAD staining, this appears to suggest that envelope damage occurred in a time-dependent manner.

4.5.3 Biochemical methods

Although extensive research has been carried out to assess the antibacterial properties of natural and synthetic nanotopographies, very few studies have utilised biochemical assays. In fact, since the bactericidal activity of cicada wings was first described in 2012, only one publication has used biochemical assays in addition to culture-based methods or microscopic investigations (Sjöström et al., 2016). This is problematic, as these non-biochemical approaches lack specificity and provide limited information on the physiological status of a cell. For example, for viable counts, bacteria are categorised as live or dead based on their ability to divide, yet bacteria may remain viable and metabolically active even if they are not dividing. The same is true for LIVE/DEAD staining, in that bacteria are recognised as live or dead based on membrane permeability, yet bacteria with intact envelopes may not be viable. Furthermore, it is possible that membrane damage could be repaired, this has been observed in *S. typhimurium* following repeated envelope penetration (Suo et al., 2009). It is therefore crucial that a combination of methods is utilised to provide more detailed information on the physiological status of bacteria.

This study sought to achieve this goal by utilising the metabolic indicator assays RTG and BTG. RTG enabled bacterial viability to be monitored continuously in a plate reader format, providing more detailed information on the physiological status of bacteria on TiO_2 nanowire arrays. The limitation of this technique was its poor sensitivity with Gram-negative bacteria. Nevertheless, using RTG, significant reductions in *S. aureus* and *S. epidermidis* growth were revealed in the presence of nanowire discs, observed at 9 and 4 hours respectively. While similar trends were observed in *E. coli* and *K. pneumoniae*, these differences did not reach statistical significance. This was attributed to the lower reducing capacity of Gram-negative bacteria compared to Gram positive bacteria. To overcome the limited sensitivity of RTG in Gram-negative bacteria in this study, BTG was utilised. Of all the approaches used in this study, BTG was the fastest, involving the least number of steps, and was able to achieve high sensitivity. The results presented for *S. aureus* showed significant reductions in viable bacteria on NW2 and NW3 after 10 hours, corroborating with RTG experiments. For *E. coli* and *K. pneumoniae*, significant reductions in viable cells were observed after 3 hours incubation, which had not been identified using RTG or LIVE/DEAD analysis. Of note, BTG analysis revealed no significant differences for *S. epidermidis* at any time point, while RTG analysis indicated a significant reduction on NW2 and NW3 after 4 hours. This inconsistency is most

likely to have been caused by the inter-experimental variation observed on control discs for *S. epidermidis*.

These findings illustrate how the data obtained from different methodologies, LIVE/DEAD, RTG and BTG, can lead to different conclusions. In this case, the underlying cell properties that are investigated are not the same; LIVE/DEAD determines envelope permeability while RTG monitors cellular redox potential and BTG measures ATP concentration. Therefore, each assay could be expected to perform differently, based on the type of bacteria and experimental parameters used (Doll et al., 2016; Kwolek-Mirek and Zadrag-Tecza, 2014). This highlights the importance of utilising several methods to study the bacterial response to nanowire arrays. Not only will this avoid incomplete or biased conclusions, but it will help to answer specific scientific questions.

4.5.4 Proteomic analysis and oxidative stress response

Proteomic analysis identified 90 *S. aureus* proteins and 27 *E. coli* proteins that had changed significantly in abundance in the presence of nanowire array NW3. Furthermore, these DEPs displayed significantly more interactions than would be expected for a random set of proteins, strongly indicating a biological connection. It was noted that a significant number of *S. aureus* and *E. coli* DEPs were involved in protection from oxidative stress. Exposure to ROS, such as superoxide anions and hydroxyl radicals, can lead to extensive cellular damage, causing defects in the structure and function of DNA, proteins and the bacterial envelope (Arts et al., 2015). As such, bacteria have evolved a number of mechanisms to survive and adapt, including detoxification and repair enzymes. Many of these proteins had been upregulated in *S. aureus* and *E. coli*. Furthermore, levels of ROS, H_2O_2, were found to be significantly higher in *S. aureus* and *E. coli* incubated on NW3 than on controls. Taken together, these data indicate that ROS generation could, at least in part, have mediated the reduction in bacterial viability and increased cell permeability seen for bacteria incubated on NW3.

The precise mechanism of ROS generation remains unclear. It is, however, very unlikely that it was caused by photocatalytic activity of NW3, since the crystal structure of TiO_2 nanowires on NW3 was shown to be predominantly rutile by GIDX, and rutile phases are known to possess low photocatalytic activity (Luttrell et al., 2014). An alternative explanation is that physical contact with nanowires may induce ROS production. Indeed, it is widely acknowledged that oxidative stress responses have overlapping activating signals (Mitchell and Silhavy, 2019). For example, antibiotics such as aminoglycosides and quinolines are known to

induce oxidative stress (Vatansever et al., 2013), as do certain metals (copper) (Baker et al., 2010) and redox stress caused by the accumulation of misfolded proteins (Arts et al., 2015). Thus, it is possible that the increased abundance of oxidative stress proteins and elevated levels of H_2O_2 are attributable to TiO_2 nanowire arrays.

Previous research has established a connection between ROS-mediated cell death and nanostructure contact. In one study, CNTs were shown to increase ROS production in *C. albicans*, *P. aeruginosa* and *S. aureus* following 24 hour incubation. ROS production was proposed to have been induced by physical contact with the CNT, that were reported to wrap around bacteria rather than pierce the envelope. Of note, ROS production was shown to occur independently of photocatalytic activation (Olivi et al., 2013). Further to this, shear stress has been reported to induce apoptosis-like cell death in *B. subtilis*, caused by the elevated presence of intracellular superoxide radicals (Sahoo et al., 2006, 2003). Importantly, reductions in *B. subtilis* viability occurred independently of lactate dehydrogenase (LDH) release, indicating that shear stress-induced cell rupture was not the mechanism of action. A recent study has shown that bacterial ROS production can occur in response to a wide variety of stressors. Of note, this mechanism is self-amplifying, meaning that ROS production is sustained, even when the initial stressor is removed (Hong et al., 2019). A similar mechanism has been reported to occur in human mesothelial cells (Met-5A) incubated with MWCNTs (diameter 110-190 nm, length 5-9 μm). The levels of superoxide anion had increased in Met-5A cells, which occurred in line with increases in membrane permeability, as determined by the LDH assay and reductions in metabolism, determined by Cell Titer-Glo. Furthermore, SOD-2 expression was upregulated at the mRNA and protein levels, which is indicative of an oxidative stress response (Yu et al., 2016). The findings of the current study are consistent with previous literature, indicating that direct contact between bacteria and TiO_2 nanowires causes a general oxidative stress response via the production of ROS.

Furthermore, the superhydrophilic wetting observed on NW3 may have enhanced this process through increased shear-stress. Planktonic bacteria within a bulk liquid must pass through the hydrodynamic boundary layer to reach the solid surface. Within the bulk liquid, bacteria can move freely and here the forces experienced are lower than in the hydrodynamic boundary layer. The level of shear force exerted at the hydrodynamic boundary layer is dependent on the bulk liquid flow rate, which is largely determined by surface chemistry. When the flow rate is increased, this reduces the size of the hydrodynamic boundary layer, which leads to increased shear stress near the surface (Berne et al., 2018). Owing to the superhydrophilic wetting of

NW3, it is possible that these conditions would lead to higher flow rates, meaning the shear forces would be greater on NW3 compared to control surfaces, and thus higher levels of ROS would be generated within the bacterial cells.

Sahoo and colleagues proposed that shear stress increased the activity of an NADH oxidase-like enzyme in *B. subtilis*, resulting in the elevated levels of superoxide radicals (Sahoo et al., 2006). Consistent with this, the abundance of NADH-dependent flavin oxidoreductase (NWMN_0315) increased nearly 6-fold in *S. aureus* on NW3 in this study. A homologous protein in *B. subtilis*, YqjM, catalyses the oxidation of NADH and NADPH in molecular oxygen (Fitzpatrick et al., 2003). Such catalysis generates superoxide radicals, which dismute to form H_2O_2 (Slauch, 2012). Thus, it is possible that NWMN_0315 caused the elevated levels of superoxide radicals within *S. aureus*, leading to significant increase of H_2O_2 on NW3. There are further similarities between the proteomic response of *S. aureus* in this study and the work of Sahoo and colleagues. Firstly, the levels of DNA fragmentation were found to be significantly raised under high shear stress (Sahoo et al., 2006), while in this study the abundance of SOS response proteins UvrA, UvrC and bleomycin resistance protein had increased significantly in *S. aureus*, which mediate repair of DNA damage (Silva et al., 2017; Sugiyama et al., 1995). Furthermore, the levels of histone-like DNA-binding protein HU had increased, which is involved in DNA stabilisation under extreme environmental conditions (Almarza et al., 2015). These findings strongly indicate that DNA damage had occurred in *S. aureus* recovered from NW3.

It is possible that oxidative stress could have contributed to the increased abundance of iron uptake proteins observed in *E. coli* recovered from NW3, as iron is an important cofactor for many oxidative stress proteins (Horsburgh et al., 2001). Furthermore, ROS can destabilise iron-sulfur clusters that are present in a number of enzymes, ranging from electron transfer proteins to dehydratases. ROS-mediated oxidation of such enzymes can lead to inactivation and iron release (Djaman et al., 2004), which could prove lethal to bacteria. Thus, the increased abundance of iron uptake proteins may be attributed to this. Alternatively, the increased abundance of iron uptake may be directly related to biofilm development. A number of studies have shown the importance of iron for efficient biofilm formation, including *P. aeruginosa*, *S. aureus* and *B. subtilis* biofilms. The quantity of ferric iron required for *B. subtilis* biofilm formation can extend to 100-fold greater than planktonic growth (Banin et al., 2005; Lin et al., 2012; Qin et al., 2019). In a recent study, iron was proposed to promote biofilm formation by enhancing the production of iron-containing proteins involved in oxidative respiration, linked

with increased matrix production. Furthermore, a large proportion of iron was associated with the extracellular matrix, which could act as electron receptors and shuttles, which may be important for bacteria at the centre of biofilms that are oxygen deprived (Qin et al., 2019).

Alongside associations with oxidative stress, a large number of upregulated *S. aureus* DEPs were directly involved in protein synthesis. It is possible that this increased the susceptibility of *S. aureus* to ROS mediated cell death on NW3, since downregulation of protein synthesis has been reported as a protective mechanism against a number of stresses. Sahoo and colleagues treated *B. subtilis* with chloramphenicol (protein-synthesis inhibitor) prior to shear stress and showed that the final ratio of viable cells to dead cells was higher in the chloramphenicol treatment group, implying a protective effect. Halting protein synthesis has also been reported to protect microbes against copper and oxidative stress. In one study, *S. aureus* was exposed to excess copper and subsequent transcriptomics revealed that protein translation had been downregulated, while proteins involved in misfolding and oxidative stress had increased, much like in this study (Baker et al., 2010). Madeo and colleagues found that inhibition of protein synthesis in *C. albicans* led to protection from oxidative stress-mediated cell death (Madeo et al., 1999). Thus, it could conceivably be hypothesised that the upregulation of protein synthesis in *S. aureus* increased susceptibility to nanowire-induced and/or shear stress-induced ROS production.

CHAPTER 5

Visualising bacteria-nanowire interactions

5.1 Introduction

Visualising the interface between bacteria and nanostructures has been of critical importance for determining the antibacterial mechanisms of natural and synthetic nanotopographies. A number of microscopy techniques have been used for this purpose, including CLSM, CLEM and EM approaches (Jenkins et al., 2018). The previous chapter discussed the use of CLSM to monitor bacteria-nanotopography interactions in-situ. However, this approach could not resolve bacterial membranes directly, instead relying on the emission of PI fluorescence to infer nanowire-induced membrane damage. Furthermore, the resolution constraints of CLSM meant that bacteria-nanotopography interactions could not be precisely investigated at the single-cell level, owing in part to the concealment of the underlying nanotopography. Thus, approaches that can visualise both nanotopography and bacteria at nanometre resolution are required.

To date, SEM techniques have been extensively used to investigate such interactions, as they provide a simple method to identify nanoscale changes in bacterial surface morphology upon adhesion to nanotopographies. Indeed, SEM analysis was the first technique to reveal that *P. claripennis* wings could mediate physical rupturing of *P. aeruginosa* cells (Ivanova et al., 2012) (Figure 5.1). Comparable methodologies have since been used to infer the antibacterial activity of nanotopographies, as indicated by deformation of bacterial cells (Tripathy et al., 2017). Because SEM analysis is normally restricted to visualising surface morphologies from the top, it cannot determine conclusively whether underneath nanotopographies penetrate the bacterial envelope. This limitation has resulted in the use of alternative techniques, such as TEM and FIB-SEM.

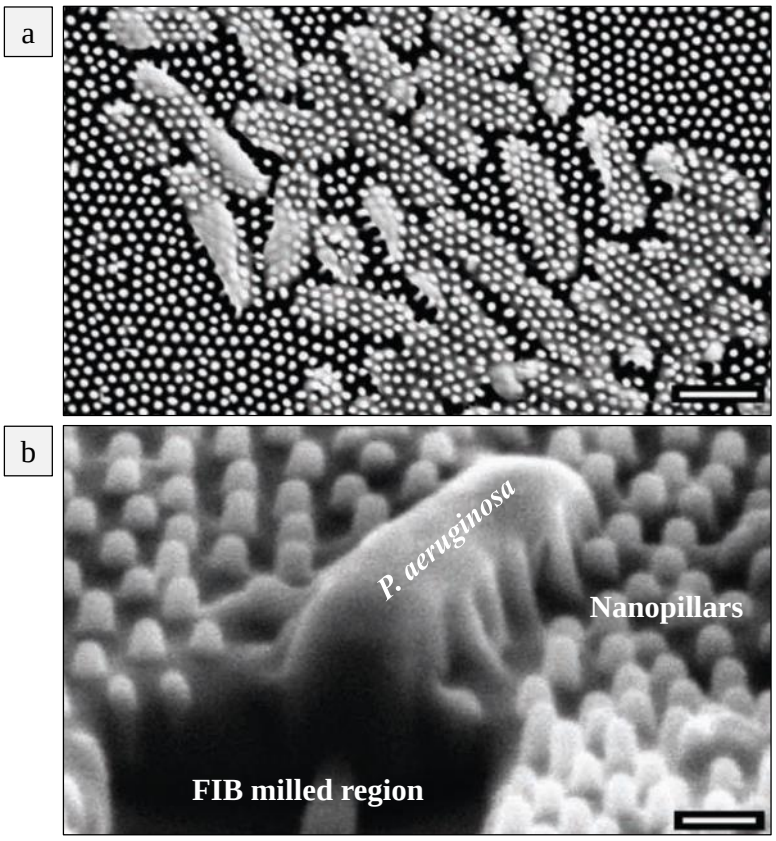

Figure 5.1 | Nanopillar-induced mechanical rupture of *P. aeruginosa*. (a) Top view SEM showing nanopillar-induced rupture of *P. aeruginosa* cells on the surface of a cicada wing. Scale bar = 1 µm. (b) Tilted SEM image of a *P. aeruginosa* cell sinking between the nanopillars on the cicada wing surface. FIB milling was used to generate a cross section in front of the cell. Scale bar = 200 nm (Ivanova et al., 2012).

A number of publications have utilised TEM to resolve the envelope and ultrastructure of bacteria in contact with nanotopographies (Figure 5.2). Since TEM involves the generation of cross sections from resin embedded sections, this approach can determine whether nanowires penetrate the bacterial envelope. Bandara and colleagues performed TEM and FIB-SEM analysis of *E. coli* cross sections that had been incubated on *O. villosovittatum* (dragonfly) wings. Interestingly, no direct contact was identified between the nanotopography and bacteria, yet there was evidence of membrane deformation and separation. It was proposed that EPS production could lead to strong adhesion forces, resulting in membrane damage (Bandara et al., 2017). Linklater and colleagues utilised FIB milling to generate TEM lamella of *S. aureus* and *P. aeruginosa* cells in contact with CNTs. TEM analysis showed the internalisation of nanotubes, thus indicating that CNTs had mediated deformation and rupture of bacterial envelopes. Morphologies consistent with these findings were also reported by direct FIB cross sectional analysis. In this case, the high flexibility of CNTs was proposed to mediate bacterial cell death through the storage and release of mechanical energy (Linklater et al., 2018).

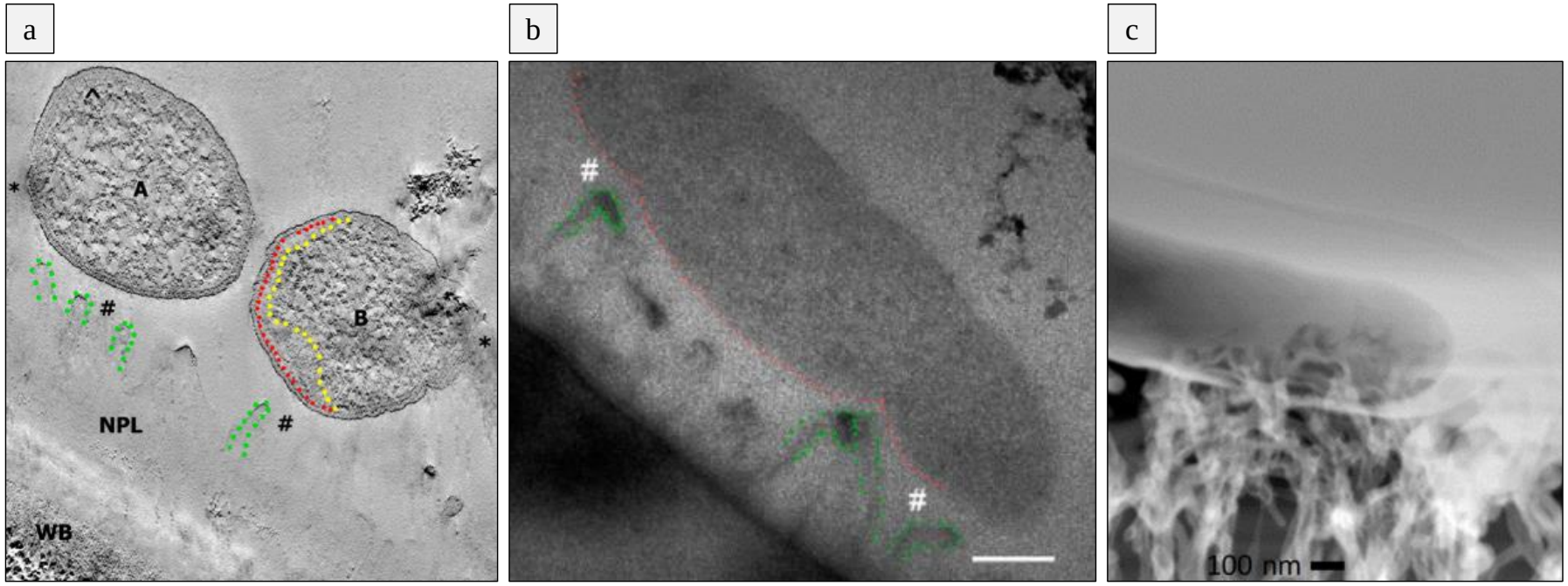

Figure 5.2 | TEM analysis of bacteria-nanotopography interactions. TEM micrographs of the interface between *E. coli* and *O. villosovittatum* dragonfly wing (a-b). Direct contact between nanopillars (green lines) and bacterial envelope is not observed, but envelope separation is seen (red and yellow lines) (a). Furthermore, the envelope is deformed inward (b). Scale bar = 200 nm (Bandara et al., 2017). TEM micrographs showing the internalisation of CNTs into *P. aeruginosa* (c) (Linklater et al., 2018).

More frequently than TEM, visualising the interactions between bacteria and nanotopographies has been achieved by FIB-SEM analysis (Figure 5.3). As for TEM, FIB-SEM enables bacterial ultrastructure and envelope morphology to be visualised at nanoscale resolution. The distinct advantage of this approach is that bacterial analysis can occur on a single cell basis, avoiding the more complex processing that is associated with resin embedded sections. In general, FIB-SEM analysis of bacteria in contact with nanotopographies is achieved via two approaches. Firstly, thin sections (lamella) of bacteria are prepared by FIB-milling. These lamella are then transferred to a FIB-liftout grid, which can be analysed by TEM or tomography (Jenkins et al., 2018; Linklater et al., 2018). Alternatively, FIB-milling of bacteria can be performed directly on the nanotopography. Single or sequential milling processes can be utilised; however, most publications have employed single sectioning. Ivanova and colleagues first reported *P. aeruginosa* cells sinking between the nanopillar arrays on the cicada wings, in which FIB-SEM was used to excavate regions of the surface in front of the ruptured cell (Ivanova et al., 2012). Nowlin and colleagues utilised FIB-milling to generate cross sections through *S. cerevisiae* adhered to a cicada wing nanotopography. This analysis clearly resolved the cell-material interface, which indicated that physical interactions had ruptured the cells, leading to a gum drop-like morphology (Nowlin et al., 2014). Bhadra and colleagues utilised FIB-SEM to investigate the engulfment of *P. aeruginosa* cells on dragonfly inspired titanium nanowire arrays. In general agreement with previous studies, membrane deformation was attributed to physical contact, resulting from the energy gain upon initial attachment to the surface (Bhadra et al., 2015). FIB-SEM analysis was also employed by Linklater and colleagues, revealing that short incubation periods on bSi surfaces are sufficient to mediate initial stretching of *S. aureus* and *P. aeruginosa* cells (Linklater et al., 2018). Furthermore, Cao and colleagues reported cytoplasm leakage from *S. epidermidis* that had been incubated on a spear-type titanium surface. FIB-SEM analysis revealed that nanostructures with sharp tips (50 nm) could deform and penetrate the bacterial envelope (Cao et al., 2018).

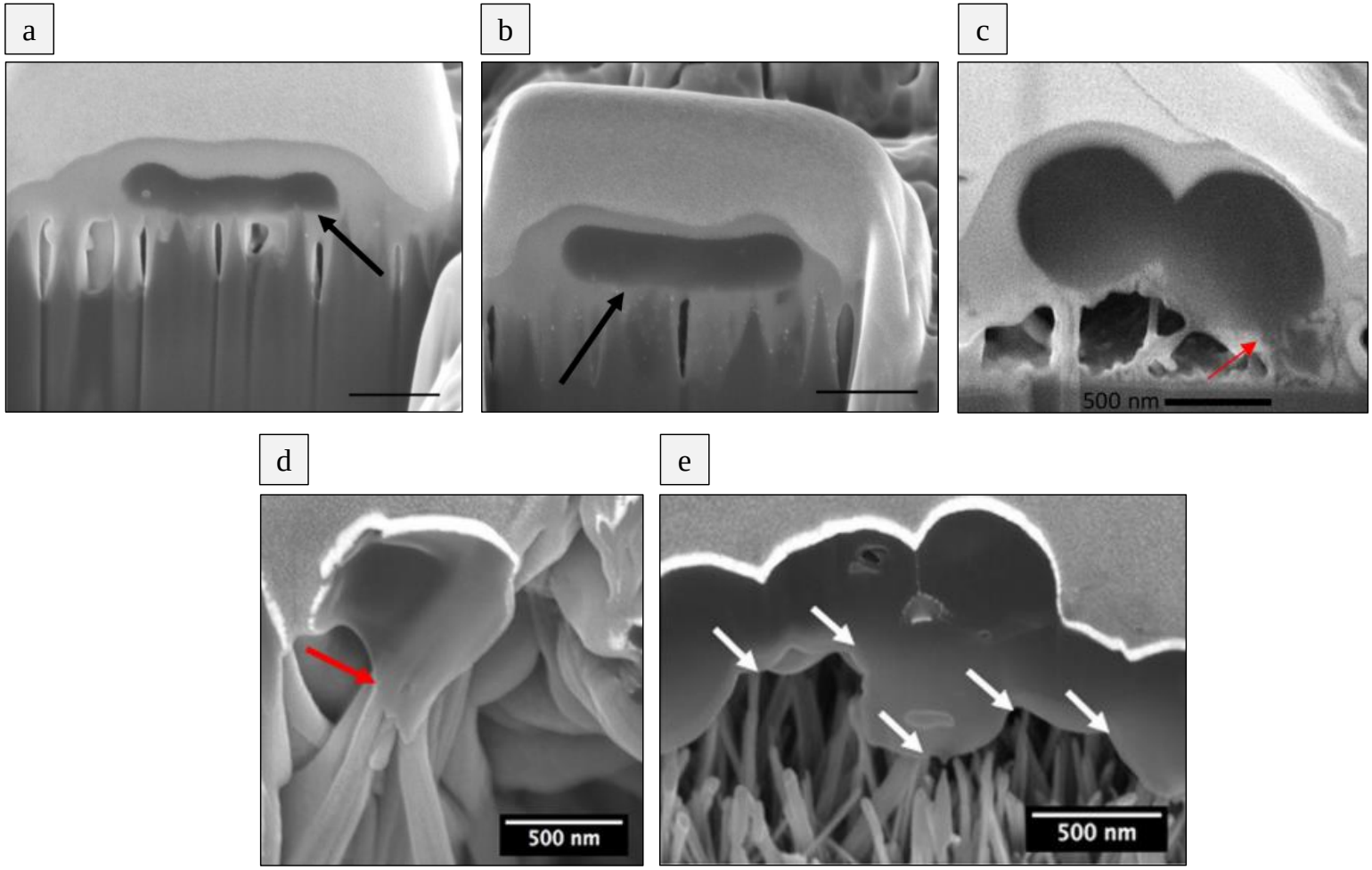

Figure 5.3 | FIB-SEM analysis of bacteria-nanotopography interactions. SEM images of *P. aeruginosa* cells adhered to bSi surface. Milling was performed after 30 minutes incubation, showing initial envelope stretching (a-b). Scale bar = 400 nm. (Linklater et al., 2017). SEM micrographs showing FIB-cross sections through *S. aureus* (c) incubated on CNTs (Linklater et al., 2018). FIB-cross sections through *S. epidermidis* showing penetration on pocket-type nanospears (d) and deformation on spear-type nanospears (e) (Cao et al., 2018).

While many studies have indicated that nanotopographies mediate mechanical rupture of bacterial and fungal cells, in most cases, this has been inferred from deformed cells that appear to sink or spread into the nanotopography (Hasan et al., 2013; Ivanova et al., 2013, 2012; Nowlin et al., 2014). Considering that the envelope forms a continuous barrier around viable bacteria and fungi, if nanotopographies are capable of penetrating or rupturing this layer, then it would be visible as a discontinuation of the envelope at the point of nanostructure entry. However, as of yet there is no conclusive evidence for this in published TEM and FIB-SEM data. Furthermore, a number of studies have reported loss of turgor pressure as an indicator of rupture. However, this could represent structural artefacts caused by EM processing, rather than a true effect of the surface on the microbial cell. Indeed, such morphologies are consistent with artefacts of cell dehydration (Golding et al., 2016). Nevertheless, on the basis of existing literature, it is evident that EM techniques have played an important role in attempting to determine the mechanistic basis of microbial cell death on different nanotopographies. However, there is still no clear consensus regarding the precise antimicrobial mechanism and, indeed, it might be expected to vary according to type of nanotopography.

In this study, SEM, TEM and FIB-SEM analyses were used to visualise the interactions between TiO_2 nanowire arrays and bacterial cells and, importantly, to determine their effects on surface morphology, envelope integrity and intracellular ultrastructure. In the previous chapter, TiO_2 nanowire arrays NW2 and NW3 were shown to reduce bacterial viability and increase envelope permeability compared to control surfaces. Furthermore, there was evidence of oxidative stress responses within *S. aureus* and *E. coli* that had been incubated on NW3, which appeared to effect bacterial morphology. On the basis of these findings, NW2 and NW3 were selected for imaging analysis.

5.2 Visualising bacteria-nanowire interactions by SEM

In the previous chapter, significant reductions in *S. aureus*, *S. epidermidis, E. coli* and *K. pneumoniae* viability were observed on NW2 and NW3 surfaces compared to control, as determined by RTG and BTG analysis. Nevertheless, on the basis of these data alone, it was unclear whether the reductions corresponded to differences in the number of bacteria per unit area or differences in their metabolic activity. To investigate this, low magnification SEM analysis was employed to determine the bioburden of *S. aureus*, *S. epidermidis*, *E. coli* and *K. pneumoniae* on control, NW2 and NW3 surfaces. In line with BTG and RTG analysis, SEM analysis was performed at discrete time points of 0.5, 1, 3 and 10 hours. The number of bacteria were enumerated at four locations per disc using Fiji software; each enumeration area measured 100 µm by 100 µm (10,000 μm^2).

5.2.1 Determination of bacterial bioburden on control and nanowire surfaces

Following 0.5 h, the densities of all bacteria tested (*S. aureus*, *S. epidermidis, E. coli* and *K. pneumoniae*) were not significantly different between control and nanowire discs (Figure 5.4). With the exception of *K. pneumoniae*, the density of bacteria remained below 100 per 10,000 μm^2. For *S. aureus* and *S. epidermidis*, the density of bacteria remained comparable at 1 h and 3 h and there were no significant differences between control and nanowire surfaces. One possible explanation for this could be that cells were adapting to environmental conditions at the surface, resulting in a lag phase. Nevertheless, after 10 h incubation, the densities of *S. aureus* and *S. epidermidis* had increased markedly to control surfaces compared to NW2 and NW3, with microcolony formation evident (Figure 5.5-5.6). Of note, the average size of *S. epidermidis* microcolonies was noticeably larger than that of *S. aureus* microcolonies, with some extending to 50 µm in diameter. These observations are broadly consistent with RTG and BTG analyses, which revealed significant reductions in *S. aureus* viability on NW2 and NW3 after 9-10 h, while for *S epidermidis,* reductions in viability were observed after 4 h on NW2 and NW3 and were maintained up to 10 h (determined by RTG).

In contrast, for *E. coli* and *K. pneumoniae*, significant differences in cell density emerged after 1 h and 3 h incubations. *E. coli* cell density had increased on control discs after 1 h, whereas densities on NW2 and NW3 after 1 h were similar to 0.5 h. After 3 h, *E. coli* cell density had only increased marginally on the control surface, while more noticeable increases were observed on NW2 and NW3. For *K. pneumoniae*, cell density was significantly lower on NW3 surfaces compared to control and NW2 after 1 h and 3 h incubations. Following 10 h incubations, *E. coli* cell density was significantly higher on control surfaces compared to nanowire surfaces, with the lowest cell density observed on NW2 surfaces (Figure 5.7). A comparable trend was observed for *K. pneumoniae* cell density following 10 h, although in this instance, *K. pneumoniae* cell density was consistently the lowest on NW3 surface at each time point (Figure 5.8). There is some agreement between these observations and the BTG analyses, which revealed significant reductions in *E. coli* viability on NW3 following 3 h and 10 h, and significant reductions on NW2 following 10 h. In contrast, significant reductions in *K. pneumoniae* viability were only revealed at 3 h using BTG.

Of note, for *S. aureus, E. coli* and *K. pneumoniae*, there were significant differences in cell density between nanowire and control surfaces at 10 hours, however, these differences were not all detected by viability indicator assays. A possible explanation for these inconsistencies is the difference in methodologies, with RTG and BTG providing a luminescence readout from the entire surface, while SEM analysis is representative of a reduced surface area. Furthermore, the automated cell counter tool in Fiji is not likely to be able to accurately count all the bacteria within larger microcolonies, because some of the bacteria will be concealed by other bacteria above them. Thus, it is possible that this method could underestimate cell densities, especially after the longer incubations when there are a greater number of microcolonies.

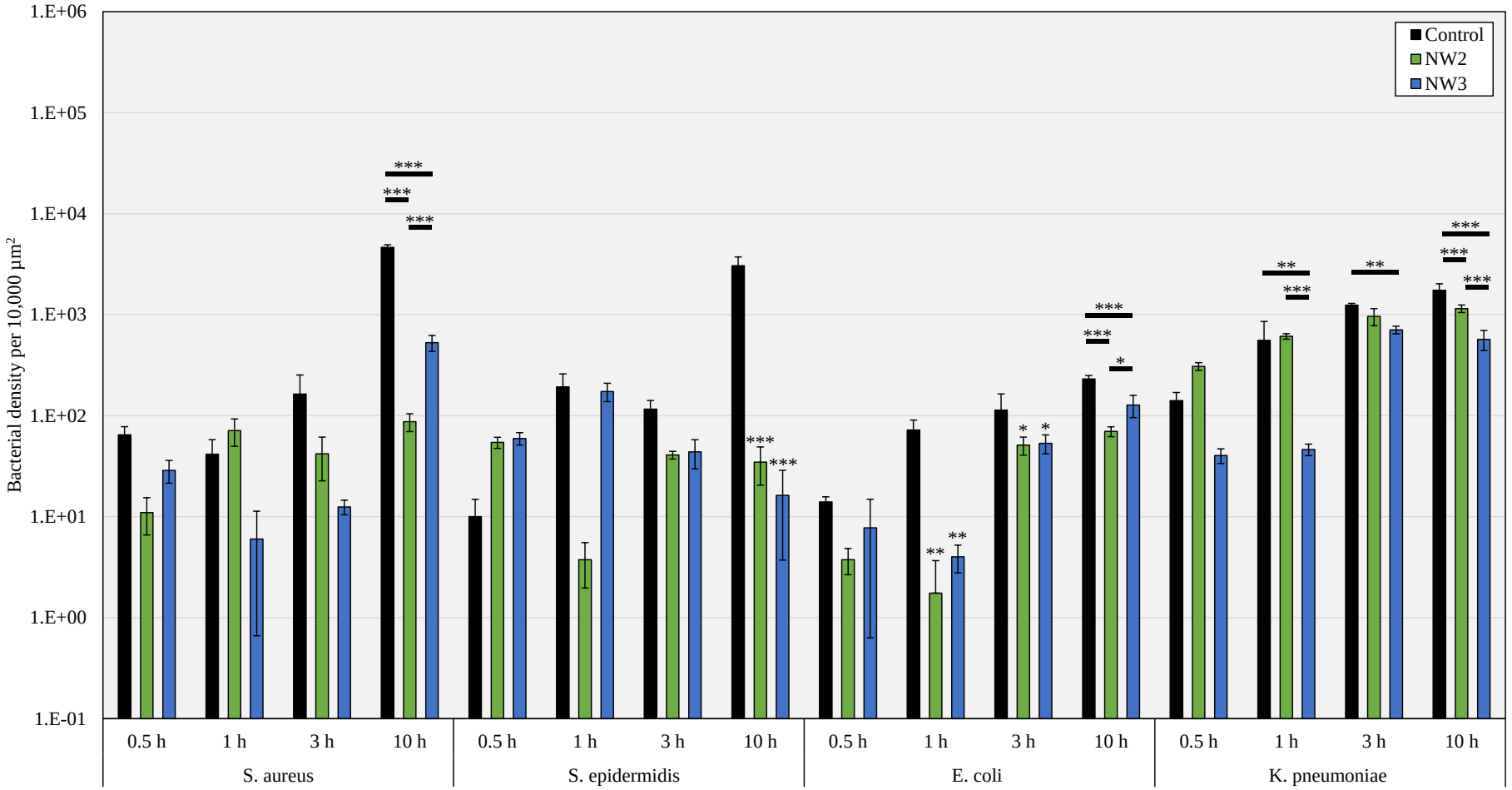

Figure 5.4 | Determination of bacterial bioburden on nanowire and control surfaces. Low magnification SEM micrographs were acquired of control and nanowire (NW2-NW3) surfaces at discrete time points of 0.5, 1, 3 and 10 h. The densities of *S. aureus*, *S. epidermidis*, *E. coli* and *K. pneumoniae* were determined using the cell counting tool within Fiji. Values given are mean ± standard deviation. *P<0.05, **P<0.01 ***P<0.001 compared to control, as determined by one-way ANOVA with post-hoc Tukey HSD; n=1 performed in quadruplicate.

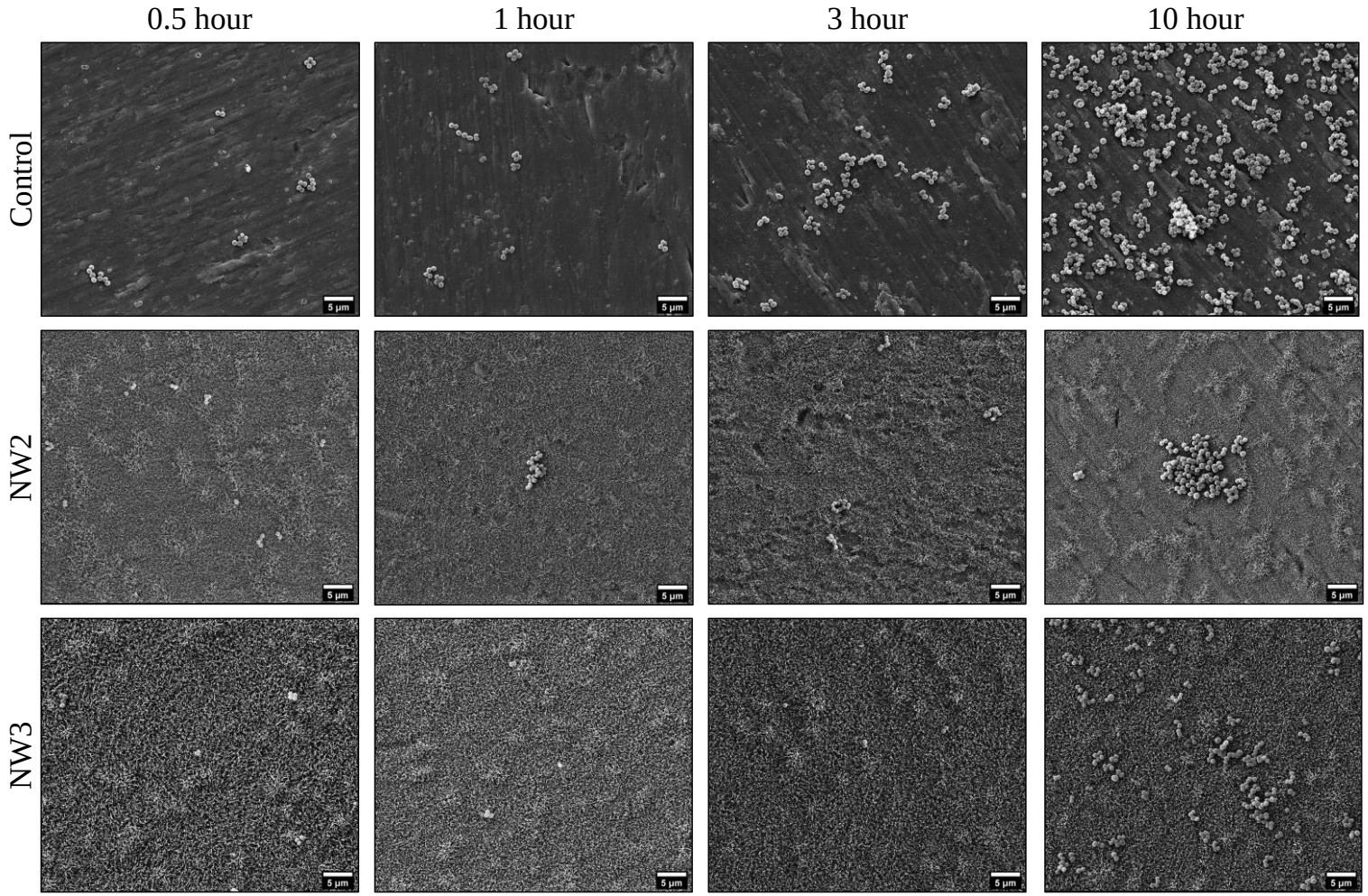

Figure 5.5 | Determination of *S. aureus* growth on TiO_2 nanowire arrays. Low magnification SEM micrographs were acquired of *S. aureus* on control and nanowire (NW2-NW3) surfaces after 0.5, 1, 3 and 10 h incubation.

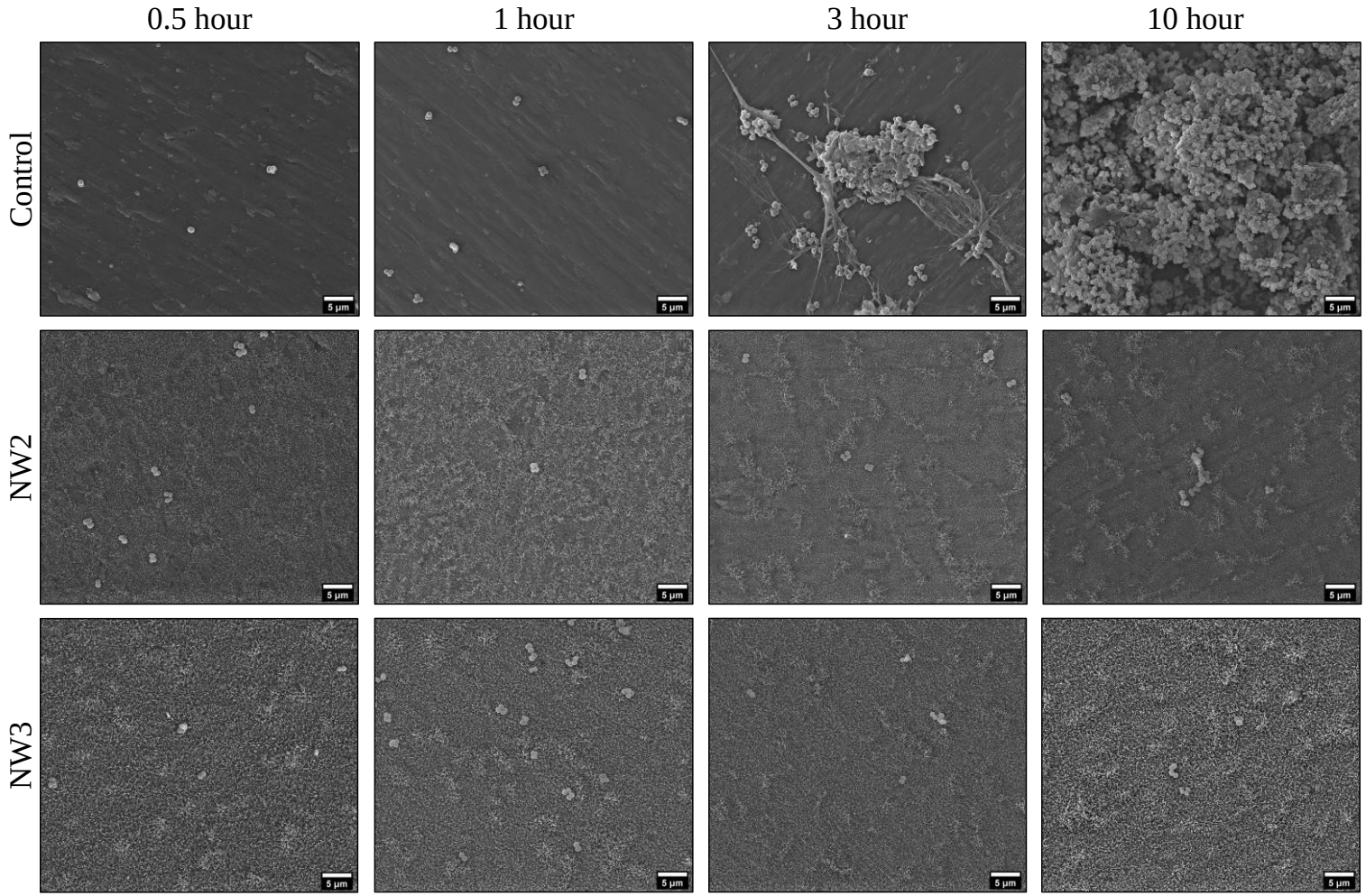

Figure 5.6 | Determination of *S. epidermidis* growth on TiO_2 nanowire arrays. Low magnification SEM micrographs were acquired of *S. epidermidis* on control and nanowire (NW2-NW3) surfaces after 0.5, 1, 3 and 10 h incubation.

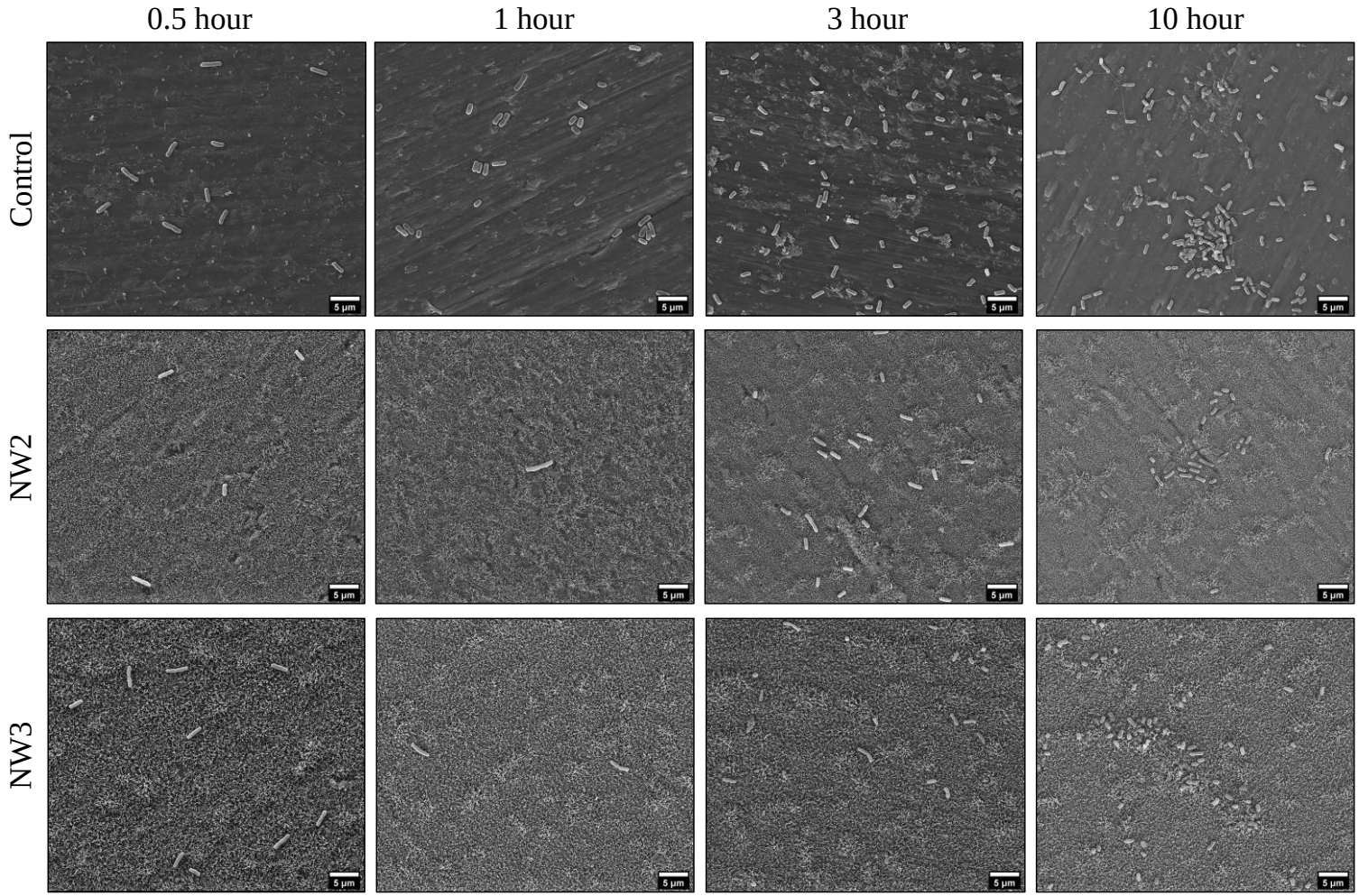

Figure 5.7 | Determination of *E. coli* growth on TiO_2 nanowire arrays. Low magnification SEM micrographs were acquired of *E. coli* on control and nanowire (NW2-NW3) surfaces after 0.5, 1, 3 and 10 h incubation.

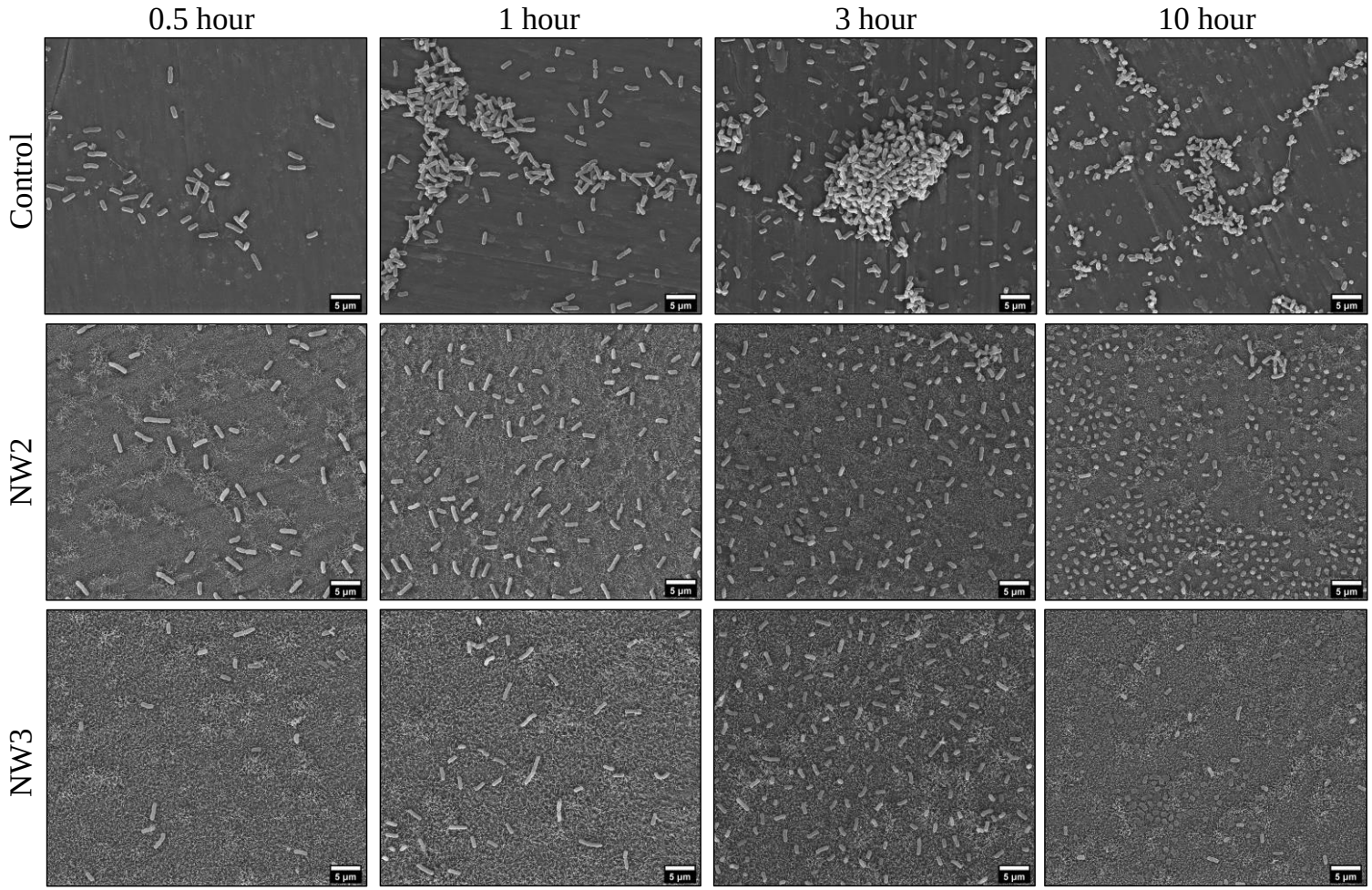

Figure 5.8 | Determination of *K. pneumoniae* growth on TiO_2 nanowire arrays. Low magnification SEM micrographs were acquired of *K. pneumoniae* on control and nanowire (NW2-NW3) surfaces after 0.5, 1, 3 and 10 h incubation.

5.2.2 Analysis of bacterial envelope morphology by SEM

Taken together, SEM determination of bacterial densities and the RTG and BTG analyses from Chapter 4 indicated that the reductions in bacterial viability on nanowire surfaces were likely attributable to differences in the number of bacteria per unit area rather than metabolic activity. This was unlikely to have been caused by variations in bacterial attachment across the surfaces, as the nanowire surfaces had been shown to generally retain greater numbers of bacteria than the control surface. Thus, it is possible that a comparable number of bacteria can initially attach to each surface, but the rate of bacterial division may be slower on nanowire surfaces. To further investigate the cause for these reductions and identify possible mechanisms that could reduce the capacity of bacteria to divide on nanowire surfaces, high magnification SEM analysis was used to examine bacterial surface morphology, as a first possible indication of nanowire-induced envelope deformation, penetration or rupture. For consistency, high magnification SEM analysis was performed at the same time points used for determination of bioburden and bacterial viability testing.

5.2.2.1 SEM analysis of Gram-positive envelope morphology

On control discs, *S. aureus* exhibited the characteristic morphology of clusters of coccoid cells over the entire 10 h incubation period (Figure 5.9). After 3 h, although some microcolonies were observed, *S. aureus* cells were mostly found in diplococcus and tetrad formations. Following 10 h, *S. aureus* microcolonies had become the predominant organisation, characterised by grape-like clusters of cells. On nanowire discs, *S. aureus* cells also displayed the distinctive coccoid morphology, yet the frequency of microcolonies was noticeably lower. Although the morphology of *S. aureus* cells was largely comparable between control and nanowire discs, there were signs that nanowires had deformed the bacterial envelope, as was evident from the concave envelope morphology (Figure 5.10). Nonetheless, this morphology was observed at a low frequency. Alike to *S. aureus*, *S. epidermidis* displayed a coccoid morphology on control and nanowire surfaces after each incubation time (Figure 5.11). Following 3 h, cells on control surfaces mainly displayed diplococcus and tetrad arrangements, while after 10 h, microcolonies had formed. Fewer *S. epidermidis* cells were seen on nanowire surfaces NW2 and NW3 than control. However, the bacterial division septum was frequently observed, indicating that binary fission may have been occurring. Although *S. epidermidis* density was reduced on nanowire discs relative to control, there was no evidence of envelope deformation.

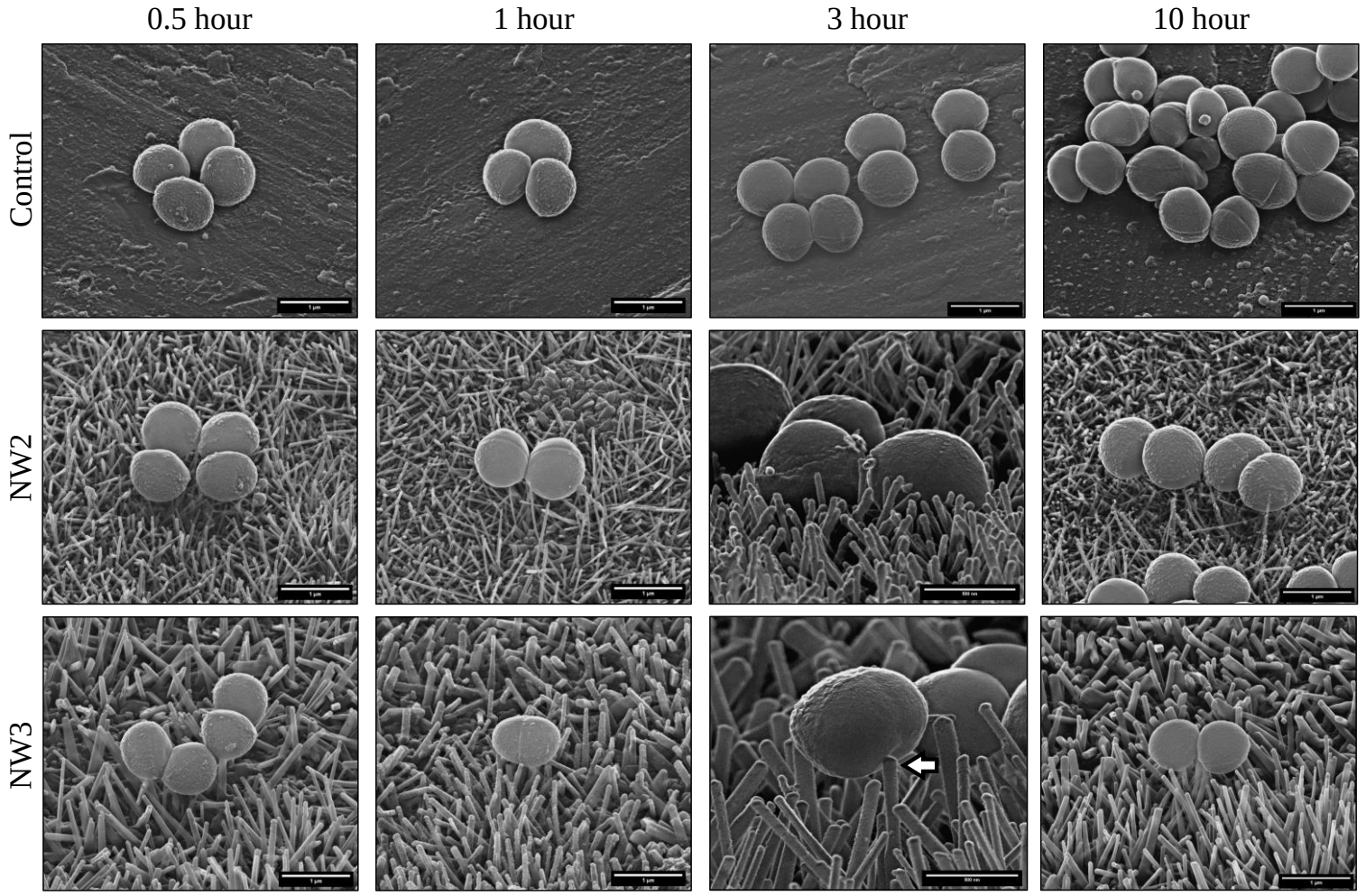

Figure 5.9 | SEM analysis of *S. aureus* envelope morphology on nanowire and control surfaces. Tilted SEMs of *S. aureus* on control and nanowire surfaces after 0.5, 1, 3 and 10 h incubations. White arrows indicate regions of nanowire-induced envelope deformation.

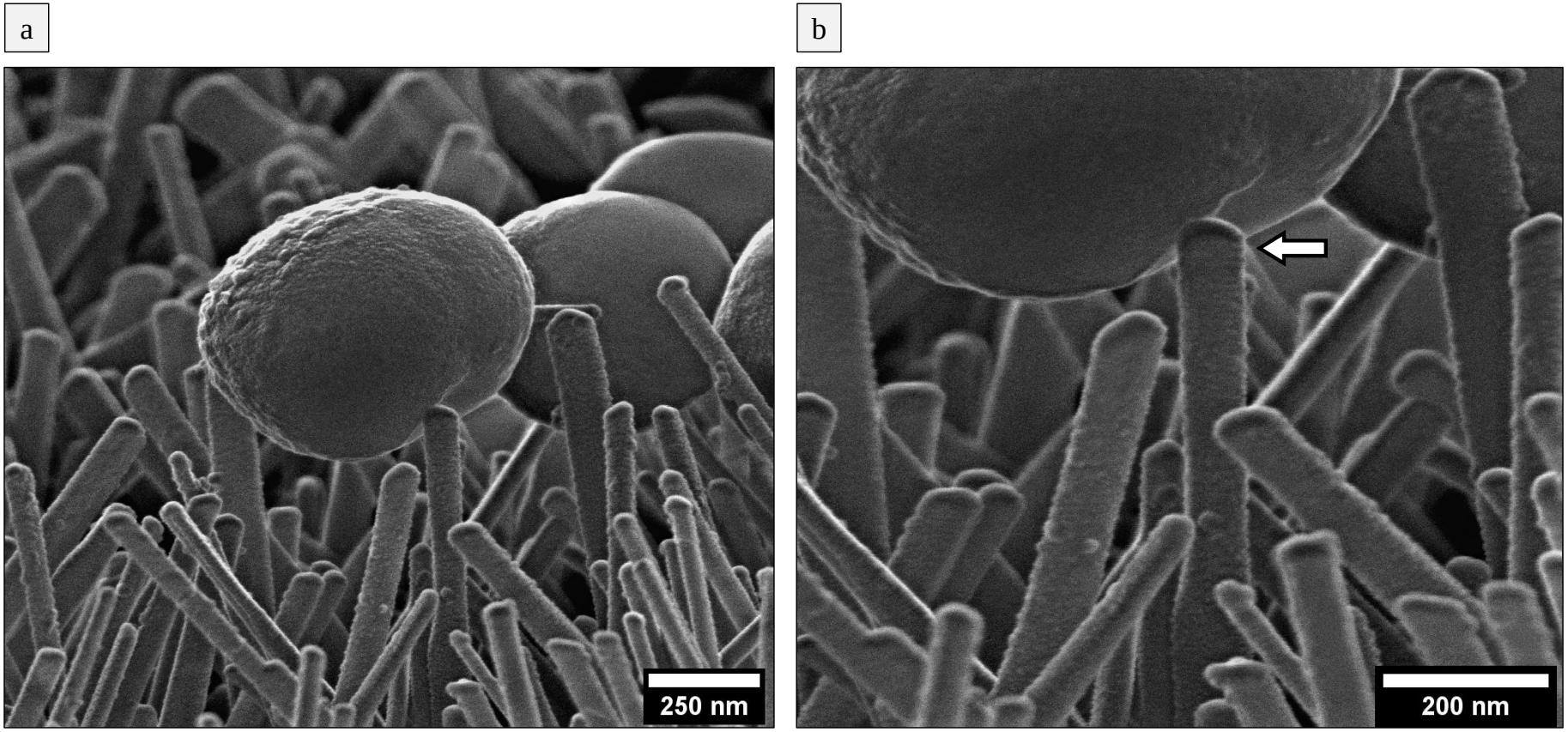

Figure 5.10 | High magnification SEM analysis of *S. aureus* envelope morphology on nanowire and control surfaces. Tilted SEMs of *S. aureus* on NW3 after 3 h incubation. The envelope of *S. aureus* appears to be deformed at the point of nanowire contact (a). The white arrow indicates a region of nanowire-induced envelope deformation (b).

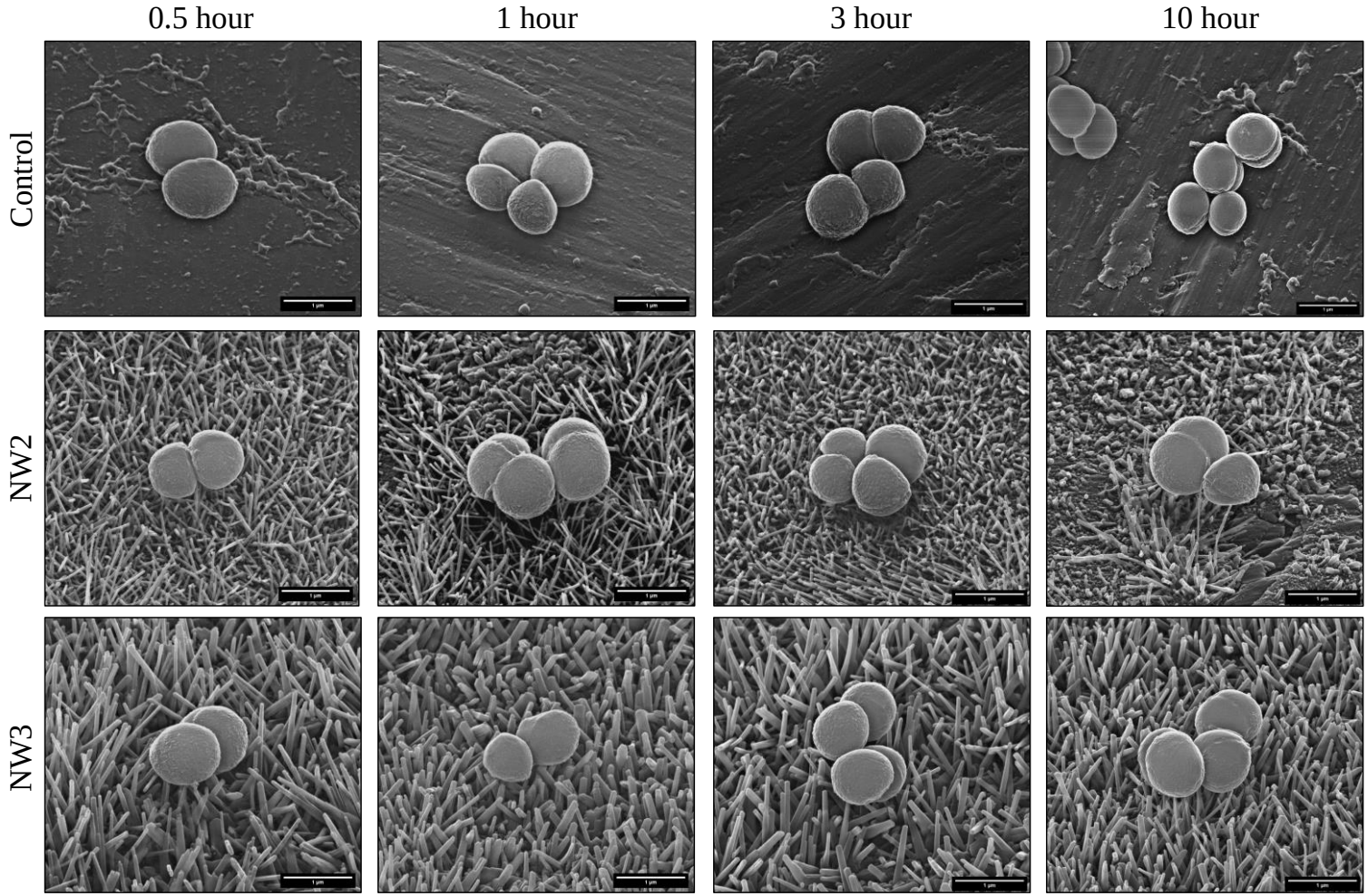

Figure 5.11 | SEM analysis of *S. epidermidis* envelope morphology on nanowire and control surfaces. Tilted SEMs of *S. epidermidis* on control and nanowire surfaces after 0.5, 1, 3 and 10 h incubations.

5.2.2.3 SEM analysis of Gram-negative envelope morphology

E. coli exhibited the characteristic bacillus morphology throughout the 10 h incubation. By 3 h on the control surface, *E. coli* cells had begun expressing fimbria-like surface appendages, resulting in the formation of connections between neighbouring cells and the titanium surface. In contrast, these structures were largely absent from *E. coli* adherent to nanowire surfaces, and rather *E. coli* cells were typically found in isolation from each other (Figure 5.12). Furthermore, at the points of contact between nanowires and bacteria, there were visible signs of envelope stretching, as was evident from areas of cell deformation around individual nanowires (Figure 5.13). Following 10 h, *E. coli* had formed multicellular arrangements on control surfaces, with an increased abundance of fimbria-like structures that were seemingly anchoring cells to each other and the surface. On nanowire surfaces, while *E. coli* cells continued to display the expected bacillus morphology, cell density had shown little change from 3 h, and the frequency of fimbria-like structures was comparatively low to controls.

Alike to *E. coli*, *K. pneumoniae* displayed a bacillus morphology on control and nanowire surfaces over the 10 h incubation period (Figure 5.14). However, in contrast to *E. coli*, the surface morphology of *K. pneumoniae* appeared to change in a time-dependent manner. After 1 and 3 h incubations, the surface of *K. pneumoniae* appeared relatively smooth, while at 0.5 and 10 h, short, uniformly spaced, fimbria-like appendages emerged from the bacterial surface. These are characteristic of surface-expressed capsular polysaccharide, a major virulence factor involved in colonisation (Evrard et al., 2010). As for *E. coli*, *K. pneumoniae* also expressed longer fimbria-like structures after 3 h, but the overall frequency was much lower for *K. pneumoniae* cells adherent to nanowires surfaces than control. Following 10 h, *K. pneumoniae* had formed microcolonies on control surfaces and the abundance of multibranched fimbria-like structures had increased. In contrast, cells were mostly in isolation on nanowire surfaces, and the density had not changed significantly from 3 h. As was previously shown for *E. coli*, nanowire-induced envelope deformation was observed for *K. pneumoniae*, providing further evidence that nanowires had the capacity to affect bacterial morphology (Figure 5.15).

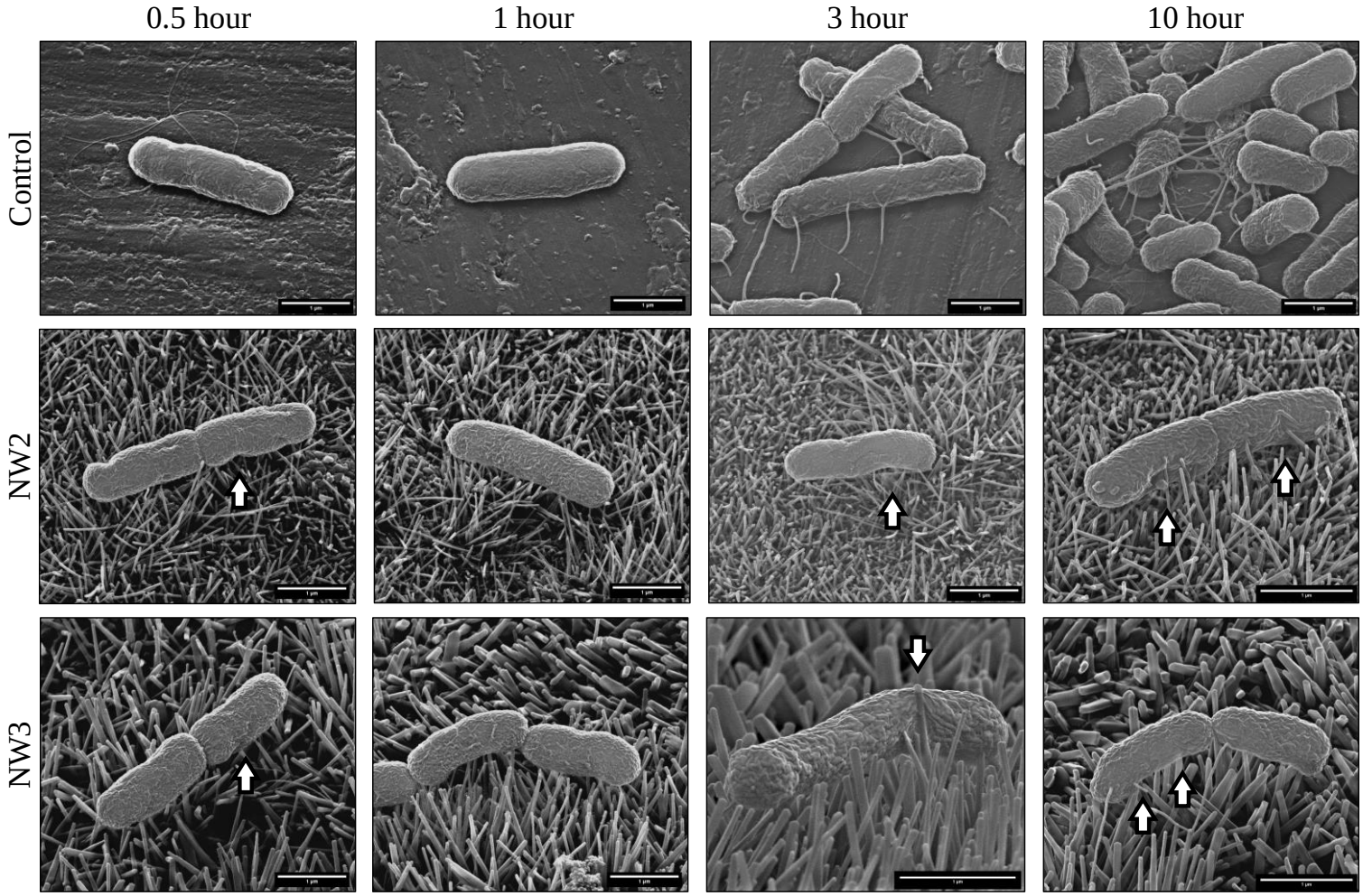

Figure 5.12 | SEM analysis of *E. coli* envelope morphology on nanowire and control surfaces. Tilted SEMs of *E. coli* on control and nanowire surfaces after 0.5, 1, 3 and 10 h incubations. White arrows indicate regions of nanowire-induced envelope deformation.

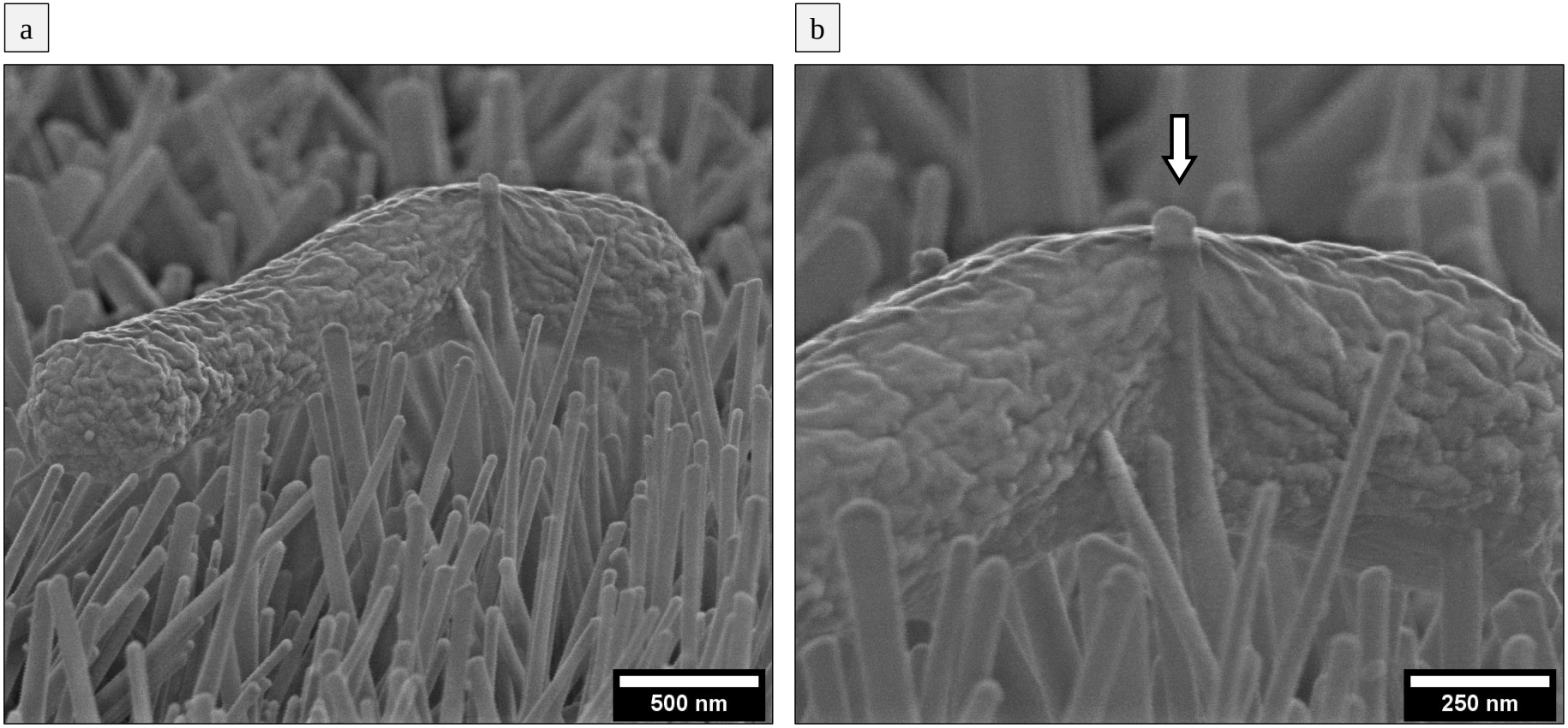

Figure 5.13 | High magnification SEM analysis of *E. coli* envelope morphology on nanowire and control surfaces. Tilted SEMs of *E. coli* on NW3 after 3 h incubation. The envelope of *E. coli* appears to be deformed at the point of nanowire contact (a). The white arrow indicates a region of nanowire-induced envelope deformation (b).

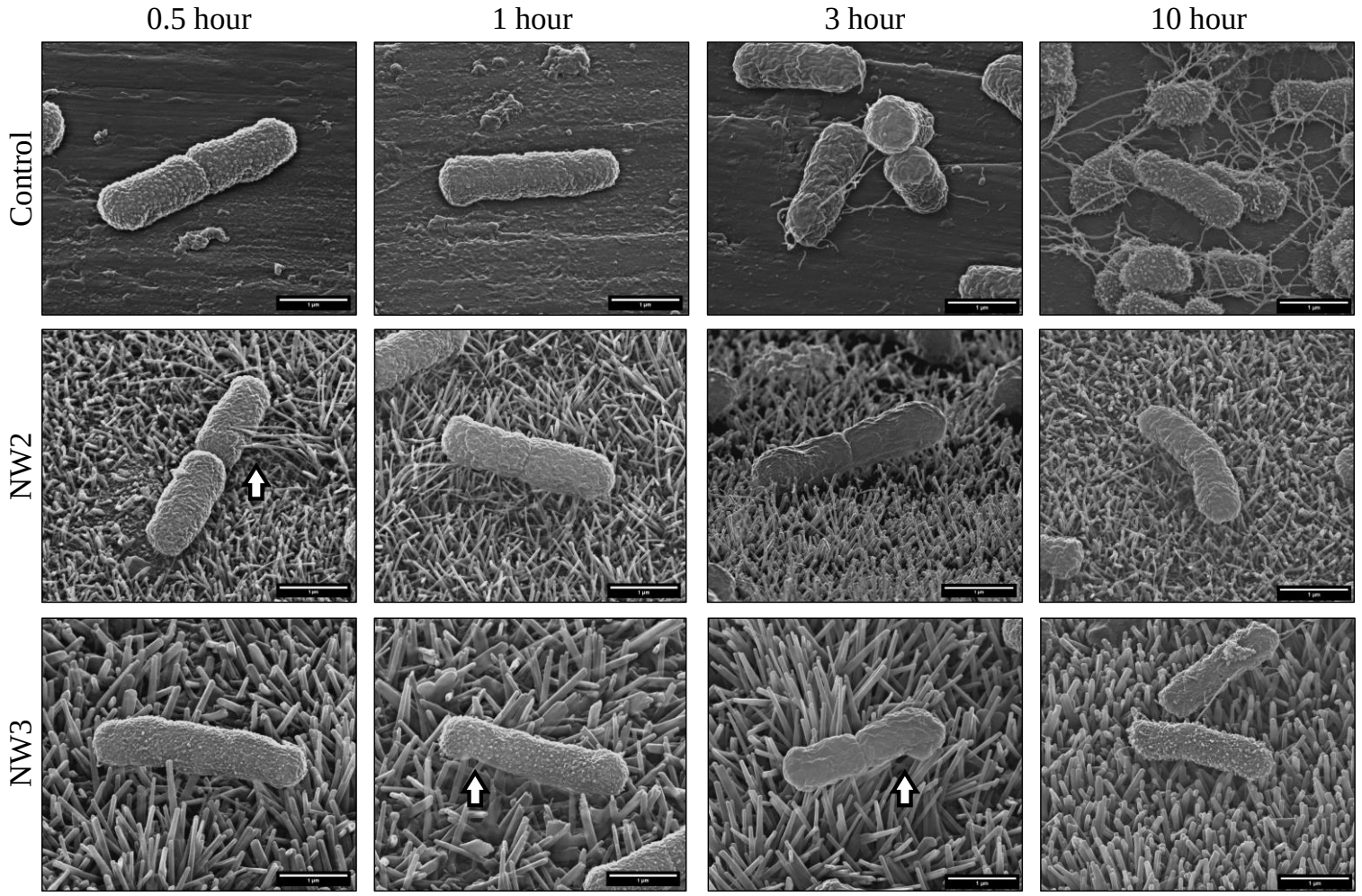

Figure 5.14 | SEM analysis of *K. pneumoniae* envelope morphology on nanowire and control surfaces. Tilted SEMs of *K. pneumoniae* on control and nanowire surfaces after 0.5, 1, 3 and 10 h incubations. White arrows indicate regions of nanowire-induced envelope deformation.

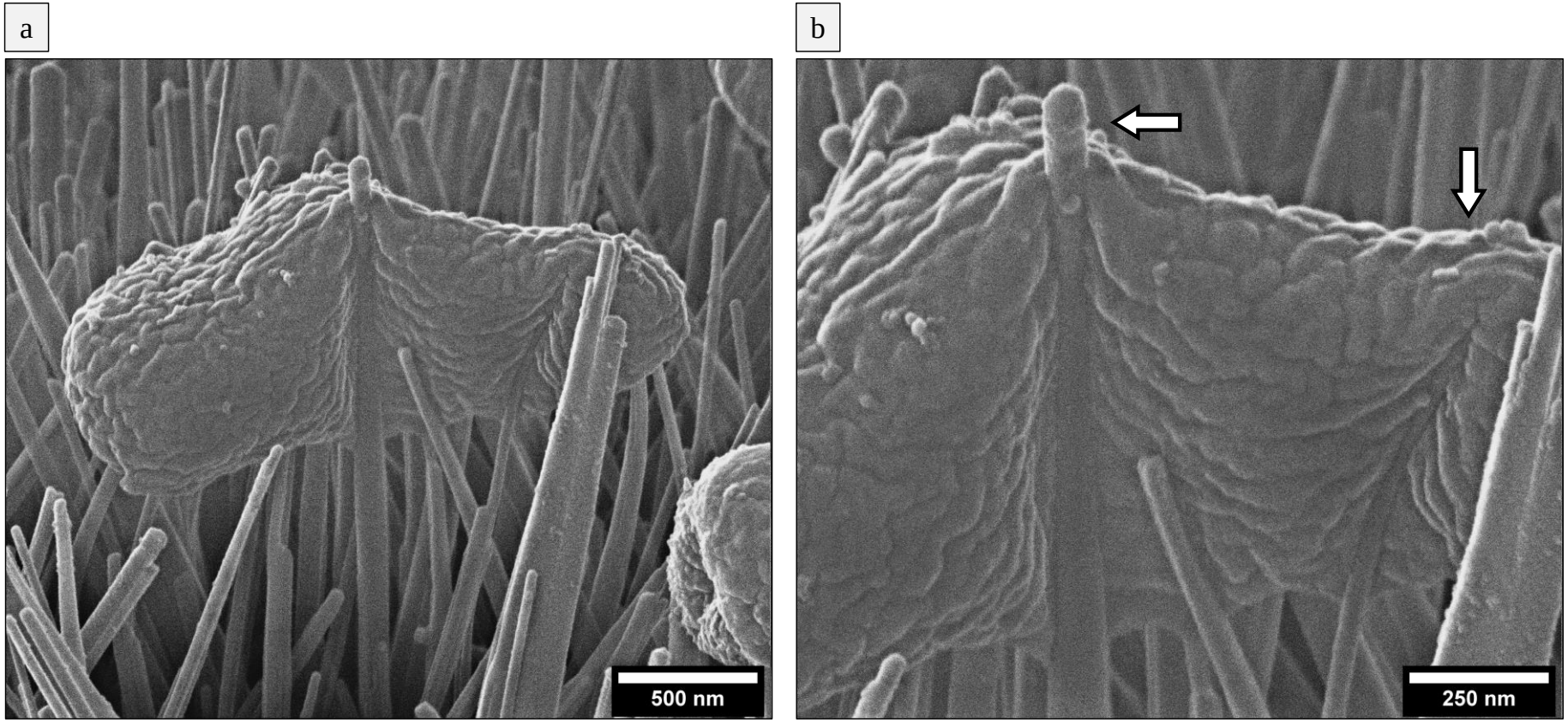

Figure 5.15 | High magnification SEM analysis of *K. pneumoniae* envelope morphology on nanowire and control surfaces. Tilted SEMs of *K. pneumoniae* on NW3 after 3 h incubation. The envelope of *K. pneumoniae* appears to be deformed at the point of nanowire contact (a). The white arrow indicates a region of nanowire-induced envelope deformation (b).

5.3 Visualising bacteria-nanowire interactions by TEM

The observation of nanowire-induced envelope deformation for *E. coli* and *K. pneumoniae* and, to a lesser extent, for *S. aureus,* was consistent with the proposed mechanism of nanowire-mediated contact killing, which proposes that as bacteria adhered to the nanopillar surface, the envelope is stretched to the point of physical rupture, leading to cell death (Pogodin et al., 2013). There was also evidence that bacteria had become trapped between nanowires following envelope deformation, which might be expected to impair growth. However, it was unclear whether deformation had caused the bacterial envelope to rupture or had changed the cytosolic ultrastructure. To investigate this in more detail, TEM analysis was utilised to study ultra-thin bacterial sections at nanometre scales.

5.3.1 Optimisation of section preparation

Conventional thin section preparation for TEM analysis involves four main steps: 1) fixation, 2) dehydration, 3) resin embedding and 4) sectioning. The final stage (sectioning) involves generating cross sections of a resin embedded sample using a diamond knife, fixed to an ultramicrotome. In this study, generating cross sections through a titanium substrate was not possible; therefore, the titanium substrate was removed from resin embedded samples, leaving only the TiO_2 nanowire layer and bacteria. Removal of the base titanium substrate was achieved by freeze thawing the sample in liquid nitrogen, with varying success. Figure 5.16 shows 70 nm cross sections generated through control and NW3 surfaces. On control surfaces, no bacteria were observed (Figure 5.16a), which prompted a change in protocol to recover bacteria from control surfaces prior to fixation. In contrast, on nanowire surfaces, while bacteria were identified, the sectioning appeared to have damaged the nanowire layer in regions, making it unclear as to whether the morphologies observed were a true representation of bacterial morphology or an artefact of processing (Figure 5.16b). To minimise damage across the nanowire layer, sample processing was next performed with two resin embedding stages, before and after removal of the titanium substrate, to provide additional support to the oxide and nanowire layer during sectioning. As a result, the nanowire layer remained intact and uniform following sectioning (Figure 5.16c).

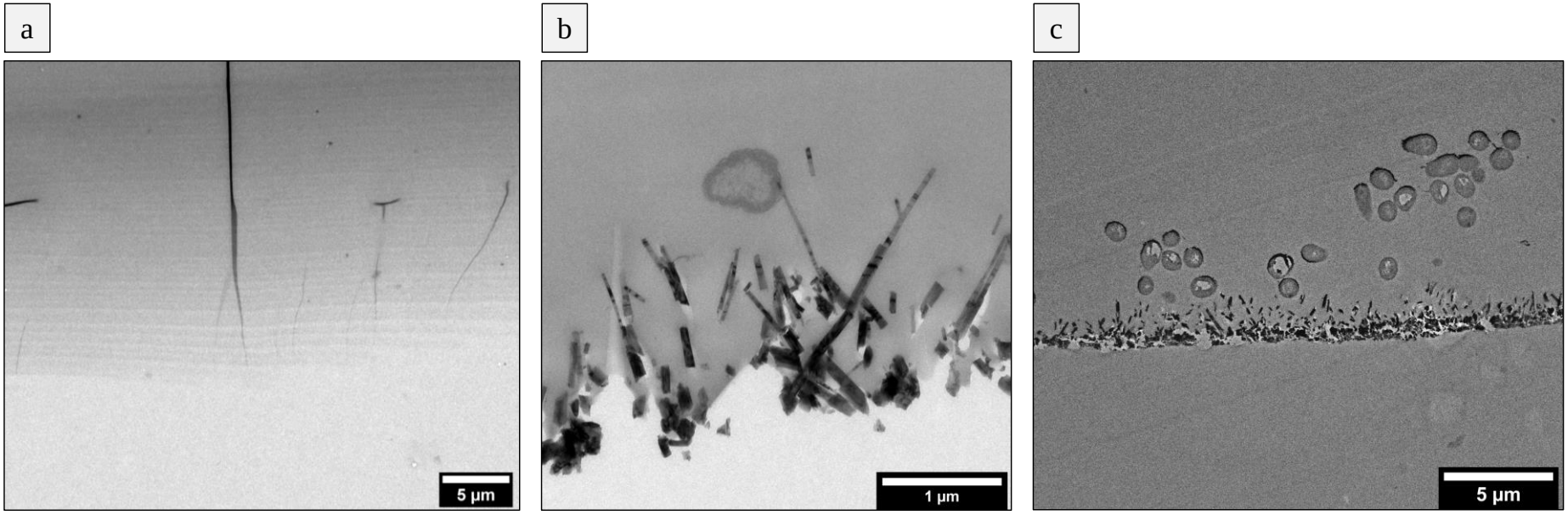

Figure 5.16 | Optimisation of TEM section preparation. Control section with one Epon® resin embedding step, with no bacteria observed (a). NW3 section with one Epon® resin embedding step. Bacteria were observed, but the oxide layer was non-uniform and damaged (b). NW3 section with two Epon® resin embedding steps, before and after titanium base removal. Bacteria were observed, and the structural integrity of the oxide layer had been maintained (c).

Once sample processing had been optimised, a diamond knife was used to generate cross sections between 70 - 250 nm thickness through *E. coli*, *K. pneumoniae* and *P. aeruginosa* that had been incubated on control and nanowire discs for 3 h. While there was limited evidence of envelope deformation in Gram-positive bacteria, the ultrastructure of *S. aureus* was also studied for comparison. To determine whether nanowires had significantly altered the bacterial morphology, the average thickness of the envelope was measured for bacteria on control surfaces compared to bacteria that had been incubated on nanowires.

5.3.2 The effect of nanowires on Gram-positive envelope structure

On control surfaces, the typical envelope architecture of *S. aureus* was observed, comprising a plasma membrane surrounded by a peptidoglycan cell wall. The average thickness of the peptidoglycan layer was 22 nm ± 2 nm, while the plasma membrane was approximately 8 nm ± 1 nm (Figure 5.17a-b). The outer periphery of *S. aureus* was coated by a darker, more electron dense layer. This region is likely to be surface-expressed determinants, such as protein adhesins. In combination, the average thickness of the envelope was approximately 30 nm ± 2 nm and with the addition of the electron dense layer, this increased the thickness to 39 nm ± 5 nm. On control surfaces the envelope was uniform and continuous around the cell. The presence of the bacterial septum indicated that *S. aureus* had been undergoing binary fission at the point of fixation. The overall morphology of *S. aureus* on nanowire surface NW3 was comparable to the control (Figure 5.17c-h). While the average peptidoglycan thickness had reduced slightly at the point of contact with nanowires, measured at 16 nm ± 5 nm compared to 26 ± 8 nm in the surrounding regions, this was not significant. Nevertheless, this subtle difference could be expected to increase the envelope permeability of *S. aureus*, considering the viscoelastic properties of bacterial envelopes.

Regarding the *S. aureus* plasma membrane, the average thickness at nanowire regions was 8 nm ± 1 nm, while at non-nanowire regions the thickness was 9 nm ± 3 nm. Although nanowires had not significantly deformed *S. aureus*, there were isolated cases where nanowires had penetrated the bacterial envelope. As can been seen from Figure 5.17c-d, two nanowires appeared to have breached the cell envelope, as the tips were located at the plasma membrane-cytosol interface. What is also interesting about this is that the internal ultrastructure of *S. aureus* was darkest at this point (blue line), indicating that the electron density was greatest in this region. Moreover, this difference was not observed in Figure 5.17e-h, where nanowires had not penetrated the envelope. The increased electron density, localised at the point of nanowire contact, is likely attributed to increased protein concentration.

On the one hand, this could indicate that cytosolic contents were exiting the cell along a concentration gradient. However, since the overall cell morphology had not changed significantly compared to control, this was unlikely. Alternatively, the increased concentration of proteins at this point could indicate that a stress response had been activated to repair damage or avoid further damage. Indeed, Gram-positive bacteria have evolved a number of response systems to maintain envelope integrity and prevent envelope damage (Jordan et al., 2008). Furthermore, bacteria (*S. typhimurium*) have been reported to survive multiple envelope piercings due to repair of the peptidoglycan and plasma membranes (Suo et al., 2009).

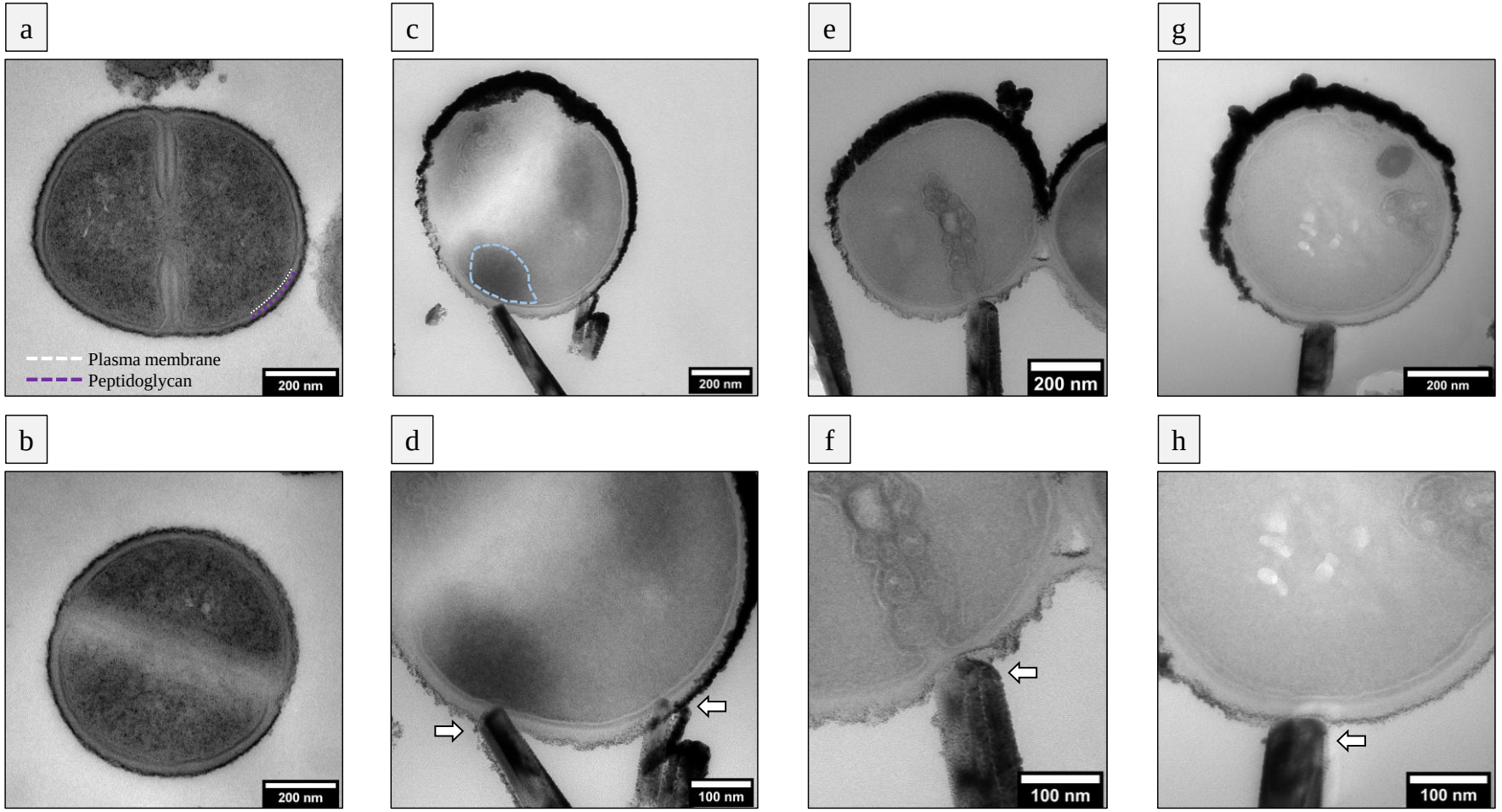

Figure 5.17 | TEM analysis of *S. aureus* envelope morphology and cytosolic ultrastructure on nanowire surfaces. Cross sections (70 nm) of *S. aureus* incubated on control (a-b) or NW3 (c-h) surfaces for 3 h. Micrographs (d), (f) and (h) are higher magnification versions of (c), (e) and (g) respectively. White arrows indicate points of contact between TiO_2 nanowires and the *S. aureus* envelope. As an example, the plasma membrane and peptidoglycan layers of *S. aureus* are highlighted in micrograph (a) by white and purple dashed lines respectively. The region outlined by a blue dashed line indicates a potential area of increased protein concentration, which could be indicative of an envelope stress response.

5.3.3 The effect of nanowires on Gram-negative envelope structure

On control surfaces, the envelope structure of *E. coli* was characteristic of Gram-negative bacteria, comprising the lipopolysaccharide outer membrane and the inner plasma membrane, separated by a thin layer of peptidoglycan. The outer and inner membranes of *E. coli* were measured at 12 nm ± 2 nm and 9 nm ± 2 nm respectively, while the peptidoglycan layer was approximately 7 nm ± 1 nm (Figure 5.18a). Although the thickness of the *E. coli* peptidoglycan layer was less than half that of *S. aureus,* the overall envelope thickness was comparable, measuring at approximately 32 nm ± 4 nm. Following recovery from control surfaces, *E. coli* displayed a continuous envelope with many cells appearing to be in the process of binary fission, as was evident from the bacterial septum. The envelope dimensions of *K. pneumoniae* and *P. aeruginosa* were very similar to *E. coli* following incubation on control surfaces. In *K. pneumoniae*¸ the outer and inner membranes contributed 9 nm ± 2 nm and 6 nm ± 1 nm respectively to the envelope, while the peptidoglycan layer was measured at 7 nm ± 1 nm (Figure 5.18b). For *P. aeruginosa,* the outer and inner membranes were 10 nm ± 1 nm and 9 nm respectively and the peptidoglycan layer was also 7 nm (Figure 5.18c). The average total envelope thickness for *K. pneumoniae* and *P. aeruginosa* was 29 nm ± 1 nm and 31 nm ± 2 nm respectively.

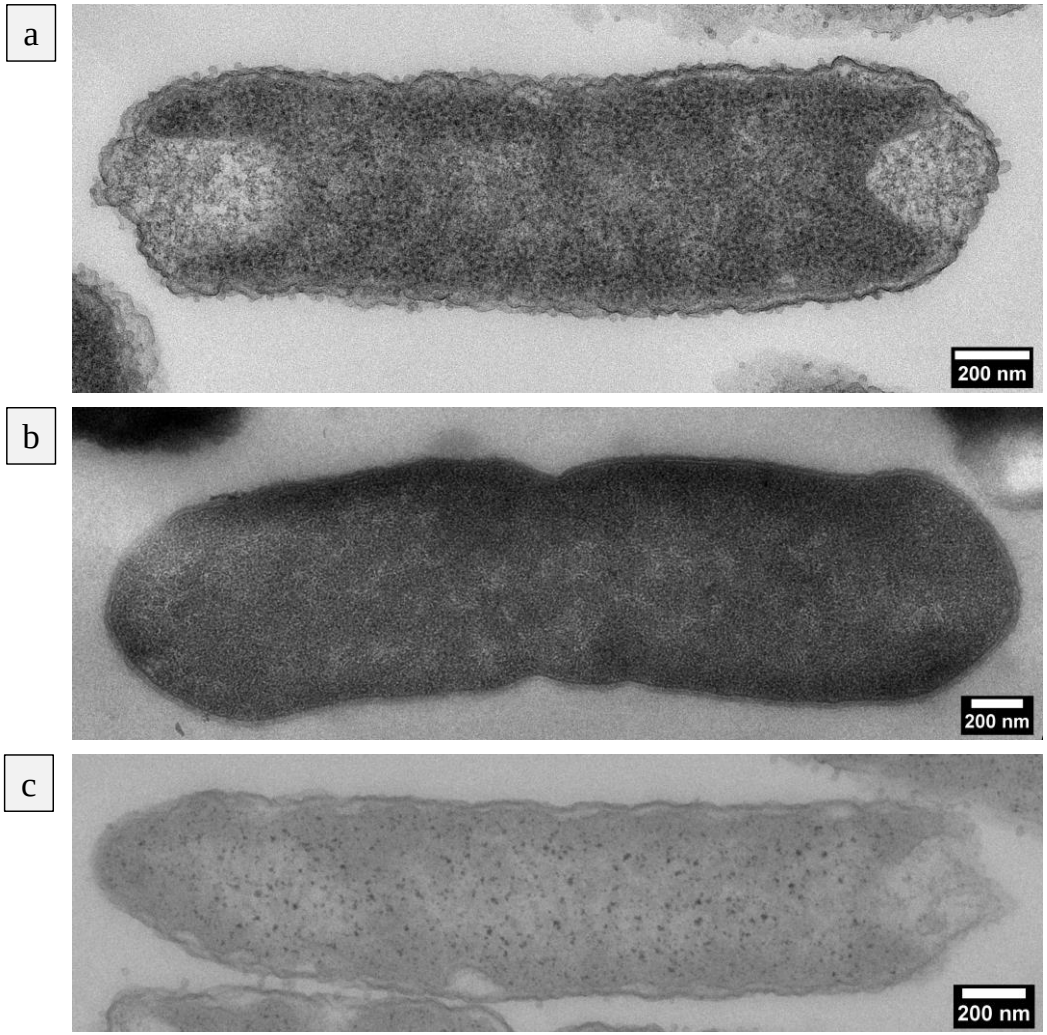

Figure 5.18 | TEM analysis of Gram-negative envelope morphology and cytosolic ultrastructure on control surfaces. Cross sections (70 nm) of *E. coli* (a), *K. pneumoniae* (b) and *P. aeruginosa* (c) incubated on control surface for 3 h.

In contrast to the *S. aureus* envelope, which showed little difference between control and nanowire surfaces, the envelope morphology of *E. coli*, *K. pneumoniae* and *P. aeruginosa* changed significantly following incubation on nanowire surface NW3. From the bacterial cross sections analysed, two possible nanowire induced changes were identified in Gram-negative bacteria: 1) Nanowire-induced envelope deformation and 2) Nanowire-induced envelope penetration.

5.3.3.1 Nanowire-induced envelope deformation

Possible nanowire-induced envelope deformation was the most common perturbation observed for *E. coli, K. pneumoniae* and *P. aeruginosa* (Figure 5.19). Surprisingly, the extent of deformation did not appear to be influenced by nanowire tip diameter. This could be attributed to the differences in nanowire height, orientation and density across each surface, meaning that, the precise forces that are exerted on each cell is likely to vary. Furthermore, the exact time duration for each interaction is likely to vary, leading to earlier or later stage deformation. Figure 5.19a shows the interface between the envelope of *E. coli* and a single nanowire tip of 40 nm diameter. This interaction resulted in approximately 273 nm of envelope deformation. In contrast, a different *E. coli* cell, interacting with a nanowire tip that was 15 nm in diameter had only deviated by 25 nm (Figure 5.19b). The same trend was observed at different regions of the section, Figure 5.19c-d highlight two different *E. coli* cells that had interacted with nanowires of approximately 45 nm diameter. These interactions had led to deformations of 20 nm and 70 nm respectively. In contrast, the interaction highlighted in Figure 5.19e comprised a nanowire of approximately 10 nm tip diameter, while deformation was less than 10 nm. Of note, for the majority of these interactions, the clarity of the envelope was often reduced, which may signify a loss of structural integrity. Comparable morphologies of possible nanowire-induced envelope deformation were observed for *K. pneumoniae* (Figure 5.19f-g) and *P. aeruginosa* (Figure 5.19h).

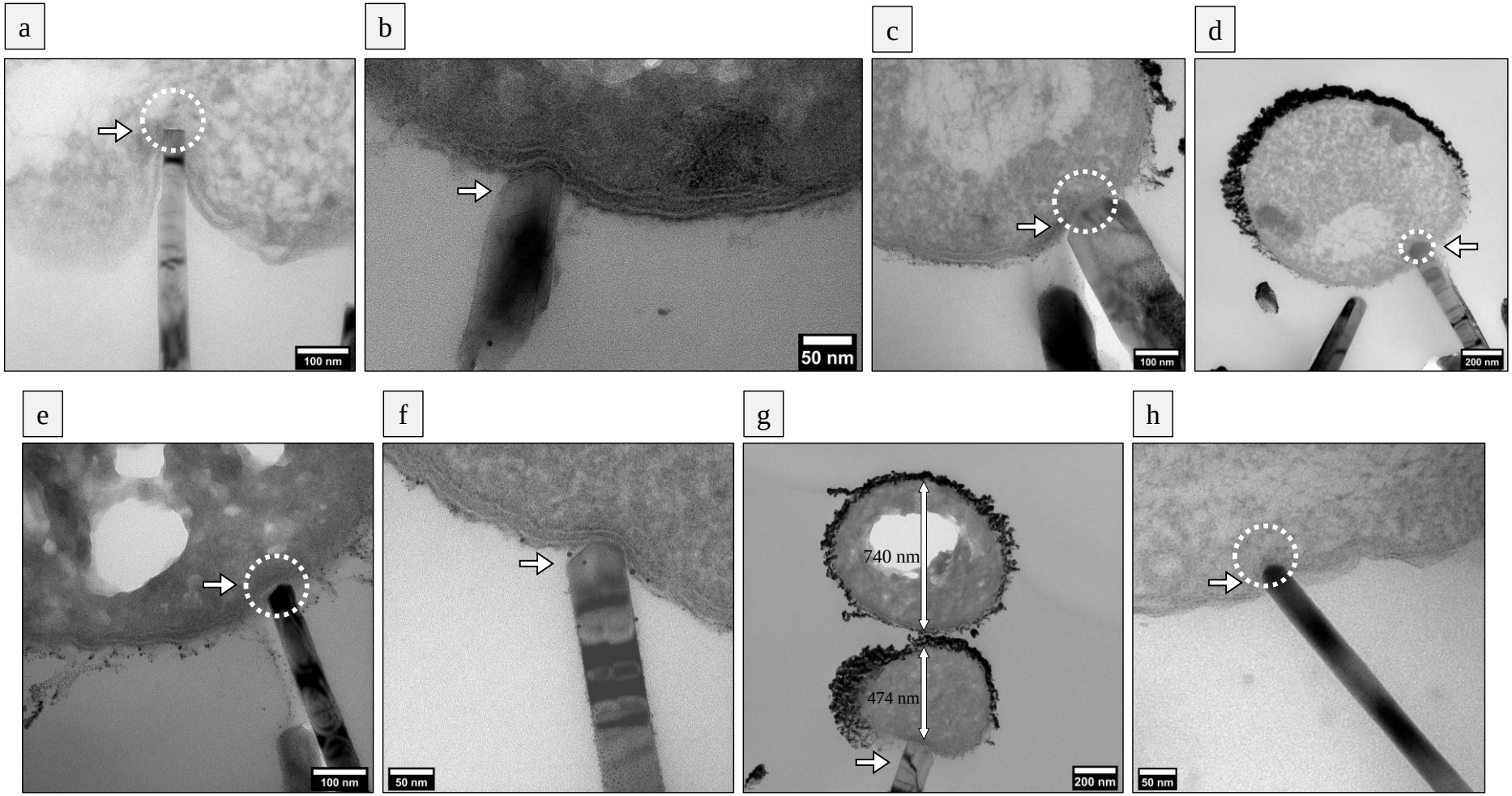

Figure 5.19 | TEM analysis of Gram-negative envelope morphology and cytosolic ultrastructure on NW3 surfaces. Cross sections (70 nm) of *E. coli* (a-e), *K. pneumoniae* (f-g) and *P. aeruginosa* (h) incubated on NW3 surface for 3 h. White arrows indicate the points of contact between TiO_2 nanowires and the Gram-negative envelope. White dashed lines highlight regions of the bacterial envelope with reduced clarity, a possible indicator of nanowire-induced envelope damage. Micrograph (g) illustrates that only bacteria in contact with nanowires undergo deformation.

Although TEM analysis provided possible evidence that nanowires had deformed the envelope of Gram-negative bacteria, it was unclear whether these interactions had caused only local deformation (at the point of contact), or if the entire envelope morphology had been affected as a consequence. To investigate this, the deviation in envelope structure and shape was analysed by tomography analysis, which enabled the three-dimensional structure of *E. coli* to be studied following interactions with NW3 surfaces (Figure 5.20).

Tomography was performed on an *E. coli* cross section measuring 250 nm in thickness. Initial TEM analysis had identified a single nanowire interacting with the cell (Figure 5.20a). However, due to the thickness of the section, it was not possible to confirm whether this nanowire had penetrated the envelope. Figure 5.20b-d represent Z-positions at the start, middle and end of the tomogram. These highlight that the envelope structure was uniform at the beginning and middle of the tomogram and as the tomogram comes closer to the nanowire, the envelope becomes increasingly concave. This provides evidence that nanowire-induced envelope deformation was localised to the point of contact. Analysis of the 3D reconstruction of *E. coli* revealed that the bacterial envelope had been deformed by approximately 80 – 100 nm but had not been penetrated (Figure 5.20e).

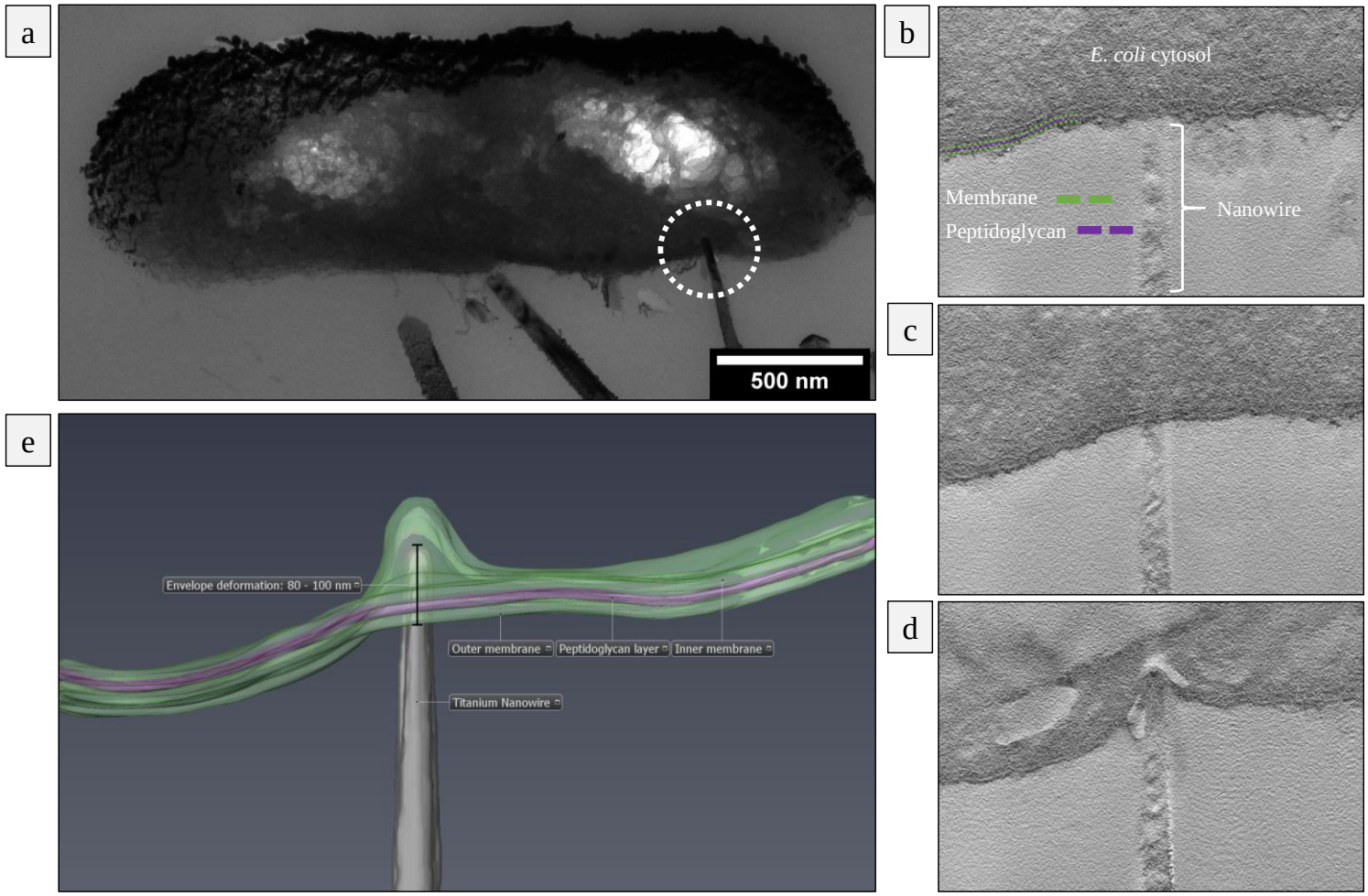

Figure 5.20 | Tomography analysis of *E. coli* on NW3. TEM of a 250 nm cross section through *E. coli* (a), with the point of contact between the bacterial envelope and nanowire marked by the white dashed line. Z-positions (tomographic slices) at the beginning, middle and end of the tomogram (b-d) highlight the localised nature of envelope deformation. As an example, micrograph (b) shows the *E. coli* cytosol, nanowire position, and the membranes (green) and peptidoglycan layer (purple) of the bacterial envelope. 3D reconstruction of *E. coli* tomogram is shown in (e).

5.3.3.2 Nanowire-induced envelope penetration

In addition to possible nanowire-induced envelope deformation, evidence that nanowires had penetrated the bacterial envelope was also found. Once more, there was significant variation with respect to the extent of penetration, and it was noted that not a single penetration event had resulted in loss of turgor pressure. For *E. coli*, three examples of envelope penetration were identified, as shown in Figure 5.21a-c. In each case, the distance from the envelope entry point to the nanowire tip was measured and was found to vary from approximately 155 nm to 270 nm. In addition to single penetration events, cases where multiple nanowires had penetrated a single bacterium were also observed, albeit at a much lower frequency. For *K. pneumoniae,* one example was found of a single bacterium that appeared to have been penetrated by six nanowires (Figure 5.22a). Tomography analysis of this cell confirmed that 5 out of 6 nanowires had penetrated, with depth varying from 103 nm to 179 nm (Figure 5.22b). Furthermore, the tips of each nanowire were located at different Z-positions within the section (Figure 5.22c-g). Nanowire-induced envelope penetration was also identified in *P. aeruginosa,* for which the tip of a single nanowire was found to have reached a distance of 130 nm from the envelope (Figure 5.23).

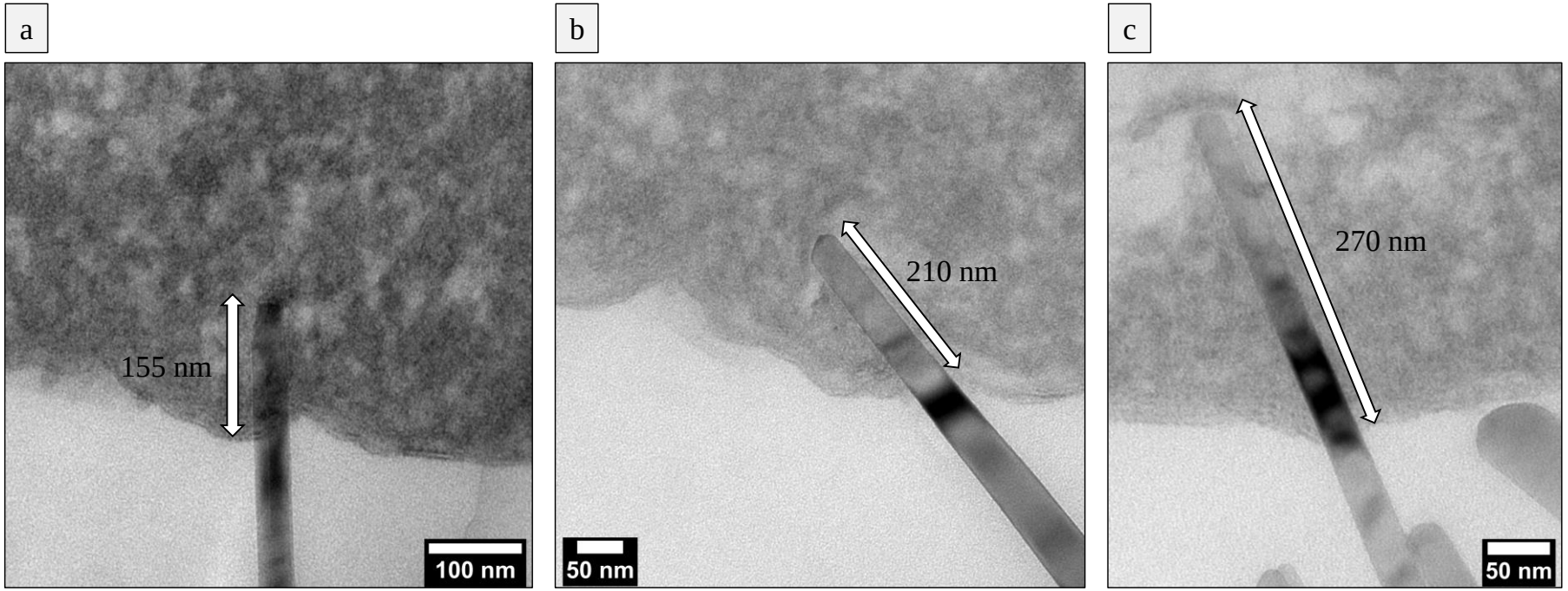

Figure 5.21 | Nanowire-induced envelope penetration in *E. coli* on NW3. TEM micrographs of 70 nm cross sections through three *E. coli* cells incubated on NW3 for 3 h. Nanowires had penetrated the envelope by variable distances of 155 nm (a), 210 nm (b) and 270 nm (c). Aside from clear envelope penetration, there was no evidence to suggest that cells had lost turgor pressure, as the cytosol was visible and the overall shape of the cells was maintained.

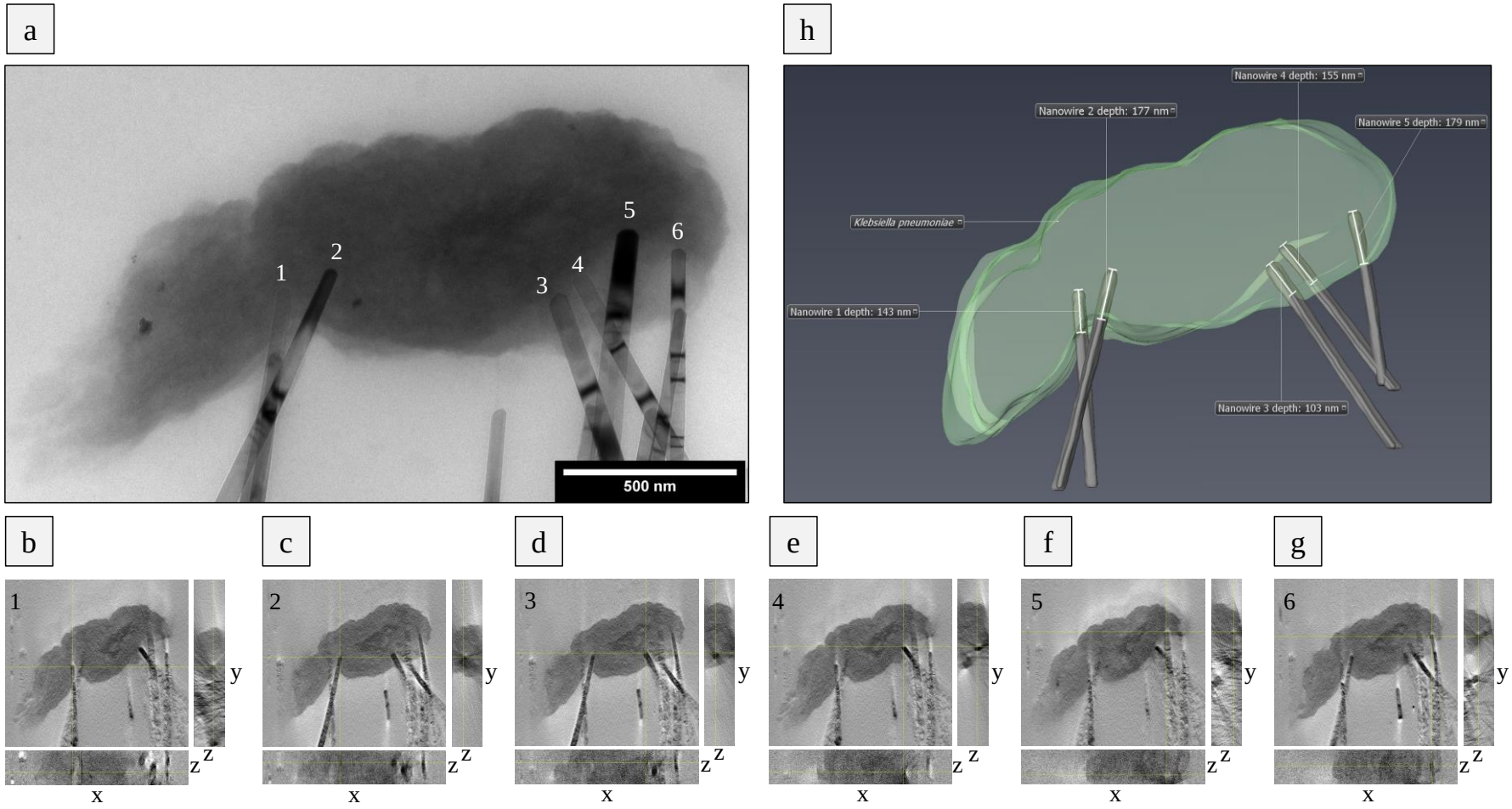

Figure 5.22 | 3D reconstruction of multiple envelope penetrations in *K. pneumoniae* on NW3. TEM of a 250 nm cross section through *K. pneumoniae* incubated on NW3 for 3 h. Six nanowires appeared to be penetrating the bacterial envelope (a). Analysis of nanowire coordinates (xy, xz and yz) in eTomo confirmed that five nanowires had penetrated the envelope of *K. pneumoniae* (1, 2, 3, 4 and 6). These can be seen in the tomographic slices (b-g). 3D reconstruction of the 250 nm cross section in Avizo, highlighting the penetration depth of each nanowire (h).

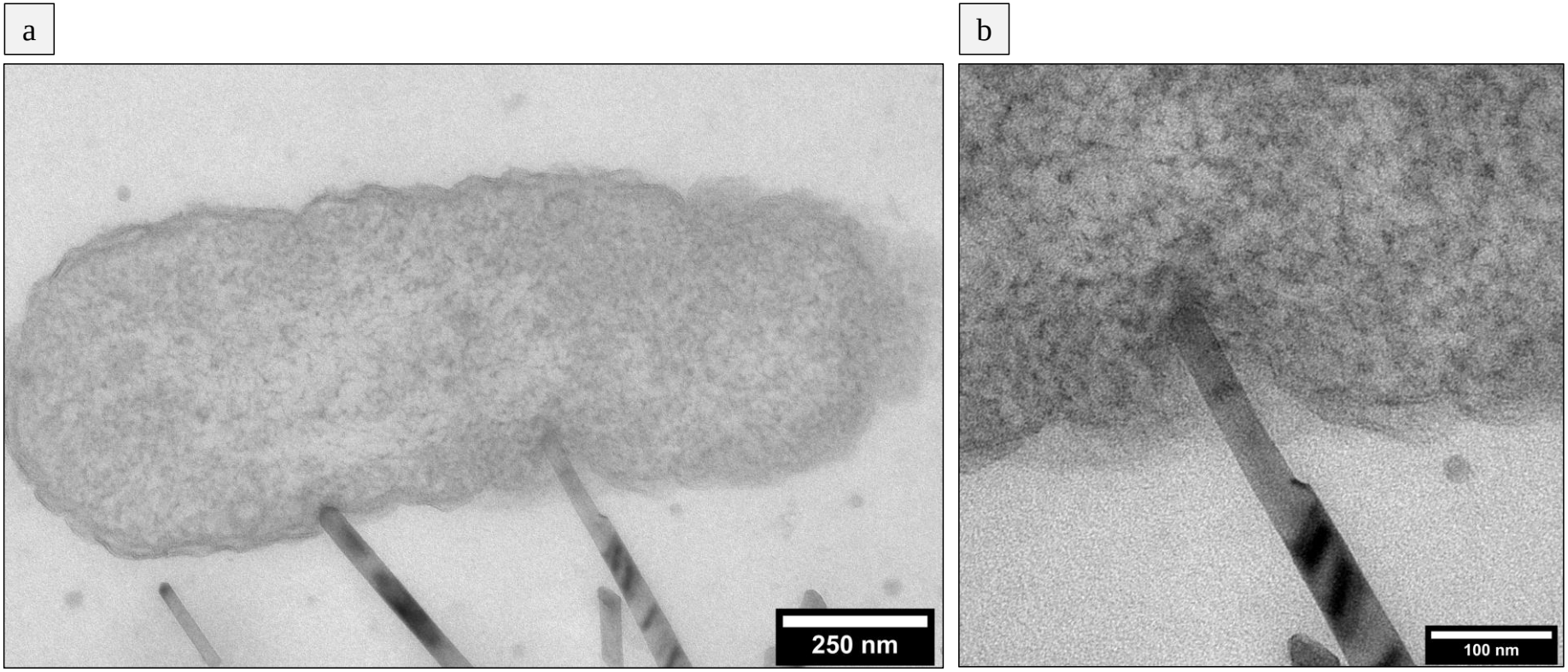

Figure 5.23 | Nanowire-induced envelope penetration in *P. aeruginosa* on NW3. TEM micrographs of 70 nm cross sections through *P. aeruginosa* incubated on NW3 for 3 h. Aside from clear envelope penetration, there was no evidence to suggest that the cells had lost turgor pressure, as the cytosol was visible and the overall shape of the cells was maintained.

5.4 Visualising bacteria-nanowire interactions by FIB-SEM

To further validate the observation of nanowire-induced envelope deformation and penetration, cross sectional analysis of *S. aureus* and *E. coli* on nanowire arrays was performed using FIB-SEM. FIB milling was carried out using two different approaches: slice by slice preparation and pie slice preparation. Slice by slice preparation involves stepwise ablation of the target material in one direction, thereby creating parallel cross sections through entire bacterial cells. Using the slice by slice approach, it is possible to generate 3D reconstructions, because the raw data is a continuous stack of images. In contrast, pie slice preparation involves ablation of the target material at two or more angles. The approach generally enables more control over the ablation position, which minimises the chance of missing areas of interest. However, it is not possible to generate 3D reconstructions, as the raw data are individual images (Friedmann et al., 2011).

5.4.1 Optimisation of slice by slice material ablation

Before bacteria of interest could be analysed using the slice by slice approach, the milling parameters were optimised to reduce the introduction of structural artefacts into the sample. Firstly, the default accelerating voltage and current for the ion and electron beams were set to the lowest possible values, which helped to minimise changes to surface morphology during area scanning, image acquisition and milling. Furthermore, slice by slice preparation was performed with and without a platinum layer, to determine the extent of surface damage caused by sequential ion beam milling.

To start, sequential ion beam milling was performed without the application of a protective platinum layer (Figure 5.24). Prior to ion beam milling, an *E. coli* cell of approximately 2.5 µm in length and 0.65 µm in width was interacting with several nanowires, as can be seen from tilted perspectives (Figure 5.24a-c). In consecutive images, the *E. coli* cell and adjacent nanowires were seen to move laterally across the field of view. This drifting artefact meant that parts of the *E. coli* cell had moved outside the image from sections 11 to 15. Nanowire charging may be one possible explanation for this movement. In addition to drifting, a curtaining effect was observed on many *E. coli* sections, resulting in an irregular and uneven surface, which made it difficult to resolve details in the envelope and intracellular ultrastructure. Curtaining presented as vertical lines across the milling face. The most probable explanation for curtaining is the differences in milling behaviour between the gold outer layer and the porous bacterial structure. However, the addition of sample drifting is likely to have exacerbated this effect.

In the next example, a protective layer of platinum (0.5 µm) was deposited on *E. coli* prior to ion beam milling (Figure 5.25). As a result, the effects of curtaining and drifting had been greatly reduced (Figure 5.25c). Twenty sections through the *E. coli* cell revealed minimal lateral movements between consecutive sections. Although curtaining was observed in some sections, the overall definition of each layer was much clearer. Based on these data, platinum deposition was applied for slice by slice preparation.

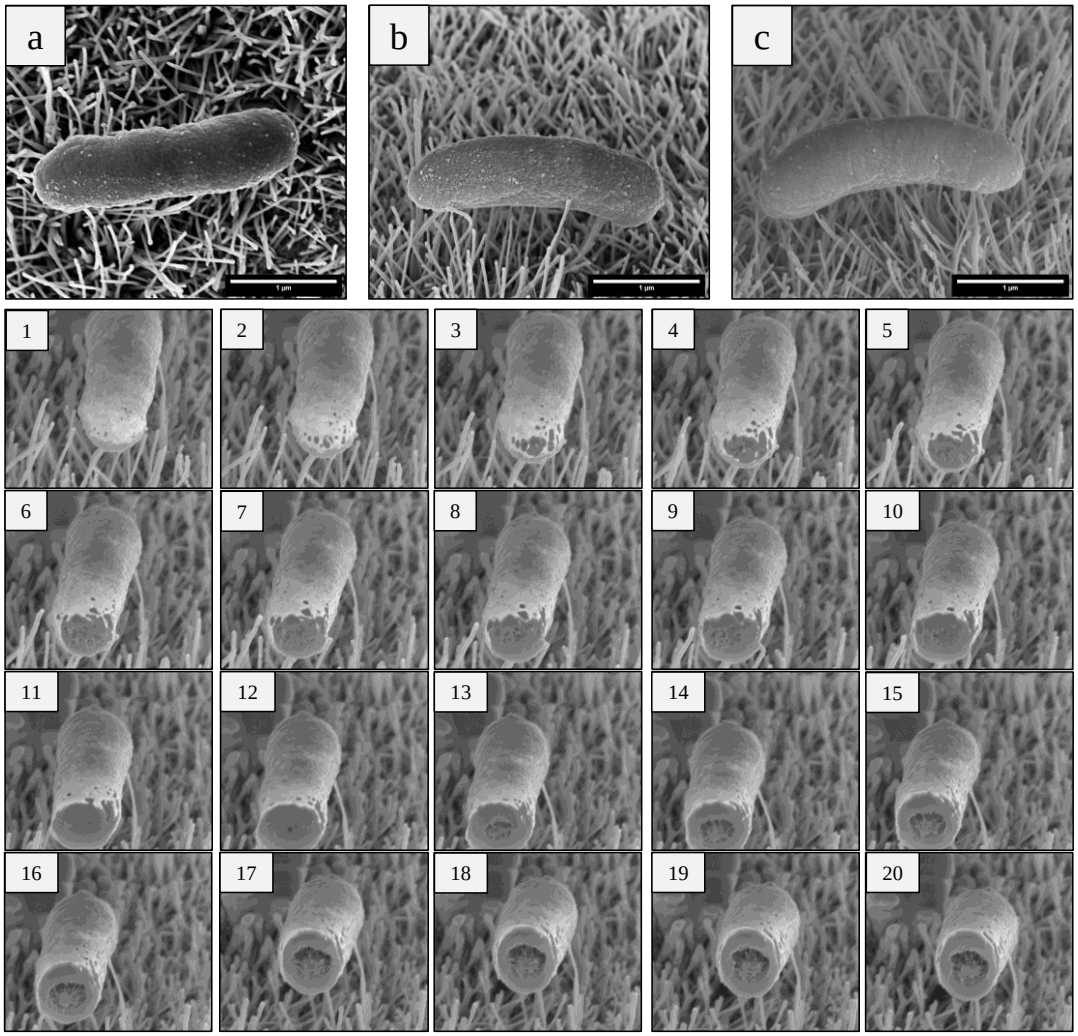

Figure 5.24 | Slice by slice preparation without platinum deposition. Original SEM of *E. coli* from top view (a), 52° tilt (b) and -52° tilt (c). The milling interface of 20 serial sections is shown.

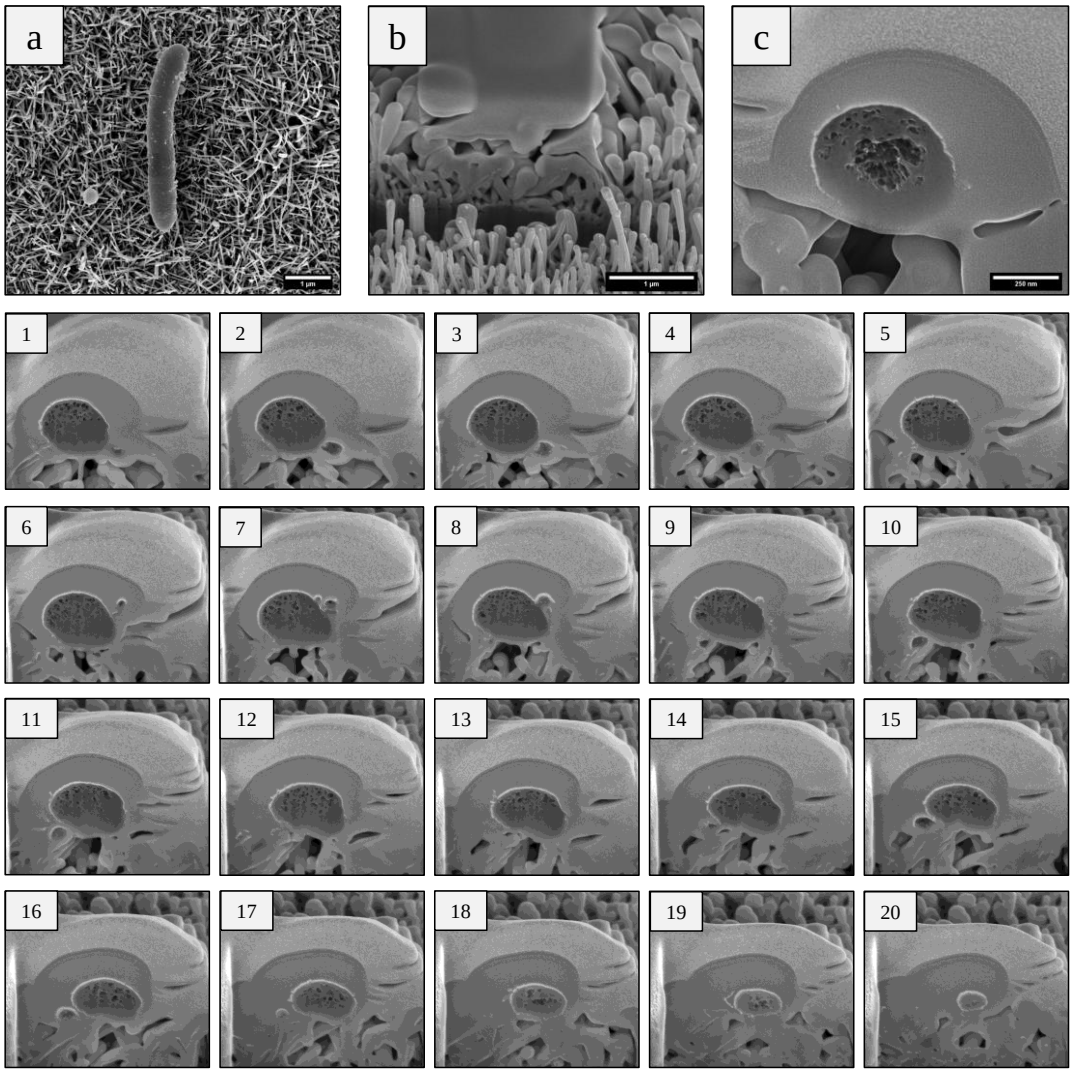

Figure 5.25 | Slice by slice preparation with platinum deposition. *E. coli* before platinum deposition (a) and after (b). SEM of milling interface (c). The milling interface of 20 serial sections is shown.

The major advantage of FIB-SEM over TEM and SEM techniques is that it enabled 3D reconstructions of entire bacterial cells to be generated. It was then possible to visualise every interaction between the nanowire surface and the bacterial envelope. Additionally, as FIB-SEM sample preparation is less complicated than TEM sample preparation, this enabled FIB-SEM analysis to be performed on a wider range of surfaces and thus a comparison could be performed. Corroborating the TEM analysis, the 3D models generated from FIB-SEM revealed evidence of nanowire-induced envelope deformation and penetration and, in some cases, these were observed in the same cell. There was also further evidence that nanowires had the capacity to physically trap bacteria. This was particularly common as the nanowire length and spacing increased.

5.4.2 Nanowire-induced envelope deformation, penetration and impedance

Preparation of bacterial cross sections on NW2 was problematic using TEM approaches, as the oxide scale tended to crack upon removal of the titanium base. As such, these were not analysed in this study. Nevertheless, FIB-SEM analysis provided a simpler route to perform cross sectional analysis of NW2, as milling could be performed regardless of the surface nanotopography. Preliminary area scanning of NW2 had identified an *E. coli* cell that appeared to be deforming into the nanowire array (Figure 5.26a-b) at each pole, while the mid-section seemed to not be in contact with NW2. The *E. coli* cell was milled in 80 cross sections, performed in 30 nm step sizes. This process identified two significant points of contact between nanowires and the envelope (Figure 5.26c-d). Surprisingly, neither of these were at the poles of the cell. Two nanowires (nanowire 1 & 2) had detached from the base substrate and had coincided at the same point along the bacterial envelope. This resulted in the envelope deforming by approximately 20 nm (Figure 5.26e-f), yet there was no penetration. However, at the mid-point of FIB milling (slice #42), a single nanowire had penetrated the bacterial envelope on the underside, as was evident from the tip being 52 nm inside the cell. However, there was no indication of a loss of cytosolic contents (Figure 5.26g-h). Moreover, the location of nanowire-induced envelope penetration coincided with the region of *E. coli* that was not in contact with the nanowire array. Taken together, these data were consistent with SEM and TEM observations, which highlighted nanowire-induced envelope deformation and penetration in Gram-negative bacteria, without loss of turgor pressure.

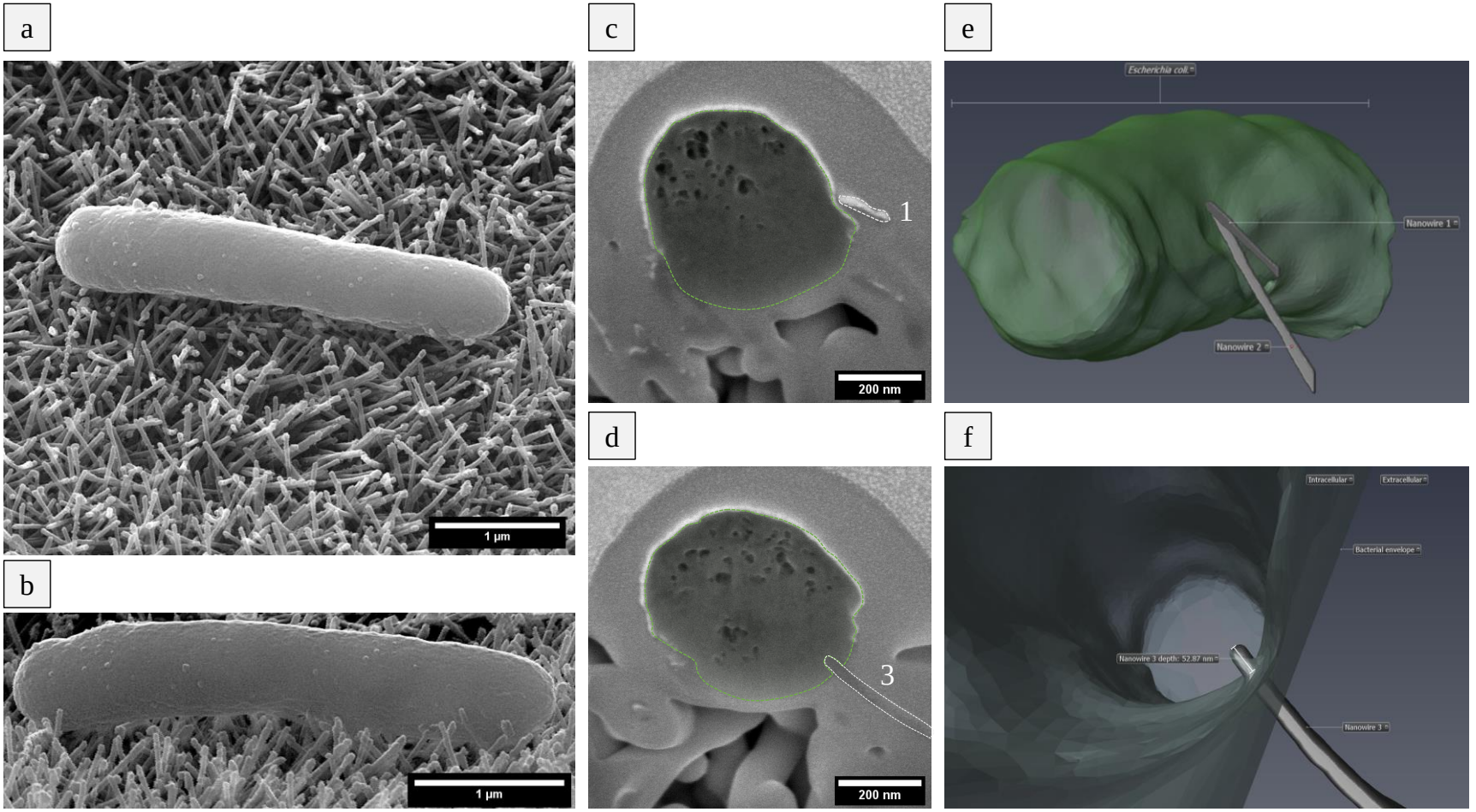

Figure 5.26 | 3D reconstruction of nanowire-induced envelope deformation and penetration on NW2. Automated FIB-SEM cross sectional analysis was performed on an *E. coli* cell (a-b) incubated on NW2 for 3 h. The focused ion beam produced 80 cross sections (30 nm each). Analysis of *E. coli* cross section #32 showed that nanowire 1 had caused envelope deformation (c) while nanowire 3, shown in section #42 (d), had penetrated the bacterial enevlope by 52 nm. Green dashed lines outline bacterial cross sections and white dashed lines outline nanowires. The resulting tomograph was reconstructed into a 3D model in Avizo, showing the interactions of nanowire 1 and 2 (e) and nanowire 3 (f) with *E. coli*.

Next, FIB-SEM milling was performed on *E. coli* that had been incubated on NW3 for 3 h. In general, this nanotopography consists of longer and less dense nanowires. Preliminary area scanning identified a single nanowire (nanowire 1) causing significant envelope deformation on one side of *E. coli*, leading to the bacterium being forced against a second nanowire (nanowire 2) on the opposite side (Figure 5.27). Automated slice by slice preparation was carried out using the focused ion beam, with 120 sections taken in 30 nm steps. Although nanowire 1 had deformed the bacterial envelope by 191 nm, it had not penetrated the cell. One possible explanation for whether nanowires deform and/or penetrate bacterial cells could relate to the location of nanowire contact with the envelope (i.e. underneath vs. side). Nonetheless, it is possible that the level of envelope deformation observed here led to the cell becoming trapped between nanowires 1 and 2. This provides evidence that nanowires may have capacity to act as physical barriers, entrapping bacterial cells and possibly impeding division, at least on the horizontal plane.

Increasing the length and spacing of nanowires could be expected to enhance nanowire-induced cell entrapment. To investigate this, cross sectional analysis was performed on *E. coli* that had been incubated on core-shell NW4 for 3 h. This nanotopography comprises longer, less dense nanowire arrays compared to NW2 and NW3. Upon scanning the surface, it was evident that more bacteria had attached between the nanowires. In one example, an *E. coli* cell had adhered between multiple nanowires (Figure 5.28) and was seen to express significant quantities of fimbria-like appendages, that were interacting with adjacent nanowires and bacteria. Sequential ion beam milling revealed two nanowires that were in direct contact with the cell envelope, yet there was no indication of nanowire-induced envelope deformation or penetration. Nevertheless, the positioning of *E. coli* between adjacent nanowires may have been significant in preventing division. Additional evidence of potential nanowire-induced impedance is shown in Figure 5.29. Similar to the previous two examples, two nanowires had interacted with the envelope on opposite sides of a cell, again towards one pole. At high magnification, it was clear the envelope had not been significantly deformed by the nanowires, but it is possible that cell division had been impeded.

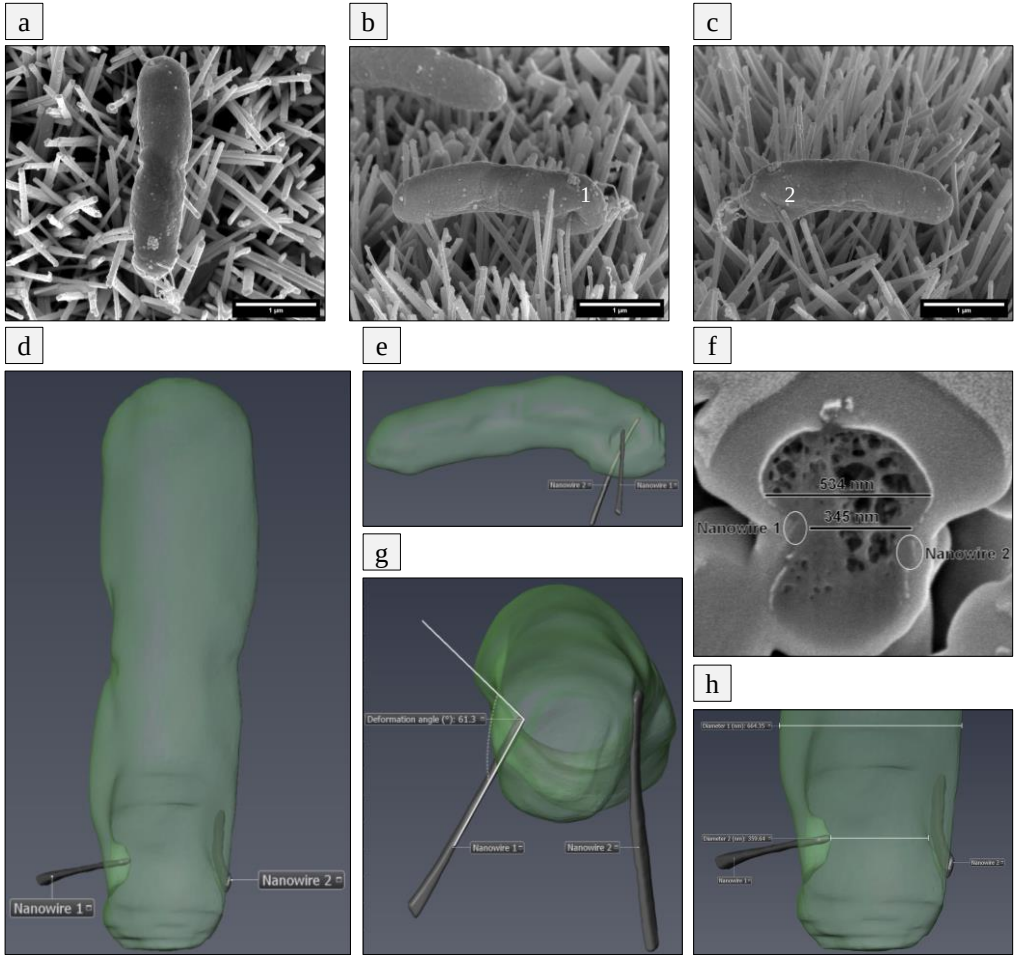

Figure 5.27 | 3D reconstruction of nanowire-induced envelope deformation and cell impedence on NW3. Automated FIB-SEM cross sectional analysis was performed on an *E. coli* cell (a) that had been incubated on NW3 for 3 h and was pinned between two nanowires (b-c). The focused ion beam produced 120 cross sections (30 nm each) that were imaged and reconstructed in Avizo (d-e). Analysis of *E. coli* cross section #30 showed that nanowire 1 had forced *E. coli* into nanowire 2, resulting in a 189 nm reduction in cell width (f). While nanowire 1 had induced significant envelope deformation, no evidence of envelope penetration was found. The width of *E. coli* quickly restored to normal either side of the contact point, indicating that the cell had not lost turgor pressure (g-h).

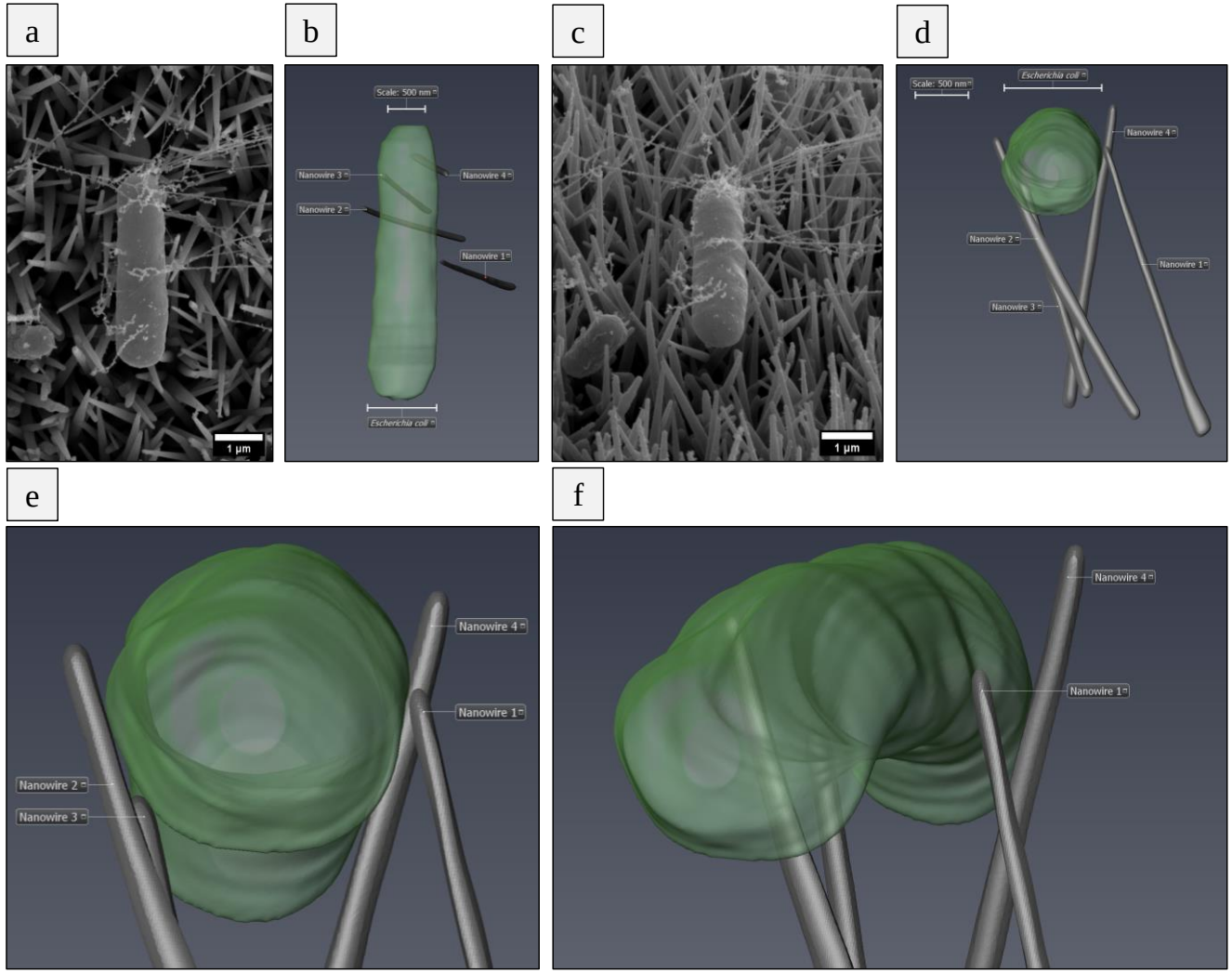

Figure 5.28 | 3D reconstruction of nanowire-induced cell impedance on NW4. Automated FIB-SEM cross sectional analysis was performed on an *E. coli* cell (a, c) that was pinned between two nanowires (nanowire 3 and 4) after incubation on NW4 for 3 h (e, f). There was no evidence of envelope deformation or penetration, and no indication of cytosolic leakage, as the width of *E. coli* remained constant from pole to pole (b, d).

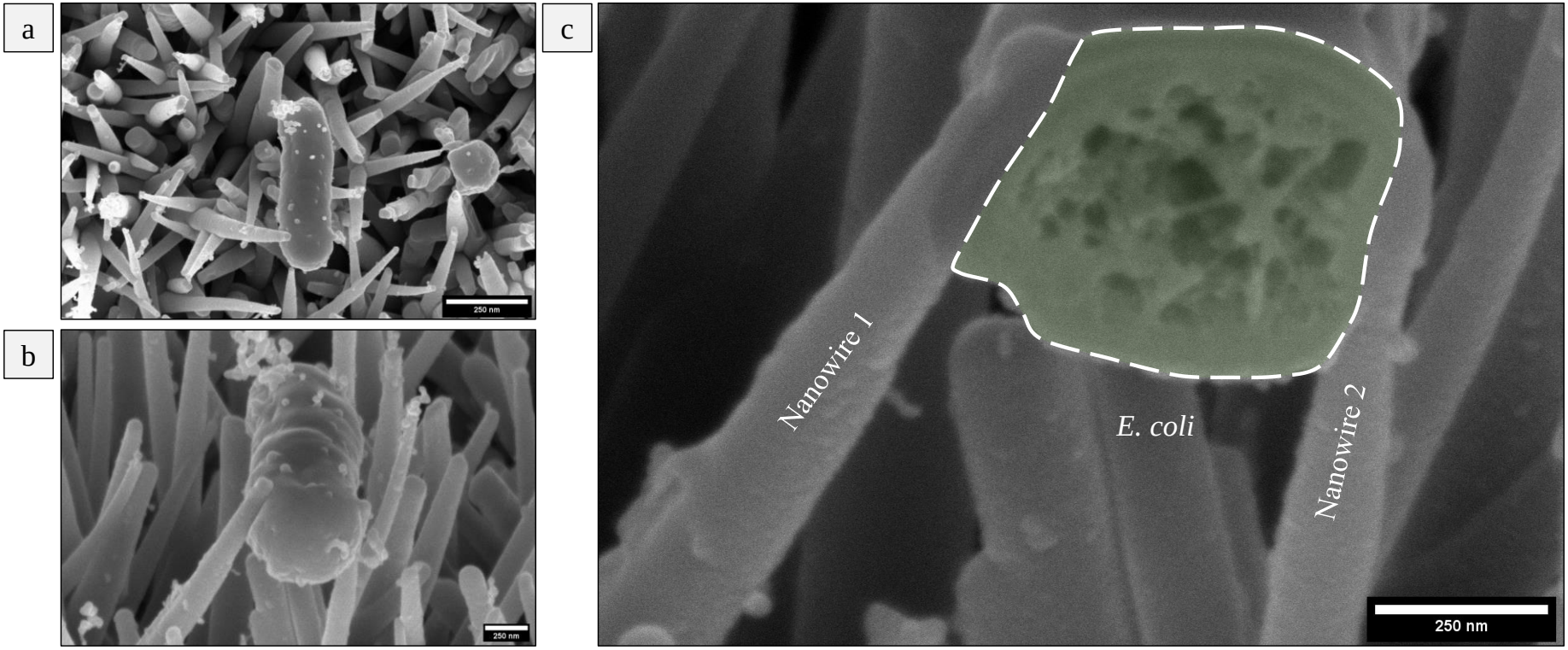

Figure 5.29 | Evidence of potential nanowire-induced cell impedance on NW4. SEM micrographs of *E. coli* cell before FIB-SEM milling (a-b). Cross sectional analysis highlights that *E. coli* is pinned between two nanowires (c). The cross section through *E. coli* is highlighted in green with a white outline.

FIB-SEM milling was also used to perform cross sectional analysis of *S. aureus* on NW3. Preliminary area scanning had identified a *S. aureus* cell in contact with 3 nanowires, one of which (nanowire 1) appeared to be penetrating at the bacterial septum (Figure 5.30). To confirm this, sequential ion beam milling was performed in 30 nm sections. Analysis of individual FIB cross sections confirmed that nanowire 1 had not penetrated the envelope. However, the cross section of nanowire 2 provided clear evidence that the tip had penetrated the bacterial envelope by 48 nm, surpassing the envelope by approximately 15 nm. Thus, in contrast to *E. coli* on NW3, where nanowires had generally induced significant local deformation, for *S. aureus*, envelope penetration did not appear to have affected cell morphology. In addition to nanowire-induced envelope penetration, there was evidence that *S. aureus* division may have been impeded by nanowires 1-3. From a top view, nanowires 1-3 could be seen in a triangle formation around the cell. Nanowire 1 appeared to be pinning the cell onto the surface, which in turn, may have forced the cell onto nanowire 2, resulting in a combination of cell impedance and envelope penetration.

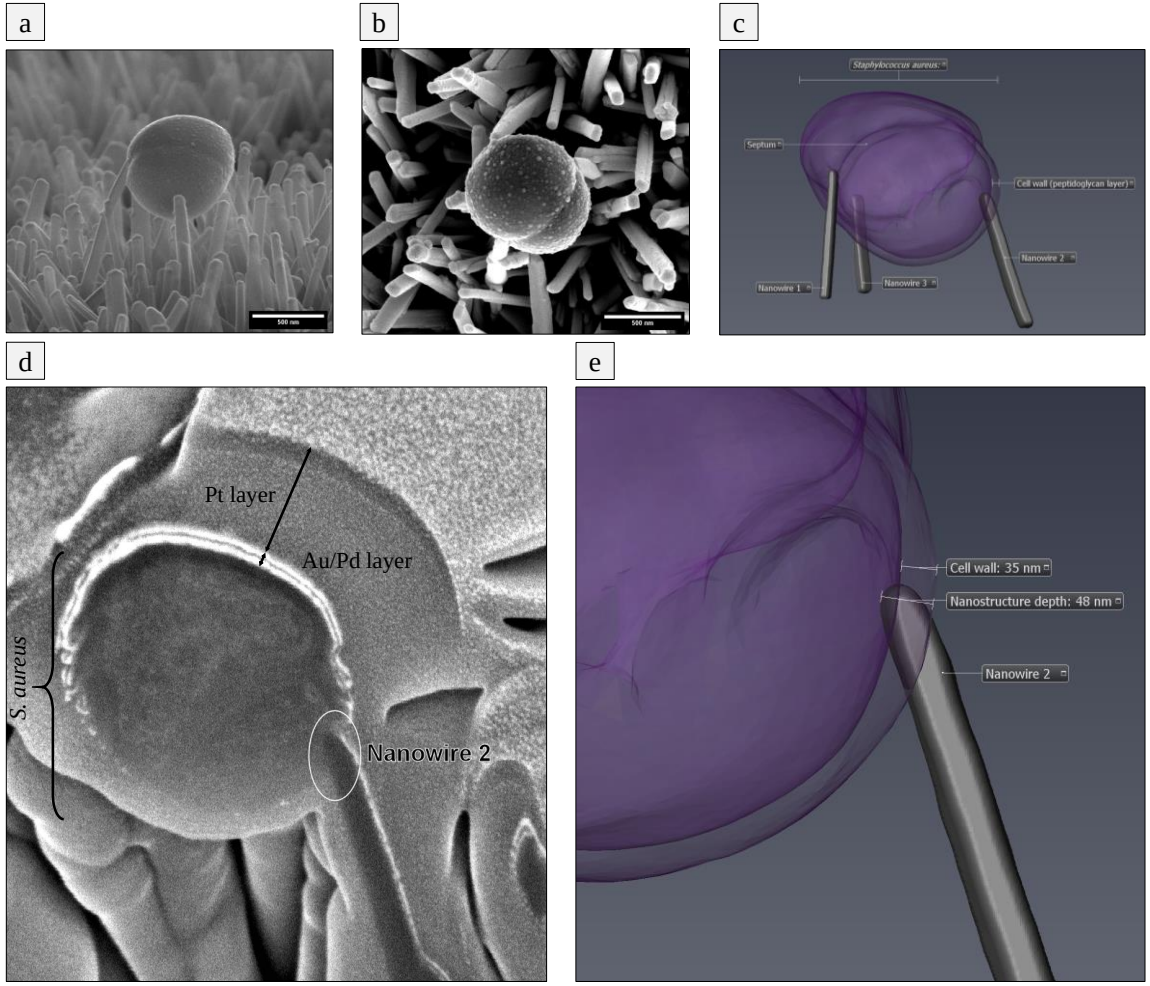

Figure 5.30 | 3D reconstruction of nanowire-induced envelope penetration and cell impedance of *S. aureus* on NW3. Automated FIB-SEM cross sectional analysis was performed on an *S. aureus* cell interacting with three nanowires after 3 h incubation on NW3 (a-b). The focused ion beam produced 57 cross sections (30 nm each) that were imaged and reconstructed in Avizo (c). Analysis of *S. aureus* cross section #40 showed the tip of nanowire 2 located approximately 50 nm into the cell, providing confirmation of cell wall and plasma membrane penetration (d-e).

5.5 Discussion

A wide variety of natural and synthetic nanotopographies have been reported to possess antimicrobial activity (Tripathy et al., 2017). To date, most of the published literature have focused on the bactericidal properties of these surfaces, with fungicidal activity having also been shown (Nowlin et al., 2014). Currently, however, no consensus has been reached with respect to the origin of bacterial cell death and indeed, the precise mechanistic basis could be expected to vary, depending on the exact surface chemistry, nanotopography and cell type. This is evident from existing literature (Bandara et al., 2017; Köller et al., 2018; Linklater et al., 2018, 2017). Nevertheless, it is generally accepted that nanotopography-induced bacterial killing is a physical, rather than chemical process, mediated by nanostructures (i.e. nanowires, nanotubes, nanospikes, nanospears) that can deform, damage, penetrate or rupture the bacterial cell envelope.

In this study, SEM analysis indicated fewer *S. aureus*, *S. epidermidis*, *E. coli* and *K. pneumoniae* cells were attached to nanowires surfaces than control after a 10 h incubation period. This implied that the reduced bacterial viability seen on nanowire surfaces by RTG and BTG assays (Chapter 4) was attributable to differences in the number of bacteria per unit area, rather than reduced metabolic activity of the adherent population. Using a range of microscopy techniques, data presented here indicate that these reductions may be due to a combination of bacterial cell death caused by nanowire-induced envelope damage and of impaired bacterial replication.

5.5.1 Nanowire-induced envelope deformation and penetration

Analysis of bacterial surface morphology using SEM identified clear signs of nanowire-induced envelope deformation. This finding was consistent with TEM and tomography analysis, which revealed localised deformation and, in some cases, envelope penetration. These data were further validated by FIB-SEM cross sectional analysis, which highlighted cases of nanowire-induced envelope deformation and penetration in both *S. aureus* and *E. coli*. In general agreement with existing biophysical models and published experimental data, envelope deformation was most prominent in Gram-negative bacteria (*E. coli*, *K. pneumoniae* and *P. aeruginosa*), which possess thin peptidoglycan layers (≈ 5 nm) (Hasan et al., 2013; Köller et al., 2018). Nonetheless, there was strong evidence that nanowires were also able to penetrate *S. aureus*, albeit at a much lower frequency. The reduced susceptibility of *S. aureus* and *S. epidermidis* to nanowire deformation may partly be explained by the increased peptidoglycan

thickness and higher turgor pressure in Gram-positive bacteria. Indeed, one study reported a lower total creep deformation in *B. subtilis* compared to *E. coli* (Vadillo-Rodriguez et al., 2009). In another study, the force required to rupture *S. epidermidis* was approximately 4-fold greater than was needed to rupture *E. coli*, measured at 13.8 µN and 3.6 µN respectively (Shiu et al., 1999).

It is also possible that the observed differences in envelope deformation and penetration were influenced by cell shape, cell attachment and cell division dynamics. To maximise the effective contact area with a surface, rod-shaped *E. coli* and *K. pneumoniae* may transition from a polar to a longitudinal orientation. In the context of nanowire surfaces, this would increase the interactions between bacteria and nanowires. In contrast, the coccoid shape of *S. aureus* and *S. epidermidis* leads to a reduced effective contact area, thereby reducing the chance of nanowire interactions. Furthermore, during binary fission, *E. coli* and *K. pneumoniae* will most likely divide in a longitudinal orientation, parallel to the surface. This could be expected to increase the stress applied across the bacterial envelope, leading to increased damage. In support of this, bacterial cell division has been reported to enhance the damage of Gram-negative bacteria on titanium nanopillar arrays (Köller et al., 2018). In contrast, *S. aureus* and *S. epidermidis* division may occur in vertical planes. Thus, daughter cells may not be in contact with the nanowire surface following binary fission (Sengstock et al., 2014).

Although nanowire-induced envelope penetration was generally observed at a low incidence compared to deformation, its frequency could be expected to increase with time, owing to the viscoelastic nature of the peptidoglycan layer (Vadillo-Rodriguez and Dutcher, 2011). Similarly, as from this study it was evident that bacterial envelope deformation had occurred from the applied force of nanowire contact, this effect would be time-dependent. Thus, longer incubation times could be expected to increase the incidence of bacterial cell penetration and permeability. This is consistent with CLSM and bacterial viability data shown in the previous chapter. Significant reductions in bacterial viability were generally observed after 3 h, rather than immediately, as has been reported in previous studies (Ivanova et al., 2013, 2012). Furthermore, LIVE/DEAD staining revealed no evidence of envelope damage after 3 h incubation yet by 18 h, the intensity had increased significantly. Thus, the combined data support that bacterial envelope damage occurred in a time-dependent manner.

The force applied across the bacterial envelope during nanowire contact is anticipated to increase cell permeability, but it remains unclear whether nanowire-induced cell impedance could have the same effects. On the one hand, if the dimensions of bacteria are less than that of the nanofeature spacings, then bacteria could be expected to settle between nanowires without any applied force across the envelope. In this scenario, no envelope damage would be anticipated, only impedance, and therefore cell permeability is not likely to change. Alternatively, if the nanofeature spacings are less than or equal to the dimensions of bacteria, as for NW2 and NW3, then it is conceivable that envelope deformation could lead to cell impedance. In this situation, it is probable that envelope integrity could be compromised.

Throughout these analyses there was limited evidence to support that nanowire arrays could induce a loss of turgor pressure or mediate cell lysis, even when nanowires had penetrated the bacterial envelope. This is somewhat surprising, as many studies have reported the sinking and spreading of bacteria into nanotopographies due to envelope rupture (Ivanova et al., 2012). Similar morphologies have been described as engulfment (Bhadra et al., 2015; Ivanova et al., 2013) or envelope wrinkling and cytosolic leakage (Bandara et al., 2017). However, in the above-mentioned studies, the structural artefacts that can arise from SEM preparation were seemingly not considered as a possible explanation for these morphologies. This is important, since such artefacts could be mistaken for nanotopography-mediated effects. Following the introduction of SEM as a tool to visualise biological samples, it has been widely reported that sample damage can arise from the processing steps; often described as shrinkage, wrinkling or surface cracking (Golding et al., 2016). Although sample damage can occur at any stage of processing, it is particularly common during the dehydration and drying steps (Katsen-Globa et al., 2016). This is largely attributed to the high surface tension of water to air. This means that large forces can be applied at the sample-air interface during evaporation, which can induce nano and micro changes in surface morphology.

In this study, to minimise shrinkage and wrinkling of bacteria, dehydration was performed using increasing concentrations of ethanol. This ensures that water is displaced gradually rather than bulk displacement with high starting concentrations, which could induce morphological changes (Ingram, 1981). Furthermore, bacterial samples were dried using critical point drying (CPD). Briefly, the critical point is defined as the temperature and pressure at which there is no difference in the physical properties of a material's liquid and gas states. CPD utilises liquid carbon dioxide (CO_2), which has a critical point of 31°C and 74 bar. These conditions are suitable for biological samples, unlike H_2O, which has a critical point of 374°C and 229 bar. Once H_2O has been displaced using a graded ethanol series, the samples are transferred to the CPD, wherein liquid ethanol is replaced with liquid CO_2 before gradually reaching the critical point. At the critical point, the density of liquid and gas CO_2 is the same, meaning the surface tension at the evaporation interface (bacterial envelope) is zero, which minimises structural distortion in the sample (Yu et al., 2014).

Although this study has shown conclusively that nanowires can penetrate the envelope of both Gram-positive and Gram-negative bacteria, the incidence was low. However, it was not possible to quantify the exact frequency of penetration, since the number of bacteria analysed represented only a small proportion of the total population. Nevertheless, it is evident from LIVE/DEAD analysis that little envelope damage had occurred after 3 h, which is consistent with TEM and FIB-SEM analysis, that identified very few cases of penetration in 3 h. Thus, the reductions in bacterial viability on nanowire surfaces cannot be fully attributed to envelope deformation and penetration. These findings are contrary to a number of studies, reporting highly efficient bactericidal action on natural and synthetic nanotopographies within the first few hours of incubation (Hasan et al., 2017, 2013; Ivanova et al., 2013, 2012).

5.5.2 Nanowire-induced cell impedance

In addition to nanowire-induced envelope deformation and penetration, imaging analysis revealed that nanowires had the capacity to act as physical barriers, entrapping bacterial cells and possibly impeding division, at least in the horizontal plane. Such effects could have contributed to the reduced number of bacteria per unit area and subsequent reduction in viability. A mechanism similar to nanowire-induced cell impedance was observed by Cao and colleagues when investigating the antibiofilm properties of titanium nanowire surfaces with pocket-like formations. *S. epidermidis* was reported to settle inside pocket-like formations, thereby isolating the bacterial cells. Once *S. epidermidis* had become trapped within these pockets, it was proposed that cell death could occur by direct membrane deformation, penetration, or through cells being squeezed between nanowires (Cao et al., 2018).

Unlike nanowire-induced envelope deformation, which was predominant for Gram-negative bacteria, nanowire-induced cell impedance appeared to be prevalent for both Gram-positive and Gram-negative cells. Nevertheless, it is possible that the size and shape of bacteria could affect the frequency of impedance. In one study, the relationship between surface microtopography and cell retention was investigated. Titanium surfaces with irregular pits ranging from 0.2-0.5 µm diameter and regular pits with diameters from 1-2 µm were incubated for 1 h with *S. aureus*, *P. aeruginosa* and *C. albicans*. *S. aureus* retention was the highest on each surface type and was found to accumulate within 0.5-2µm pit sizes. *P. aeruginosa* displayed the seconded highest retention, and was seen to accumulate within pits ≥ 1µm. In contrast, *C. albicans* retention was the lowest and were generally too large to fit within the feature sizes, with the exception of some daughter cells (Whitehead et al., 2005). Considering this, it is reasonable to hypothesise that impedance would be more frequent for *S. aureus* and *S. epidermidis* in these studies, due to the relative dimensions of bacteria and nanowire arrays. In this study, *S. aureus* and *S. epidermidis* displayed characteristic coccoid morphologies, measuring 0.5-1 µm in diameter. In contrast, *E. coli* and *K. pneumoniae* are rod-shaped, measuring 2 µm from pole to pole and 500 nm in diameter. Therefore, one might expect nanowires to more readily impede *S. aureus* and *S. epidermidis* cells, for which there is a greater probability of adhesion between adjacent nanowires, due to their average dimensions generally being similar to nanowire spacings. In contrast, *E. coli* and *K. pneumoniae* are more likely to attach on top of the nanowires. In support of this hypothesis, when the average spacing of nanowires was increased, the frequency of impedance appeared to increase for *E. coli*, as determined by FIB-SEM analysis.

Alongside impedance, it is possible that the smaller size of *S. aureus* and *S. epidermidis* could have contributed to their reduced susceptibility to nanowire-induced envelope deformation and penetration. The probability of nanowire tip contact would likely to be lower for these Gram-positive bacteria than for *E. coli* and *K. pneumoniae*. However, it is important to note that further experiments are required to test these hypotheses more robustly, as the number of bacteria analysed in this study was relatively low. A large number of images would be required to constitute a representative sample of the whole bacterial population. This, however, was not practical using high-magnification SEM.

5.5.3 The effect of nanowires on fimbriae expression

Another notable observation from imaging analysis was the difference in surface expression of fimbria-like appendages by bacteria attached to control and nanowire surfaces. In general, these structures were more abundant for *E. coli* and *K. pneumoniae* that had been incubated on control surfaces. Furthermore, the quantity appeared to increase with incubation time, most notably between 3 and 10 h. In contrast, the abundance of fimbria-like appendages was much lower for *E. coli* and *K. pneumoniae* adhered to nanowire surfaces, with minimal change over time. On the basis of these findings, it is possible to hypothesise that nanowires may alter the expression of *E. coli* and *K. pneumoniae* adhesins, which could be expected to impair their capacity to attach to nanowire surfaces. This, in turn, could have contributed to the reduced number of *E. coli* and *K. pneumoniae* cells on nanowire surfaces at 10 h relative to control. This is partly supported by the proteomic analysis in Chapter 4, which revealed a significant increase in the abundance of surface composition regulator GlgS in *E. coli* recovered from NW3. GlgS is known to negatively regulate the synthesis of type-1 fimbriae and flagella (Rahimpour et al., 2013). Thus, it is possible that nanowire contact led to reduced type-1 fimbriae expression in *E. coli* and *K. pneumoniae*, that are known to be important for surface attachment (Murphy et al., 2013; Thomas et al., 2004). The absence of fimbria-like appendages for *E. coli* on nanowire surfaces is consistent with the findings of Rizzello and colleagues, who reported the absence of type-1 fimbriae from *E. coli* cells adhered to gold nanoparticle substrates. This was supported by expression analysis, which revealed significant downregulation of type-1 fimbriae genes *fimA* and *fimI*. The presence of gold nanoparticles was suggested to have caused these reductions due to the nanoscale variations in surface topography (Rizzello et al., 2012, 2011).

CHAPTER 6

Conclusions and future work

The adhesion of bacteria to medical implants and formation of biofilms are a growing challenge in healthcare systems. This is particularly evident for orthopaedic specialties, where titanium implants are prone to bacterial colonisation, which can result in life threatening infections (Arciola et al., 2018; Darouiche, 2004). This problem is further exacerbated by the rise of antibiotic resistant bacteria, which make it difficult to successfully treat infections, often necessitating surgical revision. As the demand for orthopaedic surgery increases annually, the absolute number of such infections is likely to rise. Consequently, the socioeconomic impact of orthopaedic implant infections is immense, accounting for a large proportion of healthcare expenditure and patient morbidity (Darouiche, 2004; Tande and Patel, 2014). Thus, it is critical that efforts are made to develop novel strategies to resist or prevent bacterial contamination of titanium implants. Insects, including cicada and dragonfly, have evolved nano-protruding arrays on their wings that have been shown to impair bacterial contamination upon contact (Ivanova et al., 2013, 2012). In particular, the nanotopography of dragonfly wings has been shown to possess bactericidal activity against both Gram-positive and Gram-negative bacteria, therefore making it a suitable candidate for biomimetic titanium nanotopographies.

The inspiration obtained from natural surfaces has prompted the design of novel biomaterials that are resistant to bacterial contamination (Tripathy et al., 2017). However, our understanding of the underlying causes for bacterial cell death remains limited, yet is essential for guiding the design of next generation biomaterials that effectively inhibit biofilm growth, without reliance on antibiotics. For such technologies to be translated into clinical applications, addressing this fundamental knowledge gap is crucial. A number of nanofabrication methods have been utilised to mimic natural nanotopographies on clinical materials, including the alkaline hydrothermal method (Bhadra et al., 2015; Diu et al., 2014) and colloidal lithography (Hazell et al., 2018b). In this study, a thermal oxidation technique was used, which provided a simple and straightforward method to synthesise large areas of nanowires, in one step, and directly onto the material of choice. Importantly, the use of complex equipment and external catalysts is eliminated by thermal oxidation, which reduces costs and avoids the requirement to remove the catalyst post-fabrication, such as is required with vapour-liquid-solid growth methods (Dinan, 2012; Noor Mohammad, 2009). The material used in this study was Ti-6Al-4V, as this

can easily be modified by thermal oxidation and is widely used for dental and orthopaedic implants.

6.1 Nanowire growth by thermal oxidation

The growth of nanowires by thermal oxidation is influenced by several parameters, including the oxidising environment, temperature, duration, flow rate, crystal structure and polishing treatment. In particular, it was shown that TiO_2 nanowires grew most efficiently in the presence of acetone. This was attributed to the reduced availability of oxygen within the gaseous phase, meaning that reactions at the TiO_2 surface dominated the oxidation of Ti-6Al-4V substrates, which supported the 1D-growth of nanowires. These observations are consistent with previous literature (Peng et al., 2005; Peng and Chen, 2004). Following thermal oxidation, nanowires were shown to possess core-shell structures. EDX line scanning analysis confirmed that titanium and oxygen were mostly found in the core, with lower levels of carbon, most likely attributed to TiC, while the shell consisted of carbon only. This correlates with previous studies, indicating that the nanowire growth mechanism was the same in this study (Hu et al., 2010; Huo et al., 2008; Zhang et al., 2012). Core-shell nanowire surfaces possessed hydrophobic wetting. This was shown to be caused by the presence of carbon, rather than the nanotopography, since the removal of carbon by annealing led to superhydrophilic wetting.

By changing the processing conditions of thermal oxidation, namely the oxidation temperature and duration, it was possible to modify the type of nanotopography that formed. In contrast, the effect of flow rate was minimal. Nanowire growth occurred in a temperature window of 650°C-850°C, in which the average nanowire length and diameter increased, while density reduced, leading to increased spacing. The same trend was observed with increasing oxidation duration, albeit to a lesser extent. Although this study has focused on the thermal oxidation of planar Ti-6Al-4V substrates, it is also possible to generate nanowires on more complex 3D structures (Arafat et al., 2013; Sjöström et al., 2016), such as the non-planar surfaces of dental and orthopaedic implants. Further work could assess whether the growth of nanowires on more complex 3D substrates such as 3D printed lattices or porous scaffolds is consistent with the growth of nanowires on 2D planar substrates. Indeed, a natural progression of this work would be to determine the antibacterial properties of 3D nanowire substrates generated by thermal oxidation, using the methods that have been optimised here. Additionally, further research is required to improve the mechanical robustness and attachment of TiO_2 nanowire arrays, to

ensure they can withstand the mechanical forces and impact that are experienced during surgery and in articulating joints.

6.2 The effect of TiO_2 nanowire arrays on bacterial viability

It is generally accepted that natural and synthetic nanotopographies mediate their bactericidal effects through mechanical rupture of the bacterial cell envelope, resulting in lysis and cell death (Bandara et al., 2017; Hasan et al., 2013; Ivanova et al., 2013, 2012; Kelleher et al., 2016). Much of our understanding of this mechanism is based on data generated from culture-based methods and microscopical investigations, namely CFU analysis and LIVE/DEAD staining. In line with published literature, CFU analysis and LIVE/DEAD staining were used here to determine the viability of *S. aureus* and *E. coli* in the presence of four different TiO_2 nanotopographies (NW1-NW4) compared to flat titanium surfaces. Viable count data were found to be strongly influenced by the efficiency of bacterial recovery. In general, fewer bacteria were recovered from nanowire surfaces compared to control, and it was clear that each surface remained heavily colonised post-washing. Without evaluating the recovery method, it would be possible to misinterpret these data as a significant reduction in *S. aureus* and *E. coli* viability on nanowire surfaces, which is not an accurate representation of the true antibacterial properties. This brings into question the validity of existing published data that have reported significant reductions in bacterial CFUs on nanotopographies, without mention of relative recovery rates across the surfaces tested. Indeed, micro- and nanotopographies have been shown to influence the retention of bacteria and fungi (Whitehead et al., 2005; Whitehead and Verran, 2006).

A number of limitations have been reported with the LIVE/DEAD fluorophores SYTO9 and PI, including SYTO9 bleaching, cross signalling, false-positive and false-negative staining (Shi et al., 2007; Stiefel et al., 2015). However, many of these effects can be accounted for by designing robust experiments with sufficient internal controls. Nevertheless, this study encountered a major problem using LIVE/DEAD staining for plate reader analyses, namely the high autofluorescence of SYTO9 and PI in LB medium. This resulted in poor assay sensitivity and it was not possible to accurately compare the levels of envelope damage on each surface. In contrast, end-point fluorescence microscopy revealed minimal PI staining of *S. aureus* or *E. coli* following 3 hours on nanowire surfaces, implying that TiO_2 nanowires had not induced envelope damage. This finding is somewhat surprising, as the seminal work by Ivanova and colleagues reported high killing rates on natural and synthetic nanotopographies within 3 h

incubation (Ivanova et al., 2013, 2012). This discrepancy is unlikely to be attributed to the differences in nanotopography or staining protocol, but rather the methods used to analyse, present and interpret the data.

In this study, the images generated from end-point fluorescence microscopy analysed 35% of the total disc area. By comparison, a number of published studies show < 1% of the total surface area (Hasan et al., 2013; Ivanova et al., 2013, 2012). Considering that bacterial attachment can vary across a surface, it is clear how such approaches could lead to antibacterial performance being grossly over or under-estimated, since the data used for analysis are not representative of the whole bacterial population. To overcome this limitation, CLSM was used in this study to continuously monitor the growth of *S. aureus* and *E. coli* expressing GFP across entire surfaces. While this approach proved effective at monitoring biofilm growth on individual surfaces, it was not possible to compare the relative growth rates of *S. aureus* and *E. coli* between surface types owing to the marked difference in GFP intensity between control and nanowire surfaces. However, the intensity of PI staining after 18 h was considerably stronger on nanowire surfaces compared to control, suggesting that bacterial envelope damage had occurred. Since PI staining was not observed after 3 h, this implies that envelope damage increased with time. On the basis of these data alone, one could attribute this to the viscoelastic properties of bacterial cell walls, which exhibit time-dependent deformation under the application of force (Vadillo-Rodriguez and Dutcher, 2011). However, additional studies are needed to provide more definitive evidence for this mechanism. In particular, one could use CLSM in combination with PI staining to assess the level of envelope damage at different timepoints between 3 and 18 h, ensuring to analyse the entire surface. With further optimisation, in-situ CLSM could be a useful tool for determining the antibiofilm properties of different nanotopographies by monitoring GFP-expressing bacteria.

Considering the narrow range of microbiological tools that have been used to determine bacterial viability on natural and synthetic nanotopographies, this study explored the use of two additional biochemical assays, RTG and BTG, which provide an indication of bacterial viability based on cellular reducing power and ATP concentration, respectively. RTG revealed significant reductions in *S. aureus* and *S. epidermidis* viability in the presence of NW2 and NW3 surfaces, while no effect was observed for *E. coli* and *K. pneumoniae*. This was attributed to the lower reducing power of Gram-negative bacteria, which led to lower overall luminescent signals. For BTG analyses, significant reductions in *S. aureus* viability were observed on NW2 and NW3 after 10 h, which was consistent with RTG analyses. In contrast, for *S. epidermidis*,

while the average luminescent signal was 2-fold lower on nanowire surfaces compared to control, these did not reach statistical significance. This was attributed to the inter-experimental variation observed on control discs. Since there was minimal inter-experimental variation for other bacteria using the BTG assay, it is possible that further experimental repeats may change the significance of this result. For *E. coli* and *K. pneumoniae,* significant reductions in viability were observed in the presence of NW2 and NW3 following 3 h incubations using the BTG assay. This highlights the importance of utilising several methods to determine the antibacterial properties of nanowire arrays, as different assays provide indications of bacterial viability based on different cellular processes. For example, LIVE/DEAD staining revealed no evidence of *E. coli* envelope damage following 3 h, yet BTG analyses showed reductions in luminescence in the presence of nanowire surfaces, indicating reduced viability. Furthermore, it is important to note that each assay will likely have different sensitivities, meaning significant effects can be missed when using a single assay.

Low magnification SEM analysis revealed marked reductions in all tested bacteria on NW2 and NW3 at time points that were broadly consistent with the reductions determined by RTG and BTG analyses. Combined, these findings suggest that TiO_2 nanowire arrays reduced the capacity of bacteria to replicate and could mediate envelope damage. However, on the basis of these data alone, it remained unclear what mechanism(s) underpinned these effects. Two approaches were taken to investigate this further. Firstly, to determine whether these effects had been mediated by changes at the molecular level, TMT labelling and mass spectrometry analysis was performed to enable a direct quantitative comparison of *S. aureus* and *E. coli* proteomes in the presence or absence of nanowire array NW3. Secondly, advanced electron microscopy techniques were utilised to determine the effect of TiO_2 nanowires on bacterial envelope morphology and their capacity to rupture bacterial cells, as has frequently been reported in published literature (Hasan et al., 2013; Ivanova et al., 2012; Pogodin et al., 2013).

6.3 Antibacterial mechanisms of TiO_2 nanowires

It is generally accepted that natural and synthetic nanotopographies mediate bacterial cell death via physical contact, which can damage and rupture the cell envelope (Ivanova et al., 2013, 2012; Tripathy et al., 2017). Nonetheless, there is still ambiguity regarding exactly how this occurs. Further still, the precise mechanism(s) may vary, depending on the nanotopography and cell type (Bandara et al., 2017; Köller et al., 2018; Linklater et al., 2018, 2017). This study identified several mechanisms that are likely to have reduced the capacity for bacteria to grow and divide in the presence of TiO_2 nanowire arrays: 1) nanowire-induced ROS generation, 2) nanowire-induced envelope deformation, 3) nanowire-induced envelope penetration, and 4) nanowire-induced cell impedance (Figure 6.1).

Proteomic analysis revealed a significant number of *S. aureus* and *E. coli* DEPs were involved in oxidative stress responses. Furthermore, the levels of H_2O_2, a by-product of superoxide anions, were found to be significantly higher in *S. aureus* and *E. coli* incubated on NW3 than on controls. These findings are partly consistent with previous studies that have investigated the proteomic response of *S. aureus* or *E. coli* to oxidative stressors. In one study, *S. aureus* exposure to H_2O_2 led to increased production of DNA protection and repair enzymes, including the SOS response protein UvrA (Wolf et al., 2008). Similarly, for *E. coli*, H_2O_2 exposure is reported to activate the SOS response (Imlay and Linn, 1987) and enzymes involved in ROS detoxification (SodA) (Semchyshyn, 2009). However, further analysis is required to more precisely compare the proteomic response of *S. aureus* and *E. coli* in this study to the existing literature; this will help to determine whether the bacterial oxidative stress response to nanotopographies is similar or distinct to previously characterised bacterial stress responses.

Additionally, the density of *S. aureus* and *E. coli* was lower on NW3 after 24 h compared to control, and bacterial envelope morphology was consistent with ROS-mediated damage. These findings correlate with previous studies (Olivi et al., 2013; Rajavel et al., 2014), which have reported ROS generation upon contact with CNTs. Importantly, this CNT-mediated effect occurred independently of photocatalytic activation and without envelope penetration (Olivi et al., 2013). Similarly, interactions with CNTs have been shown to induce ROS production in human cells, leading to cytotoxicity. Again, this occurred without photoactivation (Yu et al., 2016). Bacterial ROS production has been identified as a general response to a wide variety of stressors. Of note, this mechanism is self-amplifying, meaning that ROS production is sustained, even when the initial stressor is removed (Hong et al., 2019). The findings of this

study imply that direct contact of bacteria with TiO_2 nanowires leads to oxidative stress via the generation of ROS. It is also possible that the superhydrophilic wetting of NW3 promoted ROS production, as this would enhance the shear-stress experienced at the interface, a factor that has been shown to induce ROS-mediated cell death in *B. subtilis* (Sahoo et al., 2006, 2003). Therefore, the time-dependent reductions in bacterial viability and increases in envelope damage seen with the nanowire surfaces tested here can be explained, at least in part, with a predicted accumulation of ROS with time.

The effects of TiO_2 nanowire arrays on bacterial envelope morphology were investigated using several electron microscopy techniques, namely SEM, TEM and FIB-SEM. SEM analysis revealed the first indications that nanowires could mediate deformation of the bacterial cell, demonstrating envelope indentations at the point of nanowire contact. This nanowire-induced envelope deformation was most prominent in Gram-negative bacteria (*E. coli* and *K. pneumoniae*), which possess thinner peptidoglycan layers than Gram-positive bacteria (*S. aureus* and *S. epidermidis*). This finding is consistent with published literature, which has reported that increased peptidoglycan thickness can reduce susceptibility to nanotopography-induced contact killing (Hasan et al., 2013). In agreement with SEM analysis, nanowire-induced envelope deformation was also identified by the TEM and FIB-SEM techniques used in this study.

In addition, TEM and FIB-SEM techniques revealed that nanowires could penetrate the envelope of both Gram-negative and Gram-positive bacteria. On the basis of these findings, it is very likely that nanowire-induced envelope deformation occurs as a precursor to envelope penetration. Since the bacterial envelope is viscoelastic (Vadillo-Rodriguez and Dutcher, 2011), the incidence of envelope penetration is anticipated to increase with time. Furthermore, the accumulation of ROS-mediated envelope damage could promote envelope penetration with time. These findings are in general agreement with previous studies, which have reported that nanotopographies can deform/stretch and penetrate the envelope of Gram-positive and Gram-negative bacteria (Bandara et al., 2017; Cao et al., 2018; Linklater et al., 2017). Despite conclusive evidence that TiO_2 nanowires could penetrate the bacterial envelope, this did not lead to leakage of cytosolic content or a loss of turgor pressure, as has been indicated by previous studies (Bandara et al., 2017; Ivanova et al., 2012). However, based on the techniques utilised in those studies, it is possible that such morphologies reflect structural artefacts of SEM processing rather than a nanotopography-mediated effect (Golding et al., 2016; Katsen-Globa et al., 2016).

Depending on the spacing of nanowires, it is possible for bacteria to become entrapped between them. For this study, in contrast to the mechanisms outlined above, nanowire-induced cell impedance increased with nanowire length and spacing. Since bacteria could be either pinned or trapped between adjacent nanowires, this mechanism did not always lead to direct envelope damage. Instead, impedance is predicted to have reduced the capacity for bacteria to divide, explaining, in part, the reduced cell numbers found on nanowire surfaces compared to control over time. Furthermore, the findings of this study support that envelope deformation can lead to cell impedance, through the action of bacteria squeezing between nanowires, resulting in a pinning effect.

6.4 Concluding remarks

This study has highlighted several key findings that have important implications for the development of antimicrobial nanotopographies for biomedical applications. Firstly, the mechanistic basis of contact killing is multifactorial and nanotopography dependent. While deformation and subsequent penetration of the bacterial envelope by nanowires was confirmed in this study, these mechanisms could not account for the significant reductions seen in bacterial viability, since their occurrence was comparatively low. Another notable mechanism identified in this study was nanowire-induced cell impedance, which is expected to reduce the capacity of bacteria to replicate on nanowire surfaces, and thus could have a greater influence on anti-biofilm properties of nanowire surfaces.

In addition to physical killing mechanisms, our analyses provide compelling evidence that nanowire arrays can induce oxidative stress within bacterial cells upon contact, the cumulative effects of which could impair processes such as bacterial growth, envelope integrity and biofilm formation. Indeed, this could account for the time-dependent reductions in bacterial viability and concomitant increases in envelope permeability. Better understanding of this mechanism could prove invaluable for improving the antibacterial performance of nanotextured materials. Thus, further research is needed to examine more closely the link between ROS generation, nanotopography design and bactericidal activity. It is also evident from this study that multiple experimental approaches should be exploited to robustly assess all aspects of bacterial physiology, so as to obtain a comprehensive assessment of the antibacterial properties of nanotextured materials. This will reduce experimental bias towards a single mechanism of action, and provide a more complete and accurate understanding of the antimicrobial mechanism of action.

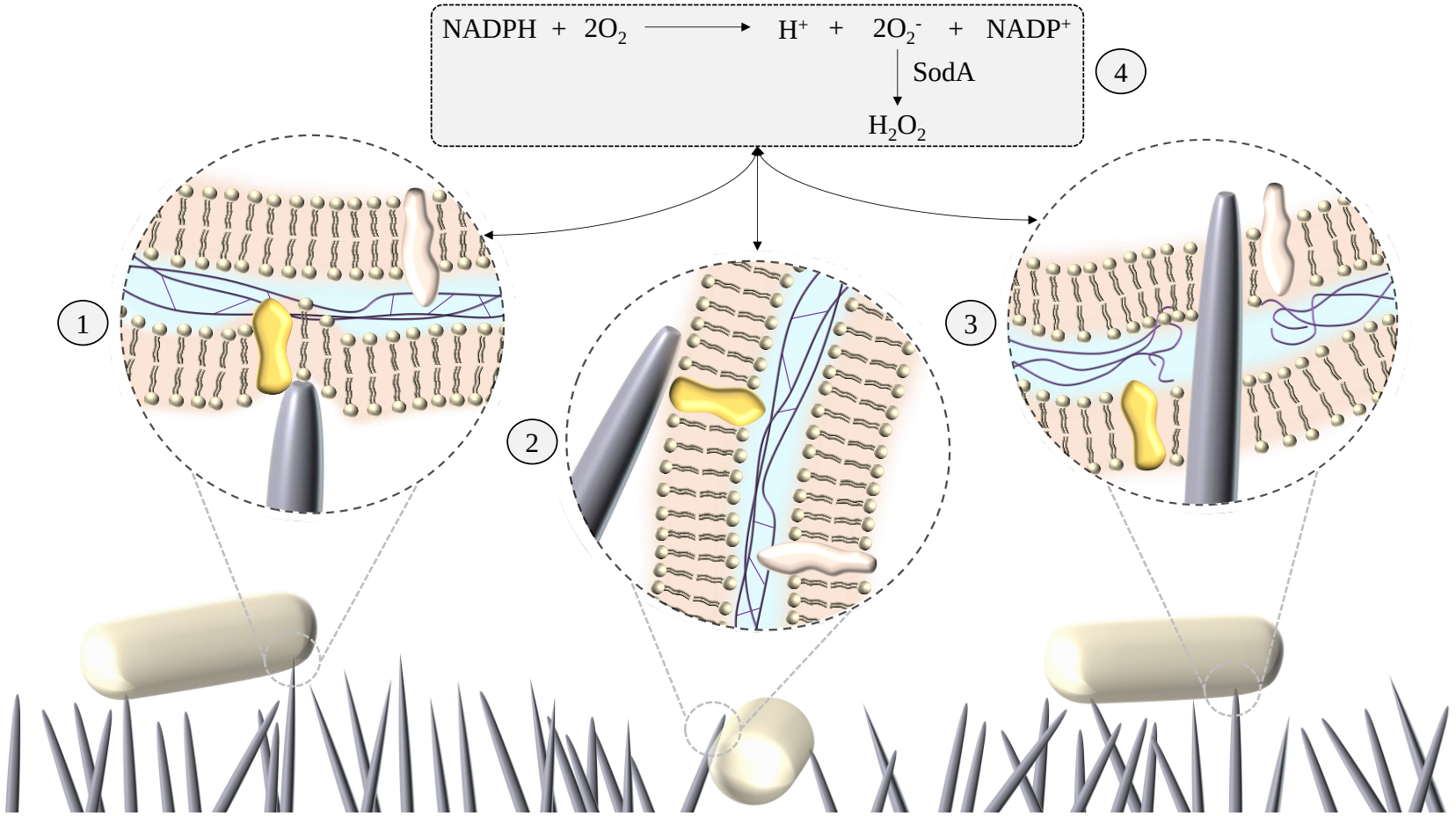

Figure 6.1 | Proposed antibacterial mechanisms of TiO_2 nanowire arrays. Adhesion of bacteria to TiO_2 nanowire arrays can lead to envelope deformation (1). Alternatively, if the spacing of nanowires is greater than the dimensions of the bacteria, it is possible for cells to adhere between nanowires (2). Both outcomes can lead to cell impedance and impaired replication. When the elastic limit of the bacterial envelope is exceeded by the applied force of a nanowire, deformation may lead to penetration of the cell envelope (3). Physical contact between bacteria and TiO_2 nanowires can also result in an oxidative stress response and the production of ROS (4). The accumulation of ROS is anticipated to lead to reduced bacterial growth and increased permeability of the cell envelope.

REFERENCES

ADA council, 2003. Titanium applications in dentistry. J. Am. Dent. Assoc. 134, 347–349.

Adedeji, W.A., 2016. The treasure called antibiotics. Ann. Ibadan Postgrad. Med. 14, 56–57.

Almarza, O., Núñez, D., Toledo, H., 2015. The DNA-binding protein HU has a regulatory role in the acid stress response mechanism in *Helicobacter pylori*. Helicobacter 20, 29–40.

Anantharaman, K., Breier, J.A., Dick, G.J., 2016. Metagenomic resolution of microbial functions in deep-sea hydrothermal plumes across the Eastern Lau Spreading Center. ISME J. 10, 225–239.

Arafat, M.M., Haseeb, A.S.M.A., Dinan, B., Akbar, S.A., 2013. Stress enhanced TiO_2 nanowire growth on Ti-6Al-4V particles by thermal oxidation. Ceram. Int. 39, 6517–6526.

Archer, N.K., Mazaitis, M.J., Costerton, J.W., Leid, J.G., Powers, M.E., Shirtliff, M.E., 2011. *Staphylococcus aureus* biofilms: Properties, regulation and roles in human disease. Virulence 5, 445–459.

Arciola, C.R., Campoccia, D., Ehrlich, G.D., Montanaro, L., 2015. Biofilm based implant infections in orthopaedics. Adv. Exp. Med. Biol. 1, 29–46.

Arciola, C.R., Campoccia, D., Montanaro, L., 2018. Implant infections: adhesion, biofilm formation and immune evasion. Nat. Rev. Microbiol. 16, 1–13.

Arora, M., Chan, E.K., Gupta, S., Diwan, A.D., 2013. Polymethylmethacrylate bone cements and additives: A review of the literature. World J. Orthop. 4, 67–74.

Arts, I.S., Gennaris, A., Collet, J.F., 2015. Reducing systems protecting the bacterial cell envelope from oxidative damage. FEBS Lett. 589, 1559–1568.

Asharani, P. V, Low, G., Mun, K., Hande, M.P., Valiyaveettil, S., 2009. Cytotoxicity and genotoxicity of silver nanoparticles in human cells. ACS Nano 3, 279–290.

Baker, J., Sitthisak, S., Sengupta, M., Johnson, M., Jayaswal, R.K., Morrissey, J.A., 2010. Copper stress induces a global stress response in *Staphylococcus aureus* and represses sae and agr expression and biofilm formations. Appl. Environ. Microbiol. 76, 150–160.

Bandara, C.D., Singh, S., Afara, I.O., Wolff, A., Tesfamichael, T., Ostrikov, K., Oloyede, A.,

2017. Bactericidal Effects of Natural Nanotopography of Dragonfly Wing on *Escherichia coli*. ACS Appl. Mater. Interfaces 9, 6746–6760.

Banerjee, I., Pangule, R.C., Kane, R.S., 2011. Antifouling coatings: Recent developments in the design of surfaces that prevent fouling by proteins, bacteria, and marine organisms. Adv. Mater. 23, 690–718.

Banin, E., Vasil, M.L., Greenberg, E.P., 2005. Iron and *Pseudomonas aeruginosa* biofilm formation. Proc. Natl. Acad. Sci. U. S. A. 102, 11076–11081.

Beenken, K.E., Blevins, J.S., Smeltzer, M.S., 2003. Mutation of sarA in *Staphylococcus aureus* limits biofilm formation. Infect. Immun. 71, 4206–4211.

Beenken, K.E., Dunman, P.M., Mcaleese, F., Macapagal, D., Murphy, E., Projan, S.J., Blevins, J.S., Smeltzer, M.S., 2004. Global Gene Expression in *Staphylococcus aureus* Biofilm. J. Bacteriol. 186, 4665–4684.

Berne, C., Ducret, A., Hardy, G.G., Brun, Y. V, 2015. Adhesins involved in attachment to abiotic surfaces by Gram-negtive bacteria. Microbiol. Spectr. 3, 1–45.

Berne, C., Ellison, C.K., Ducret, A., Brun, Y. V., 2018. Bacterial adhesion at the single-cell level. Nat. Rev. Microbiol. 16, 1–12.

Bhadra, C.M., Khanh Truong, V., Pham, V.T.H., Al Kobaisi, M., Seniutinas, G., Wang, J.Y., Juodkazis, S., Crawford, R.J., Ivanova, E.P., 2015. Antibacterial titanium nano-patterned arrays inspired by dragonfly wings. Sci. Rep. 5, 1–12.

Bhushan, B., 2012. Bioinspired structured surfaces. Langmuir 28, 1698–1714.

Bhushan, B., Jung, Y.C., Koch, K., 2009. Micro-, nano- And hierarchical structures for superhydrophobicity, self-cleaning and low adhesion. Philos. Trans. R. Soc. A 367, 1631–1672.

Bistolfi, A., Massazza, G., Verné, E., Massè, A., Deledda, D., Ferraris, S., Miola, M., Galetto, F., Crova, M., 2011. Antibiotic-Loaded Cement in Orthopedic Surgery: A Review. ISRN Orthop. 2011, 1–8.

Biswas, A., Bayer, I.S., Biris, A.S., Wang, T., Dervishi, E., Faupel, F., 2012. Advances in top-down and bottom-up surface nanofabrication: Techniques, applications & future prospects. Adv. Colloid Interface Sci. 170, 2–27.

Bjarnsholt, T., Alhede, Maria, Alhede, Morten, Eickhardt-Sørensen, S.R., Moser, C., Kühl, M., Jensen, P.Ø., Høiby, N., 2013. The *in vivo* biofilm. Trends Microbiol. 21, 466–474.

Blair, J.M.., Webber, M.A., Baylay, A.J., Ogbolu, D.O., Piddock, L.J.V., 2014. Molecular mechanisms of antibiotic resistance. Nat. Rev. Microbiol. 13, 42–51.

Bollen, C.M.L., Lambrechts, P., Quirynen, M., 1997. Comparison of surface roughness of oral hard materials to the threshold surface roughness for bacterial plaque retention: A review of the literature. Dent. Mater. 13, 258–269.

Brauner, A., Fridman, O., Gefen, O., Balaban, N.Q., 2016. Distinguishing between resistance, tolerance and persistence to antibiotic treatment. Nat. Rev. Microbiol. 14, 320–330.

Bridier, A., Dubois-Brissonnet, F., Greub, G., Thomas, V., Briandet, R., 2011. Dynamics of the action of biocides in *Pseudomonas aeruginosa* biofilms. Antimicrob. Agents Chemother. 55, 2648–2654.

Briggs, T., 2016. Royal College Surgeons England Background: MSK in the NHS [Online]. Available at: https://www.google.com/url?sa=t&rct=j&q=&esrc=s&source=web&cd=3&ved=2ahUKEwiai-uG2MvkAhX0snEKHQ-LCawQFjACegQIBBAC&url=https%3A%2F%2Fwww.rcseng.ac.uk%2F-%2Fmedia%2Ffiles%2Frcs%2Fstandards-and-research%2Fcommissioning%2Fgetting-it-right-for-orthopaedics-prof-t-briggs-27116.pdf&usg=AOvVaw1DBTJxub_k4vLXU01KmX97 (Accessed: 12 September 2019)

Briggs, T.W., 2011. Getting it right first time: improving the quality of orthopaedic care within the national health service in England [Online]. Available at: https://www.researchgate.net/publication/259390150_Getting_it_Right_First_Time (Accessed: 12 September 2019)

Cao, Y., Su, B., Chinnaraj, S., Jana, S., Bowen, L., Charlton, S., Duan, P., Jakubovics, N.S., Chen, J., 2018. Nanostructured titanium surfaces exhibit recalcitrance towards *Staphylococcus epidermidis* biofilm formation. Sci. Rep. 8, 1–13.

Cataldo, M.A., Petrosillo, N., Cipriani, M., Cauda, R., Tacconelli, E., 2010. Prosthetic joint infection: Recent developments in diagnosis and management. J. Infect. 61, 443–448.

Centers for Disease Control and Prevention, 1998. Leading Causes of Death, 1900-1998 [Online]. Available at: https://www.cdc.gov/nchs/data/dvs/lead1900_98.pdf (Accessed: 12 September 2019)

Chapman, C.A.R., Zhu, X., Chen, H., Yanik, A.A., Lein, P.J., Seker, E., 2017. Nanostructure Introduces Artifacts in Quantitative Immunofluorescence by Influencing Fluorophore Intensity. Sci. Rep. 7, 1–10.

Chen, G., Strevett, K.A., 2003. Microbial surface thermodynamics and interactions in aqueous media. J. Colloid Interface Sci. 261, 283–290.

Chen, H., Wang, B., Gao, D., Guan, M., Zheng, L., Ouyang, H., Chai, Z., Zhao, Y., Feng, W., 2013. Broad-spectrum antibacterial activity of carbon nanotubes to human gut bacteria. Small 9, 2735–2746.

Chen, M., Yu, Q., Sun, H., 2013. Novel strategies for the prevention and treatment of biofilm related infections. Int. J. Mol. Sci. 14, 18488–18501.

Chen, Y., Pepin, A., 2001. Nanofabrication: Conventional and nonconventional methods Miniaturization. Electrophoresis 22, 187–207.

Cheng, G., Zhang, Z., Chen, S., Bryers, J.D., Jiang, S., 2007. Inhibition of bacterial adhesion and biofilm formation on zwitterionic surfaces. Biomaterials 28, 4192–4199.

Cheng, Y., Feng, G., Moraru, C.I., 2019. Micro- and Nanotopography Sensitive Bacterial Attachment Mechanisms: A Review. Front. Microbiol. 10, 1–17.

Chou, S.Y., Krauss, P.R., Renstrom, P.J., 1996. Imprint Lithography with 25-Nanometer Resolution. Science 272, 85–87.

Chung, K.K., Schumacher, J.F., Sampson, E.M., Burne, R.A., Antonelli, P.J., Brennan, A.B., 2007. Impact of engineered surface microtopography on biofilm formation of *Staphylococcus aureus*. Biointerphases 2, 89–94.

Cobo, F., Rodríguez-Granger, J., Sampedro, A., Aliaga-Martínez, L., Navarro-Marí, J.M., 2017. Candida Prosthetic Joint Infection. A Review of Treatment Methods . J. Bone Jt. Infect. 2, 114–121.

Corbin, A., Pitts, B., Parker, A., Stewart, P.S., 2011. Antimicrobial penetration and efficacy in an *in vitro* oral biofilm model. Antimicrob. Agents Chemother. 55, 3338–3344.

Costa, L., Dantas, D.M., Silva-neto, J.P., Dantas, T.S., Naves, L.Z., Domingues, F., Soares, A., 2016. Bacterial Adhesion and Surface Roughness for Different Clinical Techniques for Acrylic Polymethyl Methacrylate. Int. J. Dent. 2016, 1–6.

Crick, C.R., Ismail, S., Pratten, J., Parkin, I.P., 2011. An investigation into bacterial attachment to an elastomeric superhydrophobic surface prepared via aerosol assisted deposition. Thin Solid Films 519, 3722–3727.

Damiati, L., Eales, M.G., Nobbs, A.H., Su, B., Tsimbouri, P.M., Salmeron-Sanchez, M., Dalby, M.J., 2018. Impact of surface topography and coating on osteogenesis and bacterial attachment on titanium implants. J. Tissue Eng. 9, 1–16.

Darouiche, R.O., 2004. Treatment of infections associated with surgical implants. N Engl J Med 350, 1422–1429.

Davey, M.E., O'Toole, G.A., 2000. Microbial Biofilms: from Ecology to Molecular Genetics. Microbiol. Mol. Biol. Rev. 64, 847–867.

Devlin-Mullin, A., Todd, N.M., Golrokhi, Z., Geng, H., Konerding, M.A., Ternan, N.G., Hunt, J.A., Potter, R.J., Sutcliffe, C., Jones, E., Lee, P.D., Mitchell, C.A., 2017. Atomic Layer Deposition of a Silver Nanolayer on Advanced Titanium Orthopedic Implants Inhibits Bacterial Colonization and Supports Vascularized *de Novo* Bone Ingrowth. Adv. Healthc. Mater. 6, 1–14.

Dickson, M.N., Liang, E.I., Rodriguez, L. a., Vollereaux, N., Yee, A.F., 2015. Nanopatterned polymer surfaces with bactericidal properties. Biointerphases 10, 021010.

Diebold, U., 2003. The surface science of titanium dioixde. Surf. Sci. Rep. 48, 53–229.

Dinan, B.J., 2012. Growth of Titania Nanowires by Thermal Oxidation [Online]. Available at: https://etd.ohiolink.edu/pg_10?0::NO:10:P10_ACCESSION_NUM:osu1337650302 (Accessed: 24 October 2019)

Diu, T., Faruqui, N., Sjöström, T., Lamarre, B., Jenkinson, H.F., Su, B., Ryadnov, M.G., 2014. Cicada-inspired cell-instructive nanopatterned arrays. Sci. Rep. 4, 1–7.

Djaman, O., Outten, F.W., Imlay, J.A., 2004. Repair of Oxidized Iron-Sulfur Clusters in *Escherichia coli.* J. Biol. Chem. 279, 44590–44599.

Doll, K., Jongsthaphongpun, K.L., Stumpp, N.S., Winkel, A., Stiesch, M., 2016. Quantifying

implant-associated biofilms: Comparison of microscopic, microbiologic and biochemical methods. J. Microbiol. Methods 130, 61–68.

Doll, P. W., Semperowitsch, C., Hafner, M., Ahrens, R., Spindler, B., Guber, A.E., 2018a. Fabrication of micro structured dental implant abutments for optimized soft tissue integration. Curr. Dir. Biomed. Eng. 4, 677–680.

Doll, P.W., Wolf, M., Weichert, M., Ahrens, R., Spindler, B., Guber, A.E., 2018b. Nanostructuring of titanium by anodic oxidation with sulfuric and hydrofluoric acid. Curr. Dir. Biomed. Eng. 4, 641–644.

Drury, P., Morrison, J., Newell, C., Pickford, M., Royall, M., Swanson, M., May, L., Van Der Meulen, J., Sibanda, N., 2007. National Joint Registry 4th Annual Report [Online]. Available at: http://www.njrcentre.org.uk/njrcentre/Reports-Publications-and-Minutes/Annual-reports/Archived-annual-reports (Accessed: 12 September 2019)

Dunne, W. Michael, Jr., 2002. Bacterial adhesion: seen any good biofilms lately? Clin. Microbiol. Rev. 15, 155–166.

Duran, E.C., Lucius, A.L., 2018. ATP hydrolysis inactivating Walker B mutation perturbs *E. coli* ClpA self-assembly energetics in the absence of nucleotide. Biophys. Chem. 242, 6–14.

Dutta, P, 2000. Grazing incidence X-ray diffraction. Curr. Sci. 78, 1478-1483.

Evrard, B., Balestrino, D., Dosgilbert, A., Bouya-Gachancard, J.L.J., Charbonnel, N., Forestier, C., Tridon, A., 2010. Roles of capsule and lipopolysaccharide O antigen in interactions of human monocyte-derived dendritic cells and *Klebsiella pneumoniae*. Infect. Immun. 78, 210–219.

Ewald, A., Glückermann, S.K., Thull, R., Gbureck, U., 2006. Antimicrobial titanium/silver PVD coatings on titanium. Biomed. Eng. Online 5, 1–10.

Ezraty, B., Gennaris, A., Barras, F., Collet, J.F., 2017. Oxidative stress, protein damage and repair in bacteria. Nat. Rev. Microbiol. 15, 385–396.

Fernández, I.C.S, Mei, H.C. va. der, Metzger, S., Grainger, D.W., Engelsman, A.F., Nejadnik, M.R., Busscher, H.J., 2010. *In vitro* and *in vivo* comparisons of staphylococcal biofilm formation on a cross-linked poly(ethylene glycol)-based polymer coating. Acta Biomater. 6, 1119–1124.

Fisher, L.E., Yang, Y., Yuen, M.-F., Zhang, W., Nobbs, A.H., Su, B., 2016. Bactericidal activity of biomimetic diamond nanocone surfaces. Biointerphases 11, 011014.

Fitzpatrick, T.B., Amrhein, N., Macheroux, P., 2003. Characterization of YqjM, an old yellow enzyme homolog from *Bacillus subtilis* involved in the oxidative stress response. J. Biol. Chem. 278, 19891–19897.

Flemming, H., Wingender, J., Szewzyk, U., Steinberg, P., Rice, S.A., 2016. Biofilms: an emergent form of bacterial life. Nat. Publ. Gr. 14, 563–575.

Flemming, H.C., Wingender, J., 2010. The biofilm matrix. Nat. Rev. Microbiol. 8, 623-633.

Flint, S.H., Brooks, J.D., Bremer, P.J., 2000. Properties of the stainless steel substrate, influencing the adhesion of thermo-resistant streptococci 43, 235–242.

Francolini, I., Vuotto, C., Piozzi, A., Donelli, G., 2017. Antifouling and antimicrobial biomaterials: an overview. Apmis 125, 392–417.

Friedmann, A., Hoess, A., Cismak, A., Heilmann, A., 2011. Investigation of cell-substrate interactions by focused ion beam preparation and scanning electron microscopy. Acta Biomater. 7, 2499–2507.

Gammon, L.M., Briggs, R.D., Packard, J.M., Batson, K.W., Boyer, R., Domby, C.W., 2004. Metallography and Microstructures of Titanium and its Alloys. ASM Handb. 9, 899–917.

Garrett, T.R., Bhakoo, M., Zhang, Z., 2008. Bacterial adhesion and biofilms on surfaces. Prog. Nat. Sci. 18, 1049–1056.

Gates, B.D., Xu, Q., Stewart, M., Ryan, D., Willson, C.G., Whitesides, G.M., 2005. New approaches to nanofabrication: Molding, printing, and other techniques. Chem. Rev. 105, 1171–1196.

Gautreau, S., Gould, O.N., Forsythe, M.E., 2016. Aging and orthopedics: How a lifespan development model can inform practice and research. Can. J. Surg. 59, 281–286.

Gentile, P., Chiono, V., Carmagnola, I., Hatton, P. V., 2014. An overview of poly(lactic-co-glycolic) Acid (PLGA)-based biomaterials for bone tissue engineering. Int. J. Mol. Sci. 15, 3640–3659.

Gilbert, J.A., Blaser, M.J., Caporaso, J.G., Jansson, J.K., Lynch, S. V., Knight, R., 2018.

Current understanding of the human microbiome. Nat. Med. 24, 392–400.

Goemans, C. V., Vertommen, D., Agrebi, R., Collet, J.F., 2018. CnoX Is a Chaperedoxin: A Holdase that Protects Its Substrates from Irreversible Oxidation. Mol. Cell 70, 614-627.e7.

Golding, C.G., Lamboo, L.L., Beniac, D.R., Booth, T.F., 2016. The scanning electron microscope in microbiology and diagnosis of infectious disease. Sci. Rep. 6, 1–8.

Goriainov, V., Hulsart-Billstrom, G., Sjostrom, T., Dunlop, D.G., Su, B., Oreffo, R.O.C., 2018. Harnessing Nanotopography to Enhance Osseointegration of Clinical Orthopedic Titanium Implants—An *in Vitro* and *in Vivo* Analysis. Front. Bioeng. Biotechnol. 6, 1–14.

Hall-Stoodley, L., Costerton, J.W., Stoodley, P., 2004. Bacterial biofilms: From the natural environment to infectious diseases. Nat. Rev. Microbiol. 2, 95–108.

Hasan, J., Jain, S., Chatterjee, K., 2017. Nanoscale Topography on Black Titanium Imparts Multi-biofunctional Properties for Orthopedic Applications. Sci. Rep. 7, 1–13.

Hasan, J., Webb, H.K., Truong, V.K., Pogodin, S., Baulin, V. a., Watson, G.S., Watson, J. a., Crawford, R.J., Ivanova, E.P., 2013. Selective bactericidal activity of nanopatterned superhydrophobic cicada *Psaltoda claripennis* wing surfaces. Appl. Microbiol. Biotechnol. 97, 9257–9262.

Hautefort, I, Proenca, M.J., Hinton, J.C.D, 2003. Single-Copy Green Fluorescent Protein Gene Fusions Allow Accurate Measurement of *Salmonella* Gene Expression *In Vitro* and during Infection of Mammalian Cells. Appl. Environ. Microbiol. 69, 7480-7491.

Hazell, G., Fisher, L.E., Murray, W.A., Nobbs, A.H., Su, B., 2018b. Bioinspired bactericidal surfaces with polymer nanocone arrays. J. Colloid Interface Sci. 528, 389–399.

Hazell, G., May, P.W., Taylor, P., Nobbs, A.H., Welch, C.C., Su, B., 2018a. Studies of black silicon and black diamond as materials for antibacterial surfaces. Biomater. Sci. 6, 1424–1432.

Hendriks, J.G.E., Van Horn, J.R., Van Der Mei, H.C., Busscher, H.J., 2004. Backgrounds of antibiotic-loaded bone cement and prosthesis-related infection. Biomaterials 25, 545–556.

Hermansson, M., 1999. The DLVO theory in microbial adhesion. Colloids Surfaces B Biointerfaces 14, 105–119.

Hernández-Gordillo, A., Hernández-Arana, A., Campero, A., Vera-Robles, L.I., 2014. Biomimetic sol-gel synthesis of TiO_2 and SiO_2 nanostructures. Langmuir 30, 4084–4093.

Hetrick, E.M., Schoenfisch, M.H., 2006. Reducing implant-related infections: Active release strategies. Chem. Soc. Rev. 35, 780–789.

Higaki, Y., Kobayashi, M., Murakami, D., Takahara, A., 2016. Anti-fouling behavior of polymer brush immobilized surfaces. Polym. J. 48, 325–331.

Hong, Y., Zeng, J., Wang, X., Drlica, K., Zhao, X., 2019. Post-stress bacterial cell death mediated by reactive oxygen species. Proc. Natl. Acad. Sci. U. S. A. 116, 10064–10071.

Honkanen, M., Jämsen, E., Karppelin, M., Huttunen, R., Eskelinen, A., Syrjänen, J., 2019. Periprosthetic Joint Infections as a Consequence of Bacteremia. Open Forum Infect. Dis. 6, 1–6.

Horsburgh, M.J., Clements, M.O., Crossley, H., Ingham, E., Foster, S.J., 2001. PerR controls oxidative stress resistance and iron storage proteins and is required for virulence in *Staphylococcus aureus*. Infect. Immun. 69, 3744–3754.

Hu, L., Huo, K., Chen, R., Zhang, X., Fu, J., Chu, P.K., 2010. Core-shell TiC/C quasi-aligned nanofiber arrays on biomedical Ti6Al4V for sensitive electrochemical biosensing. Chem. Commun. 46, 6828–6830.

Huo, K., Zhang, X., Hu, L., Sun, X., Fu, J., Huo, K., Zhang, X., Hu, L., Sun, X., Fu, J., 2008. One-step growth and field emission properties of quasialigned TiO_2 nanowire / carbon nanocone core-shell nanostructure arrays on Ti substrates. Appl. Phys. Lett. 93, 1–4.

Imlay, J. A., Linn, S., 1987. Mutagenesis and Stress Responses Induced in *Escherichia coli* by Hydrogen Peroxide. J Bacteriol. 169, 2967-2976.

Ingram, L.O., 1981. Mechanism of lysis of *Escherichia coli* by ethanol and other chaotropic agents. J. Bacteriol. 146, 331–336.

Ivanova, E.P., Hasan, J., Webb, H.K., Gervinskas, G., Juodkazis, S., Truong, V.K., Wu, A.H.F., Lamb, R.N., Baulin, V.A., Watson, G.S., Watson, J.A., Mainwaring, D.E.,

Crawford, R.J., 2013. Bactericidal activity of black silicon. Nat. Commun. 4, 1–7.

Ivanova, E.P., Hasan, J., Webb, H.K., Truong, V.K., Watson, G.S., Watson, J.A., Baulin, V.A., Pogodin, S., Wang, J.Y., Tobin, M.J., Löbbe, C., Crawford, R.J., 2012. Natural bactericidal surfaces: mechanical rupture of *Pseudomondas aeruginosa* cells by cicada wings. Small 8, 2489–2494.

James, E. H., Edwards, A.M., Wingneshweraraj, S, 2013. Transcriptional downregulation of agr expression in *Staphylococcus aureus* during growth in human serum can be overcome by constitutively active mutant forms of the sensor kinase AgrC. FEMS Microbiol Lett. 349, 153-162.

Jefferson, K.K., 2004. What drives bacteria to produce a biofilm? FEMS Microbiol. Lett. 236, 163–173.

Jenkins, J., Nobbs, A.H., Verkade, P., Su, B., 2018. Characterisation of bactericidal titanium surfaces using electron microscopy. Microsc. Anal. 34, 17–22.

Jiang, X., Herricks, T., Xia, Y., 2002. CuO Nanowires Can Be Synthesized by Heating Copper Substrates in Air. Nano Lett. 2, 1333–1338.

Joo, H.-S., Otto, M., 2012. Molecular basis of in-vivo biofilm formation by bacterial pathogens. Chem Biol. 19, 1503–1513.

Jordan, S., Hutchings, M.I., Mascher, T., 2008. Cell envelope stress response in Gram-positive bacteria. FEMS Microbiol. Rev. 32, 107–146.

Kang, S., Herzberg, M., F.Rodrigues, D., Elimelech, M., 2008. Antibacterial Effects of Carbon Nanotubes: Size Does Matter! Langmuir 24, 6409–6413.

Karami, A., 2010. Synthesis of TiO_2 nano powder by the sol-gel method and its use as a photocatalyst. J. Iran. Chem. Soc. 7, S154–S160.

Kasuga, T., Hiramatsu, M., Hoson, A., Sekino, T., Niihara, K., 1999. Titania nanotubes prepared by chemical processing. Adv. Mater. 11, 1307–1311.

Katsen-Globa, A., Puetz, N., Gepp, M.M., Neubauer, J.C., Zimmermann, H., 2016. Study of SEM preparation artefacts with correlative microscopy: Cell shrinkage of adherent cells by HMDS-drying. Scanning 38, 625–633.

Kaur, M., Muthe, K.P., Despande, S.K., Choudhury, S., Singh, J.B., Verma, N., Gupta, S.K.,

Yakhmi, J. V., 2006. Growth and branching of CuO nanowires by thermal oxidation of copper. J. Cryst. Growth 289, 670–675.

Kelleher, S.M., Habimana, O., Lawler, J., O' Reilly, B., Daniels, S., Casey, E., Cowley, A., 2016. Cicada wing surface topography: an investigation into the bactericidal properties of nanostructural features. ACS Appl. Mater. Interfaces 8, 14966–14974.

Kim, S., Jung, U.T., Kim, S.K., Lee, J.H., Choi, H.S., Kim, C.S., Jeong, M.Y., 2015. Nanostructured multifunctional surface with antireflective and antimicrobial characteristics. ACS Appl. Mater. Interfaces 7, 326–331.

Köller, M., Ziegler, N., Sengstock, C., Schildhauer, T.A., Ludwig, A., 2018. Bacterial cell division is involved in the damage of gram-negative bacteria on a nano-pillar titanium surface. Biomed. Phys. Eng. Express 4, 1–8.

Kong, K.-F., Schneper, L., Mathee, K., 2010. Beta-lactam Antibiotics: From Antibiosis to Resistance and Bacteriology. Apmis 118, 1–36.

Kumar, S., Sankara Narayanan, T.S.N., Ganesh Sundara Raman, S., Seshadri, S.K., 2010. Thermal oxidation of Ti6Al4V alloy: Microstructural and electrochemical characterization. Mater. Chem. Phys. 119, 337–346.

Kurtz, S., 2007. Projections of Primary and Revision Hip and Knee Arthroplasty in the United States from 2005 to 2030. J. Bone Jt. Surg. 89, 780.

Kurtz, S.M., Lau, E., Watson, H., Schmier, J.K., Parvizi, J., 2012. Economic burden of periprosthetic joint infection in the united states. J. Arthroplasty 27, 61–65.

Kwolek-Mirek, M., Zadrag-Tecza, R., 2014. Comparison of methods used for assessing the viability and vitality of yeast cells. FEMS Yeast Res. 14, 1068–1079.

Lee, H., Dregia, S., Akbar, S., Alhoshan, M., 2010. Growth of 1-D TiO_2 Nanowires on Ti and Ti Alloys by Oxidation. J. Nanomater. 2010, 1–7.

Lejeune, P., 2003. Contamination of abiotic surfaces: What a colonizing bacterium sees and how to blur it. Trends Microbiol. 11, 179–184.

Li, X., Chen, T., 2016. Enhancement and suppression effects of a nanopatterned surface on bacterial adhesion. Phys. Rev. E 93, 1–7.

Li, Z.W., Gao, W., Reeves, R.J., 2005. Zinc oxide films by thermal oxidation of zinc thin

films. Surf. Coatings Technol. 198, 319–323.

Lin, H., Zhang, M., Wang, F., Meng, F., Liao, B., Hong, H., Chen, J., Gao, W., 2014. A critical review of extracellular polymeric substances (EPSs) in membrane bioreactors: Characteristics, roles in membrane fouling and control strategies. J. Memb. Sci. 460, 110–125.

Lin, M.H., Shu, J.C., Huang, H.Y., Cheng, Y.C., 2012. Involvement of iron in biofilm formation by *Staphylococcus aureus*. PLoS One 7, 3–9.

Lin, N., Berton, P., Moraes, C., Rogers, R.D., Tufenkji, N., 2018. Nanodarts, nanoblades, and nanospikes: Mechano-bactericidal nanostructures and where to find them. Adv. Colloid Interface Sci. 252, 55–68.

Linklater, D.P., Juodkazis, S., Ivanova, E.P., 2017. Nanofabrication of mechano-bactericidal surfaces. Nanoscale 9, 16564–16585.

Linklater, D.P., Volder, M. De, Baulin, V.A., Werner, M., Jessl, S., Golozar, M., Maggini, L., Rubanov, S., Hanssen, E., Juodkazis, S., Ivanova, P., 2018. High Aspect Ratio Nanostructures Kill Bacteria via Storage and Release of Mechanical Energy. ACS Nano 12, 6657–6667.

Liu, S., Wei, L., Hao, L., Fang, N., Chang, M.W., Xu, R., Yang, Y., Chen, Y., 2009. Sharper and faster “Nano darts” kill more bacteria: A study of antibacterial activity of individually dispersed pristine single-walled carbon nanotube. ACS Nano 3, 3891–3902.

Luttrell, T., Halpegamage, S., Tao, J., Kramer, A., Sutter, E., Batzill, M., 2014. Why is anatase a better photocatalyst than rutile? - Model studies on epitaxial TiO_2 films. Sci. Rep. 4, 1–8.

Madeo, F., Fröhlich, E., Ligr, M., Grey, M., Sigrist, S.J., Wolf, D.H., Fröhlich, K.-U., 1999. Oxygen Stress: A Regulator of Apoptosis in Yeast. J. Cell Biol. 145, 757–767.

Madsen, J.S., Burmølle, M., Hansen, L.H., Sørensen, S.J., 2012. The interconnection between biofilm formation and horizontal gene transfer. FEMS Immunol. Med. Microbiol. 65, 183–195.

Magin, C.M., May, R.M., Drinker, M.C., Cuevas, K.H., Brennan, A.B., Reddy, S.T., 2015. Micropatterned Protective Membranes Inhibit Lens Epithelial Cell Migration in Posterior Capsule Opacification Model. Transl. Vis. Sci. Technol. 4, 1–9.

Mah, T.-F.C., Toole, G.A.O., 2001. Mechanisms of biofilm resistance to antimicrobial agents. Trends Microbiol. 9, 34–39.

Mann, E.E., Manna, D., Mettetal, M.R., May, R.M., Dannemiller, E.M., Chung, K.K., Brennan, A.B., Reddy, S.T., 2014. Surface micropattern limits bacterial contamination. Antimicrob. Resist. Infect. Control 3, 1–8.

Marmur, A., 2004. The lotus effect: Superhydrophobicity and metastability. Langmuir 20, 3517–3519.

Martino, D.P., Cafferini, N., Joly, B., Darfeuille-michaud, A., 2003. *Klebsiella pneumoniae* type 3 pili facilitate adherence and biofilm formation on abiotic surfaces 154, 9–16.

Mas-Moruno, C., Su, B., Dalby, M.J., 2019. Multifunctional Coatings and Nanotopographies: Toward Cell Instructive and Antibacterial Implants. Adv. Healthc. Mater. 8, 1–26.

Mcdougald, D., Rice, S.A., Barraud, N., Steinberg, P.D., Kjelleberg, S., 2011. Should we stay or should we go: mechanisms and ecological consequences for biofilm dispersal. Nat. Publ. Gr. 10, 39–50.

Medilanski, E., Kaufmann, K., Wick, L.Y., Wanner, O., Harms, H., 2002. Influence of the surface topography of stainless steel on bacterial adhesion. Biofouling 18, 193–203.

Mema, R., Yuan, L., Du, Q., Wang, Y., Zhou, G., 2011. Effect of surface stresses on CuO nanowire growth in the thermal oxidation of copper. Chem. Phys. Lett. 512, 87–91.

Mikulskis, P., Hook, A., Dundas, A.A., Irvine, D., Sanni, O., Anderson, D., Langer, R., Alexander, M.R., Williams, P., Winkler, D.A., 2018. Prediction of Broad-Spectrum Pathogen Attachment to Coating Materials for Biomedical Devices. ACS Appl. Mater. Interfaces 10, 139–149.

Miles, B.Y.A.A., Misra, S.S., 1938. The estimation of the bactericidal power of the blood. J Hyg (Lond). 38, 732–749.

Miller, M.B., Bassler, B.L., 2001. Quorum Sensing in Bacteria. Annu. Rev. Microbiol. 55, 165–199.

Mitchell, A.M., Silhavy, T.J., 2019. Envelope stress responses: balancing damage repair and toxicity. Nat. Rev. Microbiol. 17, 417–428.

Modaresifar, K., Azizian, S., Ganjian, M., Fratila-Apachitei, L.E., Zadpoor, A.A., 2019.

Bactericidal effects of nanopatterns: A systematic review. Acta Biomater. 83, 29–36.

Mohammadi, M.R., Fray, D.J., Mohammadi, A., 2008. Sol-gel nanostructured titanium dioxide: Controlling the crystal structure, crystallite size, phase transformation, packing and ordering. Microporous Mesoporous Mater. 112, 392–402.

Moran, E., Byren, I., Atkins, B.L., 2010. The diagnosis and management of prosthetic joint infections. J. Antimicrob. Chemother. 65, 45–54.

Morgan, D.L., 2010. Alkaline Hydrothermal Treatment of Titanate Nanostructures. A thesis presented to the Queensland University of Technology [Online]. Available at: https://eprints.qut.edu.au/39298/1/Dana_Morgan_Thesis.pdf (Accessed: 24 October 2019)

Mubarak, A., Hamzah, E., Toff, M.R.M., 2005. Review of physical vapour deposition (PVD) techniques for hard coating. J. Mek. 20, 42–51.

Murphy, C.N., Mortensen, M.S., Krogfelt, K.A., Clegg, S., 2013. Role of *Klebsiella pneumoniae* type 1 and type 3 fimbriae in colonizing silicone tubes implanted into the bladders of mice as a model of catheter-associated urinary tract infections. Infect. Immun. 81, 3009–3017.

Mytilineou, C., Kramer, B.C., Yabut, J.A., 2002. Glutathione depletion and oxidative stress. Park. Relat. Disord. 8, 385–387.

Neut, D., Dijkstra, R.J.B., Thompson, J.I., Kavanagh, C., van der Mei, H.C., Busscher, H.J., 2015. A biodegradable gentamicin-hydroxyapatite-coating for infection prophylaxis in cementless hip prostheses. Eur. Cells Mater. 29, 42–56.

Nobbs, A.H., Jenkinson, H.F., 2015. Interkingdom networking within the oral microbiome. Microbes Infect. 17, 484–492.

Noor Mohammad, S., 2008. Investigation of the oxide-assisted growth mechanism for nanowire growth and a model for this mechanism. J. Vac. Sci. Technol. B Microelectron. Nanom. Struct. 26, 1993–2007.

Noor Mohammad, S., 2009. For nanowire growth, vapor-solid-solid (vapor-solid) mechanism is actually vapor-quasisolid-solid (vapor-quasiliquid-solid) mechanism. J. Chem. Phys. 131, 1–13.

Nowlin, K., Boseman, A., Covell, A., LaJeunesse, D., 2014. Adhesion-dependent rupturing of *Saccharomyces cerevisiae* on biological antimicrobial nanostructured surfaces. J. R. Soc. Interface 12, 1–12.

O'Neill, J., 2014. Antimicrobial Resistance: Tackling a crisis for the health and wealth of nations [Online]. Availible at: https://amr-review.org/Publications.html (Accessed: 12 September 2019).

Olivi, M., Zanni, E., De Bellis, G., Talora, C., Sarto, M.S., Palleschi, C., Flahaut, E., Monthioux, M., Rapino, S., Uccelletti, D., Fiorito, S., 2013. Inhibition of microbial growth by carbon nanotube networks. Nanoscale 5, 9023–9029.

Osmon, D.R., Berbari, E.F., Berendt, A.R., Lew, D., Zimmerli, W., Steckelberg, J.M., Rao, N., Hanssen, A., Wilson, W.R., 2013. Diagnosis and management of prosthetic joint infection: Clinical practice guidelines by the infectious diseases Society of America. Clin. Infect. Dis. 56, 1–25.

Panáček, A., Kvítek, L., Smékalová, M., Večeřová, R., Kolář, M., Röderová, M., Dyčka, F., Šebela, M., Prucek, R., Tomanec, O., Zbořil, R., 2018. Bacterial resistance to silver nanoparticles and how to overcome it. Nat. Nanotechnol. 13, 65–71.

Paul, K., Brunstetter, D., Titen, S., Blair, D.F., 2011. A molecular mechanism of direction switching in the flagellar motor of *Escherichia coli*. Proc. Natl. Acad. Sci. U. S. A. 108, 17171–17176.

Peng, X., Chen, A., 2004. Aligned TiO_2 nanorod arrays synthesized by oxidizing titanium with acetone. J. Mater. Chem. 14, 2542–2548.

Peng, X., Wang, J., Thomas, D.F., Chen, A., 2005. Tunable growth of TiO_2 nanostructures on Ti substrates. Nanotechnology 16, 2389–2395.

Petryayeva, E., Krull, U.J., 2011. Localized surface plasmon resonance: Nanostructures, bioassays and biosensing-A review. Anal. Chim. Acta 706, 8–24.

Pitarresi, G., Palumbo, F.S., Calascibetta, F., Fiorica, C., Di Stefano, M., Giammona, G., 2013. Medicated hydrogels of hyaluronic acid derivatives for use in orthopedic field. Int. J. Pharm. 449, 84–94.

Pogodin, S., Hasan, J., Baulin, V.A., Webb, H.K., Truong, V.K., Phong Nguyen, T.H., Boshkovikj, V., Fluke, C.J., Watson, G.S., Watson, J.A., Crawford, R.J., Ivanova, E.P.,

2013. Biophysical model of bacterial cell interactions with nanopatterned cicada wing surfaces. Biophys. J. 104, 835–840.

Porter, M., Borroff, M., Gregg, P., MacGregor, A., Tucker, K., 2013. National Joint Registry 10th Annual Report [Online]. Available at: http://www.njrcentre.org.uk/njrcentre/Reports-Publications-and-Minutes/Annual-reports/Archived-annual-reports (Accessed: 12 September 2019)

Porter, M., Howard, P., Lawrence, S., Reed, M., Stonadge, J., Wilkinson, M., 2018. National Joint Registry 15th Annual Report [Online]. Available at: http://www.njrcentre.org.uk/njrcentre/Reports-Publications-and-Minutes/Annual-reports/Archived-annual-reports (Accessed: 12 September 2019)

Pozo, J.L. Del, Patel, R., 2009. Infection Associated with Prosthetic Joints. N Engl J Med 361, 787–794.

Pratt, L.A., Kolter, R., 1998. Genetic analysis of *Escherichia coli* biofilm formation: roles of flagella, motility, chemotaxis and type I pili 30, 285–293.

Price, J.S., Tencer, A.F., Arm, D.M., Bohach, G.A., 1996. Controlled release of antibiotics from coated orthopedic implants. J. Biomed. Mater. Res. 30, 281–6.

Qin, Y., He, Y., She, Q., Larese-Casanova, P., Li, P., Chai, Y., 2019. Heterogeneity in respiratory electron transfer and adaptive iron utilization in a bacterial biofilm. Nat. Commun. 10, 3702.

Rahimpour, M., Montero, M., Almagro, G., Viale, A.M., Sevilla, Á., Cánovas, M., Muñoz, F.J., Baroja-Fernández, E., Bahaji, A., Eydallin, G., Dose, H., Takeuchi, R., Mori, H., Pozueta-Romero, J., 2013. GlgS, described previously as a glycogen synthesis control protein, negatively regulates motility and biofilm formation in *Escherichia coli*. Biochem. J. 452, 559–573.

Rahman, M.M., Ninomiya, K., Ogino, C., Shimizu, N., 2010. Ultrasound-induced membrane lipid peroxidation and cell damage of *Escherichia coli* in the presence of non-woven TiO_2 fabrics. Ultrason. Sonochem. 17, 738–743.

Rajavel, K., Gomathi, R., Manian, S., Rajendra Kumar, R.T., 2014. *In vitro* bacterial cytotoxicity of CNTs: Reactive oxygen species mediate cell damage edges over direct physical puncturing. Langmuir 30, 592–601.

Riss, T.L., Moravec, R.A., Niles, A.L., Duellman, S., Benink, H.A., Worzella, T.J., Minor, L., 2016. Cell Viability Assays [Online]. Available at: https://www.ncbi.nlm.nih.gov/books/NBK144065/ (Accessed: 24 October 2019)

Rizzello, L., Galeone, A., Vecchio, G., Brunetti, V., Sabella, S., Pompa, P.P., 2012. Molecular response of *Escherichia coli* adhering onto nanoscale topography. Nanoscale Res. Lett. 7, 2–8.

Rizzello, L., Sorce, B., Sabella, S., Vecchio, G., Galeone, A., Brunetti, V., Cingolani, R., Pompa, P.P., 2011. Impact of nanoscale topography on genomics and proteomics of adherent bacteria. ACS Nano 5, 1865–1876.

Romanò, C.L., Malizos, K., Capuano, N., Mezzoprete, R., D'Arienzo, M., Van Der Straeten, C., Scarponi, S., Drago, L., 2016. Does an Antibiotic-Loaded Hydrogel Coating Reduce Early Post-Surgical Infection After Joint Arthroplasty? J. Bone Jt. Infect. 1, 34–41.

Romanò, C.L., Scarponi, S., Gallazzi, E., Romanò, D., Drago, L., 2015. Antibacterial coating of implants in orthopaedics and trauma: A classification proposal in an evolving panorama. J. Orthop. Surg. Res. 10, 1–11.

Roosjen, A., Van Der Mei, H.C., Busscher, H.J., Norde, W., 2004. Microbial adhesion to poly(ethylene oxide) brushes: Influence of polymer chain length and temperature. Langmuir 20, 10949–10955.

Roser, M., 2019. Life Expectancy [Online]. Available at: https://ourworldindata.org/life-expectancy (Accessed: 12 September 2019)

Sahoo, S., Rao, K.K., Suraishkumar, G.K., 2006. Reactive Oxygen Species Induced by Shear Stress Mediate Cell Death in *Bacillus subtilis*. Biotechnol. Bioeng. 94, 118–127.

Sahoo, S., Verma, R.K., Suresh, A.K., Rao, K.K., Bellare, J., Suraishkumar, G.K., 2003. Macro-Level and Genetic-Level Responses of *Bacillus subtilis* to Shear Stress. Biotechnol. Prog. 19, 1689–1696.

Sauer, K., 2003. The genomics and proteomics of biofilm formation. Genome 4, 1–5.

Sebastian, V., Arruebo, M., Santamaria, J., 2014. Reaction engineering strategies for the production of inorganic nanomaterials. Small 10, 835–853.

Semchyshyn, H., 2009. Hydrogen peroxide-induced response in *E. coli* and *S. cerevisiae*:

different stages of the flow of the genetic information. Cent. Eur. J. Biol. 4, 142-153

Sendi, P., Frei, R., Maurer, T.B., Trampuz, A., Zimmerli, W., Graber, P., 2010. *Escherichia coli* variants in periprosthetic joint infection: Diagnostic challenges with sessile bacteria and sonication. J. Clin. Microbiol. 48, 1720–1725.

Sengstock, C., Lopian, M., Motemani, Y., Borgmann, A., Khare, C., Buenconsejo, P.J.S., Schildhauer, T.A., Ludwig, A., Köller, M., 2014. Structure-related antibacterial activity of a titanium nanostructured surface fabricated by glancing angle sputter deposition. Nanotechnology 25, 1–11.

Shah, F.A., Trobos, M., Thomsen, P., Palmquist, A., 2016. Commercially pure titanium (cp-Ti) versus titanium alloy (Ti6Al4V) materials as bone anchored implants - Is one truly better than the other? Mater. Sci. Eng. C 62, 960–966.

Shannon, P., Markiel, A., Ozier, O., Baliga, N.S., Wang, J.T., Ramage, D., Amin, N., Schwikowski, B., Ideker, T., 2003. Cytoscape: A Software Environment for Integrated Models of Biomolecular Interaction Networks. Genome Res. 13, 2498–2504.

Shi, L., Günther, S., Hübschmann, T., Wick, L.Y., Harms, H., Müller, S., 2007. Limits of propidium iodide as a cell viability indicator for environmental bacteria. Cytom. Part A 71, 592–598.

Shiu, C., Zhang, Z., Thomas, C.R., 1999. A novel technique for the study of bacterial cell mechanical properties. Biotechnol. Tech. 13, 707–713.

Shiu, J.Y., Kuo, C.W., Chen, P., Mou, C.Y., 2004. Fabrication of Tunable Superhydrophobic Surfaces by Nanosphere Lithography. Chem. Mater. 16, 561–564.

Silhavy, T.J., Kahne, D., Walker, S., 2010. The bacterial cell envelope. Cold Spring Harb. Perspect. Biol. 2, 1–16.

Silva, L.C.N. da, Diniz, R.C., Lima, I.M. de S.F., Santos, C.I. dos, Alves, M.S., Souza, L.I.O. de, Monteiro, A. de S., 2017. SOS response and *Staphylococcus aureus*: Implication for Drug Development. Intech Chapter 6, 95–108.

Sjöström, T., Nobbs, A.H., Su, B., 2016. Bactericidal nanospike surfaces via thermal oxidation of Ti alloy substrates. Mater. Lett. 167, 22–26.

Slauch, J.M., 2012. How does the oxidative burst of macrophages kill bacteria? Still an open

question. Mol Microbiol. 18, 1089–1098.

Spurr, R.A., Myers, H., 1957. Quantitative Analysis of Anatase-Rutile Mixtures with an X-Ray Diffractometer. Anal. Chem. 29, 760–762.

International Organisation for Standarisation (ISO) 2007. Plastics-Measurement of antibacterial activity on plastics surfaces [Online]. Available at: https://www.iso.org/standard/40759.html (Accessed: 12 September 2019).

Stefánsdóttir, A., Johansson, D., Knutson, K., Lidgren, L., Robertsson, O., 2009. Microbiology of the infected knee arthroplasty: report from the Swedish Knee Arthroplasty Register on 426 surgically revised cases. Scand. J. Infect. Dis. 41, 831–840.

Stewart, P.S., 2002. Mechanisms of Antibiotic Resistance in Campylobacter. Int. J. Med. Microbiol. 292, 107–113.

Stewart, P.S., 2015. Antimicrobial Tolerance in Biofilms. Microbiol. Spectr. 3, 1–30.

Stiefel, P., Schmidt-Emrich, S., Maniura-Weber, K., Ren, Q., 2015. Critical aspects of using bacterial cell viability assays with the fluorophores SYTO9 and propidium iodide. BMC Microbiol. 15, 1–9.

Stocks, S.M., 2004. Mechanism and use of the commercially available viability stain, BacLight. Cytom. Part A 61, 189–195.

Storey, A., 2018. Living longer - how our population is changing and why it matters [Online]. Available at: https://www.ons.gov.uk/peoplepopulationandcommunity/birthsdeathsandmarriages/ageing/articles/livinglongerhowourpopulationischangingandwhyitmatters/2018-08-13 (Accessed: 12 September 2019)

Su, R., Bechstein, R., Sø, L., Vang, R.T., Sillassen, M., Esbjörnsson, B., Palmqvist, A., Besenbacher, F., 2011. How the anatase-to-rutile ratio influences the photoreactivity of TiO_2. J. Phys. Chem. C 115, 24287–24292.

Sugiyama, M., Kumagai, T., Matsuo, H., Alam Bhuiyan, Z., Ueda, K., Mochizuki, H., Nakamura, N., Davies, J.E., 1995. Overproduction of the bleomycin-binding proteins from bleomycin-producing *Streptomyces verticillus* and a methicillin-resistant *Staphylococcus aureus* in *Escherichia coli* and their immunological characterisation.

FEBS Lett. 362, 80–84.

Suo, Z., Avci, R., Deliorman, M., Yang, X., Pascual, D.W., 2009. Bacteria Survive Multiple Puncturings of Their Cell Walls 25, 4588–4594.

Szklarczyk, D., Gable, A.L., Lyon, D., Junge, A., Wyder, S., Huerta-Cepas, J., Simonovic, M., Doncheva, N.T., Morris, J.H., Bork, P., Jensen, L.J., Von Mering, C., 2019. STRING v11: Protein-protein association networks with increased coverage, supporting functional discovery in genome-wide experimental datasets. Nucleic Acids Res. 47, 607–613.

Tan, A.W., Ismail, R., Chua, K.H., Ahmad, R., Akbar, S.A., Pingguan-Murphy, B., 2014. Osteogenic potential of *in situ* TiO_2 nanowire surfaces formed by thermal oxidation of titanium alloy substrate. Appl. Surf. Sci. 320, 161–170.

Tande, A.J., Patel, R., 2014. Prosthetic joint infection. Clin. Microbiol. Rev. 27, 302–345.

Tecan Group Ltd, 2010. Infinite ® 200 PRO – luminescence sensitivity [Online]. Available at: https://lifesciences.tecan.com/plate_readers/infinite_200_pro (Accessed: 12 September 2019).

Thomas, W.E., Nilsson, L.M., Forero, M., Sokurenko, E. V., Vogel, V., 2004. Shear-dependent "stick-and-roll" adhesion of type 1 fimbriated *Escherichia coli*. Mol. Microbiol. 53, 1545–1557.

Tripathy, A., Sen, P., Su, B., Briscoe, W.H., 2017. Natural and bioinspired nanostructured bactericidal surfaces. Adv. Colloid Interface Sci. 248, 85–104.

Vadillo-Rodriguez, V., Dutcher, J.R., 2011. Viscoelasticity of the bacterial cell envelope. Soft Matter 4101–4110.

Vadillo-Rodriguez, V., Schooling, S.R., Dutcher, J.R., 2009. *In situ* characterization of differences in the viscoelastic response of individual gram-negative and gram-positive bacterial cells. J. Bacteriol. 191, 5518–5525.

Valour, F., Trouillet-Assant, S., Rasigade, J.P., Lustig, S., Chanard, E., Meugnier, H., Tigaud, S., Vandenesch, F., Etienne, J., Ferry, T., Laurent, F., 2013. *Staphylococcus epidermidis* in Orthopedic Device Infections: The Role of Bacterial Internalization in Human Osteoblasts and Biofilm Formation. PLoS One 8, 1–11.

Van De Belt, H., Neut, D., Schenk, W., Van Horn, J.R., Van Der Mei, H.C., Busscher, H.J., 2001. *Staphylococcus aureus* biofilm formation on different gentamicin-loaded polymethylmethacrylate bone cements. Biomaterials 22, 1607–1611.

Vatansever, F., de Melo, W.C.M.A., Avci, P., Vecchio, D., Sadasivam, M., Gupta, A., Chandran, R., Karimi, M., Parizotto, N.A., Yin, R., Tegos, G.P., Hamblin, M.R., 2013. Antimicrobial strategies centered around reactive oxygen species - bactericidal antibiotics, photodynamic therapy, and beyond. FEMS Microbiol. Rev. 37, 955–989.

Virginia Sáenz de Viteri and Elena Fuentes, 2013. Titanium and Titanium Alloys as Biomaterials, Tribology - Fundamentals and Advancements. Jürgen Gegner, IntechOpen 55, 561–565.

Vogel, K., Westphal, N., Salz, D., Thiel, K., Wittig, L., Ciacchi, L.C., Grunwald, I., 2014. Dental implants coated with a durable and antibacterial film. Surf. Innov. 3, 27–38.

Von Eiff, C., Jansen, B., Kohnen, W., Becker, K., 2005. Infections associated with medical devices: Pathogenesis, management and prophylaxis. Drugs 65, 179–214.

Wang, G., Li, J., Lv, K., Zhang, W., Ding, X., Yang, G., Liu, X., Jiang, X., 2016. Surface thermal oxidation on titanium implants to enhance osteogenic activity and *in vivo* osseointegration. Sci. Rep. 6, 1–13.

Watson, G.S., Green, D.W., Schwarzkopf, L., Li, X., Cribb, B.W., Myhra, S., Watson, J.A., 2015. A gecko skin micro/nano structure - A low adhesion, superhydrophobic, anti-wetting, self-cleaning, biocompatible, antibacterial surface. Acta Biomater. 21, 109–122.

Westall, F., De Wit, M.J., Dann, J., Van der Gaast, S., De Ronde, C.E.J., Gerneke, D., 2001. Early archean fossil bacteria and biofilms in hydrothermally-influenced sediments from the Barberton greenstone belt, South Africa. Precambrian Res. 106, 93–116.

Whitehead, K.A., Colligon, J., Verran, J., 2005. Retention of microbial cells in substratum surface features of micrometer and sub-micrometer dimensions. Colloids Surfaces B Biointerfaces 41, 129–138.

Whitehead, K.A., Verran, J., 2006. The effect of surface topography on the retention of microorganisms. Food Bioprod. Process. 84, 253–259.

Wolf, C., Hochgräfe, F., Kusch, H., Albrecht, D., Hecker, M., Engelmann, S., 2008. Proteomic analysis of antioxidant strategies of *Staphylococcus aureus*: Diverse

responses to different oxidants. J. Proteomics. 8, 3139-3153.

World Health Organization, 2018. Obesity and Overweigth Factsheet [Online]. Available at: https://www.who.int/news-room/fact-sheets/detail/obesity-and-overweight (Accessed: 12 September 2019)

Wysocki, B., Maj, P., Sitek, R., Buhagiar, J., Kurzydłowski, K., Święszkowski, W., 2017. Laser and Electron Beam Additive Manufacturing Methods of Fabricating Titanium Bone Implants. Appl. Sci. 7, 657.

Xu, C., Yang, X., Shi, S.Q., Liu, Y., Surya, C., Woo, C., 2008. Effects of local gas-flow field on synthesis of oxide nanowires during thermal oxidation. Appl. Phys. Lett. 92, 3–5.

Xu, C.H., Woo, C.H., Shi, S.Q., 2004. The effects of oxidative environments on the synthesis of CuO nanowires on Cu substrates. Superlattices Microstruct. 36, 31–38.

Xue, F., Liu, J., Guo, L., Zhang, L., Li, Q., 2015. Theoretical study on the bactericidal nature of nanopatterned surfaces. J. Theor. Biol. 385, 1–7.

Yang, D., Wijenayaka, A.R., Solomon, L.B., Pederson, S.M., Findlay, D.M., Kidd, S.P., Atkins, G.J., 2018. Novel insights into *Staphylococcus aureus* deep bone infections: The involvement of osteocytes. MBio 9, 1–10.

Yao, J.H., 1993. Theory and simulation of Ostwald ripening. Phys. reveiw B 47, 110–125.

Yoda, I., Koseki, H., Tomita, M., Shida, T., Horiuchi, H., Sakoda, H., Osaki, M., 2014. Effect of surface roughness of biomaterials on *Staphylococcus epidermidis* adhesion. BMC Microbiol. 14, 1–7.

Yoshimitsu, Z., Nakajima, A., Watanabe, T., Hashimoto, K., 2002. Effects of surface structure on the hydrophobicity and sliding behavior of water droplets. Langmuir 18, 5818–5822.

Yu, C.L., Zhenhua, F., Goldberg, M., Richardson, C., Gruber, D., JianSheng, G., Leisch, N., Muller, W., Rensing, K., BoTao, Z., 2014. Application Booklet Leica EM CPD300 Automated Critical Point Dryer [Online]. Available at: https://downloads.leica-microsystems.com/Leica%20EM%20CPD300/Application%20Notes/EMCPD300_Application_Booklet_05_15_screen.pdf (Accessed: 12 September 2019).

Yu, M., Chen, R., Jia, Z., Chen, J., Lou, J., Tang, S., Zhang, X., 2016. MWCNTs Induce

ROS Generation, ERK Phosphorylation, and SOD-2 Expression in Human Mesothelial Cells. Int. J. Toxicol. 35, 17–26.

Zhang, X., Huo, K., Wang, H., Gao, B., Fu, J., Hung, T.F., Chu, P.K., 2012. Controlled fabrication of core-shell TiO_2/C and TiC/C nanofibers on Ti foils and their field-emission properties. ACS Appl. Mater. Interfaces 4, 1037–1042.

Zhang, X., Shi, F., Yu, X., Liu, H., Fu, Y., Wang, Z., Jiang, L., Li, X., 2004. Polyelectrolyte Multilayer as Matrix for Electrochemical Deposition of Gold Clusters: Toward Super-Hydrophobic Surface. J. Am. Chem. Soc. 126, 3064–3065.

Zhang, X., Wang, L., Levänen, E., 2013. Superhydrophobic surfaces for the reduction of bacterial adhesion. RSC Adv. 3, 12003–12020.

LIST OF ABBREVIATIONS

Abbreviation	Meaning
2D	Two dimensional
3D	Three dimensional
ALP	Alkaline phosphatase
AMR	Antimicrobial resistance
Ar	Argon
ATP	Adenosine triphosphate
BCC	Body centred cubic
BHI	Brain Heart Infusion
bSi	Black silicon
BSP	Bone sialoprotein
BTG	BacTiter-Glo
CDC	Centre for Disease Control and Prevention
CDS	National chemical database service
CH_3	Methyl radical
CLNW	Cone-like nanowire
CLSM	Confocal laser scanning microscopy
CNT	Carbon nanotubes
CO	Carbon monoxide
CO_2	Carbon dioxide
CoNS	Coagulase negative staphylococci
CPD	Critical point drying
CVD	Chemical vapour deposition
DAC	Defensive antibacterial coating
DEP	Differentially expressed protein
DSA	Drop shape analyser
DVLO	Derjagiun, Verwey, Landau and Overbeek
EBSD	Electron backscatter diffraction
EDAX	Energy dispersive X-ray spectroscopy
EDX	Energy dispersive X-ray spectroscopy
EPS	Extracellular polymeric substance
ETD	Everhart-Thornley detector
EU	European Union
FDR	False discovery rate
FIB-SEM	Focussed ion beam scanning electron microscopy
GFP	Green fluorescent protein
GIXD	Grazing incidence X-ray diffraction
GSH	Glutathione
H_2O	Water
H_2O_2	Hydrogen peroxide
HCl	Hydrochloric acid
HCP	Hexagonal close-packed
HSNLNW	Horseshoe nail-like nanowire
ICSD	Inorganic crystal structure database
LASX	Leica application suite X
LB	Luria Bertani

LDH	Lactate dehydrogenase
LSPR	Localised surface plasmon resonance
MDK	Minimum duration of killing
MDR	Multidrug resistant
MH	Mueller Hinton
MIC	Minimum inhibitory concentration
MP	Micropattern
MRSA	Methicillin resistance *Staphylococcus aureus*
MSSA	Methicillin sensitive *Staphylococcus aureus*
MWCNT	Multi walled carbon nanotubes
NB	Nutrient broth
NHS	National Health Service
NIH	National Institute for Health
NJR	National Joint Registry
NP	Nanoparticle
np-Au	Gold nanoparticles
NW	Nanowire
O_2	Oxygen
OCN	Osteocalcin
OD_{600}	Optical density at 600 nm
OIM	Orientation imaging microscopy
OPN	Osteopontin
OTO	Osmium tetraoxide-Thiocarbohydrazide-Osmium
PBS	Phosphate buffered saline
PDMSe	Poly(dimethyl siloxane) elastomer
PEG	Poly(ethylene glycol)
PEO	Poly(ethylene oxide)
PET	Poly(ethylene terephthalate)
PI	Propidium iodide
PJI	Prosthetic joint infection
PJR	Prosthetic joint replacement
pl-Au	Planar gold
PLGA	Polylactide-co-glycolide
PMMA	Polymethylmethacrylate
PVD	Physical vapour deposition
RFU	Relative fluorescence unit
RIE	Reactive ion etching
RLNW	Rod-like nanowire
RLU	Relative luminescence unit
ROS	Reactive oxygen species
RTG	RealTime-Glo
Runx2	Runt-related transcription factor
SCCM	Standard cubic centimetres per minute
SCDLP	Soybean casein digest broth with lecithin and polyoxyethylene sorbitan monooleate
SEM	Scanning electron microscopy
SiC	Silicon carbide
SSI	Surgical site infections
SWCNT	Single walled carbon nanotubes
TEM	Transmission electron microscopy

TiC	Titanium carbide
TiO_2	Titanium dioxide
TMT	Tandem mass tagging
Tris HCl	Tris(hydroxymethyl)aminomethane – hydrochloric acid buffer
TSB	Tryptone Soya Broth
UK	United Kingdom
UV	Ultraviolet
VACNT	Vertically aligned carbon nanotubes
VLS	Vapour-liquid solid
WCA	Water contact angle
WHO	World Health Organisation
XDVLO	Extended DVLO